

The Pennsylvania State University
The Graduate School
Intercollege Graduate Program in Materials

**NONLINEAR FINITE ELEMENT MODELING
AND ANALYSIS OF A TRUCK TIRE**

A Thesis in
Materials

by
Seokyong Chae

© 2006 Seokyong Chae

Submitted in Partial Fulfillment
of the Requirements
for the Degree of

Doctor of Philosophy

August 2006

The thesis of Seokyong Chae was reviewed and approved* by the following:

Moustafa El-Gindy
Senior Research Associate, Applied Research Laboratory
Thesis Co-Advisor
Co-Chair of Committee

James P. Runt
Professor of Materials Science and Engineering
Thesis Co-Advisor
Co-Chair of Committee
Co-Chair of the Intercollege Graduate Program in Materials

Charles E. Bakis
Professor of Engineering Science and Mechanics

Ashok D. Belegundu
Professor of Mechanical Engineering

*Signatures are on file in the Graduate School.

ABSTRACT

For an efficient full vehicle model simulation, a multi-body system (MBS) simulation is frequently adopted. By conducting the MBS simulations, the dynamic and steady-state responses of the sprung mass can be shortly predicted when the vehicle runs on an irregular road surface such as step curb or pothole. A multi-body vehicle model consists of a sprung mass, simplified tire models, and suspension system to connect them. For the simplified tire model, a rigid ring tire model is mostly used due to its efficiency.

The rigid ring tire model consists of a rigid ring representing the tread and the belt, elastic sidewalls, and rigid rim. Several in-plane and out-of-plane parameters need to be determined through tire tests to represent a real pneumatic tire. Physical tire tests are costly and difficult in operations. Thus, the parameters for the rigid ring tire model are alternatively predicted by conducting virtual tire tests using a finite element analysis (FEA) tire model.

A nonlinear three-dimensional FEA tire model representing a truck tire, 295/75R22.5, is constructed by implementing three-layered membrane elements, hyperelastic solid elements, and beam elements. Then, the FEA tire model is validated by comparing its in-plane and out-of-plane responses with physical measurements. The virtual and physical responses show good agreements. After successful validations of the FEA tire model, virtual tire tests are conducted to predict the in-plane and out-of-plane parameters for the rigid ring tire models for the first time using an FEA tire model.

The predicted parameters are implemented in the rigid ring tire model, and the model undergoes water drainage ditches 90° and 45° to the tire running direction to predict dynamic in-plane and out-of-plane tire responses at various tire loads. Vertical displacement of the tire spindle, tire contact forces, and moments are plotted and compared with those of the FEA tire model. The in-plane tire responses show good

agreements between the results of the two models. On the other hand, the out-of-plane tire responses are relatively not in good agreements due to the significantly different tire contact area geometries of the two tire models on the 45° ditch.

In the simulations of the FEA and rigid ring tire models, only constant vertical tire load is applied to the tire models. Additional tire load due to the vertical acceleration of the sprung mass during tire operations is not considered. Thus, a sprung mass and suspension system is assembled with the tire models to include the effect of the vertical sprung mass motion, which represents a quarter-vehicle model and a closer model to real vehicle applications. Then, the models undergo a 90° ditch at various running speeds. The vertical accelerations of the tire spindles are predicted during the ditch runs and compared with measurements to check whether or not the rigid ring tire model in the quarter-vehicle environment predicts acceptable responses.

Modern high computational capability enables to establish a reliable virtual tire and quarter-vehicle model test environments. The developed quarter-vehicle model predicts not only dynamic tire responses but also sprung mass responses to irregular road surface inputs. Thus, a trustworthy quarter-vehicle model can replace the conventional field durability tests, which saves product development cost and time. In addition, virtual tests under similar conditions can be easily repeated. Higher quality products at lower cost are undoubtedly promising.

TABLE OF CONTENTS

LIST OF FIGURES	x
LIST OF TABLES.....	xiv
NOMENCLATURE.....	xv
ACKNOWLEDGEMENT.....	xvii
CHAPTER 1: INTRODUCTION	1
1.1 History of the Wheel and Tire	3
1.2 Objectives	5
1.3 Methodology	6
1.4 Statement of the Work	7
CHAPTER 2: LITERATURE SURVEY	10
2.1 Tire Axis System, Tire Forces, and Moments Definitions	10
2.1.1 Tire axis system	10
2.1.2 Tire forces and moments	11
2.1.2.1 Tire longitudinal force	12
2.1.2.2 Tire lateral force	15
2.1.2.3 Tire vertical force	18
2.1.2.4 Tire overturning moment	20
2.1.2.5 Tire rolling resistance moment	21
2.1.2.6 Tire vertical moment	21
2.2 Tire Models	21
2.2.1 Early Tire Models	23
2.2.2 Finite Element Analysis Tire models	31
2.3 Contact and Sliding Interfaces	44
2.3.1 Computational Contact Solution Algorithms	44
2.3.1.1 Contact search algorithm	46
2.3.1.2 Contact interface algorithm	49
2.3.2 Lagrange Multiplier Method	50
2.3.3 Penalty Method	51
2.4 Experimental Tire Testing	55

2.5 Tire Rubber Material Modeling	60
2.6 Summary	66
CHAPTER 3: NONLINEAR FINITE ELEMENT ANALYSIS TRUCK	
TIRE MODELING	67
3.1 Tire Structure, Its Components, and Materials	69
3.1.1 Carcass	70
3.1.2 Belts	71
3.1.3 Tread and Treadbase	72
3.1.4 Beads	73
3.1.5 Aspect Ratio	73
3.2 Tire Structure and Material Modeling	75
3.2.1 FEA Modeling on Carcass and Belts Using Membrane Elements	76
3.2.2 FEA Modeling on Tread, Treadbase, Tread Shoulders, Bead Fillers Using Solid Elements	81
3.2.3 FEA Modeling of Beads	83
3.2.4 FEA Rim Model	85
3.3 FEA Tire-Rim Assembly Model	87
3.4 Various Virtual Tire Test Environments	88
3.4.1 Combined FEA Truck Tire and a Rigid Flat Road Model	89
3.4.2 Combined FEA Truck Tire and a Rigid Cleat-Drum Model	90
3.4.3 Combined FEA Truck Tire and a Rigid Smooth Drum Model ...	91
3.4.4 Combined FEA Truck Tire and a Rigid Road with Water Drainage Ditches Model	92
3.5 Summary	92
CHAPTER 4: FEA TRUCK TIRE MODEL VALIDATION	
4.1 Static Validation Tests	94
4.1.1 Tire Vertical Load-Deflection Relationship	94
4.1.2 Footprint Area	96
4.2 Dynamic Validation Tests	98
4.2.1 First Mode of Free Vertical Vibration Test	99
4.2.2 Cornering Test	101
4.2.3 Yaw Oscillation Test	103
4.2.3.1 Amplitude Ratio and Phase Angle	104

4.2.3.2 Virtual Yaw Oscillation Test Using FEA	
Truck Tire Model	106
4.3 Summary	109
CHAPTER 5: DETERMINATION OF THE IN-PLANE AND OUT-OF-PLANE PARAMETERS OF A RIGID RING TIRE MODEL USING THE FEA TRUCK TIRE MODEL 111	
5.1 In-Plane Parameters Determination	112
5.1.1 Effective Rolling Radius	114
5.1.2 In-Plane Translational Stiffness of the Sidewall and Residual Vertical Stiffness at Contact Area	116
5.1.3 In-Plane Longitudinal and Vertical Damping Constants of Sidewall and Residual Damping Constant at Contact Area	117
5.1.4 In-Plane Rotational Stiffness and Damping Constant of the Sidewall	118
5.1.4.1 In-Planed Rotational Stiffness of the Sidewall	119
5.1.4.2 In-Planed Rotational Damping Constant of the Sidewall	119
5.1.5 Longitudinal Tread Stiffness and Longitudinal Slip Stiffness ...	121
5.1.5.1 Longitudinal Slip Stiffness	123
5.1.5.2 Longitudinal Tread Stiffness	123
5.1.6 Comparison of In-plane Tire Responses between the FEA and Rigid Ring Tire Models	124
5.1.6.1 90° Water Drainage Ditch Profile	125
5.1.6.2 Comparison of the Predicted Vertical Displacements .	125
5.1.6.3 Comparison of the Predicted Longitudinal Contact Forces	127
5.1.6.4 Comparison of the Predicted Vertical Contact Forces .	129
5.2 Out-of-Plane Parameters Determination	131
5.2.1 Out-of-Plane Translational Stiffness and Damping Constant of the Sidewall	132
5.2.2 Out-of-Plane Rotational Stiffness and Damping Constant of the Sidewall	134
5.2.3 Lateral Free Vibration Tests	137
5.2.4 Cornering Stiffness	139

5.2.5. Self-Aligning Stiffness	139
5.2.6 Relaxation Length	140
5.2.7 Comparison of Out-of-Plane Tire Responses between the FEA and Rigid Ring Tire Models	141
5.2.7.1 45° Water Drainage Ditch Profile	142
5.2.7.2 Comparison of the Predicted Vertical Displacements ..	143
5.2.7.3 Comparison of the Predicted Longitudinal Contact Forces	144
5.2.7.4 Comparison of the Predicted Lateral Contact Forces ..	146
5.2.7.5 Comparison of the Predicted Vertical Contact Forces ..	148
5.2.7.6 Comparison of the Predicted Overturning Moments ...	149
5.2.7.7 Comparison of the Predicted Vertical Moments	151
5.3 Summary	152
CHAPTER 6: QUARTER-VEHICLE MODELS USING RIGID RING AND FEA TIRE MODELS	154
6.1 FEA and Rigid Ring Quarter-Vehicle Models	155
6.1.1 Sprung Mass	156
6.1.2 Front Axle Suspension Characteristics	156
6.2 Durability Tests Using a Tractor-Semitrailer and Quarter-Vehicle Models	157
6.2.1 90° Water Drainage Ditch	158
6.2.2 Vertical Acceleration Measurements on the Ditch Using Tractor-Semitrailer	159
6.2.3 Vertical Acceleration Predictions on the Ditch Using Quarter-Vehicle Models	160
6.2.4 Model Validations	163
6.3 Summary	165
CHAPTER 7: CONCLUSION AND FUTURE WORK	167
7.1 Conclusions	167
7.2 Major Contributions	169
7.3 Recommended Future Work	170
7.3.1 FEA Truck Tire Model in a Full-Vehicle Model	170
7.3.2 FEA Tire Model on a Soft Soil Terrain	171
7.3.3 FEA Vehicle/Tire Model for Hydroplaning Prediction	171

REFERENCES	173
APPENDIX A: SIDEWALL DAMPING COEFFICIENT CALCULATION ..	183
APPENDIX B: DIGITIZED DITCH PROFILES	186

LIST OF FIGURES

2-1 Wheel Axis, Forces, and Moments Definitions (Wong, 2001)	11
2-2 Major Components of Rubber Friction (Haney, 2004)	14
2-3 Cornering Force Developments at Various Slip Angles (Wong, 2001)	16
2-4 Vehicle Under Cornering Maneuver and Lateral Force at the Contact Area	17
2-5 Contact Area Shapes at Different Slip Angles (Haney, 2004)	18
2-6 Normal Pressure Distributions in the Contact Areas (Gillespie, 1992)	19
2-7 Overturning Moment (Yap, 1991)	20
2-8 Tire Force Response Interactions (Allen <i>et al.</i> , 1995)	23
2-9 Tire-Road Contact Mechanisms of the Early Tire Models (Sui and Hirshey, 1999)	24
2-10 Equivalent Plane Tire-Road Contact Model (Sui and Hirshey, 1999)	25
2-11 Five Degrees of Freedom of Lumped Mass-Spring Tire Model (Takayama and Yamagishi, 1984)	26
2-12 In-Plane Rigid Ring Tire Model (Zegelaar and Pacejka, 1997)	28
2-13 Flexible Ring Tire Model (Kim and Savkoor, 1997)	29
2-14 Rigid Ring Tire Model (Bruni <i>et al.</i> , 1997)	30
2-15 Radial Tire Layout with a Belt Wedge near Tread Shoulder (Kenny and Stechschulte, 1988)	34
2-16 Passenger Car Tire, P195/75R14, FEA Tire Model (Rhyne <i>et al.</i> , 1994)	36
2-17 Inflated and Loaded Tire Model with Fixed Boundary Conditions in the Rim Contact Areas (Zhang, 2001)	39
2-18 Detail Tire Modeling of Isotropic and Anisotropic Layers (Zhang, 2001)	39
2-19 Normal Contact Pressure Distribution (Zhang, 2001)	40
2-20 Vibration Modes Test and Standing Waves Prediction (Chang, 2002)	41
2-21 Two-Dimensional and Three-Dimensional Tire Models (Yan, 2003)	41
2-22 Tire Parts Subject to Relatively High Loadings (Yan, 2005)	43
2-23 Contact-Impact Simulation Methods (ESI, 2000)	45
2-24 Search Radius (ESI, 2000)	47
2-25 Node-to-Segment Correspondence Search (ESI, 2000)	48
2-26 Deformed Shapes Corresponding to the Pressures (Hallquist <i>et al.</i> , 1985)	53
2-27 Sequence of a Single-Surface Square Tube Buckling (Benson and Hallquist, 1990)	54
2-28 Tire Tests on Internal and External Drums (Eldik Thieme, 1982)	56

2-29 Test Wheel on Flat Rotating Disc (Kollmann, 1959)	56
2-30 Tire Test on Flat Belt (Eldik Thieme, 1982)	57
2-31 Randomly Oriented Chains (a) and Oriented Chains (b) (Askeland, 1994) ...	61
2-32 Principal Stresses and Extension Ratios (Yeoh, 1993)	62
2-33 Determination of the Mooney-Rivlin Coefficients (Yeoh, 1990)	65
3-1 Heavy-Duty Radial Truck Tire (Ford and Charles, 1988)	69
3-2 Typical Tire Constructions (Wong, 2001)	70
3-3 Basic Tread Patterns of Truck Tires (Ford and Charles, 1988)	72
3-4 Bead Bundle Configurations (Ford and Charles, 1988)	73
3-5 Definitions of a Tire Cross-Sectional Shape (Tire and Rim Association Year Book, 1996)	74
3-6 Radial Truck Tire (Retrieved from www.goodyear.com)	76
3-7 Definition of Membrane Elements (ESI, 1998)	76
3-8 Three-Layered Membrane Element (ESI, 2000)	77
3-9 Carcass Wrap around Bead (Gough, 1981)	78
3-10 Locations of the Layered Membrane Elements and Their Part I.D. Numbers in FEA Truck Tire Model	78
3-11 Carcass and Belts Membrane Elements Used in FEA Truck Tire Model	80
3-12 Definitions of Solid Elements (ESI, 1998)	81
3-13 Locations of the Solid Elements and Their Part I.D. Numbers in FEA Truck Tire Model	82
3-14 Solid Elements used in FEA Truck Tire Model	83
3-15 Definition of Beam Element	84
3-16 Beam Elements and Their I.D. Number in FEA Tire Model	84
3-17 Two Beads Used in FEA Truck Tire Model	85
3-18 15° Drop Center Rim Contour (Tire and Rim Association Year Book, 1996). 86	86
3-19 FEA Truck Tire Rim Model	87
3-20 FEA Tire-Rim Assembly Model	88
3-21 FEA Truck Tire on a Rigid Flat Road Model	89
3-22 FEA Truck Tire at 4° Steer Angle on a Rigid Flat Road Model	89
3-23 FEA Truck Tire on a Rigid Cleat-Drum Model	90
3-24 FEA Truck Tire on a Rigid Smooth Drum Model	91
3-25 FEA Truck Tire on a Rigid Flat Road with the Three Water Drainage Ditches	92
4-1 Virtual Tire Load-Deflection Test	95
4-2 Vertical Tire Load versus Deflection	95
4-3 Footprint Areas and Shapes of Various Tires (Tekscan, 2006)	96

4-4 Footprint Area Prediction at Various Tire Loads	97
4-5 Footprint Area versus Vertical Static Load	98
4-6 In-Plane Tire Excitation During Cleat Impact	99
4-7 FFT Result of Vertical Reaction Force at Tire Spindle	100
4-8 First Mode of Vertical Free Vibration (Gillespie, 1992)	100
4-9 Cornering Simulation at Slip Angle of 6°	101
4-10 Cornering Forces Validation	102
4-11 Aligning Moments Validation	102
4-12 Yaw Oscillation Test	103
4-13 Yaw Oscillation Input and Lateral Force Output at the Frequency of 1 Hz ...	107
4-14 Tire Lateral Force Magnitude as a Function of Path Frequency	108
4-15 Tire Phase Angle as a Function of Path Frequency	108
5-1 In-Plane Rigid Ring Tire Model (Zegelaar and Pacejka, 1997)	113
5-2 Tire Deflection during Rolling	114
5-3 Effective Rolling Radius, Re	115
5-4 Rotational Excitation on FEA Truck Tire	118
5-5 Angular Displacement of the Tread and Damping Response of the Sidewall ...	119
5-6 Longitudinal Force versus Slip Ratio	122
5-7 90° Water Drainage Ditch Profile	125
5-8 Tire Spindle Vertical Displacements at Tire Load of 13.3 kN	126
5-9 Tire Spindle Vertical Displacements at Tire Load of 26.7 kN	126
5-10 Tire Spindle Vertical Displacements at Tire Load of 40.0 kN	126
5-11 Longitudinal Contact Force at Tire Load of 13.3 kN	128
5-12 Longitudinal Contact Force at Tire Load of 26.7 kN	128
5-13 Longitudinal Contact Force at Tire Load of 40.0 kN	128
5-14 Vertical Contact Force at Tire Load of 13.3 kN	129
5-15 Vertical Contact Force at Tire Load of 26.7 kN	129
5-16 Vertical Contact Force at Tire Load of 40.0 kN	130
5-17 Out-of-Plane Parameters for the Rigid Ring Tire Model (Volvo 3P, 2004) ...	131
5-18 Out-of-Plane Translational Excitation on Sidewall	132
5-19 Lateral Displacement and Damping Response of the Sidewall	133
5-20 Out-of-Plane Rotational Excitation on Sidewall	135
5-21 Out-of-Plane Rotational Displacement and Damping Response of the Sidewall	135
5-22 Lateral Excitation at Tire Spindle	137
5-23 Lateral Free Vibration Test Result at Vertical Tire Load 26.7 kN	137

5-24 Cornering Stiffness Prediction at Vertical Load of 26.7 kN	139
5-25 Self-Aligning Stiffness Prediction at Vertical Load of 26.7 kN	140
5-26 45° Water Drainage Ditch Profile	142
5-27 Tire Spindle Vertical Displacements at Tire Load of 13.3 kN	143
5-28 Tire Spindle Vertical Displacements at Tire Load of 26.7 kN	143
5-29 Tire Spindle Vertical Displacements at Tire Load of 40.0 kN	144
5-30 Longitudinal Contact Forces at Tire Load of 13.3 kN	145
5-31 Longitudinal Contact Forces at Tire Load of 26.7 kN	145
5-32 Longitudinal Contact Forces at Tire Load of 40.0 kN	146
5-33 Lateral Contact Forces at Tire Load of 13.3 kN	147
5-34 Lateral Contact Forces at Tire Load of 26.7 kN	147
5-35 Lateral Contact Forces at Tire Load of 40.0 kN	147
5-36 Vertical Contact Forces at Tire Load of 13.3 kN	148
5-37 Vertical Contact Forces at Tire Load of 26.7 kN	149
5-38 Vertical Contact Forces at Tire Load of 40.0 kN	149
5-39 Tire Spindle Overturning Moment at Tire Load of 13.3 kN	150
5-40 Tire Spindle Overturning Moment at Tire Load of 26.7 kN	150
5-41 Tire Spindle Overturning Moment at Tire Load of 40.0 kN	150
5-42 Tire Spindle Vertical Moments at Tire Load of 13.3 kN	151
5-43 Tire Spindle Vertical Moments at Tire Load of 26.7 kN	151
5-44 Tire Spindle Vertical Moments at Tire Load of 40.0 kN	152
6-1 Quarter-Vehicle Models	155
6-2 Spring Characteristics of the Suspension	156
6-3 Shock Absorber Characteristics of the Suspension	157
6-4 Measurement of the 90° Ditch Profile	158
6-5 90° Ditch Profile	158
6-6 Test Tractor-Semitrailer Running over the Ditch	159
6-7 Accelerometer Location at Front Left Wheel	159
6-8 Tire Spindle Vertical Accelerations at 8.2 km/h (Rated Tire Load: 26.7 kN) ...	160
6-9 Tire Spindle Vertical Accelerations at 11.1 km/h (Rated Tire Load: 26.7 kN) .	161
6-10 Tire Spindle Vertical Accelerations at 21.3 km/h (Rated Tire Load: 26.7 kN) 161	
7-1 FEA Tire Model on a Soft Soil Terrain	171
7-2 FEA Vehicle/Tire Model for Hydroplaning Prediction	172

LIST OF TABLES

3-1 Material Properties of the Layered Membrane Elements	79
3-2 Material Properties of the Solid Elements	83
3-3 Material Properties of the Beam Elements	84
3-4 15° Drop Center Rim Contour Dimensions for 22.5 × 8.25 Truck Tire Rim	86
3-5 Material Properties of the FEA Rim	87
5-1 In-plane Translational and Residual Vertical Stiffness of Sidewall at Tire Load of 26.7 kN	117
5-2 In-plane Longitudinal and Vertical Damping Constants of the Sidewall and Residual Damping Constant at Contact Area at Tire Load of 26.7 kN	118
5-3 In-plane Rotational Stiffness and Damping Constants of Sidewall at Tire Load: 26.7 kN	121
5-4 Predicted Rigid Ring Tire Model Parameters at Given Tire Load	124
5-5 Parameters Used for the Out-of-Plane Translational Damping Constant	134
5-6 Parameters Used for the Out-of-plane Rotational Damping Constant	136
5-7 Parameters Used for the Out-of-plane Slip Damping Constant	138
5-8 Out-of-Plane Characteristic Parameters of the Rigid Ring Tire Model	141
6-1 Statistical Validation of Tire Spindle Vertical Acceleration at 8.2 km/h	165
6-2 Statistical Validation of Tire Spindle Vertical Acceleration at 11.1 km/h	165
6-3 Statistical Validation of Tire Spindle Vertical Acceleration at 21.3 km/h	165

NOMENCLATURE

Symbol	Description	Unit
a	Half contact length between tire and road surface	m
C_{10}, C_{01}	Mooney-Rivlin coefficient	N/m ²
c_{bx}, c_{bz}	In-plane translational damping of sidewall	N s/m
c_{by}	Out-of-plane translational damping constant	N s/m
$c_{b\gamma}$	Out-of-plane rotational damping constant	N m s/rad
$c_{b\theta}$	In-plane rotational damping of sidewall	N m s/rad
c_c	Critical damping constant	N s/m
c_l	Out-of-plane slip damping constant	N s/m
c_{vr}	Residual damping constant	N s/m
d	Tire Deflection due to loading	m
f	Stretching force on a single chain molecule	N
f_r	Rolling resistance coefficient	-
F_x	Longitudinal or tractive force	N
F_y	Lateral force	N
f_y	Yaw oscillation frequency	Hz
F_{y_R}	Resultant lateral force	N
F_z	Vertical or normal force	N
F_{z_R}	Resultant vertical force	N
I_{ax}, I_{az}	Mass moment of inertia of wheel rim about X- and Z-axis	kg m ²
I_{ay}	Mass moment of inertia of wheel rim about Y-axis	kg m ²
I_{bx}, I_{bz}	Mass moment of inertia of tire belt about X- and Z-axis	kg m ²
I_{by}	Mass moment of inertia of tire belt about Y-axis	kg m ²
I_i	Strain invariant (i=1, 2, and 3)	-
k_{bx}, k_{bz}	In-plane translational stiffness of sidewall	N/m
k_{by}	Out-of-plane translational stiffness	N/m
$k_{b\gamma}$	Out-of-plane rotational stiffness	N m/rad
$k_{b\theta}$	In-plane rotational stiffness of sidewall	N m/rad
k_{cx}	Longitudinal tread stiffness	N/m
k_f	Cornering stiffness	N/rad
k_k	Longitudinal slip stiffness	N/slip unit
k_L	Lateral tire stiffness	N/m
k_l	Lateral slip stiffness	N/m
k_M	Self-aligning stiffness	kN m/rad
k_{tot}	Tire total vertical stiffness	N/m
k_{vr}	Residual vertical stiffness	N/m
m_a	Wheel rim mass	kg
m_b	Tire belt mass	kg
M_x	Overturning moment	N m
M_y	Rolling resistance moment	N m
M_z	Vertical or aligning moment	N m

Symbol	Description	Unit
R	Radius of the inflated tire before loading	m
R_e	Effective rolling radius	m
R_{drum}	Drum radius	m
s	Longitudinal offset between the wheel center and F_{z_R}	m
T	Absolute temperature	K
t_i	Principal stress (i=1, 2, and 3)	N/m ²
u	Current wheel orientation	-
v, v_{tire}	Tire speed	m/s
v_{drum}	Drum speed	-
v_{tr}	Tread speed	-
W	Strain energy density function	-
α	Slip angle	rad
ϕ	Phase angle	rad
γ	Amplitude ratio of the output to yaw oscillation input	-
λ	Lagrange multiplier	N
λ_i	Extension ratio (i=1, 2, and 3)	-
τ	System time constant	s
τ_d	Damped period of vibration	s
ω	Wheel angular speed	rad/s
ω_d	Damped natural frequency	rad/m
ω_{drum}	Drum angular speed	rad/s
ω_n	Undamped natural frequency	rad/m
ω_{path}	Path frequency	rad/m
ω_y	Yaw oscillation frequency	rad/s
ζ	Damping ratio	-

ACKNOWLEDGMENTS

For many years, obtaining a doctoral degree in engineering has been my highest professional goal. Taking the steps to achieve this goal has proved challenging yet rewarding. During the process, many have influenced and contributed to my development both as a student and as a person. Special thanks are owed to the members of my graduate committee: Dr. James P. Runt, Dr. Ashok D. Belegundu, and Dr. Charles E. Bakis. Each of you has provided invaluable research and teaching guidance in pursuit of my professional ambition.

Dr. Moustafa El-Gindy, chair of my committee, has provided unwavering support and leadership throughout my academic career. His professional accomplishments are inspiring and his strong encouragement has helped me remain focused and motivated throughout my tenure at Penn State. I am deeply indebted to Dr. El-Gindy for his time and thoughtful consideration.

I also thank the Goodyear Tire and Rubber Company for providing the measurements of the tire deflection and footprint area versus vertical tire loads. I would like to express my deep appreciation to Mr. Trivedi Mukesh and Mr. Fredrik Öijer of Volvo 3P, the sponsor of the research project, for their continuous technical help during the course of this study.

On a personal note, I would like to give thanks to my parents, Dr. Jungmin Chae and Taesun Son, for their endless guidance and care. They have taught me hard work, dedication, and commitment. The personal opportunities that they have provided would take more than a lifetime to repay. Also, I would like to thank Dr. Benedict Y. Oh and MD. Susan Oh, my parents of this town, State College, for their cordial encouragement and care. I also thank my brother, Seokhyun, and sisters, Sungwon and Sunghee, for their encouragement during this endeavor.

Lastly, I would like to express my sincere appreciation to my wife, Eunju Kim. She has devoted herself to support and encourage me even though she is busy in pursuing her doctoral degree. Thus, I dedicate this thesis to my wife, Eunju Kim. Without the patience, love, and understanding of my wife, this accomplishment would not have been possible.

CHAPTER 1

INTRODUCTION

Tires are among the most essential components of ground vehicles. They perform many important functions during vehicle operation. For example, they support vehicle weight enough according to its own rated load capacity. They also transmit sufficient driving, braking, and cornering efforts between the rim and road surfaces. They have the ability to resist the longitudinal, lateral, and vertical reaction forces from the road surface without severe deformation or failure. Further, they also alleviate shocks from road surface irregularities to a certain degree due to their damping and energy dissipation nature. Eventually, tires provide a safe and comfortable environment for passengers and luggage. If tires cannot perform all these tasks properly, the driver may easily lose control of the vehicle and face serious safety problems.

In order to satisfy these performance requirements mentioned above, tires need to be robust enough to withstand the applied vertical wheel load, frictional shear forces, and wear generated on the tire-road contact area. At the same time, tires need to be soft and flexible enough to absorb shocks due to road surface irregularities. Because there does not exist currently a single engineering material to serve for all these performance requirements of the tires, steel-cords embedded rubber composite materials are used. As can be observed, the tire structure is complex to fulfill the performance requirements and challenging to design and manufacture.

For the last 120 years since the first pneumatic tire was invented, many technologies have been continuously developed to satisfy the performance requirements and enhance the

quality of tires. Higher quality of passenger car tires has been developed to provide a softer and more comfortable ride for passengers. Simultaneously, stronger commercial vehicle¹ tires have been also developed to withstand and carry higher loads of freight.

Whenever a new type of tire is designed and manufactured, tire testing is required to characterize the performances of the new tire. Many tire testing set-ups have been developed to measure static and dynamic tire responses in a laboratory or a test field. However, the experimental tire testing is usually costly and difficult to build. In addition, experiment equipment, its set-up, data acquisition, and analysis need highly experienced skills and long testing time. Sometimes, the experimental tire testing is governed by weather and temperature of the test field environment. In addition, some extreme cases such as high tire loading and/or high speed of tire rotation cannot be conducted by using conventional testing equipment. It can also take large amount of time and effort to repeat same or similar tire tests. In order to overcome these limitations of the experimental tire testing, many researchers have tried to build alternative tire testing environments during the last few decades.

Fortunately, modern computer technology enables to open a new era of tire testing. Through tire model simulations, most of the laboratory tire tests can be duplicated. Even limited tire tests that cannot be performed in laboratory, such as high speed and/or loading operations, are possible with the tire model simulations. Among tire models, a rigid ring and a finite element analysis (FEA) tire models are widely used. The rigid ring tire model is simple but needs several in-plane and out-of-plane parameters to be determined through comprehensive tire tests. The rigid ring tire model is simulated not only alone but also together in multi-body vehicle model environment. On the other hand, the FEA tire model is complicated to build but versatile in its applications.

In this study, the parameters of the rigid ring tire model are predicted by using an FEA truck tire model, then, the rigid ring tire model is tested on a durability test event alone and in a quarter-vehicle environment. The predicted dynamic tire responses of the rigid

¹ Buses, trucks, trailers, and moving vans are categorized as the commercial vehicles.

ring tire model are compared with those of the FEA truck tire model and measured values using a tractor-semitrailer.

1.1 History of the Wheel and Tire

In the Paleolithic era, 15,000 to 750,000 years ago, people used round logs to move heavy objects more easily (The Evolution of the Wheel¹, 2006). They placed logs and a sledge under a heavy object and dragged the sledge over one log to the next. As the sledges started to wear grooves into the log between the two ends, the log gradually changed shape similar to a big bone. Then, the wood between two ends was cut to create the axle. The two ends finally became solid wheels even though they were primitive. The first use of the solid wheel for transportation was assumed to be used on Sumerian² chariots in 3,500 BC (Dillion and Rockefeller, 1999). The two-wheeled chariot was found in the birthplace of Sumeria and is believed to be the first form of wheeled transportation. This chariot increased the speed of travel over land and eventually led to a four-wheeled cart, which took the burden of carrying supplies and equipment off the shoulders of men.

For over a few thousands years, wooden wheels had been manufactured with different spokes, leather-tops, and iron strip-tops, in chronological order. In 1839, Charles Goodyear discovered the vulcanization process (Goodyear, 1853), which is the process of heating raw rubber with sulfur to transform sticky raw rubber to a firm but pliable material. The process makes rubber a perfect material for tires and other engineering applications. Soon after the discovery of the vulcanization process, bicycle tires could be manufactured using the vulcanized solid rubber. These solid rubber tires were strong enough to resist cuts and abrasions. They could even absorb some amount of shocks

¹ <http://www.ohtm.org/wheel.html>

² Sumeria (or Sumer) is one of the first civilized societies in southern Mesopotamia area from around 3,800 BC to 2,000 BC.

from roadway irregularities. However, despite these safety features, these tires were still very heavy and did not provide a smooth ride to driver.

Later, in 1845, Robert William Thomson, a Scottish engineer, conceived an idea of air-inflated or pneumatic bicycle tires and expected that the pneumatic tires could overcome the limitation of the solid rubber tires (Bellis, 2006). However, his idea of a pneumatic tire was only patented as a concept and was never carried out to manufacture a real pneumatic tire. Meanwhile, John Boyd Dunlop, a Scottish veterinarian, watched his son encountered difficulty riding a tricycle over cobbled ground¹. He realized that the unforgiving ride was due to the solid rubber tires of the tricycle. He started to find a way to improve the ride performance of the tires. Shortly, he considered that an air-inflated tire would be light and absorb more shocks that provided a smoother ride. Eventually, he manufactured the first pneumatic bicycle tire in 1888 and patented it, which replaced most of the solid bicycle and tricycle tires within ten years.

One day in 1889, a bicyclist brought a punctured bicycle tire to the Michelin brothers, André and Édouard Michelin, to fix (Automotive News Europe, 2001). They found a major drawback of Dunlop's tire in that the tire was firmly glued to the rim, which made punctured tire repair very difficult. The Michelin brothers decided to help the bicyclist and tried to find an easier method to repair punctured tires. Eventually, they manufactured a detachable pneumatic tire that could save time and effort to repair a punctured tire. A few years later, Michelin brothers made an effort to convince carmakers of the utility of inflatable tires. At that time, cars had used the same kind of wheel as those used on horse-drawn vehicles which was a wooden wheel with a metal rim or a solid tire. The brothers' effort was accepted and, within a few years, the Michelin firm achieved astonishing growth by serving the early stage of the automotive industry.

¹ <http://www.tartans.com/articles/famscots/jbdunlop.html>

1.2 Objectives

For an efficient full vehicle model simulation, a multi-body system (MBS) simulation is frequently adopted. In the MBS simulations, a rigid ring tire model is mostly used due to its efficiency. For the rigid ring tire model, several in-plane and out-of-plane parameters need to be determined through tire tests to represent a real pneumatic tire. The physical tire tests are costly and difficult in operations. Thus, the parameters for the rigid ring tire model are alternatively predicted by conducting virtual tire tests using an FEA truck tire model. The rigid ring tire model implemented with the determined parameters will generate tire responses in a multi-body truck model close to those of an actual tire, thus, it will contribute to obtain the efficient results of vehicle model simulations.

The first objective of this study is to build a reliable truck tire model and a virtual tire testing environment to replace the conventional expensive and limited physical tire tests. An FEA truck tire model is created based on a real truck tire, 295/75R22.5, dimensions and material data. Then, this tire model experiences validation tasks to check whether it follows the similar behaviors of the available measured data.

As the second objective of the study, in-plane and out-of-plane characteristic parameters for a rigid ring tire model to represent the truck tire are predicted by using the developed FEA tire model and virtual testing environments at various tire operation conditions. After the predicted parameters are implemented in the rigid ring tire model, the model is tested by running on water drainage ditches. The predicted in-plane and out-of-plane tire responses are compared with those of the FEA truck tire model.

As the third objective of the study, a quarter-vehicle model using the rigid ring tire model is created to test the rigid ring tire model under the influence of the sprung mass vertical acceleration during the ditch runs. The predicted vertical accelerations at the tire spindle are compared with measurements and results from FEA quarter-vehicle model for the model validation purposes and will serve for handling, ride quality, stability, and safety analyses of the vehicle.

Tire mechanics is quite complex to analyze because of highly nonlinear dynamic characteristics intrinsic to its nature. The establishment of a precise and efficient model is of critical importance to the analysis, simulation, and design of safer and more advanced tires. Once the reliable virtual tire testing environment has been established, tire model simulations will be easily repeated at various operation conditions, even severe operation conditions that cannot be accomplished in laboratory testing facilities.

1.3 Methodology

For the last 50 years, many tire models have been established to simulate transient and steady-state behaviors on various road terrains. For example, flexible ring, rigid ring, point contact, and FEA tire models have been performed to predict the tire responses. Among those tire models, the FEA tire model has performed the most reliable and versatile tasks under various operation conditions. Thus, the FEA is adopted in this study to build the truck tire model and testing environments. The FEA computer simulation software, PAM-SHOCK, is used to accomplish the tire modeling and virtual testing. Finally, the FEA tire model is completed with a validation task. The validation task of the model involves mainly checking whether the FEA model yields a reasonable behavior as a real tire behaves in a real application. For the validation of the tire model, the predicted results from the vertical load-deflection, footprint area, first free vertical vibration mode, cornering characteristics, and yaw oscillation tests will be compared with physical tire test measurement data. The measurement data are provided by the Goodyear Tire and Rubber Company and the University of Michigan Transportation Research Institute (UMTRI).

Subsequently, the developed tire model will be tested to predict characteristic tire parameters at various operation conditions, such as various vertical tire loads, speeds, and steering inputs. The tire model will be inflated at rated pressure and loaded at a given tire load on a road surface. After the tire model is stabilized, the tire model will be excited

according to the test specifications. Durability tests will also be performed on water drainage ditches using a tire model only and quarter vehicle model to predict vertical responses of the tire spindle. For this durability test, the FEA mesh model of 86 mm-deep and 736 mm-long water drainage ditch will be created. After the virtual durability test, the predicted vertical responses will be compared with real measurement data provided by one of the leading truck manufacturers.

1.4 Statement of the Work

Chapter 2 presents a comprehensive literature survey on tire models to help the understanding of tire mechanics and modeling techniques. In addition, the direction of this study can be guided by conducting the literature survey. Tire models are categorized in three different major methods: analytical tire model, rigid ring tire model, and FEA tire model. The modeling techniques of those models and their applications are summarized. The advantages and limitations of each modeling method are also described. The literature review focuses more extensively on the rigid ring tire models and FEA tire models, which cover most of this research. At the end of Chapter 2, literature on the calculation of the Mooney-Rivlin coefficients follows. The method to determine the coefficients from rubber material tensile and compression tests is described in detail.

In Chapter 3, a three-dimensional nonlinear FEA truck tire model, 295/75R22.5, including a detailed rim is constructed using the FEA simulation software, PAM-SHOCK. The methods and techniques to model tire structure, its components, and materials are described in detail. Beam elements, layered membrane elements, and solid elements are used to build the truck tire model. In addition, various virtual tire tests environments to be used to test the developed FEA tire model are presented at the end of the chapter. The FEA truck tire model will be used to predict in-plane and out-of-plane tire parameters of a rigid ring tire model after the validation tasks.

In Chapter 4, validation tasks of the developed FEA truck tire model are conducted through virtual static and dynamic tire tests. The static tests include vertical tire load-deflection and footprint area prediction tests. The dynamic tests consist of the first free vertical vibration mode, cornering, and yaw oscillation tests. The first free vertical vibration mode test is conducted on a rotating cleat-drum, and it is obtained by applying FFT algorithm to the predicted vertical force time history at the tire spindle. For the validation of the model in terms of steady-state out-of-plane motions, cornering test simulations are conducted at various slip angles and tire loads to predict cornering forces and aligning moments applied on the tire model during the tests. Yaw oscillation test is also conducted to examine the dynamic out-of-phase tire responses to sinusoidal steering angle input. As a result, the amplitude ratio and phase angle are plotted as a function of the path frequency. These predicted static and dynamic tire responses agree with physical measurements.

Chapter 5 presents the determination of the in-plane and out-of-plane parameters for a rigid ring tire model through virtual FEA tire tests. The in-plane parameters are the translational stiffness and damping constant of the sidewall along the longitudinal and vertical axes, the rotational stiffness and damping constant of the sidewall about the lateral axis, and the vertical stiffness and damping constant of the tire belt and tread. The out-of-plane parameters are the translational stiffness and damping constant along the lateral axis and the rotational stiffness and damping constant of the sidewall about the longitudinal axis. These parameters are predicted at a tire inflation pressure of 0.759 MPa under three tire loading cases, 13.3 kN (3,000 lb), 26.7 kN (6,000 lb), and 40.0 kN (9,000 lb). The predicted tire parameters are implemented into a rigid ring tire model, and the tire model is tested on 90° and 45° water drainage ditches to predict in-plane and out-of-plane tire responses at a tire speed of 19.3 km/h (12 mph) and the various tire loads. Vertical tire displacements, applied forces, and moments applied on the tire model are predicted. The predicted responses of the rigid ring tire model are compared with those from the FEA tire model simulations.

Chapter 6 presents a quarter-vehicle model to test the rigid ring tire model in an environment that includes the effect of the vertical motion of the sprung mass on the dynamic responses of the tire models. Thus, the tire model in the quarter-vehicle model generates closer dynamic tire responses to real tire behaviors. The rigid ring quarter vehicle model consists of the rigid ring tire model, suspension, and sprung mass. For the suspension, the spring and shock-absorber characteristics of a tractor front axle are implemented to connect the sprung mass and the tire model. The sprung mass is constrained to move only vertically. The quarter vehicle model runs on the 90° ditch to predict the vertical acceleration at the tire spindle at various tire running speeds. Then, the predicted vertical accelerations are compared with those from the FEA quarter-vehicle model and measured values on the front axle of the tractor-semitrailer. The rigid ring quarter-vehicle model simulations and measurements are conducted by one of the leading truck manufacturers.

In Chapter 7, the conclusions obtained throughout this study are summarized. The major contributions, advantages, and limitations of the FEA tire model are also discussed. For future work, the dynamic performances of the FEA truck tire model in a full vehicle model, FEA tire model responses on a soft terrain, FEA vehicle/tire model for hydro-planning prediction are recommended.

CHAPTER 2

LITERATURE SURVEY

In this chapter, literature previously published on various tire modelings and analysis has been reviewed to help historical understanding and to provide tire modeling methods including their capabilities and limitations. In addition, the reviews on the various solution algorithms of the computational contact problems, tire testing, and tire rubber material modeling are followed. Before various tire modeling methods and the other topics are introduced, reference axis system, definitions of forces and moments applied on the tire are described and are later frequently mentioned throughout this study.

2.1 Tire Axis System, Tire Forces, and Moments Definitions

Section 2.1 describes a conventional tire axis system, forces, and moments definitions that are widely accepted. Also, according to the axis system, the forces and moments that can be applied on the tire during operation are defined. Three forces and three moments are described.

2.1.1 Tire axis system

In order to describe the characteristics of a tire and applied forces and moments on the tire, it is necessary, first, to define an axis system that serves as a reference for the definition of various parameters. One of the commonly used axis systems is recommended by the Society of Automotive Engineers (SAE) as shown in Figure 2-1. The origin of the axis system is the center of tire contact. The X-axis is the interaction of

the wheel plane and the ground plane with a positive direction forward. The Z-axis is perpendicular to the ground plane with a positive direction downward. The Y-axis is in the ground plane and its direction is chosen to make the axis system orthogonal, which is on the right of the wheel plane.

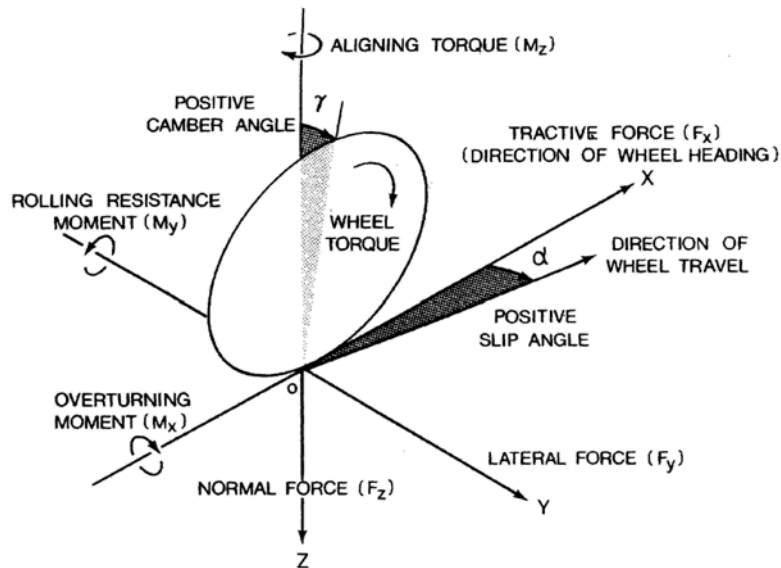


Figure 2-1 Wheel Axis, Forces, and Moments Definitions (Wong, 2001)

2.1.2 Tire forces and moments

Since the tire is the only media in a vehicle that has contact with road surface, the tire needs to support sprung mass, resist external disturbances, and transmit driving and braking torques from the vehicle to the road surface. Therefore, forces and moments are continuously applied to the tire along all three axes during vehicle operations as shown in Figure 2-1. In this section, three forces and three moments are described in detail with their origins and important functions. The forces are longitudinal or tractive force (F_x), lateral force (F_y), and vertical or normal force (F_z). The moments are overturning moment (M_x), rolling resistance moment (M_y), and vertical moment or aligning moment (M_z). These forces and moments are mainly due to the tire-road contact and its elastic deformation. When the tire doesn't have contact with road surface, no forces and moments will be applied to the tire.

2.1.2.1 Tire longitudinal force

When a tire is rolling or sliding along the longitudinal direction on a road, longitudinal force is applied to the tire at the contact area. The longitudinal force can be categorized into A) the rolling resistant force, B) longitudinal frictional force, and C) longitudinal reaction force according to their causes.

A) Rolling resistant force

During free rolling¹ along a straight direction, the rolling resistant force is applied to the tire at the contact area against the tire rolling direction. The rolling resistant force or rolling resistance of tires is primarily caused by the hysteresis in tire materials due to the carcass deflection of rolling tires. In addition to the hysteresis, many other factors can affect the rolling resistance of a pneumatic tire. The factors are known to be tire construction, materials, and its various operating conditions such as road surface condition, inflation pressure, speed, and temperature. At rated load and inflation pressure on the same size tires, bias-ply tires show higher rolling resistance than radial-ply tires due to greater hysteresis losses in bias-ply tires. Thicker treads, thicker sidewalls, and increased number of carcass plies also tend to increase the rolling resistance due to greater hysteresis losses. Tires made of synthetic rubber compounds generally have higher rolling resistance than those made of natural rubber.

Surface conditions also affect the rolling resistance. On hard and smooth surfaces, the rolling resistance is significantly lower than that on a soft and rough road. Each road surface condition shows the corresponding coefficient of rolling resistance which is defined as the rolling resistant force divided by vertical tire load. For example, for passenger car tires, the coefficient of rolling resistance is 0.013 on a concrete or asphalt road and 0.05 on an unpaved road. For general truck tires, the coefficient of rolling resistance is 0.006-0.01 on a concrete or asphalt road, which is lower than that for passenger car tires due to larger tire diameter and higher inflation pressure. On wet

¹ Free rolling condition is defined as the rolling condition without traction or braking torques applied on a tire.

surfaces, a higher rolling resistance is usually observed than on dry surfaces. In addition, a higher rolling resistance is also observed at higher speed, lower inflation pressure, and lower internal tire temperature.

B) Longitudinal frictional force

In acceleration and braking operations, there is speed difference between the rolling speed of a tire and its traveling speed, which results in a certain degree of slip between tire tread and road surface. Without acceleration and braking efforts, no slip will occur. With a certain amount of slip, a frictional force is developed in the tire-road contact area that enables the vehicle to be accelerated and decelerated. In the case of a braking operation, the degree of the slip can be expressed in slip ratio according to the equation (2-1).

$$\text{Slip ratio (\%)} = \left(1 - \frac{R_e \cdot \omega}{v}\right) \times 100 \quad (2-1)$$

Where, R_e : tire effective rolling radius,

ω : wheel angular velocity,

v : tire speed.

When the braking effort is so high that the wheel is locked and slides on the road surface, the slip ratio is defined as 100%. Normally, the slip ratio at which the frictional force reaches maximum falls between 10% and 30%. Therefore, the anti-skid brake system (ABS) maintains the slip ratios always between 10% and 30% to generate maximum braking efforts at full braking maneuvers.

Tire tread rubber generates friction in three major ways: adhesion, deformation, and tearing/wear. Figure 2-2 shows these three components that contribute to the total friction force experienced by tread rubber on the road surface at a slip speed of v .

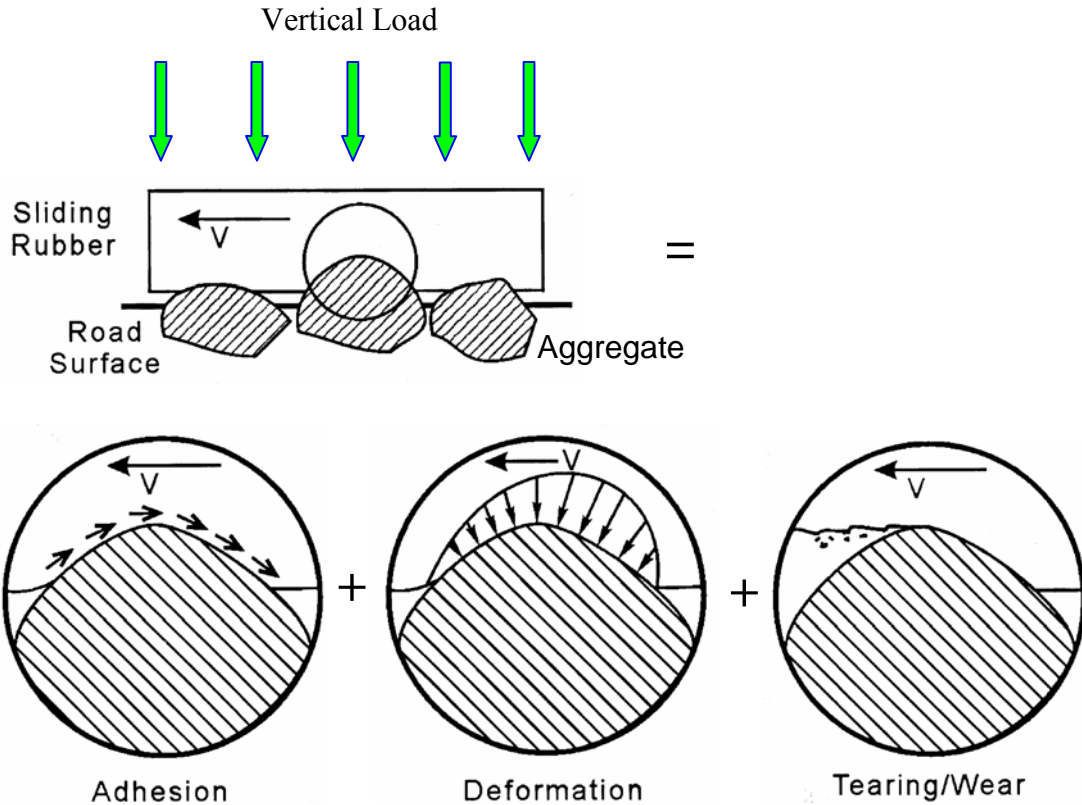


Figure 2-2 Major Components of Rubber Friction (Haney, 2004)

Surface adhesion arises from the momentary intermolecular bonds between the tread rubber and the aggregate in the road surface. The adhesion depends on the true contact area that is determined by the road surface profile, involved material properties, and contact pressure. Normally, the adhesion component is the major contributor in tire traction on dry and smooth roads. However, when the road is contaminated with dust or water, the tire loses part of the contact and formation of adhesive forces. Then, the adhesion friction is reduced substantially, which results in the loss of friction.

Tread rubber in contact with a smooth surface generates friction force mainly by adhesion. However, when rubber is in contact with a rough road surface, another mechanism, deformation, plays an important role in friction. As the tread rubber slides on a rough road surface, the local deformations of the rubber are observed on road surface irregularities. Friction forces due to those local deformations provide most of the friction force between the tire and wet road surface.

In addition to the adhesive friction and deformation friction, the rubber produces friction forces by means of tear and wear. As the applied load and sliding speeds increase, local stress can exceed the tensile strength of the rubber especially near the area of a sharp irregularity. High local stress can deform the internal structure of the rubber beyond the point of elastic recovery. When the polymer chains are stressed to failure, tearing may occur. Tearing absorbs energy and results in additional friction forces at the contact surface.

The friction force is different from the rolling resistant force. The rolling resistant force is applied on the freely rotating tire whereas the friction force is applied under acceleration or deceleration operations where slip exists. When the tire is under acceleration due to driving torque, the tractive force is applied in the direction of the motion. Conversely, when the tire is under deceleration due to braking, the braking force is applied to the tire against the tire moving direction. However, the rolling resistance is always applied against the tire moving direction.

C) Longitudinal reaction force

When the tire runs over severe road surface irregularities or obstacles such as steps, potholes, water drainage ditches, or speed bumps, a reaction force is applied to the tire longitudinally as well as laterally and vertically. This longitudinal reaction force is usually applied as a shock, which can cause damage to the tire and rim. All of these longitudinal forces are usually acting opposite to the tire moving direction at the tire-road contact area. The reaction force depends significantly on the suspension characteristics of the vehicle and tire operational conditions such as vertical load, inflation pressure, and speed.

2.1.2.2 Tire lateral force

When a vehicle undertakes a cornering operation, or subjected to cross-wind, lateral force is developed at the tire-road contact area. The lateral forces during a cornering maneuver and under irregular lateral wind are dynamic forces due to the lateral acceleration of the

vehicle. The lateral force in reaction to a cornering maneuver is called a cornering force. The cornering force is highly dependent of tire vertical load. As the vertical load on the tire increases under the same cornering operational condition, the cornering force also increases. Meanwhile, during cornering maneuvers, a higher vertical load is exerted on the right tires due to lateral load transfer. Therefore, higher cornering forces are also applied to the same right tires.

In addition, the cornering force also depends on the slip angle of the tire. As the slip angle increases under the same vertical load on the tire, the cornering force also increases. However, when the cornering force reaches a certain level, it does not significantly increase further. Instead, it tends to converge to an asymptote, which is a road surface adhesion limit as seen in Figure 2-3.

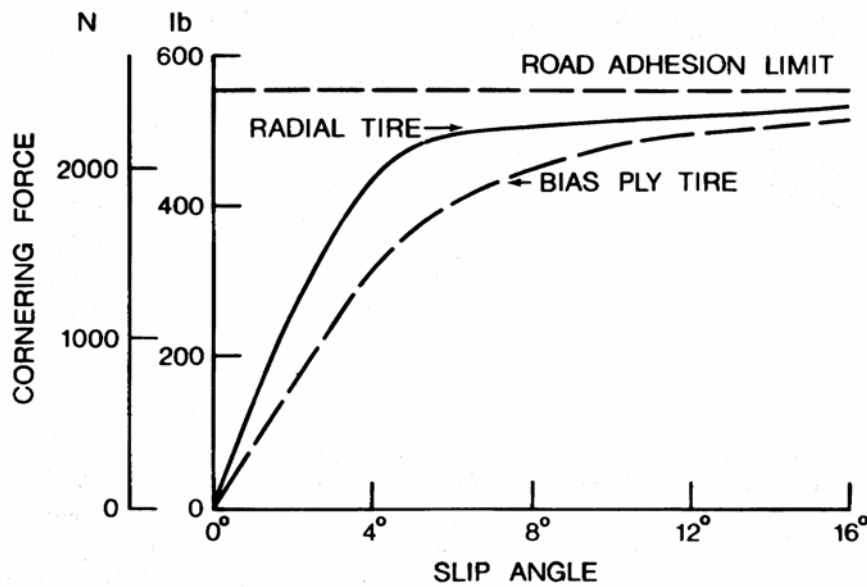
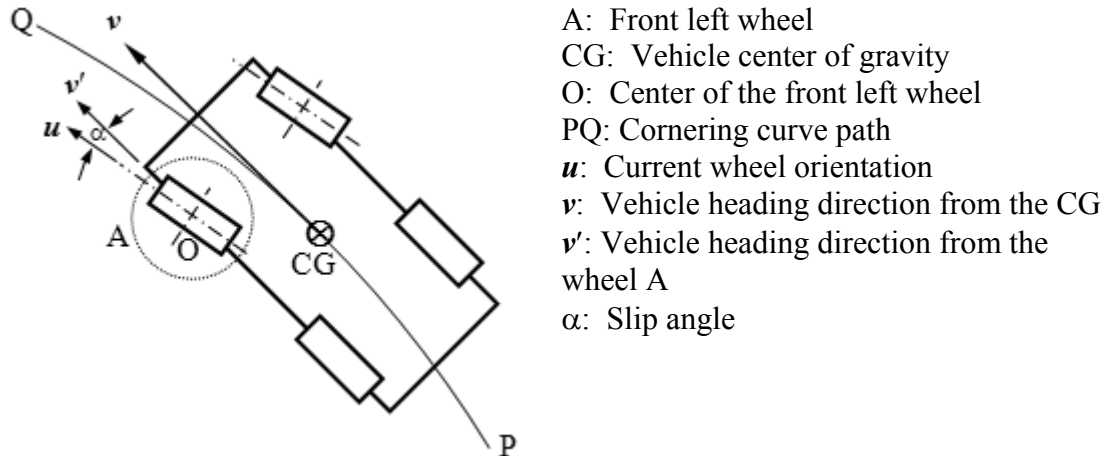


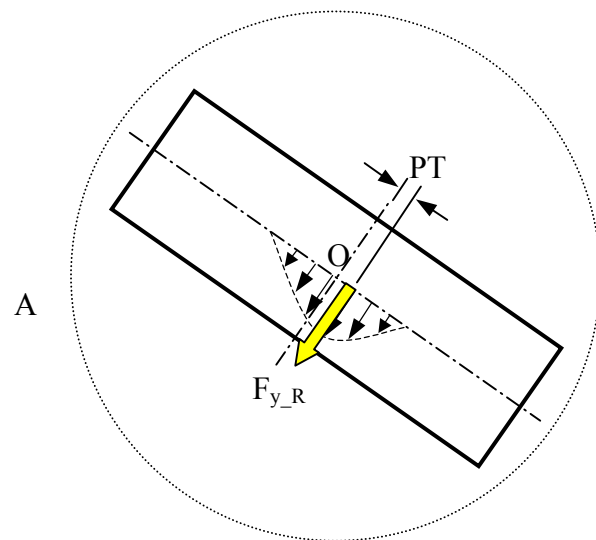
Figure 2-3 Cornering Force Developments at Various Slip Angles (Wong, 2001)

The formation of the slip angle is attributed to the elastic nature of the tire. The tire tread grips the road surface due to friction. However, the tire also resists movement with an opposing force, yields to external force, and recovers when the external force is removed. This elastic characteristic allows the tire to have an orientation (u) different from the direction in which the vehicle is traveling (v) as shown in Figure 2-4 (a). The angle, α ,

between the two orientations is defined as slip angle and plays an important role in cornering operations.



(a) Vehicle under cornering maneuver with slip angle



(b) Lateral force distribution at tire-road contact area during cornering maneuver

Figure 2-4 Vehicle Under Cornering Maneuver and Lateral Force at the Contact Area

The developed cornering force at the contact area is illustrated in detail in Figure 2-4 (b). When the vehicle is turning left, a cornering force is applied on the tire to the left at the contact area. However, the cornering force is not distributed symmetrically on the contact area around the tire center. Instead, the peak cornering force moves behind the center of

the tire due to the longitudinal force against the tire. Therefore, the resultant cornering force, $F_{y,R}$, can be drawn behind the tire center with offset, PT, as shown in Figure 2-4 (b). The offset is called the pneumatic trail (PT). This pneumatic trail and the resultant cornering force generate an aligning moment about the vertical axis.

The schematic contact area shapes are illustrated in Figure 2-5 at different slip angles. Originally, the tire is rolling in the direction of the top of the page and is currently turning left. As a result, effective stationary contact (adhesive area) occurs always at the leading edge of the contact area as the tire rolls. On the other hand, slip is confined to the rear of the contact area because the resultant cornering force is applied behind the tire center. In the region of the slip, the tangential surface stresses, necessary to maintain the geometric distortion of the tread surface, exceed the local frictional stresses available. The leading edge is pointing in the steering direction while the rearward portion lags behind on the old heading due to slip.

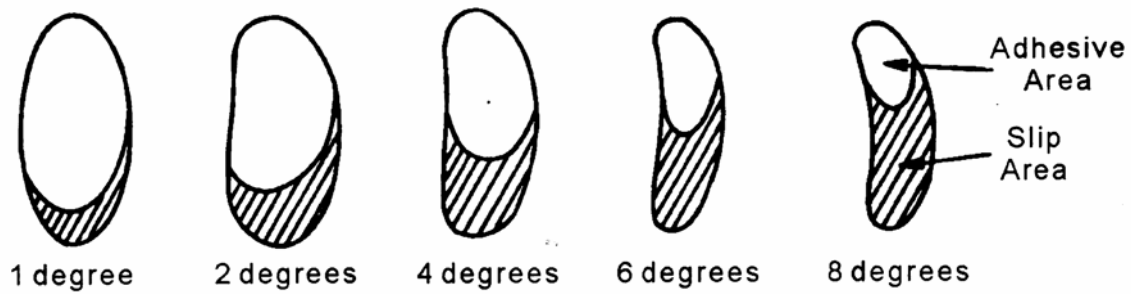


Figure 2-5 Contact Area Shapes at Different Slip Angles (Haney, 2004)

2.1.2.3 Tire vertical force

When a vehicle is placed on the road, it is obvious that a vertical contact force exists between the tire and road surfaces. It is a static force due to gravity. However, when the vehicle is running on a rough road, the tire and sprung mass have vertical accelerations. Due to their vertical accelerations, the dynamic vertical force acts on the tire-road contact area that can reach up to three times higher than a static vertical force. The vertical force on the tire is affected mostly by the vertical acceleration of the sprung mass rather than

by the vertical acceleration of the tire itself because the weight of the sprung mass is much higher than that of the tire. The vertical forces on the tire are not applied at a point but are distributed as normal pressure in the contact area as seen in Figure 2-6.

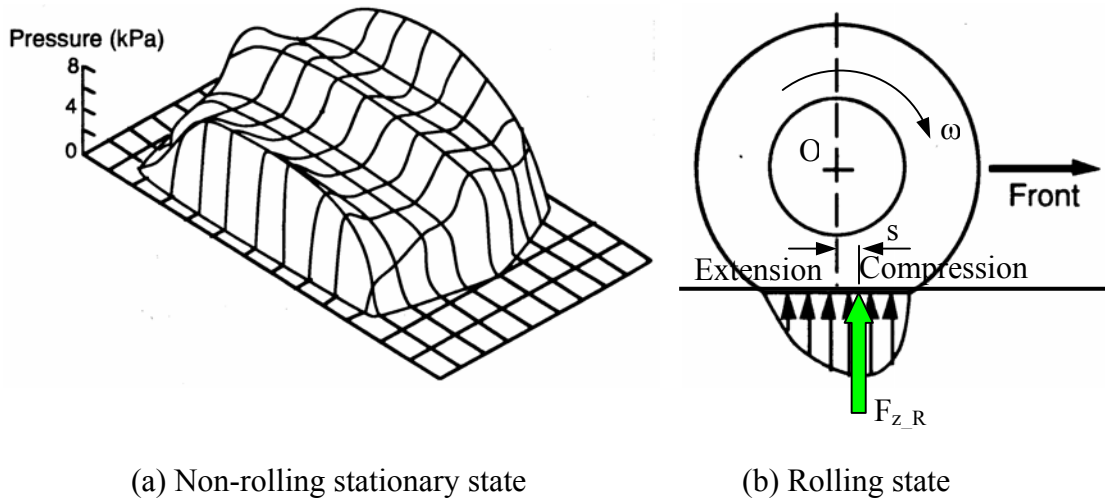


Figure 2-6 Normal Pressure Distributions in the Contact Areas (Gillespie, 1992)

Figure 2-6 (a) shows the normal contact pressure distribution in the contact area for a non-rolling stationary tire. Because tire geometry and boundary conditions are symmetric about the center of the contact area, the pressure distribution is also symmetric. It is noted that at rated vertical load and inflation pressure, greater normal contact pressures are observed under the sidewalls and centerline of the tire due to higher vertical stiffness at those local areas. Meanwhile, Figure 2-6 (b) shows the normal contact pressure distribution in the contact area for a rolling tire. In this case, the boundary conditions are not symmetric about the center of the contact area. Instead, compression in the leading portion of the tire and extension in the trailing portion of the tire near the contact area are observed. Therefore, relatively greater normal contact pressures are exerted in the leading area of the contact. As a result, the resultant vertical force to the tire, F_{z_R} , can be drawn toward the leading edge with an offset, s , as seen in Figure 2-6 (b). This resultant force and offset generate a moment about the tire center, O , oppositely to the tire rotational direction, which is called the rolling resistance moment.

2.1.2.4 Tire overturning moment

An overturning moment is defined as the moment acting on the tire spindle about the longitudinal axis (X-axis) due to non-symmetric vertical pressure distribution across the tire width in the contact area. Deformation of the tire casing and tread due to steering input not only affects cornering forces but also affects the pattern of the vertical contact force distribution in the contact area as shown in Figure 2-7.

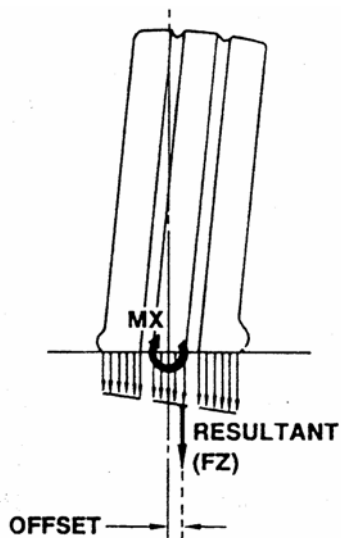


Figure 2-7 Overturning Moment (Yap, 1991)

The magnitude and direction of the contact forces are skewed across the width of the contact area, which results in the lateral offset slightly from the non-steered center line. The coupling of this lateral offset and the resultant vertical force (FZ) produces an overturning moment (MX) acting on the tire about the longitudinal axis. The overturning moment increases linearly as slip angle and/or vertical load increase. The magnitude of the moment is about half of that observed for self-aligning moment in the slip angle range that is less than 4°.

2.1.2.5 Tire rolling resistance moment

When the tire is loaded and rolls on a road, the vertical contact pressure is distributed over the contact area unevenly. Since the leading part of the tire at the contact area undergoes compression and the trailing part of the tire undergoes extension, the vertical resultant reaction force tends to shift toward the leading edge as shown in Figure 2-6 (b). Due to the offset and resultant reaction force from the ground, the moment can be developed against the tire rotational direction, which is defined as the rolling resistance moment.

2.1.2.6 Tire vertical moment

The moment acting on the tire spindle about the vertical axis (Z-axis) is defined as the vertical moment. Non-symmetric contact force distribution on tire-road contact plane determines the vertical moment. In addition, during a cornering maneuver, the resultant cornering force acts on the tire with some offset behind the center of the contact area, called the pneumatic trail, PT, in Figure 2-4 (b). The cornering force and offset creates the vertical moment that tends to restore the steered tire to the original unsteered tire orientation. Therefore, this vertical moment is called the self-aligning moment or aligning moment. The self-aligning moment increases with increasing slip angle input, similarly to the cornering force response. The self-aligning moment increases as slip angle increases until a peak self-aligning moment is developed at approximately 4° to 6° of slip angle. However, once the peak is reached, the self-aligning moment tends to decrease with further increase of the slip angle because of the decrease in the moment arm, PT.

2.2 Tire Models

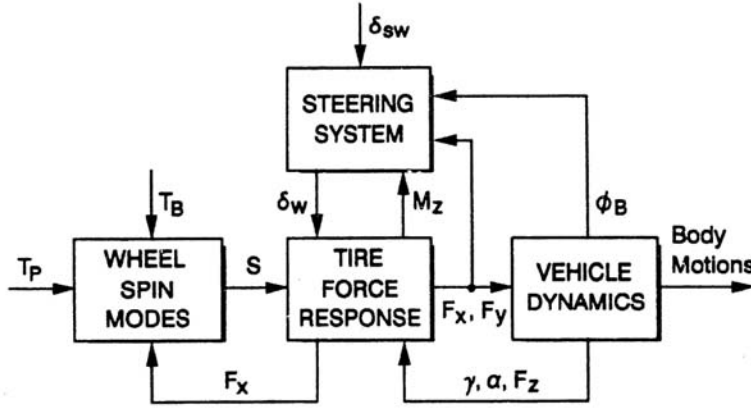
Much research has been conducted in the area of tire manufacture, testing, and model development since Charles Goodyear invented the first pneumatic bicycle tires in 1839. To accomplish laboratory tire testing, large scale experiment set-up and highly

experienced measurement skill and effort are required. Specifically, the transient response measurements of a tire need more complex experiment facilities and data acquisition system. Therefore, modern scientists started to develop an alternative method to minimize the amount of physical laboratory tire testing.

A number of tire models and virtual testing environments have been extensively developed since early 1980's. Analytical composite material models, flexible or rigid ring model, FEA tire models, two-dimensional models, three-dimensional models, half models, and full models of tires have been developed and analyzed. However, tire modeling has always been challenging because of the highly nonlinear nature of tires. Geometric nonlinearity due to large deformations of rubber compounds, material nonlinearity, incompressibility constraint on the deformation of rubber, and nonlinear contact boundary conditions contribute to the difficulty of tire modeling (Oden *et al.*, 1982; Rother, 1984; Kenny, 1988; Tseng, 1989). Therefore, tire models that cover only specific topics of interest have been developed.

Tire models that can predict tire responses precisely play an important role in dynamic vehicle simulations. Allen *et al.* (1995) emphasized the importance of accurate tire force modeling in dynamic vehicle simulations because these tire forces considerably affect the dynamic vehicle handling. As shown in Figure 2-8, the tire force responses interact with wheel spin modes, steering system, and vehicle dynamics. In other words, steering, braking, driving torque, and vertical load play roles as inputs to the tire. Therefore, Allen *et al.* concluded that all these complex interactions should be taken into account in order to accurately model tire force responses and eventually to predict reasonable and acceptable vehicle body motions.

As mentioned above, tire modeling is considerably challenging. Therefore, much research is still continuing to develop more reliable and efficient tire models. Once a good tire model is developed, it is obvious that the tire model simulation will minimize the amount of expensive tire testing and serve for efficient dynamic vehicle simulations.



F_x :	Longitudinal tire force
F_y :	Lateral tire force
F_z :	Vertical tire force or load
M_z :	Tire aligning moment
S :	Tire longitudinal slip ratio
T_B :	Brake torque
T_p :	Engine power torque
α :	Tire side slip angle
γ :	Tire camber angle
δ_{sw} :	Steering wheel angle
δ_w :	Front wheel angle
ϕ_B :	Body roll angle

Figure 2-8 Tire Force Response Interactions (Allen *et al.*, 1995)

2.2.1 Early Tire Models

Since the 1950's, string models, ring models, and beam-on-elastic foundation models have been developed. These early tire models generally considered the tread to be a pre-stressed string or a ring and the sidewalls to be elastic foundations supporting the tread structure. These models mostly include a set of equivalent tire parameters that can be determined from comprehensive tire test experiments. These analytical tire models were useful in predicting overall tire characteristics such as vibration and responses to cornering, braking, and traction. They provided an understanding of such behavior before more direct techniques were applied to tire analysis. However, these early models showed limited accessibility and capability because (a) they required extensive experiments to determine the characteristic tire parameters, (b) their validity was limited to specific ranges of those parameters, and (c) their domain of validity could not always be predicted in advance.

The early tire models mostly adopted the point contact mechanism because of its simplicity (Captain *et al.*, 1979; Loo, 1985; Loeb *et al.*, 1990). The point contact mechanism was established based on the assumption that a tire contacts the road surface only through a single point which is just located under the wheel center as seen in Figure 2-9 (a). Because only the single point has contact with the road surface, the tire response

is quite sensitive to road irregularities especially to short wavelength of road profile that is usually filtered through a contact area in real tire applications. Therefore, the point contact tire model is more useful for long wave road profile inputs.

To overcome this limitation of the point contact tire model, an effective road input model and an equivalent plane tire model were established. The effective road input tire model was developed to provide more realistic road input to the tire model as seen in Figure 2-9 (b). Due to the curvature effect of the imaginary rigid ring which contacts the road profile, the lower frequency of the modified road profile, called the effective road profile, could be generated as represented by the dotted line in Figure 2-9 (b). This effective road profile provided more realistic road input to the tire than the point contact mechanism did.

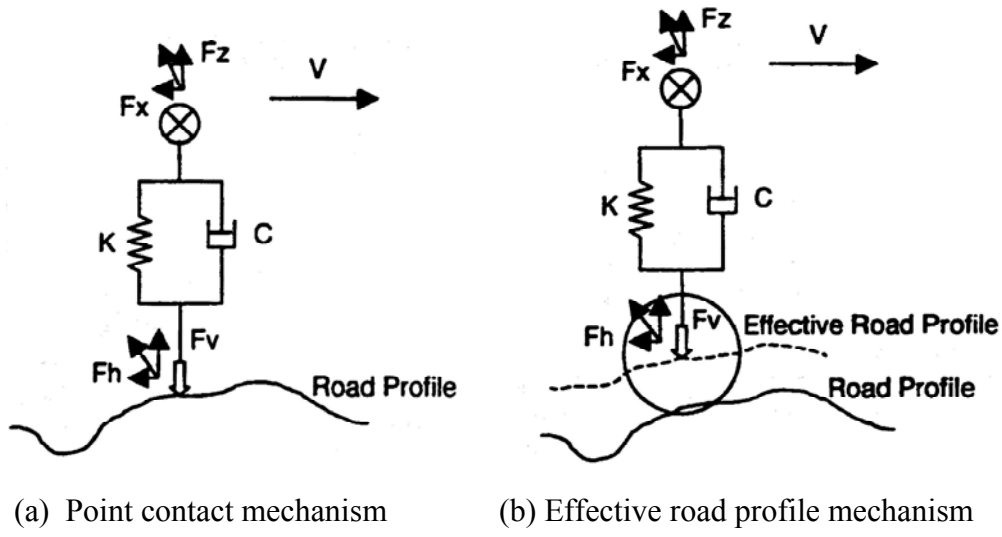


Figure 2-9 Tire-Road Contact Mechanisms of the Early Tire Models
(Sui and Hirshey, 1999)

Meanwhile, an equivalent plane tire-road contact model was created under the assumption that the tire could be simplified as a series of linear radial springs that connected the wheel center and the imaginary equivalent plane as seen in Figure 2-10 (b).

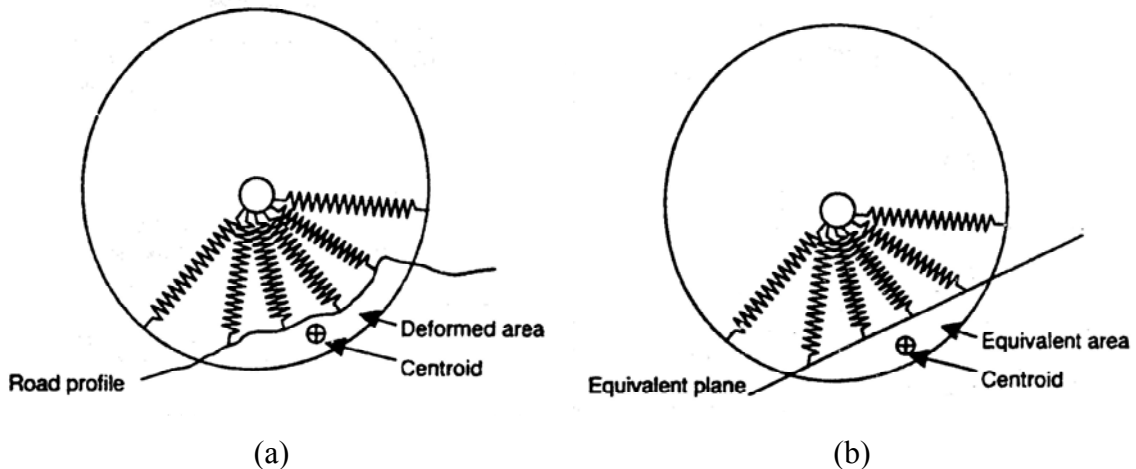


Figure 2-10 Equivalent Plane Tire-Road Contact Model (Sui and Hirshey, 1999)

The equivalent plane represented the road profile whose position and orientation could be determined according to the original road profile and deformed area. Therefore, the centroid locations of both the deformed area in Figure 2-10 (a) and the equivalent areas in Figure 2-10 (b) are identical. In addition, the resultant force applied to the tire center due to the spring deformations of the equivalent plane tire model was identical to the force from the real road profile. This equivalent plane tire model could filter high frequency road profile input and worked more precisely for concave road surfaces rather than convex road surfaces. Still, the equivalent plane tire model has difficulty in determining the equivalent plane and out-of-plane behavior since the model consists of only two-dimensional in-plane radial springs (Davis, 1974). The effective road input model implemented a virtual road profile, which represented the wheel center trace when the vehicle travels very slowly over the real ground surface. The point contact tire model on this effective road profile resulted in good correlation to the real measurement output (Guo, 1993; Guo, 1998).

In 1984, Takayama and Yamagishi introduced a lumped mass-spring tire model to analyze the in-plane tangential and radial axial forces during cleat-drum excitation. The tread and belts were modeled by using a rigid ring, and the tire deflection due to cleat excitation was allowed by line or plane springs attached to the rigid ring as seen in Figure 2-11.

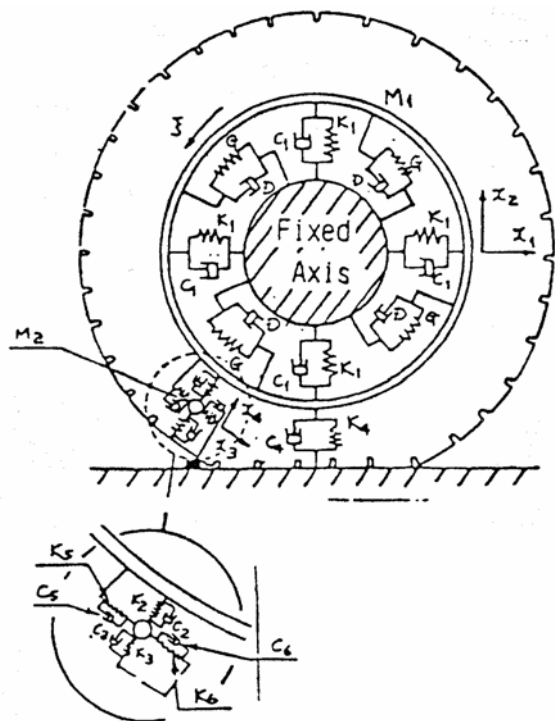


Figure 2-11 Five Degrees of Freedom of Lumped Mass-Spring Tire Model
(Takayama and Yamagishi, 1984)

As shown in the Figure, the tire model consists of five degrees of freedom including longitudinal (x_1) and vertical (x_2) motion of the rigid ring, local longitudinal (x_3) and vertical (x_4) deflections on the cleat, and rotational motion of the rigid ring (ξ). The tire axle was fixed after loading to detect the tangential and vertical reaction force during cleat excitation. Thus, the effects on or by the suspension system were ignored. The displacements and forces out of the tire plane were also neglected. The parameters for the rigid ring tire model were determined through comprehensive experiments to represent a passenger car tire, 165SR13. The tire model was loaded at 3,780N (850 lb) on a cleat-drum and driven at 40 km/h (25 mph) to predict longitudinal and vertical axial force and vibration modes. The predicted axial forces agreed well with the measured forces. It was found that the lowest frequency of vibration mode was detected at 40 Hz for the rotational vibration mode. The predicted lowest frequencies of longitudinal vibration mode at 67 Hz and vertical vibration mode at 74 Hz also agreed well with experimental results.

In 1985, Loo developed an analytical tire model which consisted of a flexible ring under tension with a nest of radially arranged linear springs and dampers to represent a pneumatic tire model. He was concerned with the prediction of the tire's vertical load-displacement characteristics and its free rolling resistance. The ring, which represented the tread band of the tire, was assumed to be massless and completely flexible. The mathematical formulation of the tire contact with the smooth hard surface was based on the theory of a tensioned string supported by an elastic foundation. Forces developed within the contact area were computed from a geometrical perspective. The experimental verification was conducted and showed good correlation by comparison with the predicted vertical load-deflection characteristics for the normal working range of inflation pressure, deflection, and increasing surface curvature. The predicted rolling resistance characteristics were also found to be in good accord with the experimental measurements.

Since 1987, Pacejka and his colleagues have established mathematical formulas to predict cornering forces and aligning moments. These formulas, called the Magic Formulas, are based on tire measurement data and calculate tire forces or moments at similar operation conditions (Bakker *et al.*, 1987; Bakker *et al.*, 1989; Apetaur, 1991; Hirschberg, 1991; Lidner, 1991; Oosten and Bakker, 1991; Pacejka and Bakker, 1991, Pacejka *et al.*, 1997). To complete a set of Magic Formulas, tire measurement data, such as cornering force versus slip angle, self-aligning moment versus slip angle, or brake force versus slip ratio, should be prepared in advance. Therefore, extensive tire measurements need to be performed to cover a certain range of vertical tire loads. Once the Magic Formulas are established for a certain operation condition, the calculated output correlates quite well with the measurement data. Meanwhile, in order to generalize the Magic Formulas at a wide range of vertical loads, 13 coefficients need to be calculated from the extensive and costly tire measurements at various vertical tire loads. Because of the great number of the coefficients, the Magic Formulas method is frequently criticized. The example of the coefficients in the Magic Formula for a car tire is provided in Bakker *et al.*'s work in 1987.

In 1997, Zegelaar and Pacejka constructed a rigid ring tire model to represent a passenger car tire as seen in Figure 2-12. In the rigid ring tire model, the tread and steel belts were modeled together as a rigid ring and placed on an elastic foundation that represented the tire sidewall. Since the tread and steel belts were modeled as a rigid ring, a new parameter such as a vertical residual stiffness was required to describe the large deformation of the tire in the contact area. A longitudinal slip model was also introduced that generated the longitudinal contact force in the contact area. In order to determine the required parameters for the rigid ring tire model, measured tire frequency response on a rotating 2.5 m-diameter drum was used.

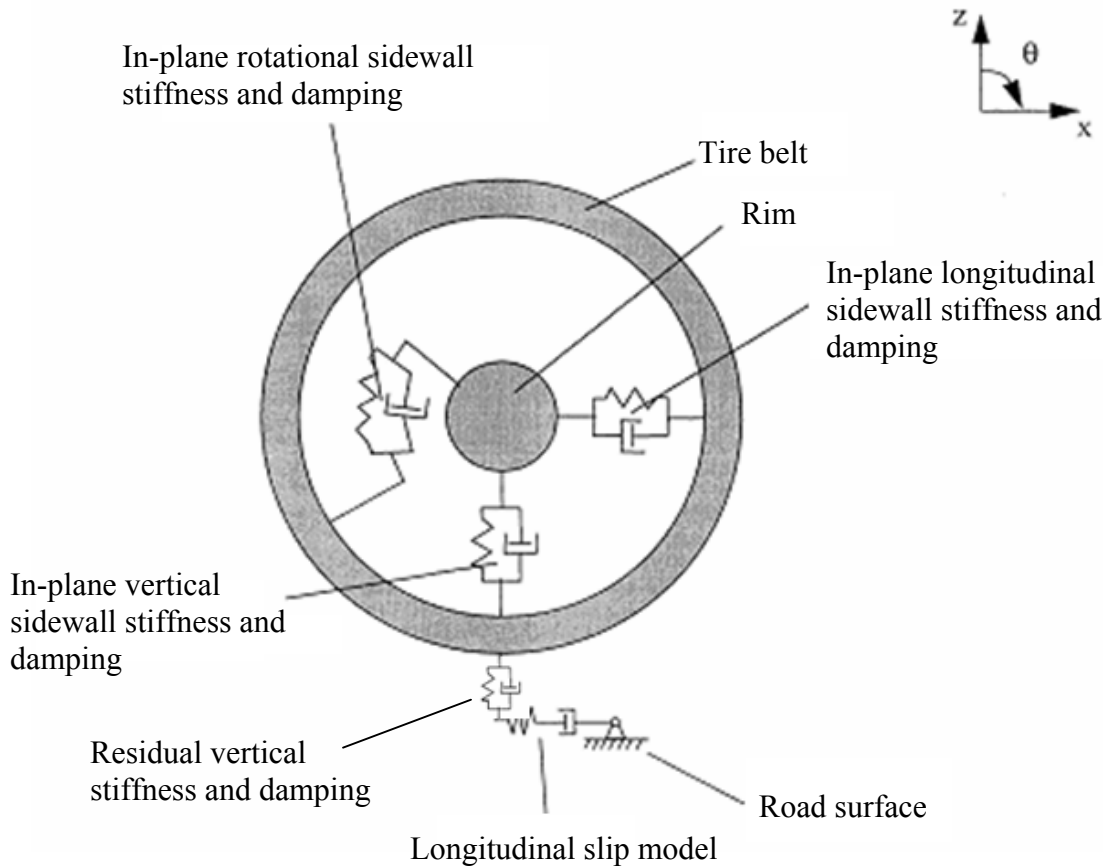


Figure 2-12 In-Plane Rigid Ring Tire Model (Zegelaar and Pacejka, 1997)

Zegelaar and Pacejka stated that tire in-plane vibrations are attributed to three major sources: brake torque fluctuations, road unevenness, and horizontal and vertical oscillations of the axle. Previously, they had presented the dynamic tire responses on

uneven roads. In this study, longitudinal force and rotational velocity at brake pressure variations were predicted by using the rigid ring tire model. The results from the simulation showed good correlation with measurements. Meanwhile, from free rolling simulations, the rigid ring tire model could successfully present an increasing effective rolling radius and vertical contact force as the tire rolling speed increased, which was due to the increased centrifugal forces of the tire sidewall and tread.

In 1997, Kim and Savkoor performed an analysis of the in-plane contact problem of free rolling pneumatic tires on a flat road by using a ring tire model. The tire model was mainly constructed with an elastic ring supported on a viscoelastic foundation as shown in Figure 2-13.

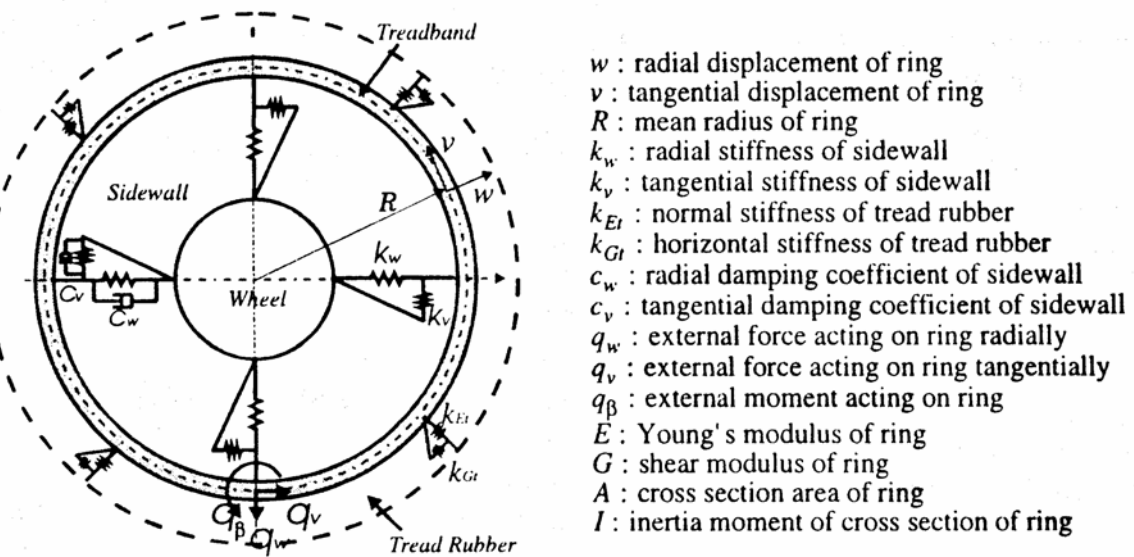


Figure 2-13 Flexible Ring Tire Model (Kim and Savkoor, 1997)

The elastic ring represented a flexible tread band and belts of the tire while the elastic foundation described deformable sidewalls. In addition, elastic spring components, K_{Et} and K_{Gt} , were introduced on the outer surface of the elastic ring to model the radial and tangential flexibility of tire tread rubber. The input parameters required to complete the ring tire model are listed in Figure 2-13. They determined those parameters based on measurements such as vertical load versus deflection of a radial passenger car tire,

205/60R15. Then, traction force distributions at contact area and rolling resistance coefficients were predicted at different speeds. However, no experimental measurements were provided to validate their predicted tractive contact forces and rolling resistance coefficients from the ring model.

Bruni *et al.* in 1997 proposed a methodology to determine the in-plane tire parameters for a rigid ring tire model from limited experimental tests. The rigid ring tire model was devised such that it could perform vehicle comfort, braking, and driving analysis as seen in Figure 2-14.

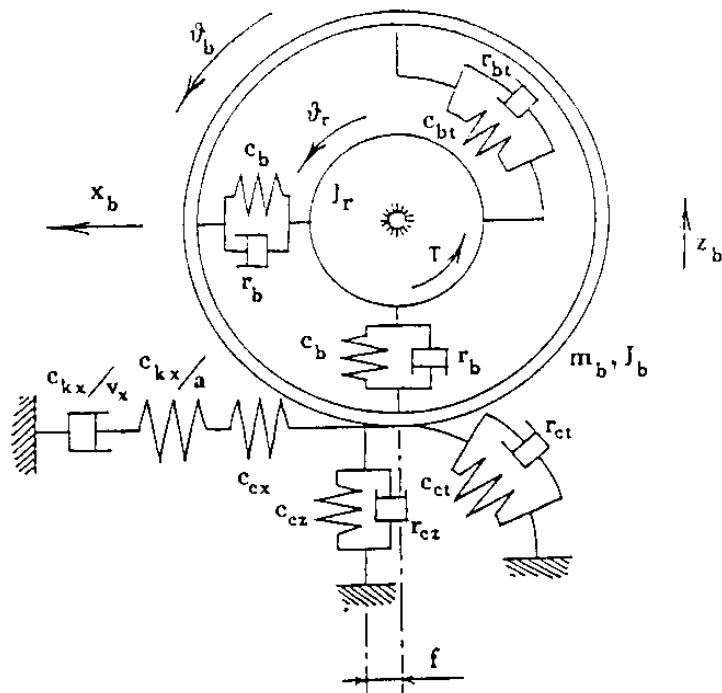


Figure 2-14 Rigid Ring Tire Model (Bruni *et al.*, 1997)

To complete the rigid ring tire model, basic parameters such as the moment of inertia of the rigid ring, rigid ring mass, and effective rolling radius were directly measured through torsional pendulum and free rolling tests. Then, most of the rest of the parameters, such as sidewall stiffness and damping as well as residual stiffness and damping were estimated by minimizing the difference between the experimental and analytical damped natural frequencies. The required in-plane tire parameters were determined for a

passenger car tire, 185/60R14, at inflation pressure of 0.20 MPa (29 psi) and vertical load of 1,990 N (450 lb) and validated through natural frequency and damping factor tests.

Allison and Sharp (1997) also examined this simple rigid ring model to approach the low frequency (up to about 100 Hz) in-plane longitudinal vibration problems of vehicles. Schmeitz *et al.* (2004) presented a quarter vehicle model by combining the rigid ring tire model, suspension, sprung mass and elliptical cams together. The elliptical cams were adopted to generate an effective road profile. They predicted vertical tire motions and longitudinal forces for different heights of step road inputs. Then, the predicted results were compared with measurements and showed good correlations. They also conducted modal analyses on the quarter vehicle system to find a vertical mode at 71.5 Hz and a horizontal mode at 84.4 Hz.

2.2.2 Finite Element Analysis Tire models

The finite element analysis (FEA) is a useful numerical tool especially in evaluating a complicated design model. Since 1970, FEA has been widely adopted in analyzing stress, strain, and elastic/plastic deformation of more complicated structural models which cannot be accomplished with ease by experimental measurements or other simple models. For example, structural models in very high pressure or temperature application, vehicle crashworthiness, and high speed impact simulations of deformable bodies have been constructed and analyzed by using FEA.

Since 1970s, FEA has been adopted in the development of effective and efficient tire models because traditional structural analysis techniques could no longer offer sufficiently detailed results for advanced tire designs. Moreover, the FEA tire models can reflect real-world boundary conditions more directly without adjustments compared to the previous non-FEA tire models. The FEA tire models can also directly handle large deformations around the contact area without additional adjustments such as the residual stiffness and damping used in ring tire models. The FEA tire models can also use an actual road profile, without any modification of the original profile. Early FEA tire

models can predict basic characteristic tire responses, such as tire-road contact areas, stiffness, vibration modes, cornering forces, and self-aligning moments.

The FEA simulation of a tire is still a challenging task due to computational contact problems as well as the nonlinearity nature of the tire. The handling of the contact boundary is the most challenging and has attracted much intention. In many cases, a Lagrange multiplier, penalty term, or gap element is adopted to describe the interaction between tire treads and the road surface. A gap element is the easiest way to handle contact problems. However, it cannot easily deal with contact-impact and contact on an arbitrarily shaped surface. In this section, the FEA tire models with contact are reviewed. The development of the contact solution algorithms are reviewed in Section 2.3. Due to computational limitations, most tire simulations using the finite element method have been limited to the static or quasi-static analyses in early ages of FEA tire models. It was not until in late 1990s that transient responses have been studied using an explicit FEA option.

Padovan (1977) employed a two-dimensional curved axis-symmetric thin shell element model to examine the power dissipative rolling resistance and thermo-viscoelastic problem of steady-state rolling tires. Trivisonno (1977) also examined the similar thermal problem by a two-dimensional finite difference model. Noor and Anderson (1982) stated that thin shell models neglect transverse shear deformation. Therefore, they used a two-dimensional thick and curved shell FEA tire model. This model can handle the laminated construction, anisotropic material behavior, transverse shear deformation, inflation pressure (pressure stiffness), and thermo-viscoelastic material response.

Noor *et al.* (1985) again sharpened and focused their general study on two-dimensional shell models of the tire by incorporating elliptic cross-section and linear material response. The analytical formulation was based on shell theory with transverse shear deformation, anisotropic material behavior, and geometric nonlinearities in moderate rotations.

In 1984, Tielking developed a three-dimensional FEA tire model by using shell elements to investigate tire-pavement interaction. A four-ply bias tire model was constructed to evaluate whether the model could predict the different effects of nylon and polyester cords on tire deformation, contact pressure distribution, and traction. The modulus input of polyester was four times greater than that of nylon. The tire, G78-14, was inflated at 0.22 MPa (32 psi) and loaded to investigate the vertical deflection behavior of the two tire models with different cord materials. As a result, the tire with lower cord modulus, nylon, showed greater vertical deflection and contact patch area at the same vertical load. Meanwhile, the peak locations of the contact pressure were different between the two tire models. The tire with polyester cords had the peak location of the contact pressure closer to the sidewall due to greater sidewall stiffness. The experimental measurements on the contact pressure done by Freitag and Green (1962) confirmed Tielking's contact pressure prediction.

In 1986, Nakajima and Padovan developed the transient sliding contact model by using a two-dimensional FEA tire and an arbitrarily-shaped road obstacle. Then, the tire sliding and impact events with holes and bumps were simulated using the finite element code, ADINA. The tread and sidewalls were modeled by a linear viscoelastic ring on an elastic foundation. They discussed the dynamic responses of the vertical and horizontal forces transmitted to the tire spindle when the tire slides over a bump and a hole at different velocities. The computed and experimental results were in good agreement.

In 1988, Kenny and Stechschulte performed shear strain analyses of the carcass through FEA bias-ply and radial-ply light truck tires, 9.50-16.5. For the bias-ply tire, they adjusted cord-ply endings considerably narrower than those in the original conventional construction. Then, the shear strain in the carcass after inflation was monitored from the tire center and shoulder to sidewall regions. It was found that shear strains of the narrow cord-ply construction sharply increased in the shoulder region. Therefore, the cord-ply endings were extended from the shoulder to sidewall region in order to reduce the shear strains in the shoulder. Meanwhile, for the radial tire, a wedge between the second and third belts, as shown in Figure 2-15, was inserted to reduce shear strain in the shoulder

region. Through this study, Kenny and Stechschulte presented the practical utilization of the FEA to design tire construction with less shear strain in the carcass, which could not be done by conventional experimental method at that time.

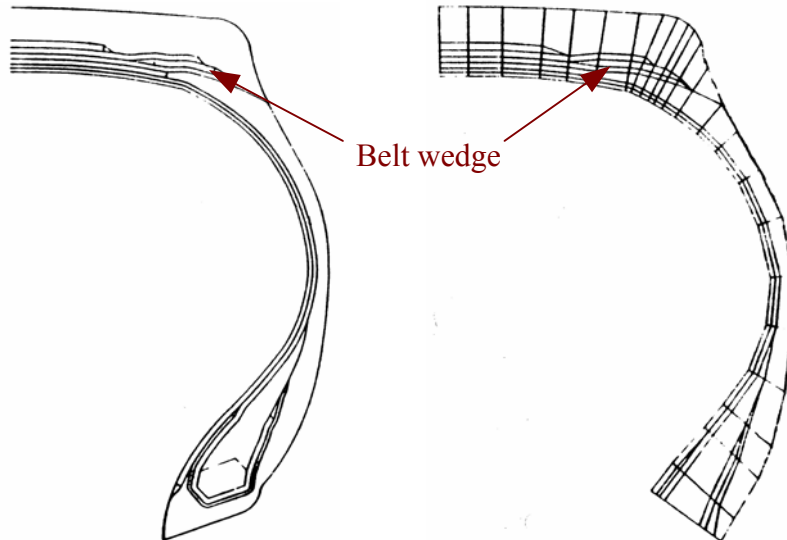


Figure 2-15 Radial Tire Layout with a Belt Wedge near Tread Shoulder (Kenny and Stechschulte, 1988)

In 1989, Tseng *et al.* developed a two-dimensional half FEA passenger car tire model, P195/75R14, to simulate the tire-rim interface at an inflation pressure of 0.24 MPa (35 psi). Rubber materials were modeled as nonlinear incompressible elements whereas plies were modeled by cord-rubber composites elements. In the developed tire model, gap elements were especially used to represent the initial opening between tire and rim at zero inflation pressure. The gap elements were modeled by using a nonlinear and fully compressible material. This opening was designed to be closed when the inflation pressure increased. Contact pressure distributions of the tire-rim interface under various geometry and loading conditions, such as different interference fits, bead profiles, bead heel diameters, and inflation pressures, were predicted and compared with the measurements. The predicted contact pressure distribution agreed quite well with their measured values.

In 1990, Eskinazi *et al.* intended to determine whether it was possible to predict relative belt edge endurance for a radial passenger car tire, 175R14, using FEM. Three groups of tires with different belt edge configurations were tested to validate the predicted results. A two-dimensional axisymmetric finite element tire model was first performed to determine if the results from such an analysis could be used to predict a relative ranking for belt edge endurance. As a result, it was found that two-dimensional analysis could lead to erroneous conclusions. Instead, a three-dimensional analysis under static vertical loading and free rotation was performed for the same belt edge endurance test. This new approach resulted in an improvement in the quality of the correlations. The differences in the predicted values of various stress analysis parameters for the three belt edge configurations were studied. In addition, their implication on predicting belt edge endurance was discussed.

In 1991, Ishihara developed a two-dimensional cord-rubber composite membrane element for tire belts model that could be incorporated into his in-house FEA code. Due to limited computational capabilities at that time, an efficient tire model was required to predict complicated tire responses. He built a passenger car tire model, 175SR14, at the inflation pressure of 0.23 MPa (33 psi) by using newly developed membrane elements and performed load-deflection virtual tests, contact pressure distribution predictions, and interply shear strains predictions at the belt edge. The predicted tire responses were compared with physical measurements. Ishihara also built a three-dimensional FEA tire model by using solid elements to compare the efficiency. Finally, it was concluded that the FEA tire model with the proposed membrane elements could yield reasonable predictions without loss of confidence.

In 1993, Scavuzzo *et al.* also discussed the importance of tire vibration modes in terms of vehicle ride quality and the influence of the parameters controlling these modes by using two passenger car tires, P205/70R14 and P185/75R14. They also described how the two different modes influence vehicle ride comfort. They focused their study especially on the parameters that affect the frequency of tire vibration modes. The parameters investigated were tire size, construction, inflation pressure, and operating conditions such

as speed, load, and temperature. Road irregularities such as a single impact from a bump, chuckhole, or a series of small impacts from rough road surfaces were enveloped by the tire. These impacts excite tire vibration modes in much the same way a hammer impact does during a modal test. This behavior could be demonstrated by measuring accelerations at the spindle of a passenger car. The spindle vertical acceleration was measured and compared to the vehicle interior receptions. Results from both the FEA approach and modal testing were discussed.

In 1994, Rhyne *et al.* developed a full three-dimensional FEA passenger car tire model, P195/75R14, as shown in Figure 2-16. They investigated the influence of rim imperfections on the tire-rim assemblies and ride comfortability at the inflation pressure of 0.207 MPa (30 psi). Based on the fact that non-uniformity of wheel contributes strongly to the radial wheel force variation, lateral and radial imperfections of a rim were the focus of this study. It was found that the non-uniformity sensitivity to lateral rim imperfection was usually about an order of magnitude less than the sensitivity of radial rim imperfections. However, the lateral rim imperfection cases were usually much greater than the radial rim imperfection cases. Thus, the non-uniform signal produced by both lateral and radial rim imperfections needs to be investigated to study radial wheel force variations.

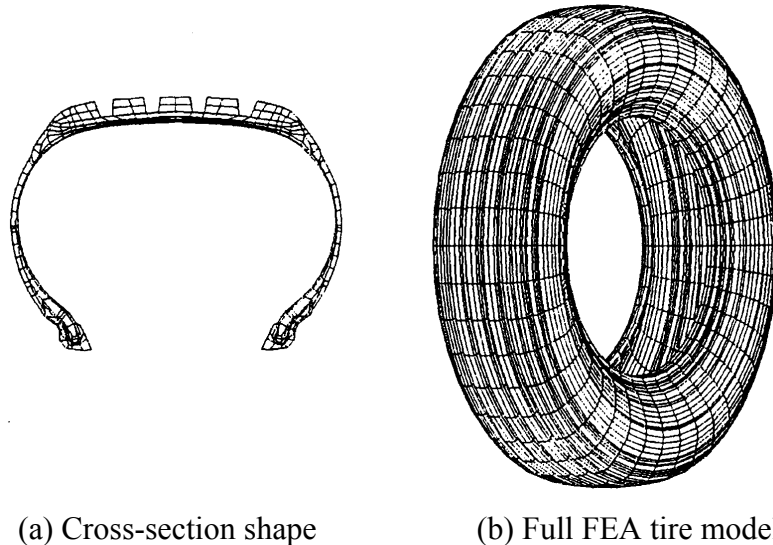


Figure 2-16 Passenger Car Tire, P195/75R14, FEA Tire Model (Rhyne *et al.*, 1994)

Kao and Muthukrishnan (1997) used a nonlinear FEA code to simulate a simple tire test and demonstrated that it was possible to predict tire transient dynamic responses from the tire design data. Here, for the first time, an FEA tire model incorporated geometry, material properties of the various components, fiber reinforcement, layout, and other features of a commercial passenger car radial-ply tire P205/65R15. Before Kao and Muthukrishnan, almost all of the research using FEA tire models was built using only a single type of element under reasonable simplifications and assumptions; these simplifications meant the loss of some detail at the same time.

Kamoulakos and Kao (1998) again verified the same setup as Kao and Muthukrishnan (1997) using another finite element commercial code, PAM-SHOCK, and they improved the model's correspondence to reality. They also extended this simulation further (for six more cleat impacts, corresponding to twenty one tire revolutions) to demonstrate the reliability of the program in providing an instability-free scenario for the tire impact problem. It was concluded that when the vertical load on the tire is low, higher contact pressure peaks occur in the inner rib areas. However, as the vertical load increases, the contact pressure peaks in the outer ribs tend to be higher than those in the inner ribs. This phenomenon was found to be noticeable especially under conditions of low inflation pressure. This relationship between tire-road contact pressure distributions and inflation pressure and/or vertical load was already established experimentally by Browne *et al.* (1981) and Sakai (1995).

In 1998, Koishi *et al.* demonstrated the feasibility of the tire cornering simulation using the explicit FEA software, PAM-SHOCK. They built a three dimensional FEA passenger car tire model for a cornering simulation. They investigated the effect of inflation pressure on the cornering power¹ and the effect of belt angle and rubber modulus on the cornering force. A higher inflation pressure led to lower cornering power for vertical loads under 3.0 kN because the higher inflation pressure resulted in a shorter contact length. However, for vertical loads over 3.0 kN, a higher inflation pressure led to higher cornering power because the higher tire stiffness due to the higher inflation pressure

¹ The cornering power is defined as the cornering force at a slip angle of 1°.

dominated. The results from both simulation and experiment showed good correlation. By examining the effect of the belt angle, they found that the cornering forces of the tire with 0° belt angles are about 67% of those of a tire with $\pm 20^\circ$ belt angles. They explained that this result was caused by the difference in the contact lengths of the tires. This study showed the importance of contact length as a validation parameter for tire models. The authors found that a higher rubber modulus led to a higher cornering force. The predicted cornering forces agreed well with experimental data.

In 2000, Chang *et al.* presented their first attempt to simulate the high-speed tire impact problem of MD-11 aircraft tire landing on the runway using PAM-SHOCK. This simulation focused particularly on tire transient dynamic response. The vertical and horizontal axle force histories and contact patch vertical stresses distribution extracted from this simulation were carefully studied.

In 2001, Chae *et al.* published their study on standing wave predictions of an SAE Formula-1 racing car tire. The FEA tire model was constructed from three-layered membrane elements which represented the carcass and belts with specified fiber directions. Rim, spokes, and brake disc were also included in the model and rotated with appropriate rotational inertias. The effects of tire inflation pressures and loads on the speed at which standing waves might occur were investigated by using the tire model. The results showed that as inflation pressure increased or load decreased, the standing wave initiation speed increased. Using this model, the relationship between the wavelength and tire speed could be clearly predicted from the observation of the animations. It was also found that the wavelength increased as the tire speed increases over the standing wave initiation speed.

In 2001, Zhang *et al.* developed a nonlinear FEA tire model to estimate the tire-road contact pressure distribution on the contact area as a function of tire inflation pressure and vertical load as shown in Figure 2-17. The model was a full-scale truck tire, 12.5R22.5. The hyper-elastic solid rubber elements were adopted to represent large magnitude nonlinear deformations. A total of four sets of alternating rubber and belt

layers were considered to model the four layers of steel belts under the treads as seen in Figure 2-18. The beads were not included in this model. Since this model incorporated clamped boundary conditions at the rim contact areas, no slip could be observed between the tire and rim.

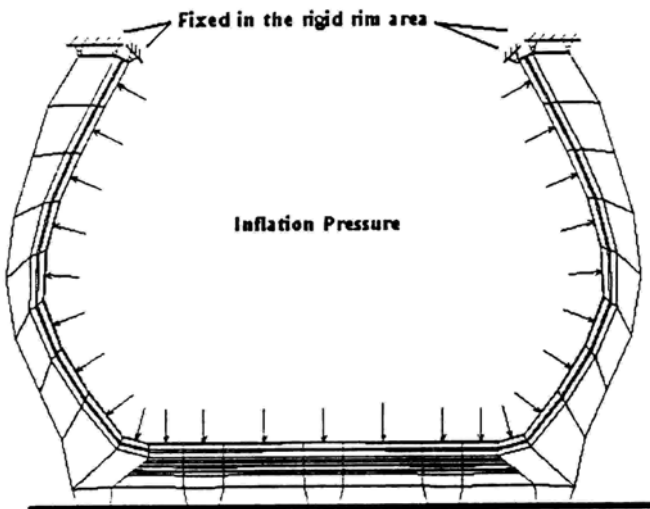


Figure 2-17 Inflated and Loaded Tire Model with Fixed Boundary Conditions in the Rim Contact Areas (Zhang, 2001)

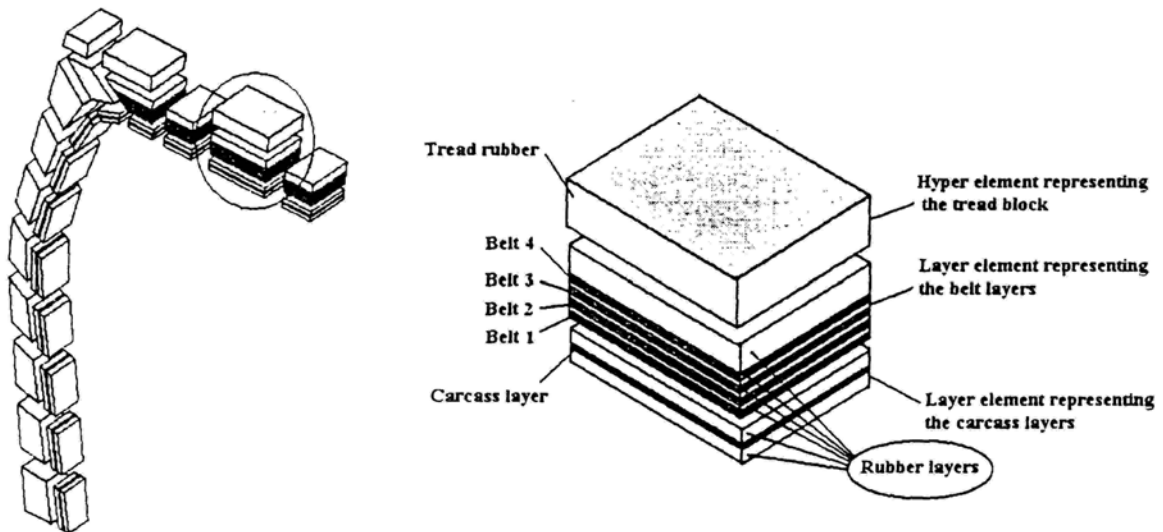


Figure 2-18 Detail Tire Modeling of Isotropic and Anisotropic Layers (Zhang, 2001)

In this study, the characteristic pressure distribution was confirmed successfully as a function of vertical load through static FE simulations. When the vertical load on the tire is low, higher contact pressure peaks occur in the inner ribs areas as seen in Figure 2-19

(a). However, as the vertical load increased, the contact pressure peaks in the outer ribs tend to be higher than those in the inner ribs as shown in Figure 2-19 (b). This phenomenon was found to be noticeable particularly when the inflation pressure is low. These relationships between tire-road contact pressure distributions and inflation pressure and/or vertical load were established in Browne *et al.*'s (1981) and Sakai's (1995) experimental work.

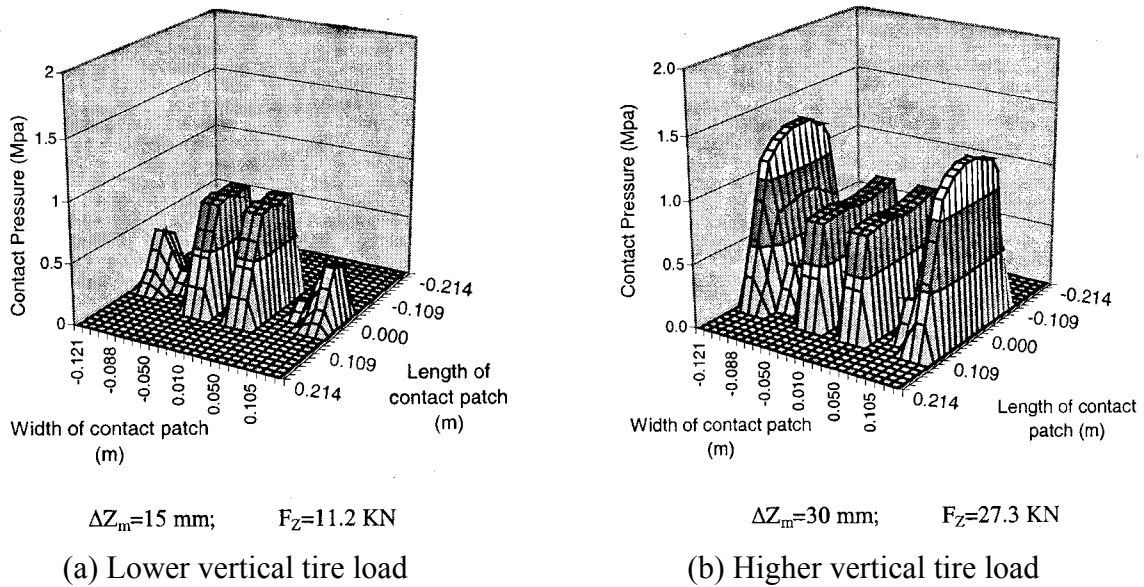
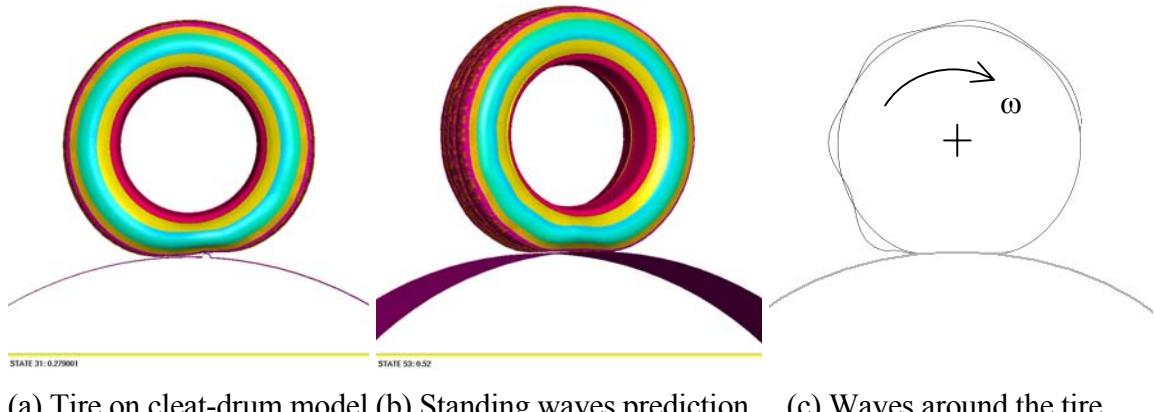


Figure 2-19 Normal Contact Pressure Distribution (Zhang, 2001)

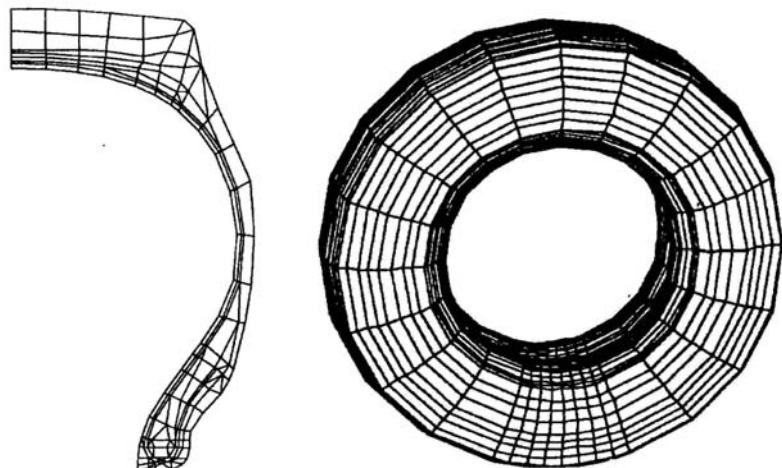
In 2002, Chang developed a passenger car tire-drum model to predict tire standing waves and tire free vibration modes as seen in Figure 2-20 (a). The detection of the tire in-plane free vibration modes was achieved by recording the reaction force histories of the tire axle at longitudinal and vertical directions when the tire was rolling over a cleat on the road. Then, an FFT algorithm was applied to examine the transient response in the frequency domain. They reported 84 Hz resonance vertically and 45 Hz resonance longitudinally for a P185/70R14 tire. In addition, visualized simulations of the standing wave phenomenon were carried out for the first time as shown in Figure 2-20 (b and c). The results were compared with more than ten previous theoretical or experimental studies and showed good agreements with the previously published studies.



(a) Tire on cleat-drum model (b) Standing waves prediction (c) Waves around the tire

Figure 2-20 Vibration Modes Test (a) and Standing Waves Prediction (b and c)
(Chang, 2002)

In 2003, Yan developed an FEA truck tire model, 9.00R20, to investigate maximum sectional width and resultant reaction force with tire speed and vertical load as shown in Figure 2-21. Furthermore, an in-house FEA code was developed with a contact algorithm that had been introduced by Wu (1993).



(a) Half cross-section shape (b) Full FEA tire model

Figure 2-21 Two-Dimensional and Three-Dimensional Tire Models (Yan, 2003)

In Yan's tire model, the rubber materials were treated as incompressible solid elements based on the Lagrangian multiplier method. The non-linear mechanical properties of elastomers were modeled by the Mooney-Rivlin model. The two Mooney-Rivlin

constants were obtained from experimental test data. The belts, carcass, and beads were modeled by an equivalent orthotropic material model where the effective moduli were determined from the individual material properties of the rubber compound and cords using Halpin-Tsai equations.

The half cross-sectional shape and full-scale FE model of Yan's truck tire are shown in Figure 2-21. Due to the symmetry of its structure and loading conditions, only half of the full-scale tire model was used in analyzing the steady rolling tire. By using this model, maximum sectional widths were predicted as the tire speed increased. As a result, narrower sectional width and higher reaction force were observed with increasing tire speed. Yan explained that this result is associated with the centrifugal inertia force of the tread materials. The centrifugal force pushes the tread materials outward radially, which resulted in inward movement of the sidewall materials. This result is coincident with the results of Chae *et al.*, (2001) and Chang (2002). They also observed increasing vertical contact forces with increasing tire speed between tire and road surface from FEA simulations. For the calculation of the contact forces, Lagrange multiplier method was used.

In 2005, Yan performed a study of the relative belt edge endurance of a radial truck tire, 9.00R20, following from his previous research in 2003. He stated that a modern radial tire generally has two particular regions that undergo high loading; the belt edge region and the region around body turn-up end. In addition, he emphasized that the tire shoulder is also a critical region in which delamination failure on the interface between the shoulder rubber and body ply can occur. Therefore, he performed a qualitative predictability analysis on those important regions in the radial truck tire. First, he prepared three FEA radial truck models with different belt widths. In order to examine the effect of different belt widths on internal force development during inflation and tire loading, stress and strain energy states in the belt edge regions were predicted. Secondly, he performed a similar analysis to observe the effect of the different belt widths on the stress and strain energy states of the selected regions around body turn-up end as shown in Figure 2-22 (b). Thirdly, he investigated the stress and strain energy states in the

region of tread shoulder as seen in Figure 2-22 (a). Finally, he predicted tensile forces exerting on the belt from the three truck tire models. Throughout the comprehensive finite element tire model analyses, especially in the critical regions of the tire, the relative belt edge endurance was successfully predicted and the numerical results showed reasonable values.

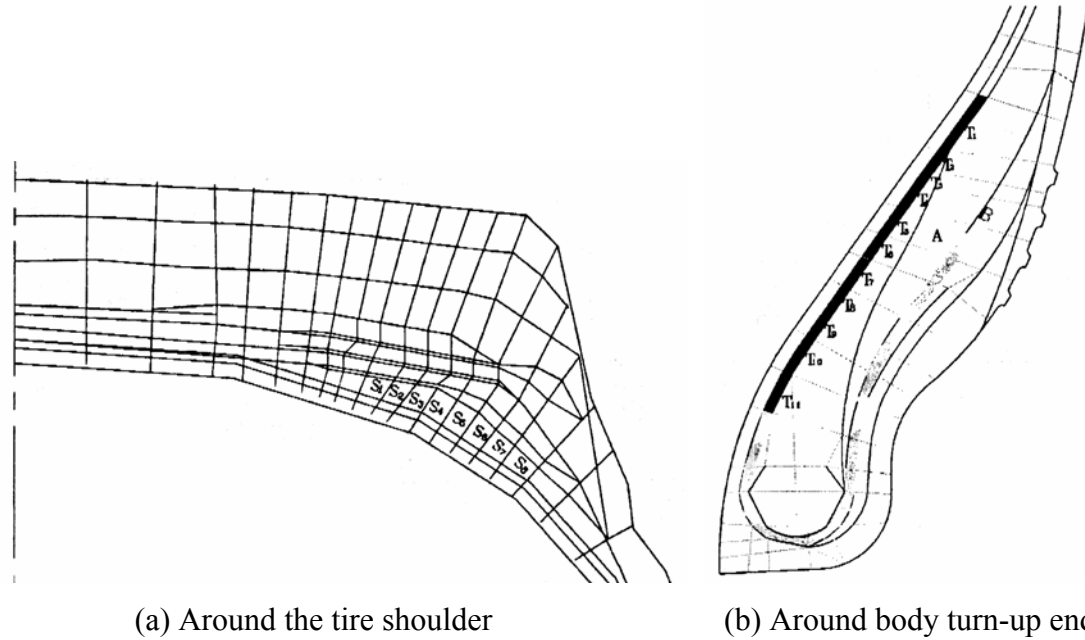


Figure 2-22 Tire Parts Subject to Relatively High Loadings (Yan, 2005)

In summary, a number of FEA tire models have been developed and analyzed for various tire applications. Most of the predictions from the models were validated by comparison with physical measurements. In the primitive FEA tire models, two-dimensional, coarsely-meshed, and/or half tire models were frequently created due to limited computational capabilities. Later, three-dimensional, finely-meshed, and full FEA tire models were gradually developed to handle more specific tire responses by means of significantly enhanced computational capabilities. The three-dimensional full tire models can perform versatile simulations under non-axisymmetric loadings and boundary conditions.

2.3 Contact and Sliding Interfaces

Contact is very important in engineering applications as well as in human life. For human beings, no one can walk without frictional contact with the ground surface. No one can grab any objects or tools to use them without frictional contact either. Similarly, in engineering applications, many important contacts can be found in power transmission systems such as machinery gears, cams, and bearings.

Solutions for the computational contact problem have been obtained since the late 1960s (Goodman *et al.*, 1968; Wilson and Parsons, 1970; Chan and Tuba, 1971). Since then, researchers have incessantly paid attention to accurate and efficient contact algorithm developments. In the past, those contact conditions were dealt with by using simple boundary conditions due to computational limitations. However, thanks to rapidly increasing modern computational power, more accurate and efficient contact algorithms closer to real world applications are being developed.

In this section, contact solution algorithms commonly adopted in computational contact mechanics are reviewed. Contact search, contact pair match, and two important methods for contact force calculation are included.

2.3.1 Computational Contact Solution Algorithms

In computational simulations that include contact events between objects, a contact simulation algorithm is of prime importance because the algorithm searches for contact prone parts and applies the contact condition after contact has been detected. The former is commonly called the contact search algorithm while the latter is called the contact interface algorithm. Without the contact algorithm implemented in computational simulations, no contact will occur even though two bodies are supposed to collide with each other. As a result, no deformations and no contact forces can be predicted. Figure 2-23 shows a schematic of the two major algorithms used in the contact-impact simulations; contact search algorithms and contact interface algorithms.

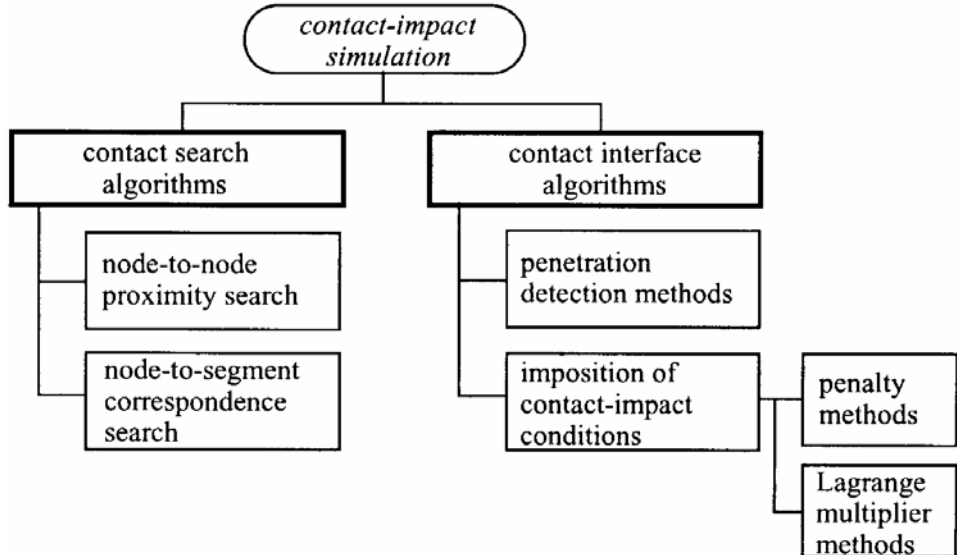


Figure 2-23 Contact-Impact Simulation Methods (ESI, 2000)

Figure 2-23 can be summarized as follows: The solution to the computational contact problem is to detect penetration between two objects and calculate an appropriate response that eliminates, minimizes, or reduces the penetration. Contact proximity and node-to-segment contact pair match are performed by search algorithms. Then, the contact interface algorithms check for penetration and establish contact. The equations of contact constraints are activated by using the Penalty method or the Lagrange multiplier method that are widely adopted for computational contact mechanics.

There are two types of contacts, master-slave contact and self-contact. Master-slave contacts require the definition of two surfaces: slave and master sides. Each node of the slave side is checked for penetrations to the segments/edges of the master side. For the symmetric treatment, the inverse configuration (master nodes versus slave segments/edges) is tested as well. This type of contact could be used for well-determined contact situations such as impact.

Self-contact requires the definition of one slave surface only. Each node/edge of the slave side is checked for penetrations to the segments/edges of the slave side. This is the basic contact to solve problems such as vehicle crash simulation or airbag unfolding, where there are contact events with an initially undetermined contact situation. In fact, even

though the contact situation is determined, it is easier, safer, and more efficient to define one large self-contact which includes the full model.

2.3.1.1 Contact search algorithm

A contact search algorithm evaluates which part of the structure is likely to contact a rigid wall, an other part of the structure, or itself, which can be subdivided into two major methods, node-to-node proximity search and node-to-segment correspondence search. The node-to-node proximity search evaluates the present closest master node to a given slave node. In 1990, Benson and Hallquist established a search technique that subdivides the contact body into three-dimensional cubic buckets and restrict the search to the bucket that contains a slave node and to all neighboring buckets. Due to structural deformation, the contents of the buckets need to be updated continuously.

The proximity between nodes is given by their spatial distance. The calculation of the distance from all nodes of a structure (or defined smaller region) to a given slave node is a time consuming process. Therefore, the nodes of a structure are sorted according to their distance along a given search direction for a fast and efficient search algorithm. The order in which they occur along this line is stored. The search direction can be chosen as the global axis direction of greatest structural extension. Then, the search starts on both sides of the search line using simply the nodal coordinates. This scanning operation is restricted to those nodes that fall into a given search interval around the slave node. The search interval is determined from a search radius (R) in Figure 2-24, where the search radius is defined as the largest possible radius around a slave node which does not include any nodes connected to the slave node.

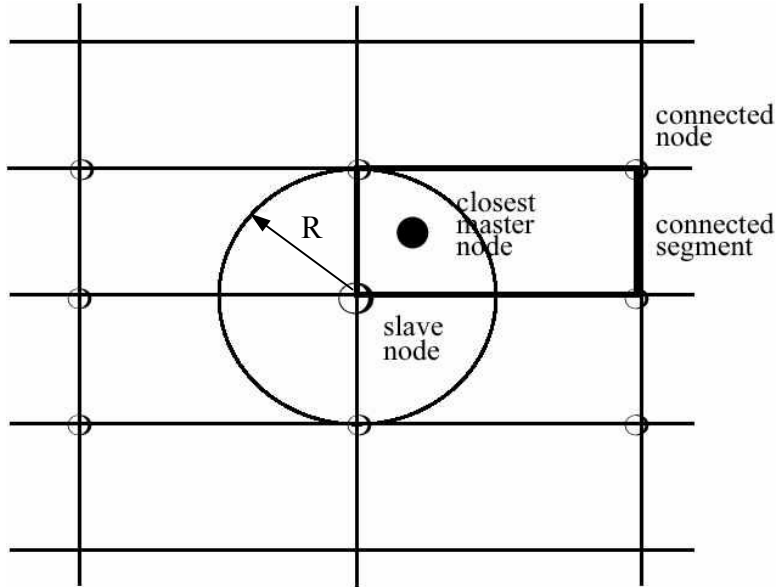


Figure 2-24 Search Radius (ESI, 2000)

All contact solutions start with an initial guess and proceed in a given search direction in a step-by-step manner. Finding the proper direction in the high-dimensional search space is critical for the efficiency of the algorithm.

In 2001, Hirota *et al.* summarized two major direction search methods. The first method is the maximum gradient descent method that chooses the direction of the force propagation for the search direction. This method is very slow because it takes many steps for a local force to propagate through the entire mesh. Moreover, it is impossible to predict sudden force variations caused by the deformation of objects. The second method, the Newton method, uses the derivative of the forces, which provides information about how the forces vary as a function of deformation. Each Newton step computes the residual, stiffness matrix, and solution for a linear system. The process continues until the residual drops below a given tolerance. Hirota *et al.* concluded that the Newton method is faster and more reliable than the maximum gradient descent method.

Once the master node closest to a slave node within its contact sphere has been located (Figure 2-24), the segment to which this master node is connected and which the slave node is likely to hit needs to be determined. Based on equation (2-2), the contact

segment, the closest master node and the slave node, can be determined from neighboring elements around the closest master node (Hallquist *et al.*, 1985).

$$\mathbf{s} = \mathbf{g} - (\mathbf{g} \cdot \mathbf{e}_3) \mathbf{e}_3 \quad (2-2)$$

The vector, \mathbf{g} , originates from the closest master node to slave node above the master surface. The vector, \mathbf{s} , is obtained from the closest master node to the projection node of the slave node on the master surface. The projection node is called the defense node in Figure 2-25. The vector, \mathbf{e}_3 , is the unit vector normal to the master surface near the closest master node. In order for it to be determined, two more vectors, \mathbf{c}_i and \mathbf{c}_{i+1} , need to be established. The two vectors point to the two different connected nodes from the closest master node, respectively, as seen in Figure 2-25. For example for contact segment $i=1$, the two vectors, \mathbf{c}_1 and \mathbf{c}_2 , indicate the two different directions from the closest master node. The unit normal vector, \mathbf{e}_3 , can be determined by using the equation (2-3).

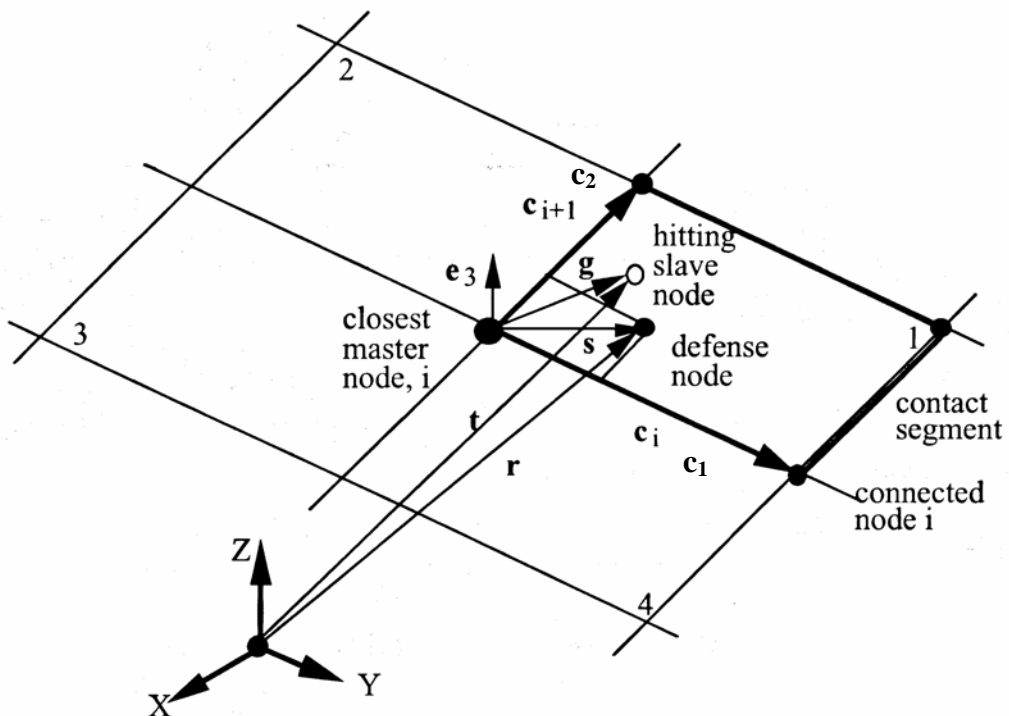


Figure 2-25 Node-to-Segment Correspondence Search (ESI, 2000)

$$\mathbf{e}_3 = \frac{\mathbf{c}_1 \times \mathbf{c}_2}{|\mathbf{c}_1 \times \mathbf{c}_2|} \quad (2-3)$$

Finally, the position vector of the slave node projection onto the master surface, \mathbf{s} , can be calculated by using equation (2-2) and complete the slave node-master contact segment pair correspondence search. The calculated position vector, \mathbf{s} , should satisfy the following two constraints to ensure that the slave node projects onto contact segment 1 in Figure 2-25.

$$(\mathbf{c}_1 \times \mathbf{s}) \cdot (\mathbf{c}_1 \times \mathbf{c}_2) > 0 \quad (2-4)$$

$$(\mathbf{c}_1 \times \mathbf{s}) \cdot (\mathbf{s} \times \mathbf{c}_2) > 0$$

The fictitious “defense node” was first introduced by Zhong in 1988 near the tip of the projection vector, \mathbf{s} , which served to defend the contact segment against the hitting slave node. Since then, this defense node has frequently been used in the contact interface algorithm theory.

Even though many contact algorithms have been defined for various specific contact events, no contact algorithm has significantly reduced the simulation CPU time to complete the contact events. Therefore, detailed research is still being conducted to establish efficient and reliable contact algorithms.

2.3.1.2 Contact interface algorithm

Once contact nodes and contact segments have been matched, the conditions of contact are applied whenever the contacting slave node penetrates the surface of the contact segment. Major formulations of contact constraints such as the Lagrange multiplier method and the Penalty method are reviewed in Sections, 2.3.2 and 2.3.3. These methods are widely used in most standard finite element analyses to handle contact problems.

2.3.2 Lagrange Multiplier Method

The solution of a contact problem in which the motion is constrained can be calculated by using the Lagrange multiplier method. The multiplication terms of the Lagrange multiplier, usually denoted as λ , and a gap function are added to the total energy equation of the system. The Lagrange multiplier, λ , is equivalent to the reaction force. Therefore the method focuses on the contact forces between the hitting and the defense nodes as primary unknowns.

In 1982, Oden *et al.* introduced various basic finite element methods and new nonclassical friction laws for the analysis of nonlinear problems in rubber elasticity. Several different finite element schemes such as the Lagrangian method, continuation or incremental loading methods, and associated Riks-type method were discussed. It was assumed that the rubber material was hyperelastic, isotropic, and homogenous. Therefore, the rubber material could be characterized by a strain energy function, W , which was expressed as a function of invariants of the deformation tensor. Since they noticed that the classical Coulomb law of friction was inadequate on both physical and mathematical grounds when modeling friction effects in real materials, new nonclassical friction laws were introduced. The new friction laws included nonlocal effects to approximate the deformed asperities, the adhesion effects, and the damage model on the contact surface.

In 1983, Guerra and Browning performed several contact simulations by implementing two major contact treatment algorithms, the Lagrange multiplier method and the Penalty method, into FEA software (ADINA) to compare the methods from the viewpoint of efficiency, reliability, and ease of use. They found that the Lagrange multiplier method satisfied the contact constraint more precisely. Also, the determination of spring stiffness at the contact interface was not required to calculate the contact force. On the other hand, the Lagrange multiplier method added extra degrees of freedom that demanded additional storage and computation. Meanwhile, the Penalty method had the advantages in that no extra degrees of freedom needed to be considered. Thus, no extra storage and fewer

computations were required. On the other hand, the Lagrange multiplier method tried to reach a good solution several times because adjustments of the spring constants were required to minimize unacceptable penetrations of slave nodes. It was also mentioned that the solution might converge very slowly or even diverge if very high stiffness had been used.

In 1985, Bathe and Chaudhary developed a solution algorithm of general two-dimensional contact problems between flexible-flexible and flexible-rigid bodies at sticking or sliding conditions. A sticking condition was assumed when the frictional resistance during contact was sufficient to prevent sliding. On the other hand, a sliding condition was assumed if the tangential force exceeded the frictional capacity between two contact surfaces. The Lagrange multiplier method was used to impose the deformation constraints along the contact surfaces. The contact forces were evaluated from distributed tractions that could be calculated from the nodal forces and the frictional conditions.

In 1990, Marques and Martin developed a three-dimensional plastic finite element formulation including frictional contact algorithm based on Lagrange multiplier method. A friction term was included which acted oppositely to the relative movement between a working metal material and a forming tool. Then, two metal forming examples, such as the formation of a rectangular block and forging of a rib-and-web component, were conducted to demonstrate the capabilities of their contact algorithm formulation. The predicted results showed agreement with theoretical and experimental findings.

2.3.3 Penalty Method

The Lagrange multiplier method satisfies the zero gap condition between the slave node and the master contact surface while the Penalty method does not. In the Penalty method, the contact conditions are further relaxed and penetration of the impinging slave node into the contact segment is allowed. Based on the penetration depth, the penalty forces are computed. A penalty parameter is interpreted as a spring stiffness in the contact

interface and multiplication of the penalty parameter and penetration distance computes the reaction force.

In 1985, Hallquist *et al.* developed comprehensive two- and three-dimensional contact algorithms to computationally solve static and dynamic impact problems. They focused mostly on the Penalty method to calculate contact interface forces between the slave node and the master surface. Three steps were introduced for a general contact interface treatment. The first step was to determine the pair of master segment and slave node which were supposed to contact. The second step was to locate the contact point or defense node on the master segment. Finally, the third step was to update the nodal force. Each slave node was checked for penetration through its master segment. If the slave node did not penetrate, nothing was activated. However, if a penetration was detected, an interface force was applied between the slave node and its defense node. The magnitude of this contact force was proportional to the amount of penetration and could be calculated using the bulk modulus, volume, and surface area of the master part. Then, the force was distributed over the master segment nodes based on their distances to the defense node. Hallquist *et al.* analyzed several examples where contact-impact algorithms were required. One of them was a forming bellows, which involved a large amount of sliding along the contact interface. The objective of this simulation was to determine the pressure required to collapse a stainless steel sleeve into an elastic die as shown in Figure 2-26.

In 1990, Benson and Hallquist investigated the behavior of a shell structure after it buckled. They stated that when a structure collapsed completely, a single surface might buckle enough to come into contact with itself. They also claimed that the traditional approach defining master and slave contact pair would not work because the pair definition was not sufficiently clear for a single surface. Therefore, they developed a contact algorithm that demanded only a single surface definition for its input, which was called later, the self-contact algorithm. As a result, the sequence of a square tube axial buckling occurred under initial perturbation at the right end as seen in Figure 2-27. The contact forces were calculated by using the Penalty method that had been employed in the

previous research of Hallquist *et al.*, (1985). Even though the local contact search and the force evaluation remained the most time-consuming part of the analysis, the new single surface contact algorithm displayed the effective and robust results.

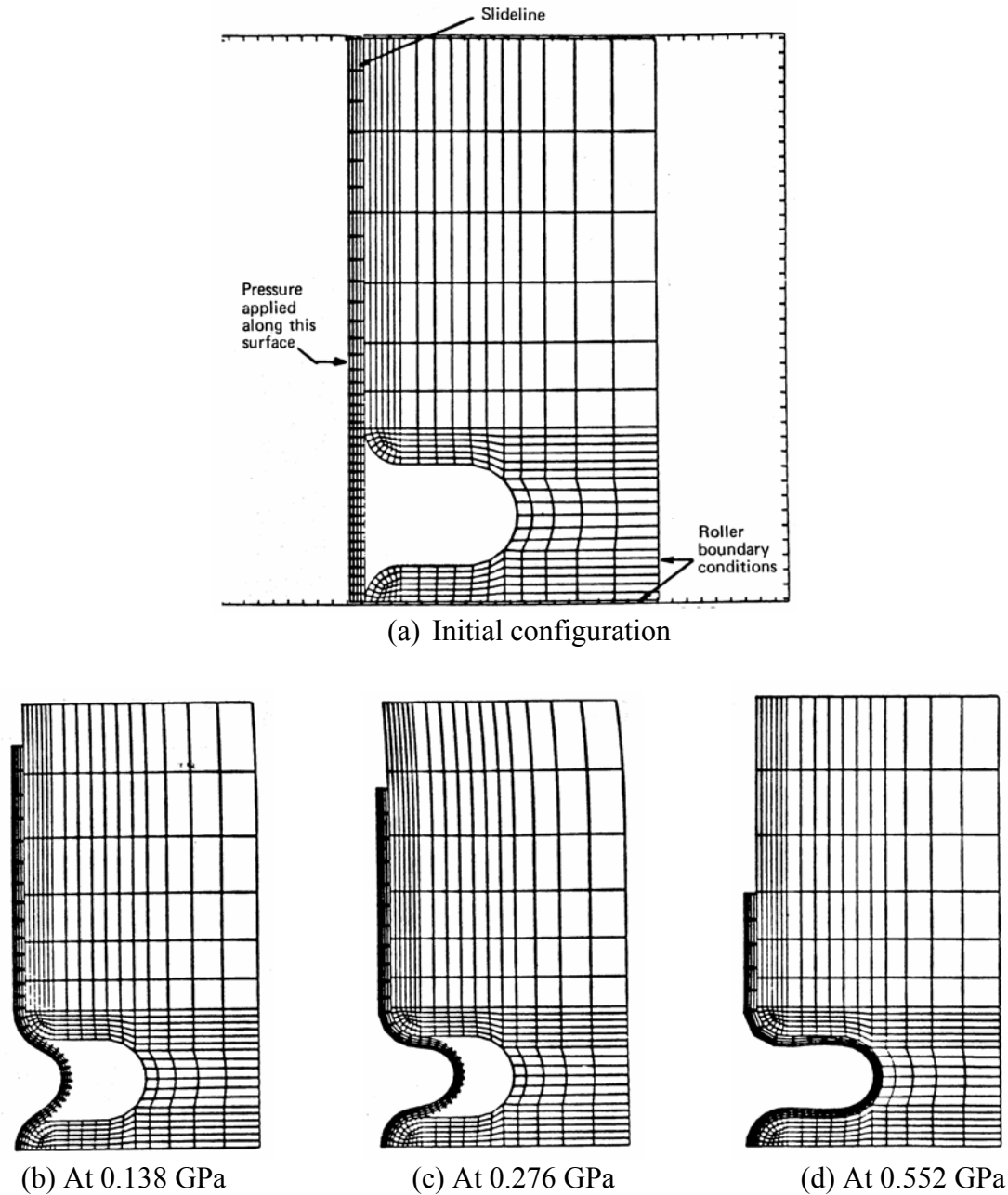


Figure 2-26 Deformed Shapes Corresponding to the Pressures (Hallquist *et al.*, 1985)

In 2001, Hirato *et al.* performed computational contact simulations of elastic solids using an implicit FEM approach. Their research focused on the simulation of mechanical contact between nonlinearly elastic objects such as the skin of the human body. The computation of the contact forces was a major objective because traditional methods could not handle continuous and complicated self-contact such as skin folds. Therefore, Hirato *et al.* developed a new penalty FE formulation based on the concept of material depth, which represented the distance between a particle inside an object and the object's boundary. Then, contact forces could be integrated over contact surfaces by linearly interpolating material depths without increasing computational cost. The new algorithm was implemented in their in-house implicit FE program for static and quasi-static analysis of nonlinear viscoelastic solids. As a result, they could successfully demonstrate effectiveness of the algorithm on an animation showing folding skin and sliding contacts of tissues involved in knee flexion.

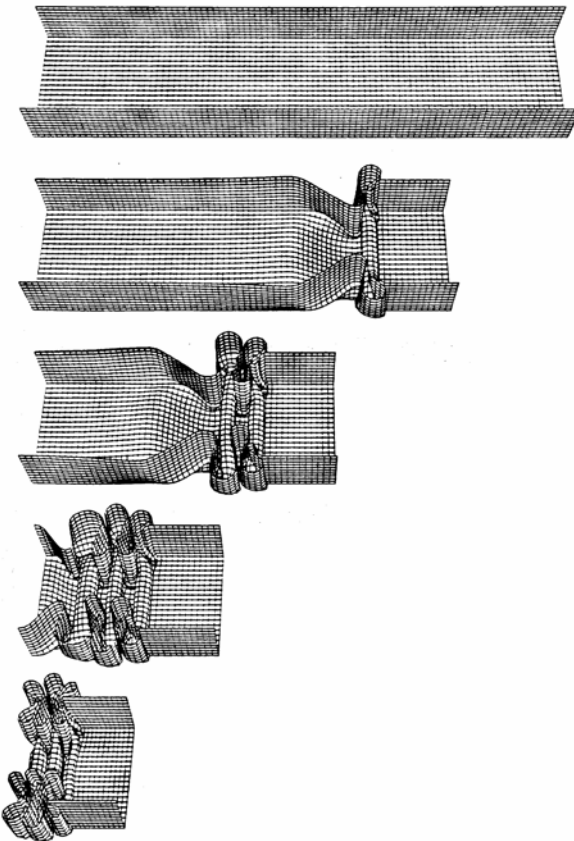


Figure 2-27 Sequence of a Single-Surface Square Tube Buckling
(Benson and Hallquist, 1990)

2.4 Experimental Tire Testing

Since Charles Goodyear invented the first pneumatic bicycle tires in 1839, a variety of measuring devices have been designed to determine the forces and moments that arise in the contact area. Although initially the interest was in load-deflection relationships in a radial direction, later, research emphasized the rolling resistance and nonskid qualities of tires during braking and traction. The need to evaluate the cornering force and the slip angle was discussed as early as 1930 by Bradley and Allan. Later, in 1950's, a number of simple tire tests, such as vertical displacement measurement at various loads, rolling resistance measurements, and cornering characteristics, were actively performed (Garner and Worswick, 1951; Turner, 1954; Powell, 1957; Gough and Robert, 1957; Kollmann, 1959). Since then, more complicated research has been conducted in the area of viscoelastic tire material, rubber-cord composite material, and in-plane and out-of-plane transient responses of tires. In order to accomplish this complicated laboratory tire testing, large scale experimental set-ups and highly experienced measurement skills and effort are usually required. Transient response measurements of a tire in particular need complex experiment facilities and data acquisition systems.

Many tire test methods have been established to measure forces and moments acting on a rolling tire. Mobile dynamometers are available which run the tire over the road using a towed trailer rig. This equipment has the advantage of providing data on actual road surfaces. However, the majority of tests have been conducted in laboratories using a large drum because the tire-drum system occupies relatively small space and speed control of tire is easy.

Figure 2-28 shows internal and external drum tire test machines. These drum test machines are useful for comparing the characteristics of different tires. However, they do not provide exact information of the tire behavior observed on flat surface because significant difference in the tire behavior can be induced by the curvature of the drum.

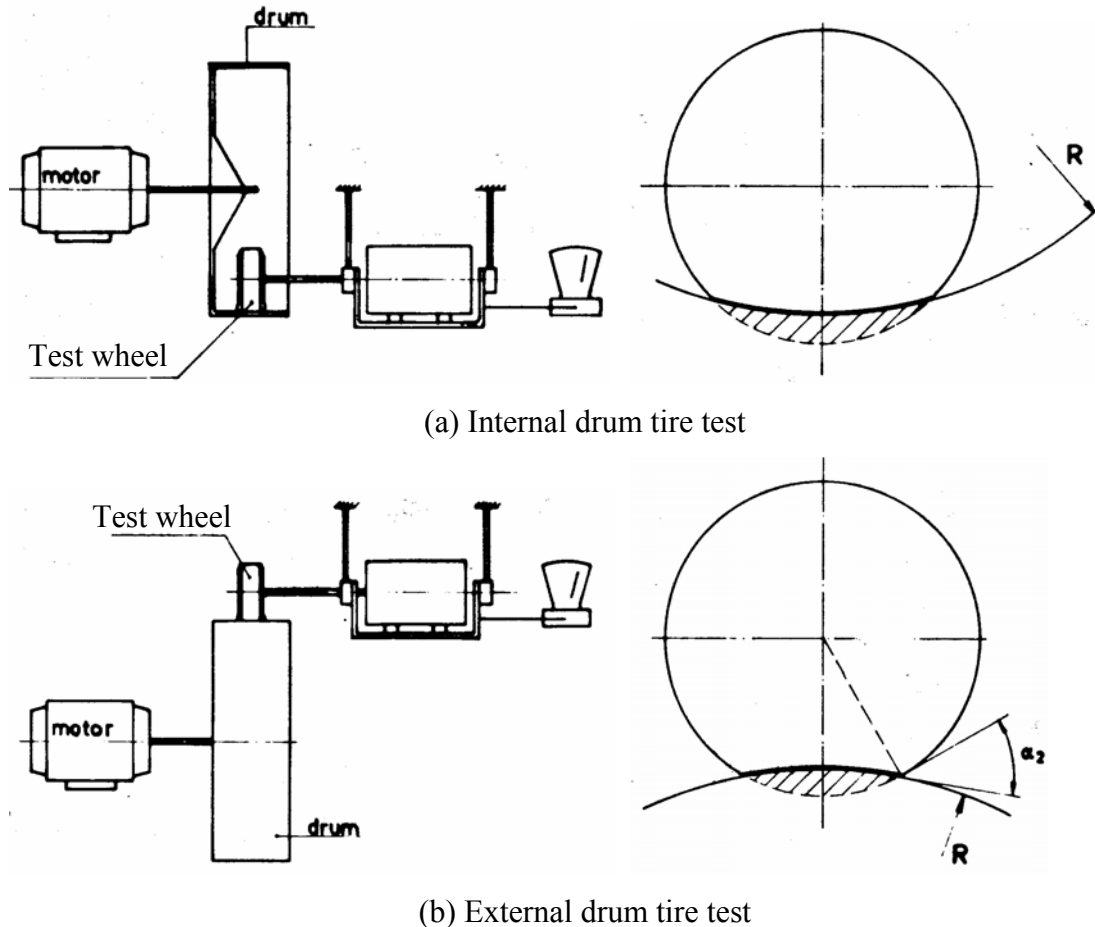


Figure 2-28 Tire Tests on Internal and External Drums (Eldik Thieme, 1982)

To eliminate the effects caused by drum curvature, a flat rotating disc was used as seen in Figure 2-29. However, due to the finite width of the tire tread, the rotational speeds of the inner and outer tread edges are different, which results in slip in the contact area.

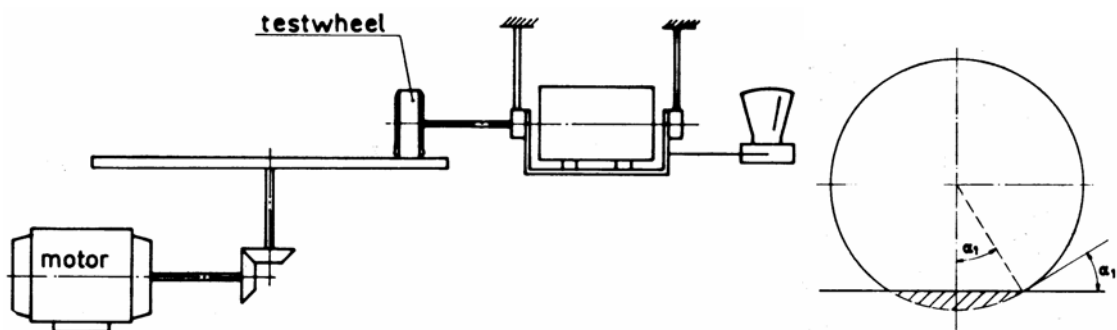


Figure 2-29 Test Wheel on Flat Rotating Disc (Kollmann, 1959)

Other tire tests are also available using a flat belt as shown in Figure 2-30. The test machine consists of a steel band or conveyor belt running on two drums. The flexible belt is supported in the contact area by an extremely stiff and thin air bearing in order to minimize the air gap variation. A drawback of such an air bearing is the large air consumption [Bruinsma, (1968); Altena, (1975)]. Appropriately surfaced steel belts can simulate road surfaces from low to high skid resistance. Dry or wet pavement simulated conditions up to full dynamic hydroplaning from low speed to 322 km/h (200 mph) could be obtained (Bird and Martin, 1973).

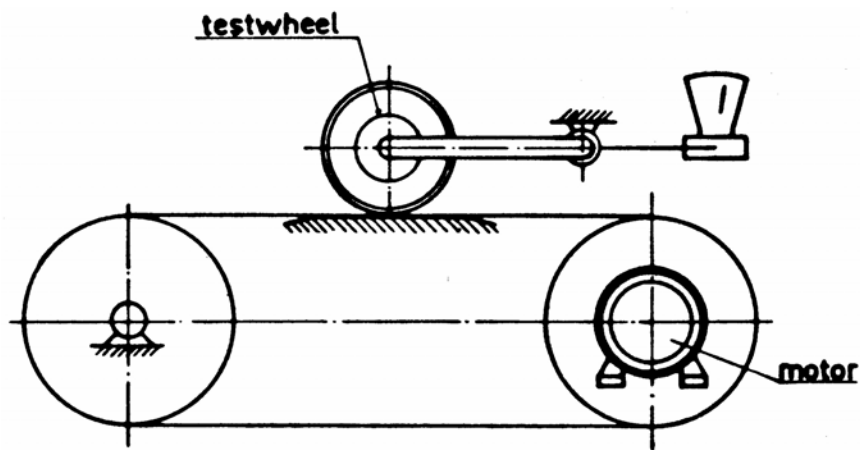


Figure 2-30 Tire Test on Flat Belt (Eldik Thieme, 1982)

Using all of the available tire test machines, many researchers have performed tire tests measure tire forces and moments in the contact area, rolling resistance, braking and traction efforts, and cornering characteristics. In 1969, Davisson mentioned three important elements to consider in tire engineering; application requirements, performance properties, and design factors. He first described design factors including tire structure, materials, stress relationships, and tread and sidewall pattern. Then, he continued with performance properties including stiffness, damping, cornering characteristics, energy loss, and durability. Finally, he completed his study with application requirements including vehicle requirements, service requirements, and economics. In his study, he included the number of tire testing data which were obtained from real experiment measurements, such as cornering forces of radial and bias-ply tires versus slip angle, contact pressure distribution, and rolling resistance versus inflation and speed.

Similarly, in 1988, Ford and Charles described heavy-duty truck tire engineering in an extensive fashion similar to Davisson in 1969. In their study, they emphasized three important elements in heavy-duty tire engineering: tire engineering factors, performance properties, and application requirements. In the section on tire engineering factors, they updated the Davisson's section on the design factors. For example, they updated the cross-sectional shape and structural components figure with a modern heavy-duty radial truck tire, since radial tires had popularity over bias-ply or bias-belted tires. Ford and Charles also introduced tire modeling techniques using computer aided engineering (CAE) software, such as NASTRAN and CADAM. They developed an FEA truck tire model and simulated tire inflation and loading conditions. In the performance properties section, several stiffness test measurements of the latest tires in three directions (vertical, lateral, and tangential directions) were plotted. It was noted that dynamic vertical stiffness for radial heavy duty truck tires was approximately five percent less than static values. In lateral stiffness, the radial tire was somewhat less stiff than the bias tire. It was found through experimental measurements that the radial tire carcass was less stiff than the bias tire in the tangential direction. In addition, in the application requirements section, three parts were categorized, i.e., vehicle requirements, service requirements, and economics similar to Davisson (1969). However, this research provided more information about new topics, such as modal analysis results, steering and handling, and tire selection. This large amount of information and experimental data furnished insights for tire model developments and validation.

In 1991, Yap performed cornering characteristics measurements on radial truck tires, 11R22.5, to investigate the effect of tread designs on cornering characteristics using a flat belt type of Calspan TIRF machine. In order to limit the study to the tread design parameters, the truck tires in this study had different rib and lug tread designs, and the tread rubber compound of the tires was the same. Yap measured tire cornering forces and moments at various vertical loads, inflation pressures, slip angles, and cambers. As a result, significantly different responses between the designs could be observed with respect to cornering force and self-aligning moment, even though the tire cornering

characteristics were found to be more dependent on vertical loads than on the different tread designs.

In 1997, Davis measured mechanical properties such as stiffness and damping constant of bias-ply and radial-belted 30×11.5-14.5/26PR aircraft tires under a variety of test conditions. The bias-ply tire was inflated at the rated inflation pressure of 1.69 MPa (245 psi) while the radial-belted tire was inflated at the rated inflation pressure of 2.14 MPa (310 psi). These inflation pressures correspond to a 35-percent deflection¹ at the rated load of 111 kN (25,000 lb). The objective of this study was to measure and compare quasi-static and dynamic response characteristics of the aircraft tire.

The vertical, lateral, and fore-and-aft deflections were recorded to determine the corresponding stiffness and damping constants. In addition, footprint area and moment of inertia were also measured and compared between the two tires. Then, the radial-belted tire was evaluated as a replacement for the bias-ply aircraft tire. Davis found that the vertical load stiffness characteristics of the two tire designs were similar. However, it was found that significantly different lateral and for-and-aft stiffness properties of the radial-belted tire might result in an increase in tire shimmy and affect the performance of an anti-skid braking system (ABS) tuned for bias-ply tires. It was also found that the smaller and more elliptical footprint shape of the radial-belted tire might be more sensitive to hydroplaning conditions. From moment of inertia testing, it was found that the radial-belted tire required less energy to spin up, which could result in reduced tire wear and heating during high-speed landings.

¹ Percent deflection is defined as the ratio of the tire sidewall deflection to its free height.

$$\text{Percent_deflection} = \frac{\text{Deflection}}{\text{Section_height} - \text{Flange_height}} \times 100$$

The Section height and Flange height are defined in Section 3.1.5.

2.5 Tire Rubber Material Modeling

“Rubber” has been recognized as a useful engineering material since Charles Goodyear pioneered the vulcanization process in 1839. Due to its flexible and resilient properties, vulcanized rubbers have been widely adopted in many engineering applications such as springs, shock absorbing bushes, seals, and tires. Many researchers have tried to describe the low modulus of the hyper-elastic rubber material by using a few characteristic properties and simple equations similar to Hooke’s Law. However, they found that the behavior of rubber was so complex that it could not be described in such a simple way. Moreover, the behavior of rubber was highly dependent on the temperature, strain history, loading rate, and the amount of strain. Amount and type of filler such as carbon black also had a significant effect on the elastic behavior of rubber. Since all these variables govern the elastic behavior, the applications of rubber have largely relied on trial and error rather than on systematic calculations.

Even though the elastic behavior of rubber is quite complex to predict, as mentioned above, many theoretical models have been developed since the 1940s in an attempt to characterize the elastic mechanical behavior of rubber. The mechanical behavior of rubber has been described mainly by two different approaches, statistical thermodynamics approach and phenomenological approach. The statistical thermodynamics approach is based on observations that the rubber elastic force arises almost entirely from the decrease of entropy due to the elongation of rubber. Before the deformation of rubber, the molecular chains are highly amorphous and randomly oriented, i.e., in a high entropy state. However, when a tensile force is applied, the molecular chains slide each other to become aligned along the loading direction, which results in lower entropy state. Figure 2-31 shows the randomly oriented chains in undeformed rubber (a) and oriented chains in deformed rubber due to shear stress, τ .

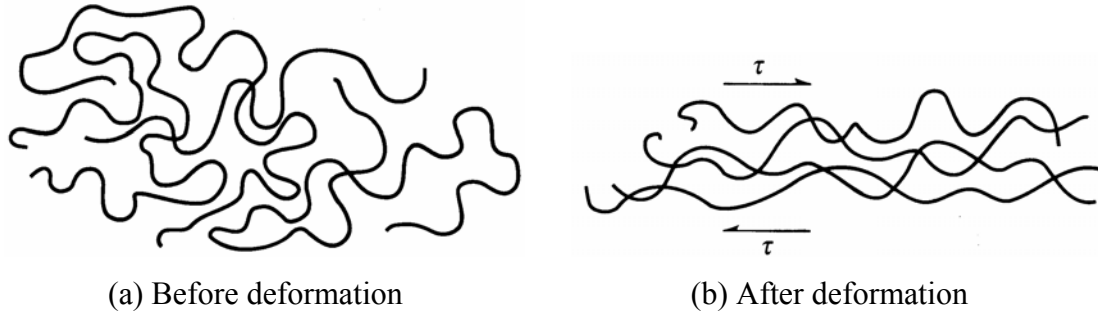


Figure 2-31 Randomly Oriented Chains (a) and Oriented Chains (b) (Askeland, 1994)

From this entropy change, the stretching force on a single chain molecule, f , can be calculated by using equation (2-5). The amount of work required to increase the end-to-end length of a chain (l) to $l + dl$ is

$$dW = f \cdot dl = -T \cdot \frac{dS}{dl} \quad (2-5)$$

Where dW is the amount of work done during an isothermal displacement, dl , T is the absolute temperature, and dS is the entropy change.

This approach has generally dealt with assumed statistical distributions of chain lengths, orientations and structure of rubber molecular networks. Therefore, it was inevitable that there existed some limitations in the use of equation (2-5). In 1988, Shaw and Young suggested that this statistical theory should only be applicable up to around 50% of strain.

The majority of research work that characterizes the mechanical behavior of rubber has been conducted by adopting the phenomenological approach, which is independent of any molecular theory and is based on the observation of rubber under various conditions. The phenomenological theory of rubber elasticity was developed by Mooney (1940) and Rivlin (1956) on the basic premises that the rubber material is isotropic and its elastic properties can be represented in terms of a strain energy function, W , which is defined as the stored strain energy per unit volume. Mooney (1940) and Rivlin (1956) showed that the elastic law for large deformations of incompressible and isotropic elastic materials

could be established experimentally. In 1940, Mooney proposed a strain energy function, W , in terms of three extension ratios, λ_1 , λ_2 , and λ_3 , in Figure 2-32.

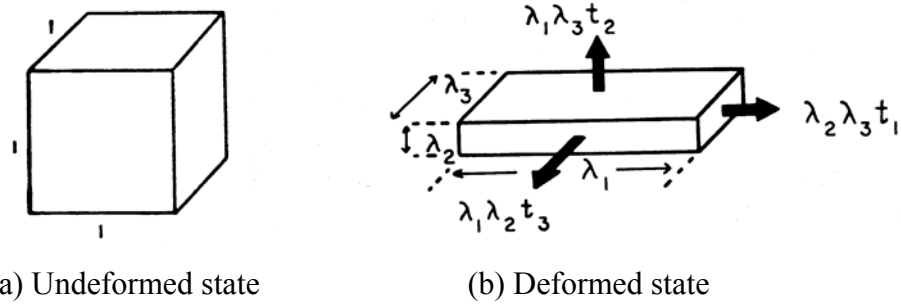


Figure 2-32 Principal Stresses and Extension Ratios (Yeoh, 1993)

The extension ratio, λ_i , is defined as length after deformation (l)/original length (l_o) along the loading direction. The extension ratio is sometimes denoted as $1+\varepsilon$, where ε is the strain. These relations are summarized in equation (2-6).

$$\lambda_i = \frac{\text{Length_after_Deformation}}{\text{Original_Length}} = \frac{l}{l_o} = \frac{l_o + \Delta l}{l_o} = 1 + \varepsilon \quad (2-6)$$

Where, Δl is an extension length from the original length.

Rivlin also developed the strain energy function, W , for the isotropic elastic rubber materials in terms of three strain invariants, I_1 , I_2 , and I_3 as shown in equation (2-7).

$$W = \sum_{i=0}^n \sum_{j=0}^n \sum_{k=0}^n C_{ijk} (I_1 - 3)^i (I_2 - 3)^j (I_3 - 1)^k \quad (n = 1, 2, 3, \dots, \infty) \quad (2-7)$$

The three strain invariants are defined as

$$\begin{aligned} I_1 &= \lambda_1^2 + \lambda_2^2 + \lambda_3^2 \\ I_2 &= \lambda_1^2 \cdot \lambda_2^2 + \lambda_2^2 \cdot \lambda_3^2 + \lambda_3^2 \cdot \lambda_1^2 \\ I_3 &= \lambda_1^2 \cdot \lambda_2^2 \cdot \lambda_3^2 \end{aligned} \quad (2-8)$$

Furthermore, for an incompressible isotropic rubber material, I_3 becomes 1 and λ_2 is equal to λ_3 , which is $\frac{1}{\sqrt{\lambda_1}}$. Therefore, I_3 term can be eliminated from the equation so that the strain energy density function, W , can be expressed in terms of two independent variables, I_1 and I_2 , including only λ_1 as follows:

$$\begin{aligned} I_1 &= \lambda_1^2 + \frac{2}{\lambda_1} \\ I_2 &= 2\lambda_1 + \frac{1}{\lambda_1^2} \end{aligned} \quad (2-9)$$

Consequently, Equation (2-7) can be reduced to

$$W = \sum_{ij=0}^n C_{ij} (I_1 - 3)^i (I_2 - 3)^j \quad (2-10)$$

Equation (2-10) is a power series which is usually truncated to the first few terms. The strain energy function with the first two terms yields the well-known Mooney-Rivlin model:

$$W = C_{10}(I_1 - 3) + C_{01}(I_2 - 3) \quad (2-11)$$

Where C_{10} and C_{01} are constants that can be determined experimentally.

The Mooney-Rivlin equation had been extensively tested and debated (Treolar, 1958; Krigbaum *et al.*, 1965; Varga, 1966) and it was found that the expression gave reasonable agreement with experiment data. Varga (1966) revealed that the strain energy stored in a material was a function of strain components at any point. This strain energy function is characteristic of the material such as its stress-strain relationship. He also added that the nature of the stored energy function for a pure homogeneous strain completely determines the elastic properties of the material.

Rivlin also established a relationship between the principal extension ratios, λ_1 , λ_2 , and λ_3 , the principal stresses, t_1 , t_2 , and t_3 , and the partial derivatives of W with respect to the invariants, I_1 and I_2 . These relations are

$$\begin{aligned}\frac{t_1 - t_2}{\lambda_1^2 - \lambda_2^2} &= 2 \cdot \left(\frac{\partial W}{\partial I_1} + \lambda_3^2 \frac{\partial W}{\partial I_2} \right) \\ \frac{t_2 - t_3}{\lambda_2^2 - \lambda_3^2} &= 2 \cdot \left(\frac{\partial W}{\partial I_1} + \lambda_1^2 \frac{\partial W}{\partial I_2} \right) \\ \frac{t_1 - t_3}{\lambda_1^2 - \lambda_3^2} &= 2 \cdot \left(\frac{\partial W}{\partial I_1} + \lambda_2^2 \frac{\partial W}{\partial I_2} \right)\end{aligned}\tag{2-12}$$

For uniaxial extension or compression test ($t_2 = t_3 = 0$), the stress-strain relation can simply be derived from equation (2-12). Meanwhile, from Figure 2-32 (a), the applied force along the direction 1 is σ_1 -unit area, which is $\lambda_2 \cdot \lambda_3 \cdot t_1$ in Figure 2-32 (b). Therefore, the principal stress along direction 1, t_1 , can be expressed in terms of an engineering stress, σ_1 , and extension ratio, λ_1 , as shown in equation (2-13).

$$t_1 = \frac{\sigma_1}{\lambda_2 \lambda_3} = \sigma_1 \cdot \lambda_1\tag{2-13}$$

Finally, from the combination of equations (2-12) and (2-13), the stress-strain relation for uniaxial extension or compression can be calculated by equation (2-14).

$$\frac{\sigma}{\lambda - \lambda^{-2}} = 2 \cdot \left(\frac{\partial W}{\partial I_1} + \frac{1}{\lambda} \frac{\partial W}{\partial I_2} \right)\tag{2-14}$$

From equation (2-11), the partial derivatives of $\frac{\partial W}{\partial I_1}$ and $\frac{\partial W}{\partial I_2}$ of equation (2-14) are simply defined as C_{10} and C_{01} , respectively. Therefore, equation (2-14) can be rewritten as follows:

$$\frac{\sigma}{\lambda - \lambda^{-2}} = 2 \cdot \left(C_{10} + \frac{1}{\lambda} C_{01} \right) \quad (2-15)$$

A plot of $\frac{\sigma}{\lambda - \lambda^{-2}}$ versus $\frac{1}{\lambda}$ exhibits a straight line with slope $2 \cdot C_{01}$ and intercept $2 \cdot C_{10}$ at extension ratio of 1 within the low strain range as seen in Figure 2-33. The left half of Figure 2-33 shows a typical Mooney-Rivlin plot for a tensile test on natural rubber vulcanizates. On the other hand, the right half shows the plot for a compressive test whose behavior is almost symmetric about the vertical axis at $1/\lambda=1$. It is obvious that the Mooney-Rivlin's straight line does not fit over all the entire strain range. Therefore, it is advised that the straight line should be fitted in the application range of strain. Normally, the two constants, C_{10} and C_{01} , of the Mooney-Rivlin equation are determined in the low strain range because engineering applications usually fall within the low strain ranges.

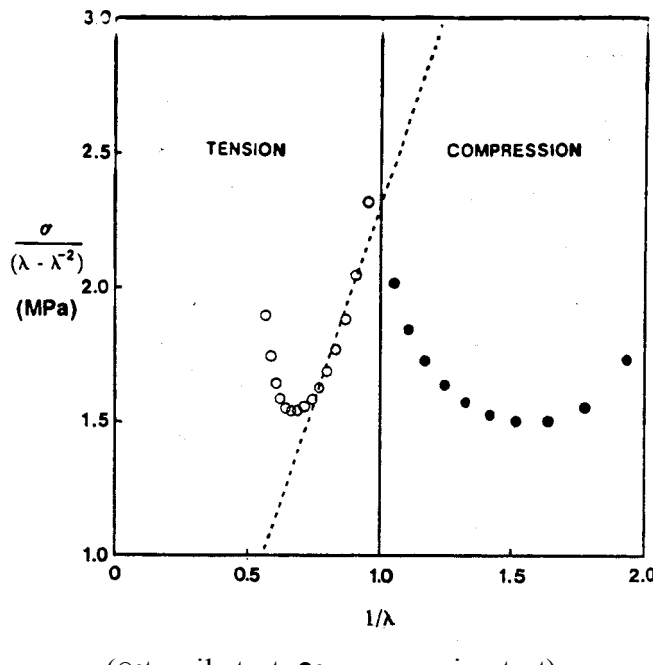


Figure 2-33 Determination of the Mooney-Rivlin Coefficients (Yeoh, 1990)

2.6 Summary

In this chapter, literature on the following topics has been surveyed to obtain insights on computational tire modeling and testing: tire axis system, definitions of forces and moments on a tire, various tire models, contact algorithms, tire testing, and the tire rubber material modeling. As a result, it is still relatively rare to find a versatile full three-dimensional FEA tire model with solid elements. Moreover, considerable time and cost as well as expensive tire testing equipment are required to measure tire responses and characteristic in-plane and out-of-plane parameters. In particular, studies on the measurements of out-of-plane parameters are relatively rarely found. Therefore, in this thesis, an effective and efficient full three-dimensional FEA tire model will be established and it will be validated by comparison with available test measurements. Various virtual tire testing environments will then be constructed, combining the developed FEA tire model and test roads to predict in-plane and out-of-plane characteristic tire parameters that can be used as input in other tire model or dynamic vehicle simulation environments.

Tires play an important role in vehicle dynamics because most excitations are transmitted to the vehicle chassis from ground irregularities through the tires. Therefore, an efficient and accurate tire testing simulation that can replace conventional tire testing will contribute considerably to tire manufacturing and testing areas from the beginning concept design evaluation to the detailed final manufacturing process stage.

CHAPTER 3

NONLINEAR FINITE ELEMENT ANALYSIS TRUCK TIRE MODELING

Tires in ground vehicles support the vehicle weight and cushion road surface irregularities to provide a comfortable ride to driver and passengers. The tires also need to provide adequate tractive, braking, and cornering forces which are important for safe and stable operation of the ground vehicle. Thus, tire manufacturers conduct many physical laboratory tests such as in-plane and out-of-plane stiffness, damping constant tests, cornering tests, and durability tests in order to examine tire performance. However, laboratory tests consume large amounts of time and money. Experimental equipment, their set-up, and data acquisitions and analyses need highly experienced skills and long testing time. Besides, actual tire tests under severe operating conditions, such as high speed and/or high loading, are not always achievable by traditional testing facilities. Therefore, many researchers have attempted to build alternative tire test environments during the last few decades.

Fortunately, modern computer technology enabled a new era of virtual tire testing. Effective and efficient FEA tire models have been developed to design safer, more precise, and more advanced tires for the challenging operation environments of ground vehicles. Through FEA tire model simulations, most laboratory tire tests could be duplicated. The ultimate goal of this chapter is to build a nonlinear FEA truck tire model that enables the running of a virtual FEA tire-road testing environment to simulate real-world operating conditions as an effective alternative of the physical tire test.

A radial-ply FEA tire model for a Boeing MD-11 aircraft, H54×21.0-24, was originally developed by researchers at ESI North America. Later, Chang (2002) modified this tire model to represent a radial-ply passenger car tire, 185/70R14. Then, he predicted in-plane free vibration modes and transmissibility of the tire model using a cleat-drum model. He also visualized the standing wave phenomenon at high speeds using a tire-smooth drum model.

In this chapter, a detailed, full three-dimensional radial-ply truck tire, 295/75R22.5, is modeled in association with nonlinear FEA software, PAM-SHOCK. The material properties of the FEA truck tire model (Tables 3-1 to 3-3) are originally provided by ESI North America for Boeing MD-11 aircraft tire. Some material properties are modified to tune up the characteristics of the FEA truck tire model. The developed FEA tire model consists of over 9,200 nodes and 27 different parts including beam elements for beads, layered membrane elements for carcass and belts, and solid elements for bead fillers, tread base, and treads. In this tire model, solid elements are only added for bead fillers (apexes), tread shoulders, tread base, and tread in which sudden curvature change or significant shear deformations are encountered during loading and normal operation conditions. The tire model is assembled with a rigid rim that was built for the truck tire model by using shell elements. The masses of the tire and rim are 51 kg and 32 kg, respectively.

The developed FEA truck tire model will be validated statically and dynamically by comparing predicted tire responses with available measurement data in Chapter 4. For the validation of the FEA tire model, basic characteristic responses such as load-deflection curve, footprint area size, free vertical vibration mode, cornering characteristics, fore-and-aft free vibration, and yaw oscillation tests will be virtually conducted. Then, in Chapter 5, the tire model will be used to determine characteristic in-plane and out-of-plane tire parameters required for a rigid ring tire model through virtual tire tests, which have never been accomplished previously. In Chapter 6, the developed FEA tire model will be combined with spring-and-damper suspension and sprung mass to build an FEA quarter vehicle model for durability tests.

Section 3.1 discusses basic truck tire structures and their components to help an understanding the complex truck tire structure. Based on the radial-ply truck tire structure, an FEA tire and rim model is constructed in Section 3.2. Then, the various virtual tire testing environments that will be used in Chapters 4, 5, and 6 are introduced in Section 3.3.

3.1 Tire Structure, Its Components, and Materials

A pneumatic tire is defined as a toroidal shape of flexible cord-rubber composite structure that is filled with compressed air. Rubber is an essential material of the pneumatic tires. It offers flexibility, low hysteresis, good friction on most surfaces, high abrasion resistance, and good impermeability to contained air. The basic rubber characteristic of low resistance to tensile forces requires inextensible but flexible reinforcement to avoid excessive tire deformations upon loading. Especially for truck tires, natural rubber has extensively found the greatest degree of application due to its cool running temperature, high tensile strength, and excellent abrasion resistance. The tire consists mainly of a carcass, a few layers of belts, beads, tread, and tread base as shown in Figure 3-1. These main components are discussed in Sections 3.1.1 to 3.1.4.

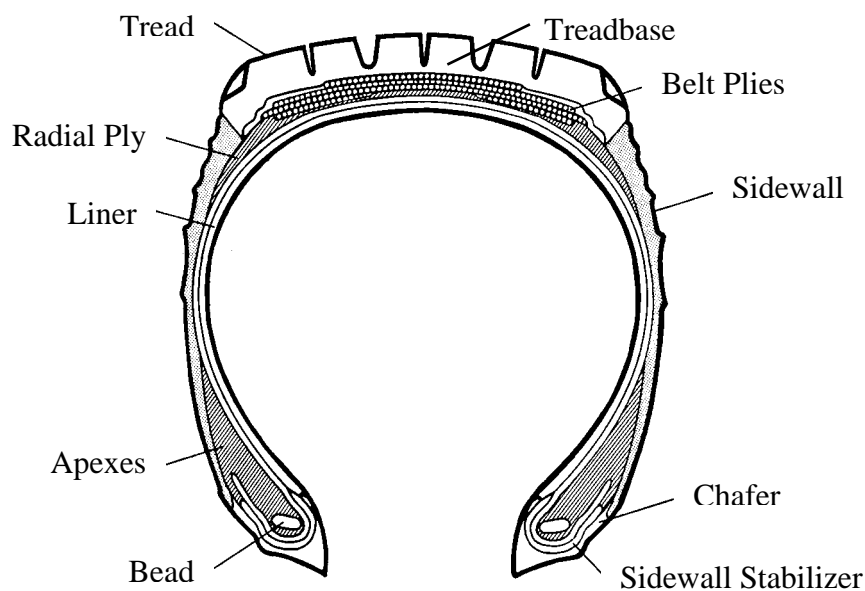


Figure 3-1 Heavy-Duty Radial Truck Tire (Ford and Charles, 1988)

3.1.1 Carcass

The carcass is located inside the tire from one bead to the other and plays a very important role because it sustains load and absorbs shock. Therefore, the carcass must have a strong anti-fatigue attribute that inhibits bending and stretching during driving. Flexible but high modulus cords are embedded in a low modulus rubber matrix to form the carcass. The number of plies is determined by tire type, tire size, inflation pressure, and loads in service.

According to the carcass structure, there are two types of tires, bias-ply and radial-ply tires, as illustrated in Figure 3-2. In bias-ply tires, the reinforcing cords extend diagonally across the tire from bead to bead, as shown in Figure 3-2 (a). The cords run in opposite directions in each successive ply, thus the cords overlap in a diamond-shaped pattern. In a rolling tire, the diagonal plies flex and rub, thus, elongating the diamond-shaped elements and the rubber filler. This flexing action yields a wiping motion between the tread and the road, thus increasing the rolling resistance and the rate of tire wear in a bias-ply tire. The crown angle, defined as the angle between the cords and the circumferential centerline of the tire, plays a significant role in the mechanics of the tire. The crown angle affects the vehicle ride quality and cornering characteristics considerably. Tires with low crown angle provide good cornering characteristics but harsh ride. On the other hand, tires with large crown angle provide good ride but poor cornering characteristics. The crown angle ranges from 25° to 40° for bias-ply tires.

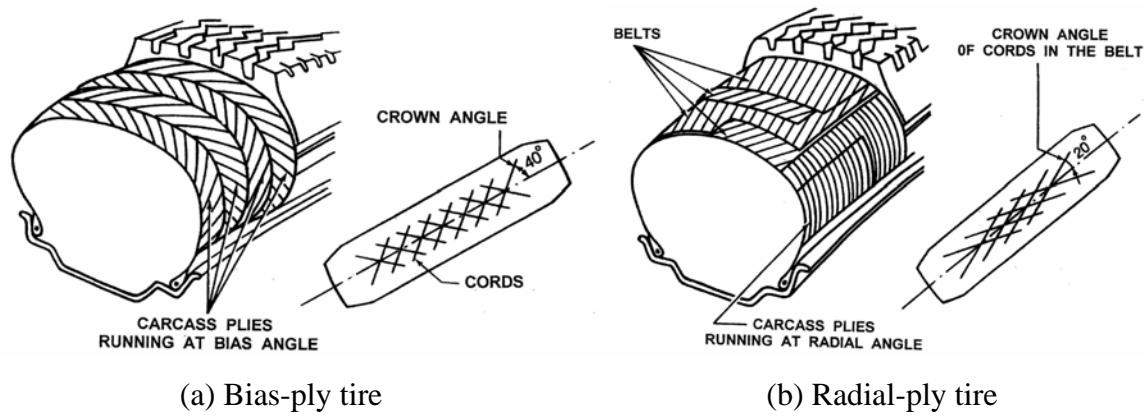


Figure 3-2 Typical Tire Constructions (Wong, 2001)

The bias-ply tires are used for bicycles, motorcycles, racing cars, aircraft, agricultural machinery, and some military machinery.

In contrast, the construction of a radial tire differs considerably from that of a bias-ply tire. The cords in the carcass of a radial ply tire are disposed in a radial direction, leading to a 90° crown angle, as shown in Figure 3-2 (b). For a passenger car tire, cords made of synthetic polymer fibers, such as polyester or nylon, are used while cords for a truck tire are made up of fine hard drawn steel. Large crown angle of the cords yields extremely good ride but poor cornering performances. Such a tire structure is extremely soft for vertical compressive and extensive loads. The radial tire is stiffened by belts with a low crown angle around 20° . During operation, the flexing of the carcass involves relatively small motion of the belt cords, thus the wiping motion between the tire and the road is small. The power dissipated by the radial tires could be as low as 60 percent of that of the bias-ply tires.

Since radial-ply tires were first introduced by Michelin in 1948, their popularity has continuously increased in most tire applications due to lower rolling resistance, fuel efficiency, longer tread life, and increased load carrying capability compared to bias-ply tires. Radial-ply tires have been adopted for almost all passenger cars, sport utility vehicles (SUV), minivans, even trucks, buses, aircraft, and motor cycles.

3.1.2 Belts

Belts are composite materials made up of reinforcing steel cords and rubber matrix and are located between the carcass and the tread base as already seen in Figures 3-1 and 3-2. The belt layers are essential to the proper functioning of the radial tire. They restrict deformation of the carcass plies and provide added stiffness to the tread. They also mitigate the impacts due to road surface irregularities. In the absence of the belt, the tire periphery, when inflated, may develop into a series of buckles due to irregularities in cord spacing leading to an unstable tire carcass.

Bias-ply tires can be also built with belts having low crown angles. The cords in the belts are usually made of materials with higher modulus of elasticity than those in the bias-ply. The belts in such belted bias-ply tires provide high rigidity to the tread against distortion and reduce tire wear.

3.1.3 Tread and Tread Base

The tread is the only part of the tire that contacts the road surface directly under normal operations. It is made of solid rubber with reinforcement of carbon black to resist wear in service. It also protects the belt plies and carcass and provides the frictional contact required to transmit driving, braking, and cornering forces.

Depending on tire type, the tread outer surface may be smooth, as observed in some race car tires, or it may have a pattern as in the other types of tires. A completely smooth tread would be satisfactory in nearly all aspects if the tire runs only on hard, dry surfaces. However, under general operation environments of highway and off-road surfaces, the tread pattern enhances the ability of the tire to transmit driving, braking, and lateral forces. Among them, the primary purpose of the tread pattern is traction.

Tread patterns can be characterized by repetitive elements of ribs, grooves or voids, rugs, and sipes. The protruding circumferential elements are called ribs, which are separated by depressions, called grooves or voids. Individual protruding elements are called rugs. Patterned treads usually include sipes, which are slots in rugs for the purpose of improving traction. Figure 3-3 shows basic examples of these tread patterns of truck tires.



(a) Highway rib (b) Highway rug (c) On/off highway (d) Off highway
Figure 3-3 Basic Tread Patterns of Truck Tires (Ford and Charles, 1988)

The tread base under the tread is made of softer solid rubber than the tread rubber, and provides a soft cushion and solid bonding of the tread and belt.

3.1.4 Beads

The beads anchor the carcass plies and strengthen the tire-rim assembly on the wheel rim. Thus, they prevent the tire from rocking and slipping. It is made of hard drawn steel wires, flat or round, put together to provide the desired strength and rigidity. Ford and Charles (1988) stated that performance requirements for tire beads are uniformity, mountability, rim roll-off resistance, tire-to-rim fitment, maximum strength at lowest weight, lateral and circumferential stiffness, torsional and in-plane rigidity, fatigue resistance, and high adhesion level. Typical bead bundles used in radial truck tires are shown in Figure 3-4.

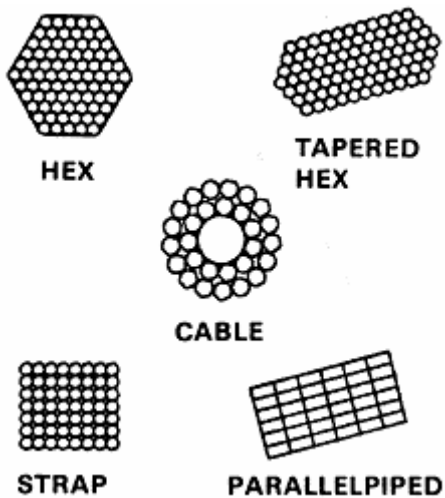


Figure 3-4 Bead Bundle Configurations (Ford and Charles, 1988)

3.1.5 Aspect Ratio

A typical tire cross section is shown in Figure 3-5. According to the Year Book of the Tire and Rim Association (1996), the section width is defined as the width of a new tire from sidewall to sidewall. Protective side ribs, bars, and decorations in the section width are not included.

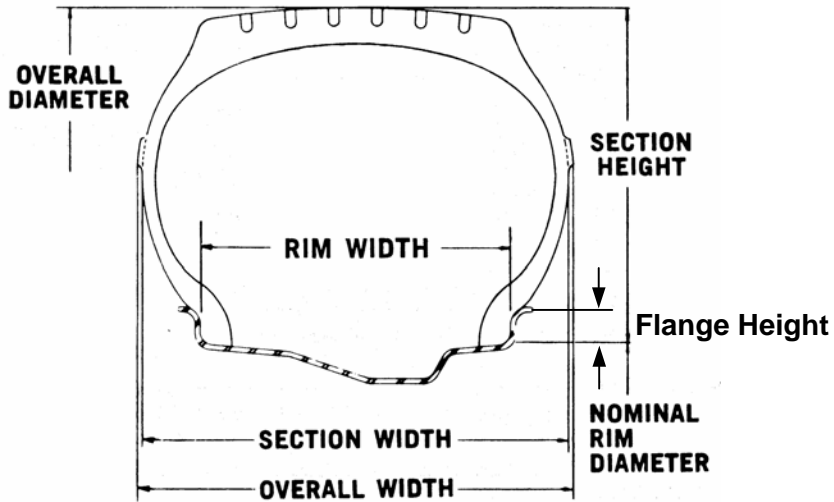


Figure 3-5 Definitions of a Tire Cross-Sectional Shape
(Tire and Rim Association Year Book, 1996)

The overall width is defined as the width of an unloaded new tire from sidewall to sidewall that includes protective side ribs, bars, and decorations. The section height refers to the radial distance from the crown to the beads. The overall diameter is the outer diameter of a tire that is twice the section height plus the nominal rim diameter. All the measurements listed above are recommended to be measured after 24-hour inflation growth on an unloaded new tire.

An aspect ratio of the tire is the percent ratio of its section height divided by section width. In the early days of automobiles, pneumatic tires had an aspect ratio of around 100. With advances in tire technology, the aspect ratios have steadily decreased. Lower aspect ratios are more common on high performance tires. Modern race car tires are built with aspect ratio as low as 30. Lowering aspect ratio is advantageous with respect to rolling resistance because of the increased radial stiffness or less vertical deformation, which results in decrease in hysteresis loss. In addition to the increased radial stiffness, the rotational stiffness of the tire is also increased. Hence, inertial losses at high speed are reduced.

In addition to the individual dimensions of the tire, other engineering factors such as load, inflation pressure, tread geometry, and compound and reinforcement properties affect the

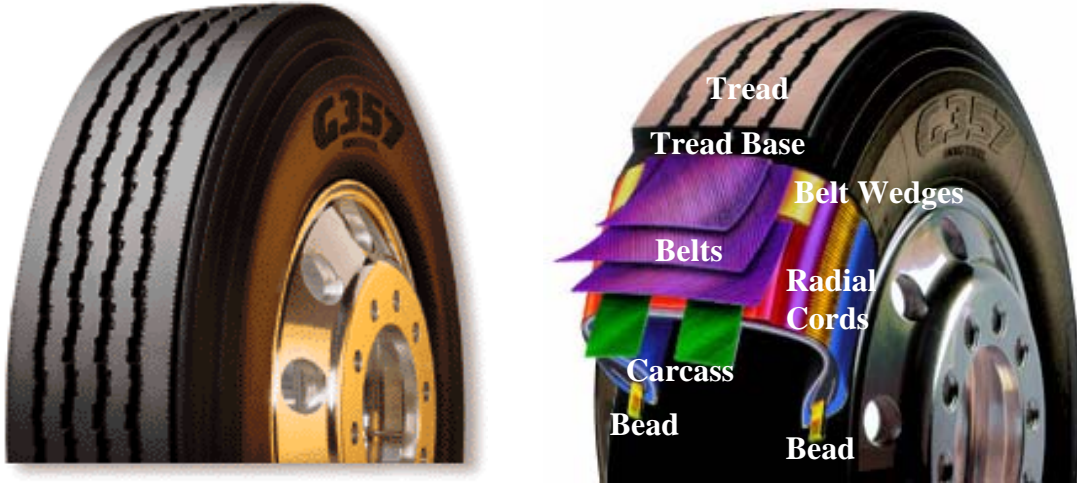
characteristics of the tire. Among them, a change in one factor could have a positive effect, a negative effect, and no effect on the performance of the tire. Therefore, the tire engineer's task is to define the interrelationship and optimize the tire design for the targeted application.

3.2 Tire Structure and Material Modeling

A pneumatic tire consists primarily of rubber materials and reinforced rubber composites. The tire is modeled as an assembly of three-dimensional Mooney-Rivlin hyperelastic solid elements for the rubber material, two-dimensional fiber-reinforced layered membrane elements for reinforced rubber composites, and one-dimensional beam elements for the two beads. The truck tire-rim assembly model is comprised of 27 different material definitions with 4,200 solid elements, 1,680 membrane elements, and 120 beam elements.

Most of the materials in the tire exhibit a nonlinear stress-strain relationship under a wide range of loading conditions. Therefore, it is a challenging effort to establish an analytical material model that can entirely describe the stress-strain relationship under all loading conditions. Instead, a reasonable material model needs to be selected to define material behavior pertinent to the loading conditions of interest such as strain rate, strain direction, maximum strain, relaxation, cyclic behavior, and temperature.

This research adopts a tire size of 295/75R22.5 used for the front axle of a truck. The section width is 295 mm. The aspect ratio is 75-percent. It is a radial-ply tire with rim diameter 22.5 inches. Figure 3-6 shows a picture of the tire and its components.



(a) 295/75R22.5 Truck tire

(b) Components of the tire

Figure 3-6 Radial Truck Tire (Retrieved from www.goodyear.com)

3.2.1 FEA Modeling on Carcass and Belts Using Membrane Elements

Two-dimensional membrane finite elements discretize structures that are composed of thin and flexural membrane material such as fabrics. Membranes have zero flexural stiffness and constant stress distribution across the thickness, and need no numerical integration in the thickness direction. Figure 3-7 shows the definition of the membrane elements and the local coordinate system used in PAM-SHOCK.

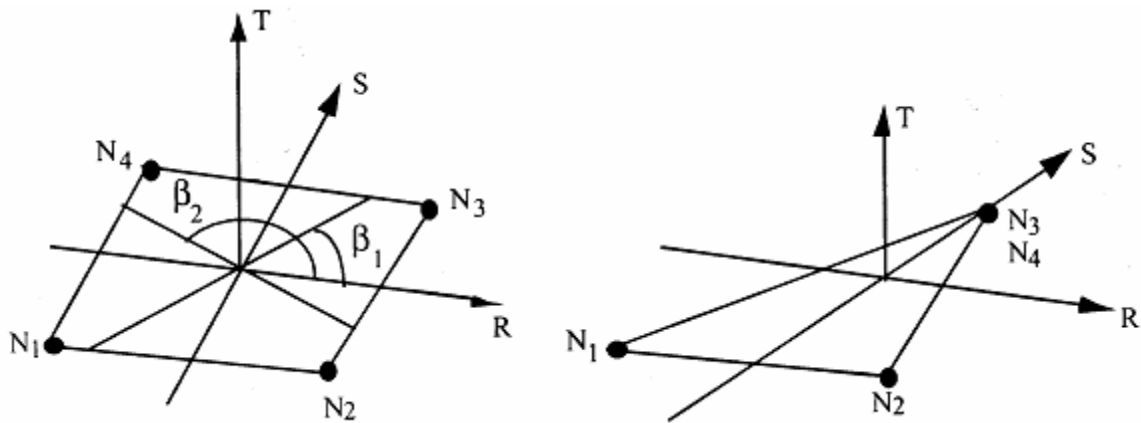


Figure 3-7 Definition of Membrane Elements (ESI, 2000)

The carcass and belts are modeled using elastic, three-layered membrane elements that consist of two layers of the cords controlled in two directions and a single layer of isotropic matrix as seen in Figure 3-8.

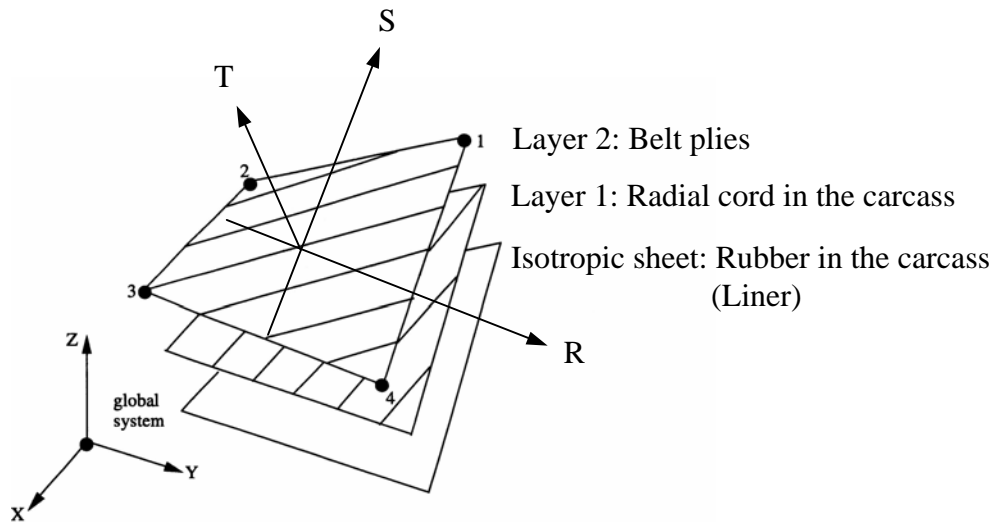


Figure 3-8 Three-Layered Membrane Element (ESI, 2000)

In Figure 3-8, the single layer of isotropic matrix is used to represent the rubber material in the carcass of the radial tire model. The radial cord ply in the carcass is modeled using layer 1 and the belt plies are modeled using layer 2. In fact, in a radial-ply tire, three different orientations of cords are required as shown in Figure 3-2 (b), two different directions in belt plies, and one radial cord direction in the carcass. However, only two different directions of cords are available in the membrane elements. Therefore, material properties in two different directions of belt plies are smeared to create equivalent material properties in a direction perpendicular to the radial cord direction.

The radial-ply cords are embedded in the carcass from one bead to the other. The zero cord angle from the R-axis is input in the Layer 1 to represent the radial cord because the radial direction coincides with the R-axis. In fact, the carcass wraps the bead and ends in the middle of the sidewalls in the truck tire as shown in Figures 3-6 (b) and 3-9. Therefore, Young's modulus from the bead area to the middle of the sidewall in Layer 1 is roughly double the modulus observed in the other locations.

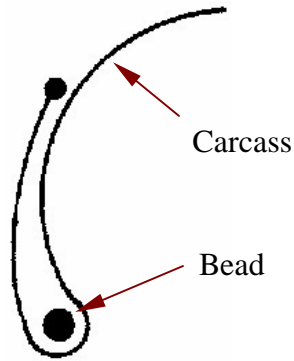


Figure 3-9 Carcass Wrap around Bead (Gough, 1981)

Meanwhile, the characteristics of the cords running at \pm crown angle in belt plies are smeared at 90° angle direction from the R-axis and modeled in Layer 2. The belt plies are placed only under the tread base. Therefore, material properties in Layer 2 near sidewalls are nearly ignored and defined only at the locations under the tread base.

The locations of the layered membrane elements used for the FEA truck tire model are illustrated in Figure 3-10 in red and their material properties are summarized in Table 3-1. The whole cross-sectional tire shape is symmetric about the dotted center line.

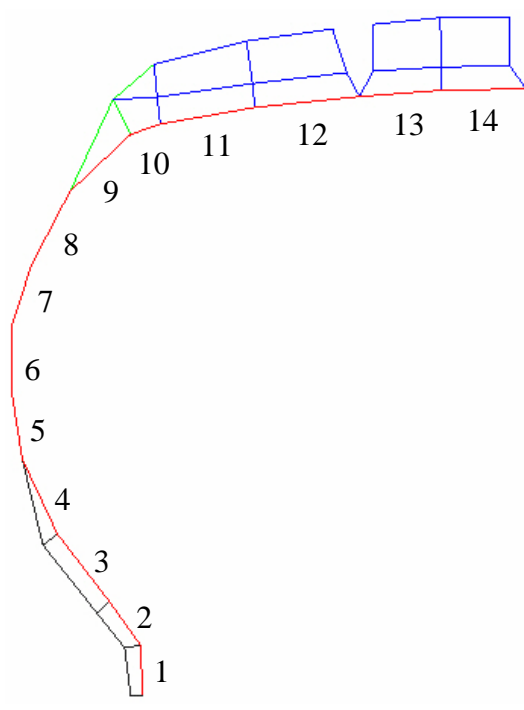


Figure 3-10 Locations of the Layered Membrane Elements and Their Part I.D. Numbers in FEA Truck Tire Model

Table 3-1 Material Properties of the Layered Membrane Elements

Tire component	Radial ply and rubber liner of the carcass				
Material I.D.	1	2	3	4	5
Density (ton/mm³)	7.63E-10	7.64E-10	7.63E-10	7.33E-10	7.21E-10
Thickness (mm)	6.75	4.5	3.75	3.75	3.75
Isotropic parent sheet Young's modulus (MPa)	28	24	22	12	7
Isotropic parent sheet Poisson's ratio	0.3	0.3	0.3	0.3	0.3
Layer 1 Young's modulus (MPa)	365	315	498	429	406
Layer 1 Shear modulus (MPa)	0.0001	0.0001	0.0001	0.0001	0.0001
Layer 1 Angle of fibers with R-axis	0°	0°	0°	0°	0°
Layer 2 Young's modulus (MPa)	0.0003	0.0003	0.0003	0.0003	0.0003
Layer 2 Shear modulus (MPa)	0.0001	0.0001	0.0001	0.0001	0.0001
Layer 2 Angle of fibers with R-axis	90°	90°	90°	90°	90°

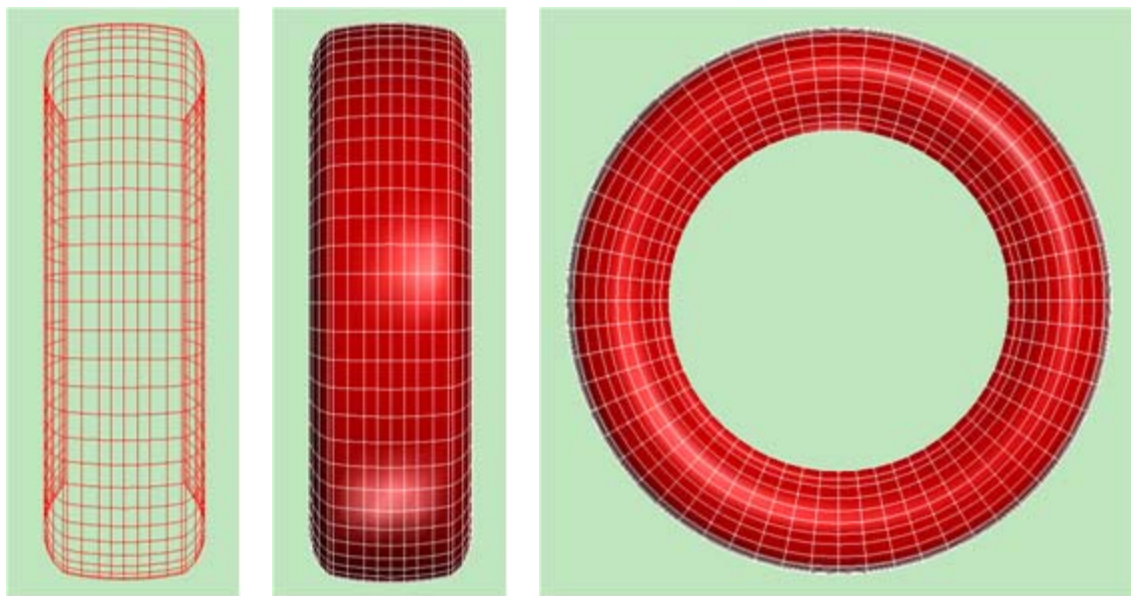
Table 3-1 Material Properties of the Layered Membrane Elements (Cont.)

Tire component	Radial ply and rubber liner of the carcass			
Material I.D.	6	7	8	9
Density (ton/mm³)	7.23E-10	7.19E-10	7.25E-10	7.44E-10
Thickness (mm)	3.75	3.75	3.75	3
Isotropic parent sheet Young's modulus (MPa)	7	7	7	9
Isotropic parent sheet Poisson's ratio	0.3	0.3	0.3	0.3
Layer 1 Young's modulus (MPa)	392	180	193	207
Layer 1 Shear modulus (MPa)	0.0001	0.0001	0.0001	0.0001
Layer 1 Angle of fibers with R-axis	0°	0°	0°	0°
Layer 2 Young's modulus (MPa)	0.0003	0.0003	0.0003	0.0003
Layer 2 Shear modulus (MPa)	0.0001	0.0001	0.0001	0.0001
Layer 2 Angle of fibers with R-axis	90°	90°	90°	90°

Table 3-1 Material Properties of the Layered Membrane Elements (Cont.)

Tire component	Radial ply, rubber liner of the carcass, and belt plies				
Material I.D.	10	11	12	13	14
Density (ton/mm³)	8.73E-09	1.07E-09	1.07E-09	1.06E-09	1.06E-09
Thickness (mm)	3.75	3.75	4.5	3.75	3.75
Isotropic parent sheet Young's modulus (MPa)	12	14	14	14	14
Isotropic parent sheet Poisson's ratio	0.3	0.3	0.3	0.3	0.3
Layer 1 Young's modulus (MPa)	155	202	200	155	198
Layer 1 Shear modulus (MPa)	0.0001	0.0001	0.0001	0.0001	0.0001
Layer 1 Angle of fibers with R-axis	0°	0°	0°	0°	0°
Layer 2 Young's modulus (MPa)	3,400	10,700	10,600	10,600	10,500
Layer 2 Shear modulus (MPa)	0.0001	0.0001	0.0001	0.0001	0.0001
Layer 2 Angle of fibers with R-axis	90°	90°	90°	90°	90°

It should also be noted that the Young's moduli of Layer 2 from material I.D.s 10 to 14 are very high compared to the others in the layer to represent the belt layers at 90° from the radial R-axis. Finally, a three-dimensional model of the carcass and belts plies is created by rotating the whole cross-section one full rotation about the tire axle axis in 60 equal pieces. Figure 3-11 shows the FEA three-layered membrane model representing the carcass and belt layers of the truck tire.



(a) Wire frame view (b) Front view

(c) Side view

Figure 3-11 Carcass and Belts Membrane Elements Used in FEA Truck Tire Model

Since the carcass is modeled by using membrane elements which cannot show the effect of bending, it may not be sufficient to represent a whole tire model. Ridha and Clark (1981) noted the limitation of the membrane element model:

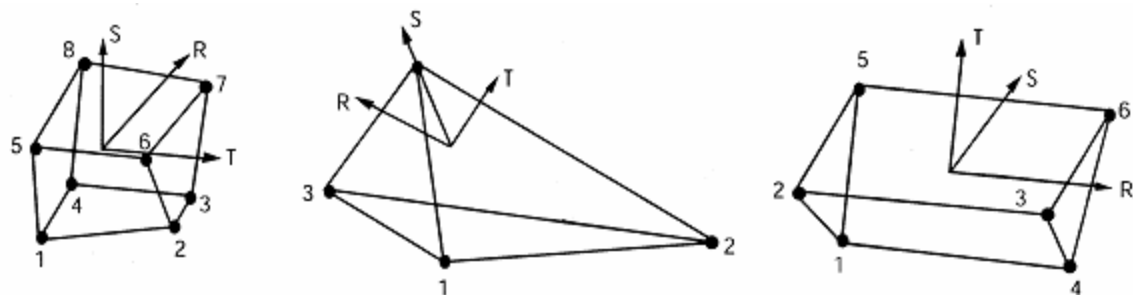
- a) It cannot handle abrupt changes in geometry, material properties, or loading.
- b) It cannot account for the effects of transverse shear deformations in the contact area.
- c) It cannot predict local forces in zones of significant curvature change or discontinuity in ply orientation.

Therefore, three-dimensional solid elements are added to the tread and the bead areas to handle the bending moments due to a sudden change of curvature and large deformation of a pneumatic tire. Only after that, more accurate contact pressure distribution and shear deformation can be predicted in the tire-road contact area.

At the sidewall region (Material I.D. 5 to 8), damping is applied to simulate the damping effect of the tire sidewall. Since the damping is applied only at the sidewall region, tire contact forces at the tire-road contact area do not directly affected by the sidewall damping. In PAM-SHOCK, mass-proportional damping coefficient is formulated, which can be calculated by using the first mode of free vertical vibration and 5% of critical damping effect. The detailed calculation steps are included in Appendix A.

3.2.2 FEA Modeling on Tread, Tread Base, Tread Shoulders, Bead Fillers Using Solid Elements

Three-dimensional solid finite elements can be used to discretize bulk materials with eight nodal points as shown in Figure 3-12 (a). The first face (nodes 1, 2, 3, and 4) has its normal pointing inward to the solid element, according to the right hand rule, while the second face (nodes 5, 6, 7, and 8) has normal pointing outward from the solid element, according to the right hand rule. On 4-node and 6-node elements, the first face has the normal pointing inward to the solid elements using the right hand rule.



(a) 8-node solid element (b) 4-node solid element (c) 6-node solid element

Figure 3-12 Definitions of Solid Elements (ESI, 1998)

Since the tread, the tread base, the tread shoulders, and the bead fillers are made of relatively thick rubber material and experience shear stresses and sudden changes of curvature during service, three-dimensional solid elements are required to model those parts in the truck tire. Since rubber materials exhibit hyperelastic behavior during loading, the behavior can be generally described by a constitutive law obtained from Mooney-Rivlin's strain energy density function, W . As reviewed in the previous chapter, the Mooney-Rivlin's formulation for a hyperelastic rubber material predicts precise results reasonably and efficiently. Usually, the first two terms in the strain energy density function are adopted and the method to determine two coefficients, C_{10} and C_{01} , are described in detail in Section 2.5 in Chapter 2. The location of the solid elements used for the FEA truck tire model are shown in Figure 3-13 and their material properties are summarized in Table 3-2.

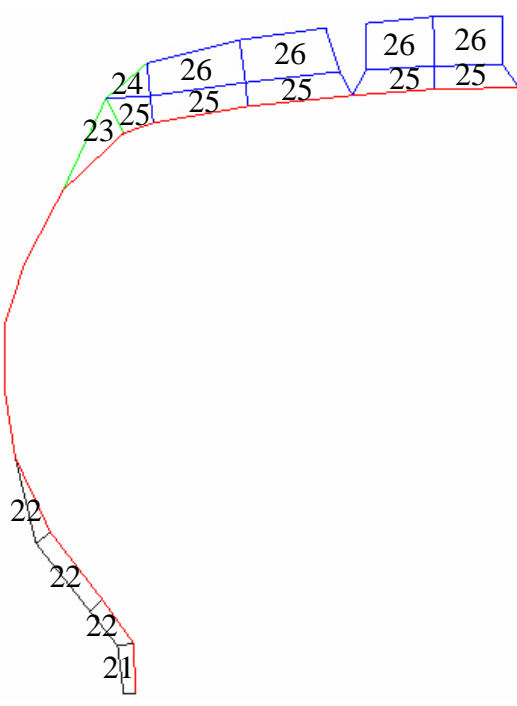


Figure 3-13 Locations of the Solid Elements and Their Part I.D. Numbers in FEA Truck Tire Model

Table 3-2 Material Properties of the Solid Elements

Tire component	bead fillers		tread shoulders		tread base	tread cap
Material I.D.	21	22	23	24	25	26
Density (ton/mm³)	8.82E-10	8.81E-10	8.69E-10	6.93E-10	5.96E-10	6.93E-10
1st Mooney-Rivlin coeff. (C₁₀)	0.392	0.392	0.41	0.67	0.51	0.67
2nd Mooney-Rivlin coeff. (C₀₁)	1.268	1.268	1.44	2.46	1.86	2.46
Poisson's ratio	0.499	0.499	0.499	0.499	0.499	0.499

Finally, a three-dimensional model of solid parts is created by rotating the whole cross-section one full rotation about the tire axle axis in 60 equal pieces. Figure 3-14 shows the solid elements used in the FEA truck tire model representing the tread, tread base, tread shoulders, and bead fillers. It should be noted that the hysteresis of rubber is not considered in the solid rubber element models.

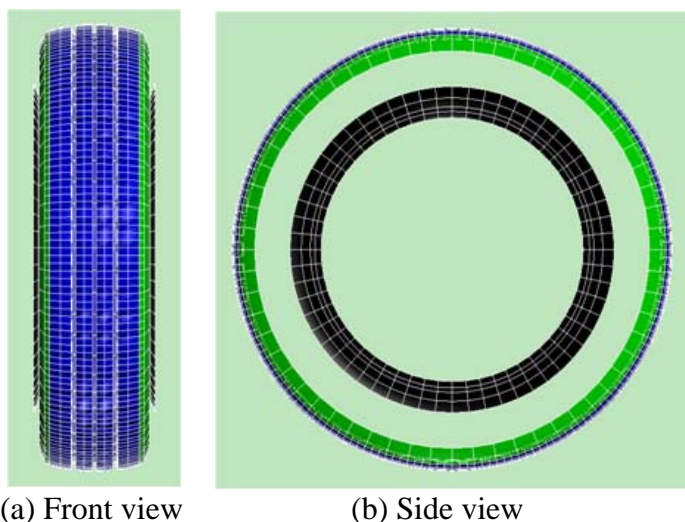


Figure 3-14 Solid Elements used in FEA Truck Tire Model

3.2.3 FEA Modeling of Beads

One-dimensional beam elements discretize beam and frame structures that can transmit axial forces, shear forces, bending, and torsion moments. The local axis system of the beam element, r, s, and t, is defined by user defined nodes, N₁, N₂, and M₁, as shown in Figure 3-15.

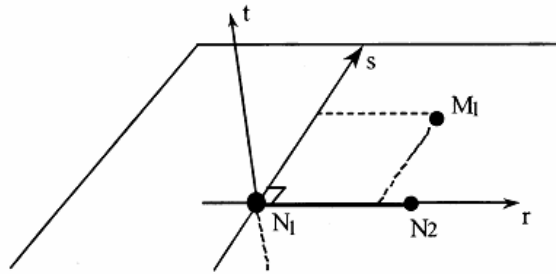


Figure 3-15 Definition of Beam Element

In the FEA truck tire model, the bead is modeled by using beam elements and the location is shown in Figure 3-16. The material properties used in the study are summarized in Table 3-3.

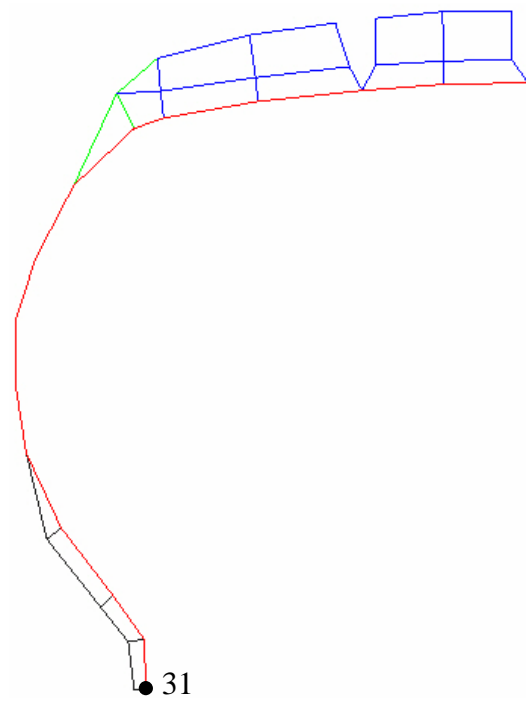


Figure 3-16 Beam Elements and Their I.D. Number in FEA Tire Model

Table 3-3 Material Properties of the Beam Elements

Tire component	Beads
Material I.D.	31
Density (ton/mm ³)	4.26E-08
Young's modulus (MPa)	92,100
Poisson's ratio	0.4
Yield stress (MPa)	1.00E+20
Cross section description	solid circular section
Cross section circular radius (mm)	2.5

Very high number for the yield stress is artificially input in the model. The bead point of Figure 3-16 is rotated one full revolution about the tire axle axis in 60 segments representing the bead of the FEA truck tire model. The bead on the right hand side is created in symmetry to the solid-dotted center line and both beads are shown in Figure 3-17.

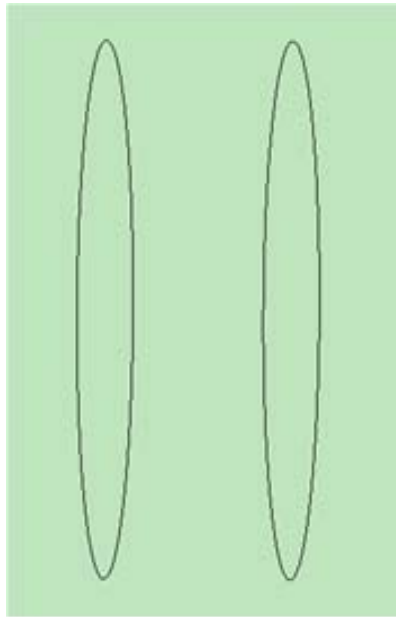


Figure 3-17 Two Beads Used in FEA Truck Tire Model

3.2.4 FEA Rim Model

An FEA rim model has been newly built for a truck tire-rim assembly. Rim dimensions are standardized by The Tire and Rim Association for size and contour. Tire and rim combinations are designated to assure proper mounting and fit of the tire to the rim. The load and cold inflation pressure imposed on the rim and tire must not exceed the rim and tire manufacturers' recommendations even though the tire may be approved for a higher load or inflation. Figure 3-18 shows a 15° drop center rim contour for a truck tire and its detailed dimensions are summarized in Table 3-4.

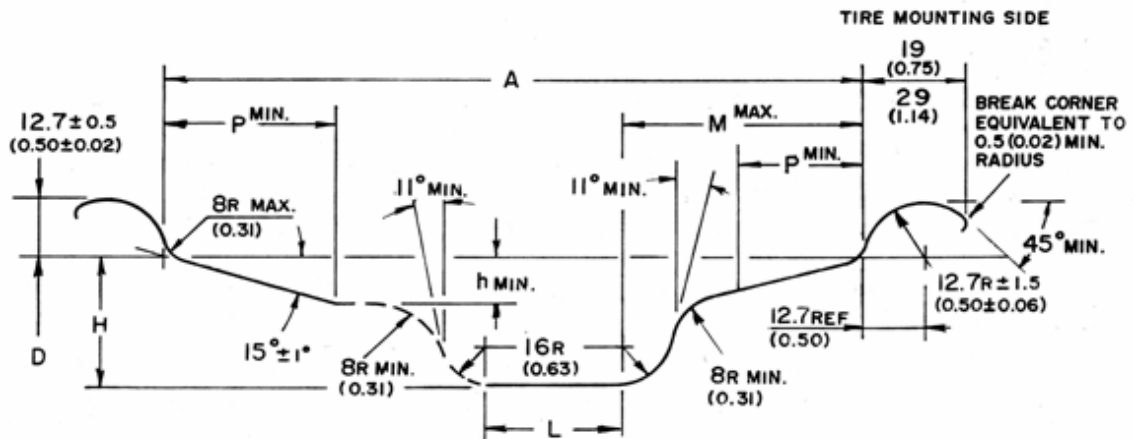


Figure 3-18 15° Drop Center Rim Contour (Tire and Rim Association Year Book, 1996)
[Unit: mm (in)]

Table 3-4 15° Drop Center Rim Contour Dimensions for 22.5 × 8.25 Truck Tire Rim

Rim size Designation	H minimum		h minimum		L minimum		M maximum		P minimum	
D (in) × A (in)	mm	in	mm	in	mm	in	mm	in	mm	in
22.5 × 8.25	30	1.17	10	0.394	28	1.10	74	2.90	36	1.42

As the tire is inflated, the tire model sits tightly inside of the rim and is constrained by the tire-rim contact. The tire contact parts with the rim, called rim strips, and rim contact are extremely important because pressurized air is sealed by the contact. The sealing should always be secured during normal vehicle operations. In addition to air sealing, traction and braking efforts are transmitted only through the tire-rim contact.

This detailed rim model can be also used to perform a comprehensive study of tire-rim contact mechanics. For example, research on the friction and slip between the tire and the rim or the effect of the tire or the rim weight can be conducted under various loadings, tractions, cornering, and braking maneuvers. A rim model whose size is 8.25×22.5 is shown in Figure 3-19 and its material properties are summarized in Table 3-5. It is made of steel and its weight is 32 kg.

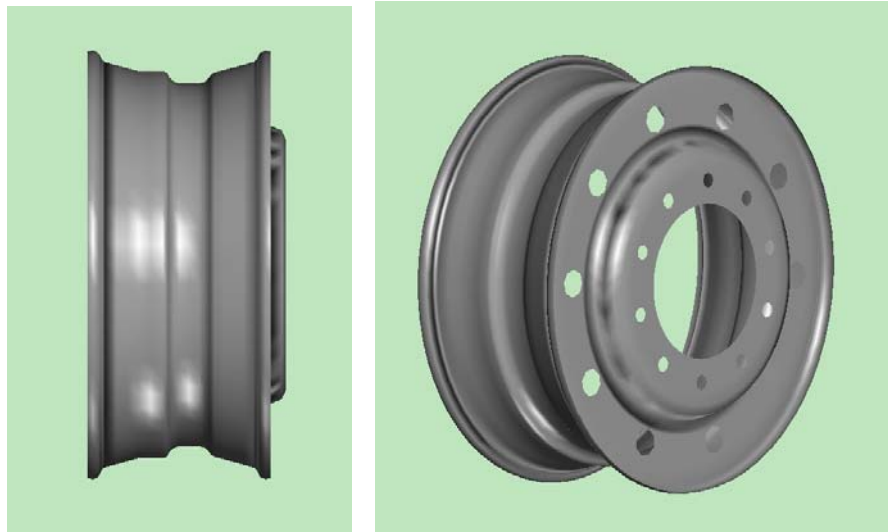


Figure 3-19 FEA Truck Tire Rim Model

Table 3-5 Material Properties of the FEA Rim

Wheel component	Rim
Material I.D.	41
Density (ton/mm ³)	8.00E-09
Young's modulus (MPa)	200,000
Poisson's ratio	0.3
Thickness (mm)	1.5

3.3 FEA Tire-Rim Assembly Model

The developed full three-dimensional FEA truck tire model, 295/75R22.5, is shown in Figure 3-20. The tire model is constructed using the following finite element components:

- 9,200 nodes,
- 1,680 layered membrane elements,
- 4,200 solid elements,
- 120 beam elements,
- 27 material definitions, and
- 1 rigid body definition.

The rim is defined as a rigid body for the simplicity of the model because the deformation of the rim is negligible. Some nodes of the tire rim strips are included in the rim rigid body definition representing a tire-rim connection. This assembly is a very secure method in terms of transmission of load, traction, and braking efforts when the slip at tire rim strips-rim contact is not of interest and ignored. Reaction forces from the ground can be delivered to the axle. Tire rotational or linear velocity can be directly controlled by the center of gravity (COG) node of the rigid rim model. Moreover, time history plots of the tire spindle, for example, displacements, velocity, and acceleration along three different axes, can be obtained from the COG node. Boundary conditions also can be defined at the COG node to constrain degree(s) of freedom of the tire model.

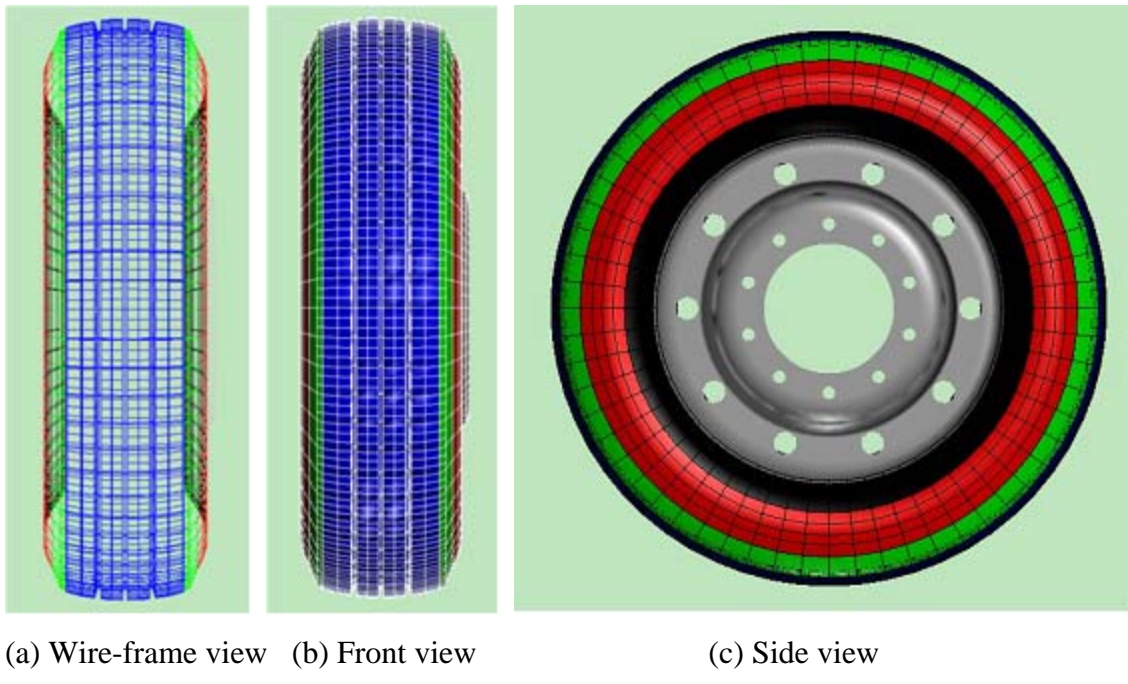


Figure 3-20 FEA Tire-Rim Assembly Model

3.4 Various Virtual Tire Test Environments

The FEA truck tire model has been placed on various road conditions to perform virtual tire and durability tests. FEA road models such as a flat road, rigid drum, and flat road

with water drainage ditches are introduced in the following Sections 3.4.1 to 3.4.3. The road models are set for rigid bodies because the deformation of the road is negligible.

3.4.1 Combined FEA Truck Tire and a Rigid Flat Road Model

Figure 3-21 shows the combined model of FEA truck tire and a rigid flat road. A contact interface between the tire tread and the road surface is defined so as not to penetrate each other. Thus, the tire model can be deformed against the rigid road under vertical loading conditions, where the static vertical stiffness can be predicted. Free rolling condition can be achieved by moving the road model itself at a constant speed toward the tire. As a result, the tire rotates due to the friction force developed at the tire-road contact area. The rolling resistant force and rolling resistance coefficient can be predicted. Under the free rolling condition, the cornering characteristics of the tire also can be predicted at a slip angle as seen in Figure 3-22.

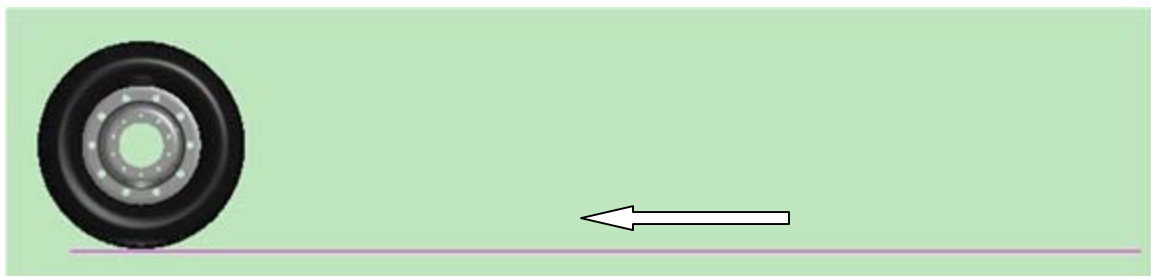


Figure 3-21 FEA Truck Tire on a Rigid Flat Road Model

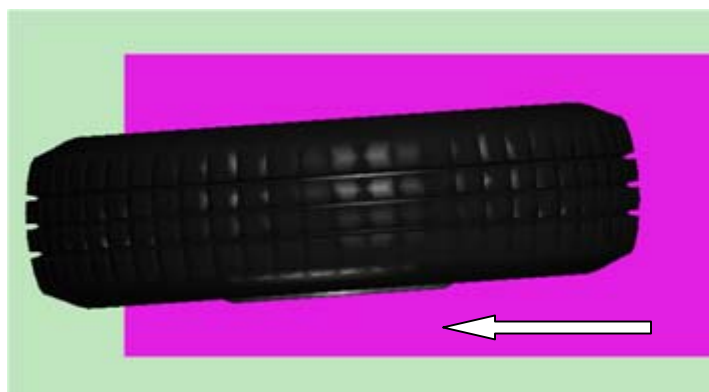


Figure 3-22 FEA Truck Tire at 4° Steer Angle on a Rigid Flat Road Model

3.4.2 Combined FEA Truck Tire and a Rigid Cleat-Drum Model

Figure 3-23 shows the combined model of the FEA tire and a circular drum. The circular drum can be considered as infinitely long road during tests. After inflation and loading on the tire, the tire center is usually constrained vertically so as not to move to predict the transmitted forces to the tire center from the contact area. Then, the drum starts to rotate the tire by the frictional force generated at the tire-drum contact area. The coefficient of friction is set to 0.8, corresponding to the value between the tire and dry asphalt or concrete surface. This coefficient of friction can be changed according to different road surface conditions.

A 10 mm-radius semicircular cleat is placed on the drum to excite the tire vertically and cyclically as the drum rotates. From this tire-cleat drum virtual test, the free vibration modes can be predicted by applying an FFT algorithm to the time history result of tire spindle forces.

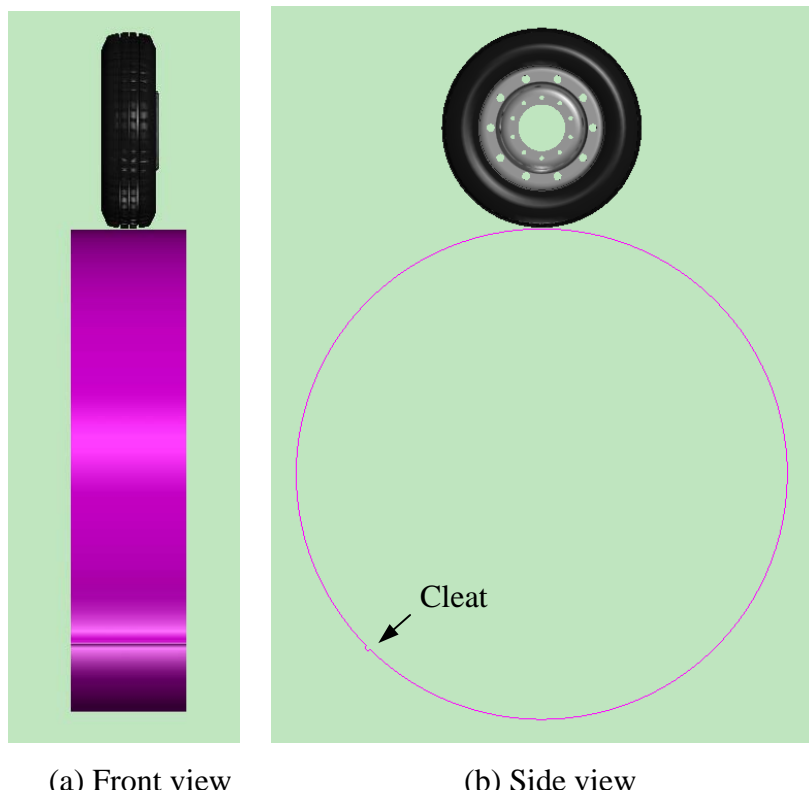


Figure 3-23 FEA Truck Tire on a Rigid Cleat-Drum Model

Since the deformation of the drum is not of interest, the drum is modeled as a rigid body that has no elastic or plastic deformation along any directions. The diameter of the drum is 2.5 meters. Larger drum diameters are desirable to minimize the effect of the drum curvature.

3.4.3 Combined FEA Truck Tire and a Rigid Smooth Drum Model

Figure 3-24 shows the combined model of the FEA truck tire model and a rigid smooth drum model. High rotational drum speed without external excitations can be achieved until standing wave phenomena on the tire model is observed, which is quite challenging in physical laboratories. Acceleration, braking, and yaw oscillation tests are also achievable with this tire-drum setup.

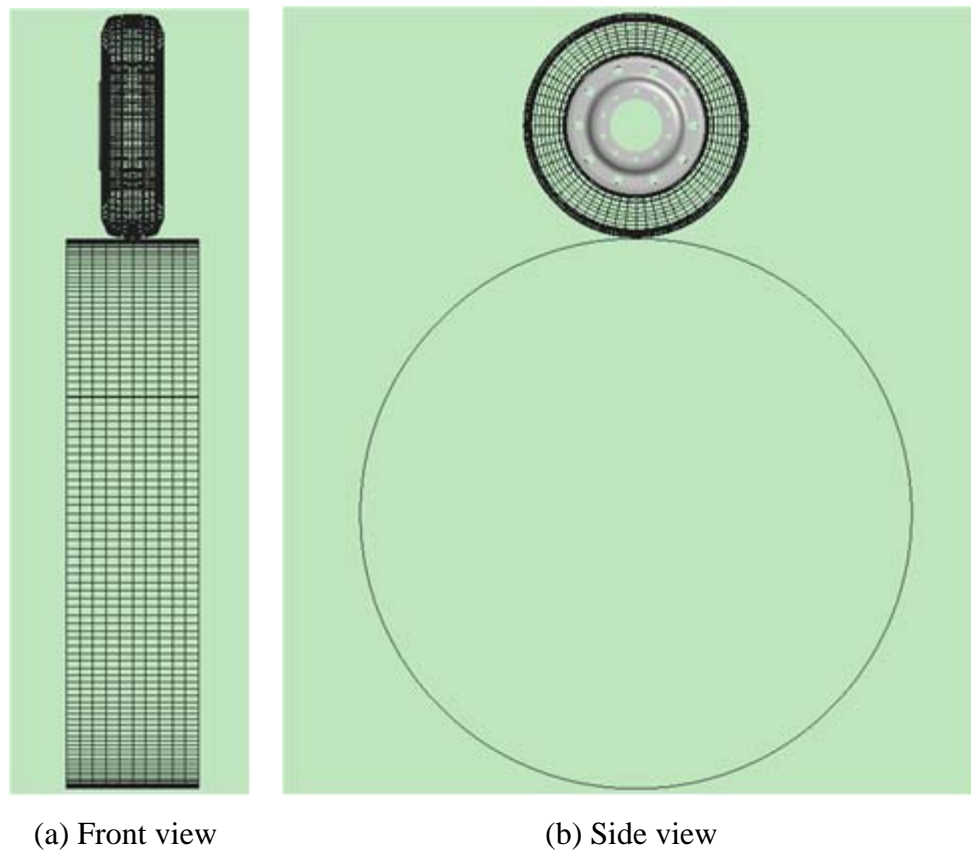


Figure 3-24 FEA Truck Tire on a Rigid Smooth Drum Model

3.4.4 Combined FEA Truck Tire and a Rigid Road with Water Drainage Ditches Model

Tire tests running on road obstacles such as potholes, steps, ditches, and high-speed avoidance bumps are usually called durability tests. The developed FEA truck tire model will experience the durability tests on the ditches in Chapters 5 and 6. Figure 3-25 shows the combined model of the FEA truck tire and a rigid flat road with three water drainage ditches that can be seen in construction areas.

Ditches 1 and 3 are placed at $\pm 45^\circ$ oblique from the tire traveling direction, respectively, while ditch 2 is placed at 90° . When the tire model crosses ditches 1 and 3, longitudinal, vertical, lateral forces, overturning, and vertical moments can be observed on the tire due to the different left and right contact area geometries. However, when the tire model crosses ditch 2, only longitudinal and vertical forces can be observed because there is no lateral excitation to the tire. Ditch 2 is chosen to have a length of 690 mm and a depth of 120 mm. The cross-section shape of ditch 2 is illustrated in Figure 5-7 and its digitized points are included in Appendix B.



Figure 3-25 FEA Truck Tire on a Rigid Flat Road with the Three Water Drainage Ditches

3.5 Summary

Two different types of tire structure, bias-ply and radial-ply tires, their components, and material characteristics have been reviewed. The number of radial tire applications have continuously increased in most types of ground vehicles by virtue of longer tread life, lower rolling resistance, better fuel efficiency, and higher load carrying capability.

compared to bias-ply tires. The major components of the radial-ply tire, carcass layer, radial cord layer, belts layers, tread base, and tread, are examined in terms of their functions and structures.

Based on radial tire structure, its components, and material characteristics, a three-dimensional FEA full tire model has been constructed with three-dimensional solid, two-dimensional layered membrane, and one-dimensional beam elements. In addition to the tire model itself, a rim model is also included and rotated with the tire with proper mass and rotational inertial effects. Figures displaying images of those components are inserted to help understanding.

For the first objective of this doctoral study, various virtual FEA tire-road test environments have been established to predict static and dynamic responses. The FEA tire on a rigid flat road model, on a rigid cleat-drum model, on a rigid smooth drum model, and on a rigid road with ditches model are created. By using these virtual test environments, most of the physical laboratory tests, such as the vertical load-deflection test, cornering test, free vibration modes test, yaw oscillation test, and durability tests such as ditch test and speed bump test can be virtually duplicated.

CHAPTER 4

FEA TRUCK TIRE MODEL VALIDATION

In Chapter 3, a detailed nonlinear FEA model of a radial-ply truck tire has been developed using explicit FEA software, PAM-SHOCK. The tire model will be used to determine the characteristic tire parameters that are required to represent a rigid ring tire model. Before the tire parameters are determined through virtual tire tests, the tire model needs to be validated by checking whether it shows real tire characteristics. For the validation, static and dynamic tire simulations are conducted at various tire loads. The results of the validation tests are compared with physical measurements.

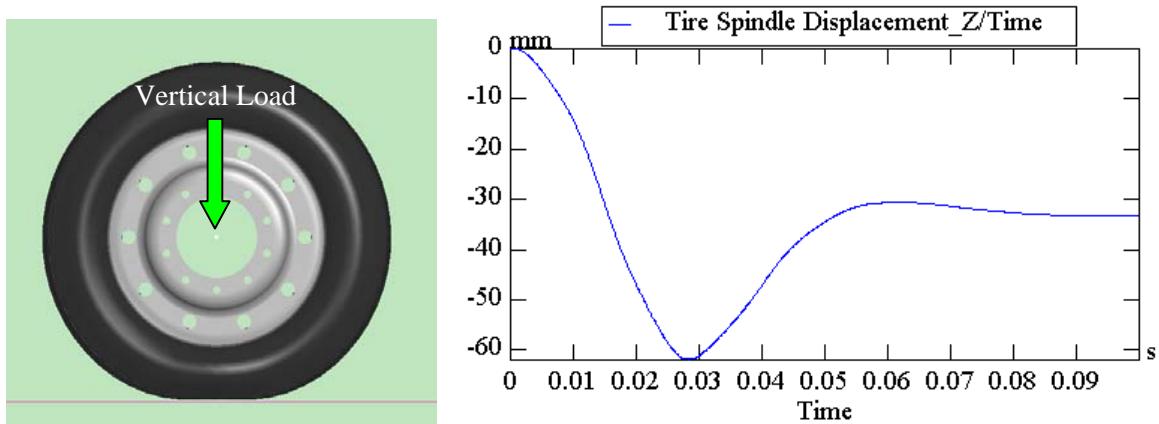
4.1 Static Validation Tests

For the vertical static validation tests of the FEA truck tire model, tire load-deflection relationship and footprint area tests are virtually performed at various tire loads.

4.1.1 Tire Vertical Load-Deflection Relationship

For the vertical static tests, the truck tire model is inflated at the rated pressure of 0.759 MPa (110 psi) and loaded at the spindle of the tire model on a flat road surface as seen in Figure 4-1 (a). Due to the sudden loading on the tire model, the tire deforms excessively. However, the tire rebounds shortly thereafter due to its vertical stiffness and becomes stabilized due to its damping effect. Figure 4-1 (b) shows the vertical displacement history of the tire spindle with time at the rated vertical load of 26.7 kN (6,000 lb). After

the tire model reaches stabilization, the steady-state vertical deflection of the tire model is recorded.



(a) Vertical tire load at the spindle (b) Time history curve for the tire load at 26.7 kN

Figure 4-1 Virtual Tire Load-Deflection Test

Vertical tire loads are applied up to 40.0 kN (9,000 lb) and their corresponding vertical deflections are plotted in Figure 4-2. The tangential slope at a specific point represents the vertical stiffness at the tire load. The predicted vertical displacements are compared with physical measurements provided by Goodyear Tire & Rubber and show good agreement with the measurement data.

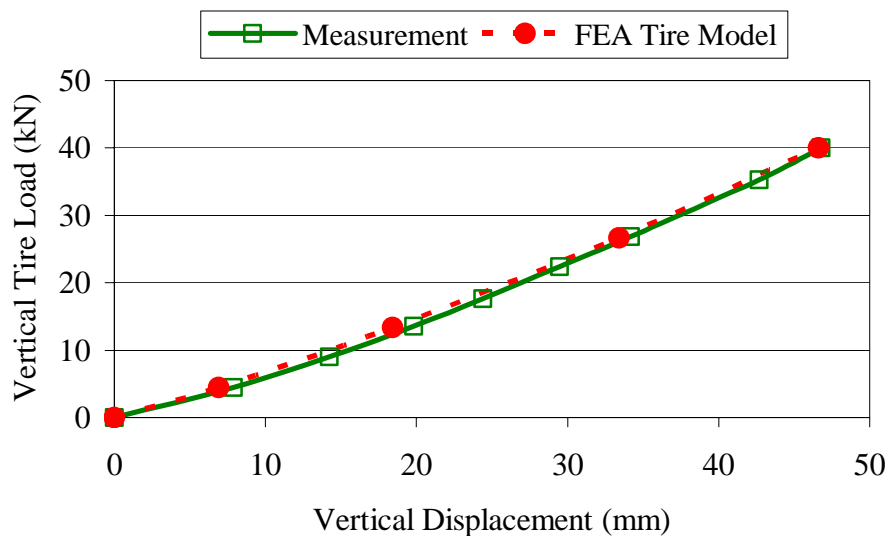


Figure 4-2 Vertical Tire Load versus Deflection

Ford and Charles (1988) stated that dynamic stiffness for radial heavy duty truck tires are approximately five-percent less than static values. They also mentioned that single tire load rating is determined between 14 to 18 percent deflection¹ at a given inflation pressure, which is a typical range for highway operation.

4.1.2 Footprint Area

Even though the tire deflections are the same at a given vertical tire load, their footprint shapes and areas between tires and road surface can be different according to their cross section shapes and structures. The different footprint areas can cause different tire forces during operations, as noted by Koishi *et al.* in 1998. It was stated that different cornering forces were observed due to different footprint areas obtained from two tires with different crown angles. Therefore, the footprint area also plays an important role independently as a validation parameter of the tire model, as well as the tire load-deflection relationship.

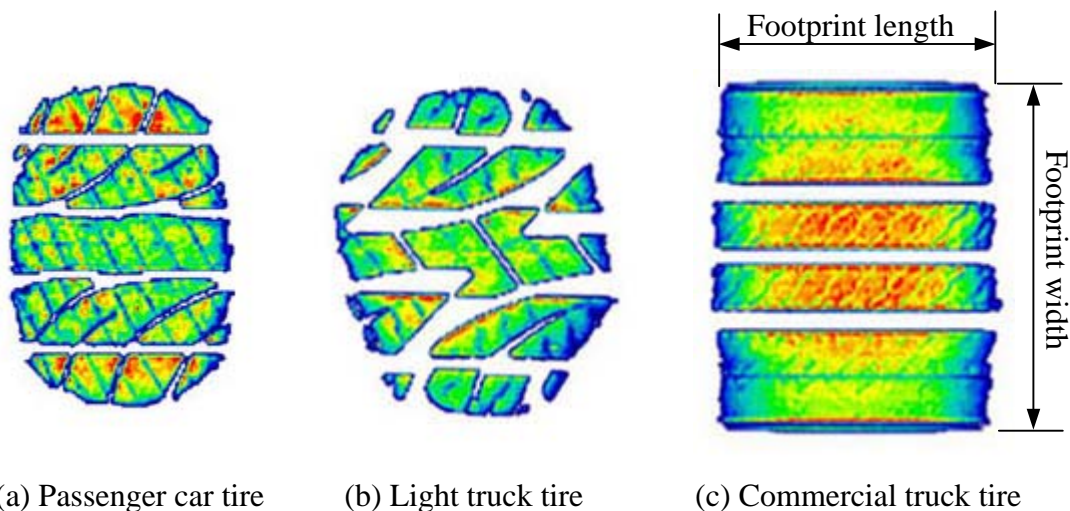


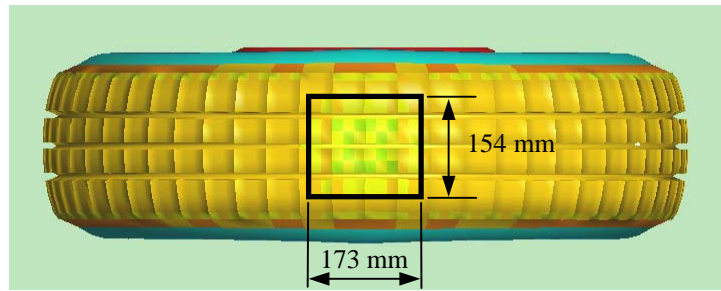
Figure 4-3 Footprint Areas and Shapes of Various Tires (Tekscan, 2006)

Some of the ways to obtain footprints are by (1) loading the tire against carbon paper, (2) against pressure-sensitive paper, and (3) taking a photograph of the tire through a glass plate. With more advanced technology, electronic pressure sensors embedded in a test

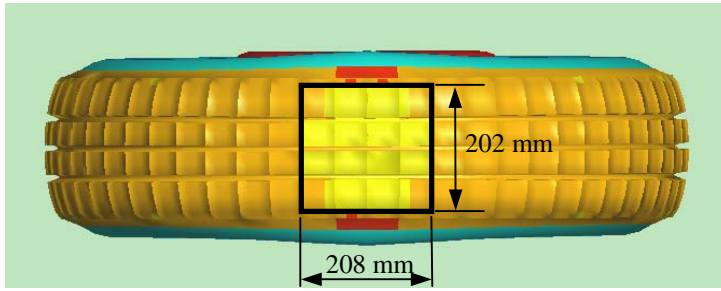
¹ Percent deflection is defined in page 61. Please refer to that page.

bed is also available to measure footprints and even contact pressure distribution, as seen in Figure 4-3. It should be noted that the footprint shape of the commercial truck tire is nearly rectangular [Figure 4-3 (c)] while the shapes of the other two tires represent ellipses. Therefore, the footprint area for the commercial truck tire can be calculated approximately by multiplication of footprint length and width.

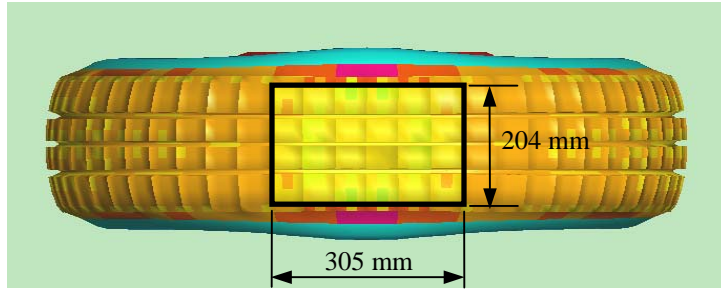
The footprint can also be virtually determined by loading the FEA tire model against a flat road and defining the contact area. Vertical static loads from 13.3 kN (3,000 lb) to 40.0 kN (9,000 lb) are applied to the center of the tire model to obtain footprints at various loads. Figure 4-4 shows the predicted footprint shapes and their sizes at various tire loads.



(a) Footprint Area at Vertical Tire Load of 13.3 kN (3,000 lb)



(b) Footprint Area at Vertical Tire Load of 26.7 kN (6,000 lb)



(c) Footprint Area at Vertical Tire Load of 40.0 kN (9,000 lb)

Figure 4-4 Footprint Area Prediction at Various Tire Loads

Average contact pressure can be calculated by dividing vertical tire load with footprint area, which plays an important role in road pavement and damage engineering.

The predicted footprint areas at various tire loads are plotted and compared with those from the measurements provided by Goodyear Tire & Rubber as shown in Figure 4-5. It can be noted that the footprint area prediction using the FEA tire model generally agree to overlap on the measurements even though small differences between the FEA and measured points are observed. The shape of the tire model is not exactly a circle since the tire model is sliced in 60 pieces circumferentially. If the tire model is sliced in 120 or 180 pieces and finer solid tread elements, no differences will be detected.

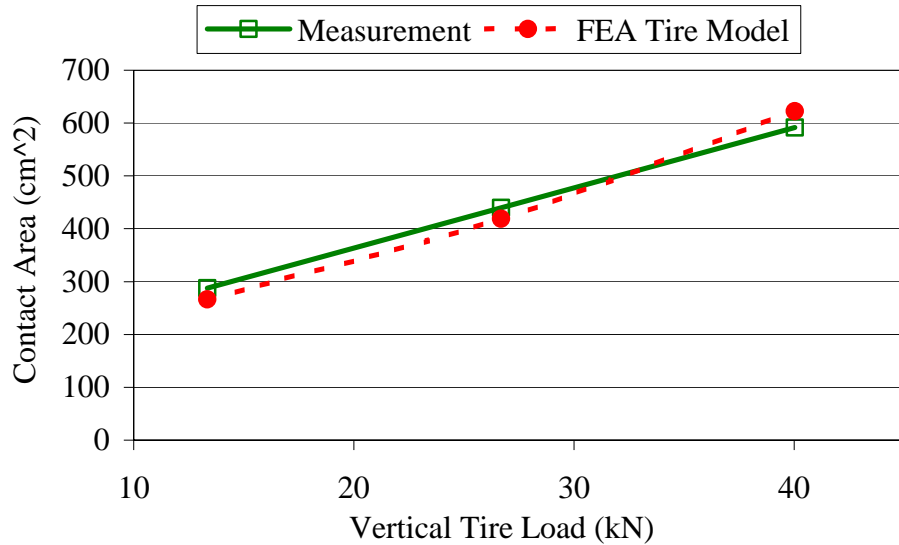


Figure 4-5 Footprint Area versus Vertical Tire Load

4.2 Dynamic Validation Tests

The tire system responds not only to vertical tire loads but also to dynamic road or steering inputs with resonance. For the dynamic validation tests, the first mode of the free vertical vibration test, the cornering test, and the yaw oscillation test have been virtually conducted and their results are compared with available measurements.

4.2.1 First Mode of Free Vertical Vibration Test

Most of the tire mass is concentrated near the tread, tread base, and belt layers, which are located on the outer portion of the tire. Thus, these masses can be considered to be connected to the rim through the elastic sidewalls. This combination of the mass and elasticity allows the tread to vibrate and even to resonate when the tread is excited by road inputs. A combined FEA tire and cleat-drum model has been built to determine the first mode of vertical free vibration as seen in Figure 4-6. In this model, the truck tire model is inflated to a pressure of 0.759 MPa (110 psi) and loaded vertically by 26.7 kN (6,000 lb) on a cleat-drum. The semicircular cleat on the drum has a radius of 10 mm. The diameter of the drum is 2.5 m.

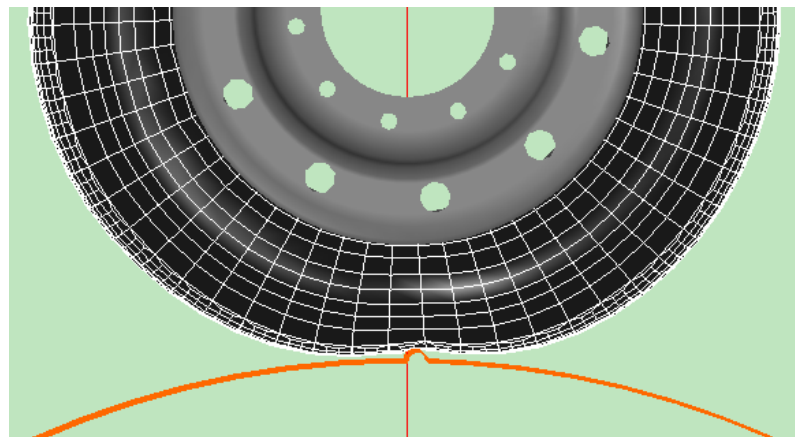


Figure 4-6 In-Plane Tire Excitation During Cleat Impact

After the tire model is inflated and loaded, the tire spindle needs to be fixed in all three translational directions to detect transmitted vertical force on the spindle and to be free only in rotational direction. Angular velocity is given to the center of the drum to enable free rolling of the tire at 50 km/h. As the drum rotates, the cleat on the drum excites the tire vertically. Since the tire spindle is fixed vertically, the vertical reaction force due to the cleat excitation can be predicted at the tire spindle. In addition, the in-plane free vibration mode can be obtained by applying an FFT algorithm to the predicted vertical force time history output as shown in Figure 4-7.

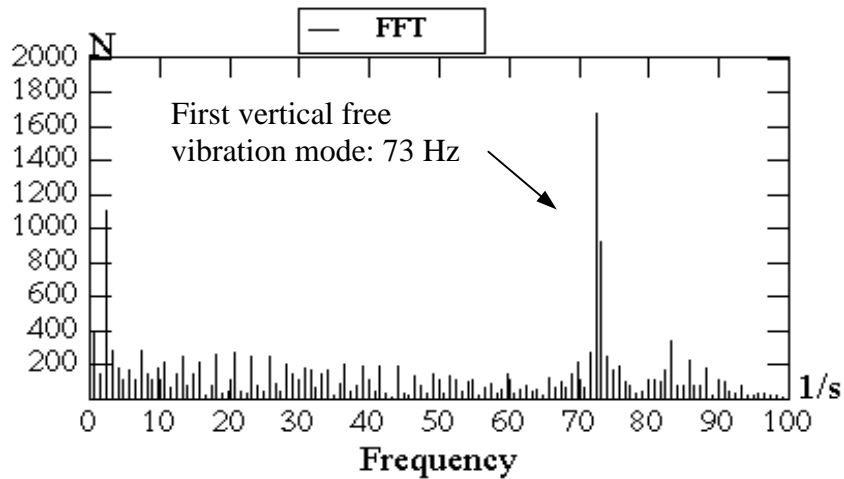


Figure 4-7 FFT Result of Vertical Reaction Force at Tire Spindle

From Figure 4-7, the first vertical free vibration mode is detected at 73 Hz, where the entire tread band vibrates up and down without distortion about the vertically fixed rim. Since the entire tread band moves up and down, the force associated with the resonance is transmitted to the wheel and axle. The predicted first mode falls within the mode range of radial-ply tires measured by, for example, Potts and Csora (1975), Takayama and Yamagishi (1984), and Allison and Sharp (1997).

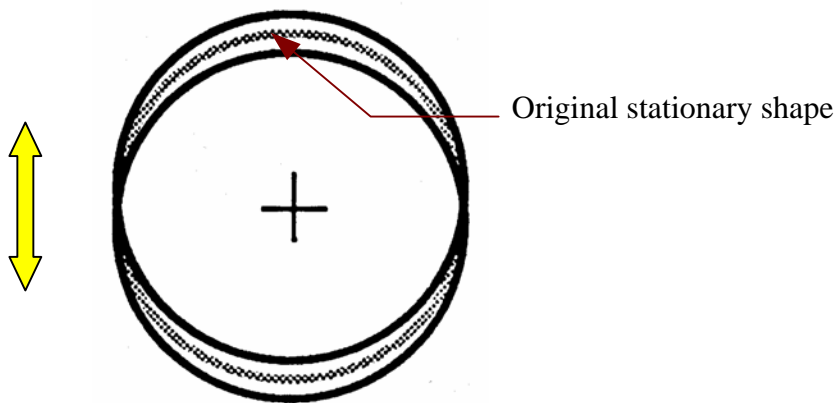


Figure 4-8 First Mode of Vertical Free Vibration (Gillespie, 1992)

4.2.2 Cornering Test

When a tire is steered and the vehicle is under cornering conditions, the tire is subjected to a lateral deflection due to a lateral force on the tire resisting centrifugal force of the vehicle sprung mass. The cornering test is virtually conducted to examine the characteristic cornering performances of the FEA truck tire model. The truck tire model is inflated at a pressure of 0.759 MPa (110 psi) and loaded vertically up to 35.6 kN (8,000 lb) at the spindle of the tire model. Then, the tire model is steered at slip angles up to 12°. A flat road is moving at constant speed of 5 km/h toward the tire to rotate the tire model, which is the same test condition in real laboratory tests. Figure 4-9 shows the cornering simulation at a slip angle of 6° and the lateral deformation of the tire at the contact area with road surface.

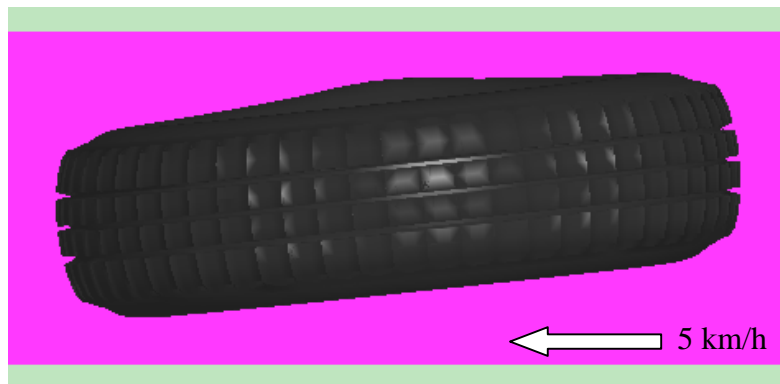


Figure 4-9 Cornering Simulation at Slip Angle of 6°

The predicted cornering forces with respect to different slip angles up to 12° are plotted in Figure 4-10 and compared with the measurement data from University of Michigan Transportation Research Institute (UMTRI). The applied vertical loads are 17.8 kN (4,000 lb), 26.7 kN (6,000 lb), and 35.6 kN (8,000 lb). The predicted cornering forces and slopes at slip angle 0°, cornering stiffness, are generally in good agreement with the measurements, especially for the two cases of lower vertical loads, 17.8 kN and 26.7 kN.

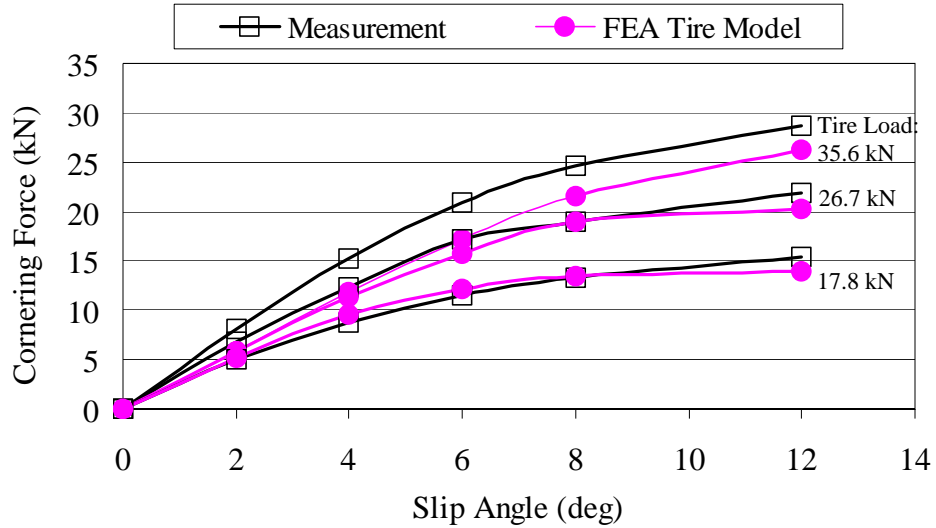


Figure 4-10 Cornering Forces Validation

Meanwhile, another important cornering characteristic parameter, aligning moment, is also predicted with respect to various slip angles, and compared with UMTRI's measurement as seen in Figure 4-11. In the regions of slip angles from 0 to 4°, the predicted aligning moments show good agreement with the measurements at the lower two tire load cases. For slip angles > 4°, considerable discrepancies are observed. The discrepancies are considered to be due to the differences in cross-sectional shapes, contact areas, and tread patterns between the FEA and real truck tires.

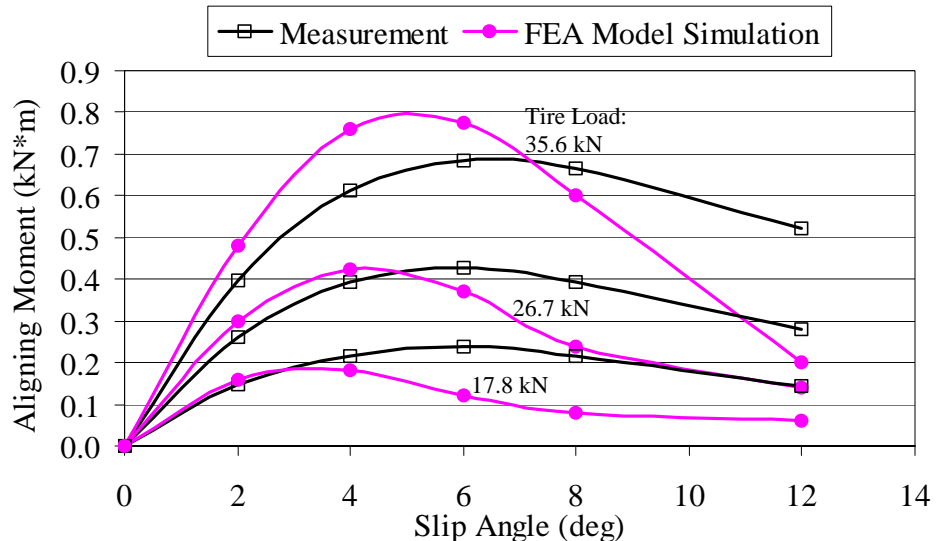


Figure 4-11 Aligning Moments Validation

4.2.3 Yaw Oscillation Test

The dynamic tire response to time-varying steering angle input is known to be quite different from those observed under constant steering angle input condition (Schuring, 1976). The dynamic tire response such as the dynamic lateral force is dependent on the cornering stiffness, lateral stiffness, tire speed, and oscillation frequency. The varying steering angle maneuver can be observed during vehicle handling, especially in emergency events such as quick lane-change or accident-avoidance steering events. In these cases, the steady state cornering responses, such as Figures 4-10 and 4-11, do not provide sufficient information to predict the dynamic tire responses to varying steering angle input. The developed lateral force at varying steering angle input does not reach a steady state value, and is delayed a certain amount of time from the input. Thus, dynamic tire response to varying slip angle input, namely a yaw oscillation test, is conducted as an independent validation test of the FEA tire model.

The laboratory test set-up to accomplish the yaw oscillation test is quite complicated as seen in Figure 4-12 (a). The test set-up consists of the tire, drum, trapezoid, and hydraulic actuator.

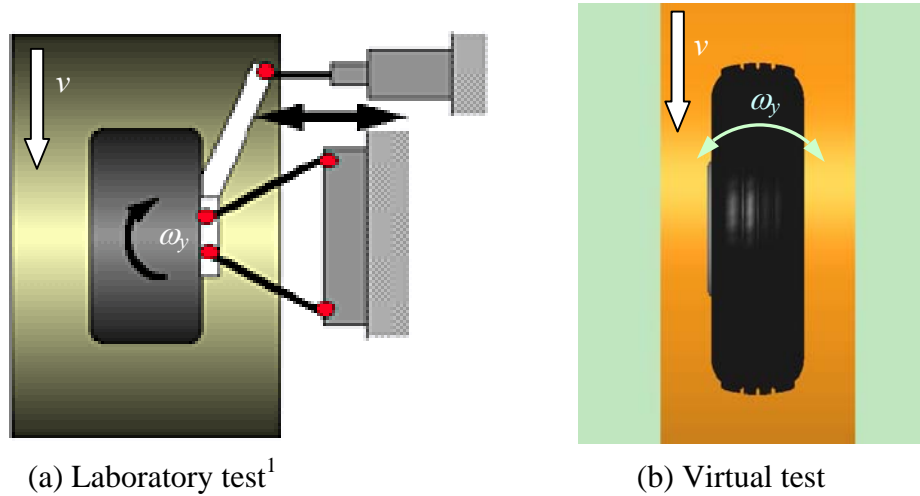


Figure 4-12 Yaw Oscillation Test

¹ The picture is retrieved from the website:
http://www.tut.fi/plastics/tyreschool/moduulit/moduuli_10/hypertext/9/9_1.html#9_1_6

The two rigid beams in the trapezoid connect the measuring hub to the frame which is rigidly connected to the side foundation, which guarantees center point steering. The displacement of a hydraulic actuator is transformed to wheel rotation through a rigid excitation arm. The tire load is applied by adjusting and fixing the axle height. The virtual yaw oscillation test can be conducted by using a combined FEA tire and rigid drum model without the sophisticated test set-up and operational difficulty as shown in Figure 4-12 (b). In the figure, v is the drum speed, and ω_y is the input frequency of the yaw oscillation.

4.2.3.1 Amplitude Ratio and Phase Angle

In order to conduct the yaw oscillation test, continuous and sinusoidal steering angle variation input is applied to the tire center after the vertical tire loading. As a result, the peak lateral force and the phase angle can be plotted as a function of path frequency. In fact, instead of just the peak lateral force, an amplitude ratio is used in the plot to emphasize the differences between the two forces. The amplitude ratio is defined as the dimensionless ratio of the dynamic peak lateral force during time-varying slip angle input to the steady state cornering force at constant slip angle. The steady state cornering force within a small slip angle range can be calculated by multiplying the cornering stiffness and slip angle (Loeb *et al.*, 1990). The phase angle is obtained from the time delay, Δt , between the neighboring peak locations of the yaw oscillation input and the dynamic lateral force output. The phase angle, ϕ , can be calculated using the following Equation (4-1).

$$\phi = \omega_y \cdot \Delta t = 2\pi \cdot f_y \cdot \Delta t \text{ (rad)} = 360 \cdot \Delta t \cdot f_y \text{ (degree)} \quad (4-1)$$

Where, ω_y is the angular speed of the sinusoidal input in rad/s, and f_y is the oscillation frequency in Hertz.

The dynamic tire responses are dependent more on the distance traveled than the time elapsed at low speed ranges (Lippmann and Oblizajek, 1976; Weber and Persch, 1975;

and Schuring, 1976). Thus, the path frequency (ω_{path}) in radians per unit distance used for the abscissa in the amplitude ratio and phase angle plots, rather than the time frequency in radians per unit second. The path frequency is calculated as the ratio of the angular speed of the yaw oscillation input, ω_y , to vehicle or tire speed, v , as seen in Equation (4-2). By using the path frequency in the plots, the oscillation frequency and vehicle speed can be considered together as an input variable to the dynamic tire response, and the dynamic tire response can be easily monitored in terms of the distance traveled from the plots.

$$\omega_{path} = \frac{\omega_y}{v} \text{ (rad/m)} \quad (4-2)$$

Loeb *et al.* (1990) derived a first-order differential equation that predicted the lateral displacement of the tire tread at small slip angle input. For the study of the frequency response on the lateral force, a sinusoidal input, $\alpha(t)$, with an amplitude of A and an oscillation frequency of ω_y was applied to the first-order system as follow:

$$\alpha(t) = A \cdot \sin(\omega_y t) \quad (4-3)$$

As a result, the sinusoidal output, $y(t)$, could be obtained with new amplitude and phase angle difference (ϕ), but the same oscillation frequency:

$$y(t) = \gamma \cdot A \cdot \sin(\omega_y t - \phi) \quad (4-4)$$

Where, γ is the amplitude ratio of the output to input.

The amplitude ratio and phase angle can be obtained by substituting Equations (4-3) and (4-4) into the first-order differential equation and solving for them as follows:

$$\gamma = \frac{1}{\sqrt{1 + (\omega_y \cdot \tau)^2}} \quad (4-5)$$

$$\phi = \tan^{-1}(-\omega_y \cdot \tau) \quad (4-6)$$

Where τ is the system time constant of the first-order differential equation, and this time constant can be expressed in terms of cornering stiffness (k_f), lateral stiffness of the tire (k_l), and tire speed (v) as follows:

$$\tau = \frac{k_f}{v \cdot k_l} \quad (4-7)$$

The time constant is frequently called the relaxation time because it is closely related to the relaxation length, a characteristic parameter in the analysis of the out-of-plane dynamic tire responses. The relaxation length is obtained by multiplying the time constant by the tire speed, and the relaxation length becomes a function of only the cornering stiffness and lateral stiffness. Since the cornering and lateral stiffnesses are constant values at a given vertical tire load, the relaxation length is also independent of the tire speed or elapsed running time. This is the reason why the dynamic tire response is distance-dependent rather than time-dependent.

By inspecting Equations (4-5) and (4-6), as the oscillation frequency approaches zero, the amplitude ratio approaches one, and the phase angle approaches zero asymptotically. On the contrary, as the oscillation frequency increases, the amplitude ratio decreases close to zero, and the phase angle approaches -90° asymptotically.

4.2.3.2 Virtual Yaw Oscillation Test Using FEA Truck Tire Model

The FEA truck tire model is inflated at the rated pressure of 0.759 MPa (110 psi) and loaded at 26.7 kN (6,000 lb) on a smooth drum. After the tire model is stabilized, it is vertically fixed and is oscillated about the vertical axis (Z-axis) at a sinusoidal yaw frequency of 1 Hz with a maximum amplitude of $\pm 1.65^\circ$. Simultaneously, the drum rotation provides tire speeds of 6.4 km/h (4.0 mph) to 40.2 km/h (25.0 mph) similar to

Loeb *et al.*'s study. Figure 4-13 shows the sinusoidal input and the predicted dynamic lateral force at the tire speed of 6.4 km/h (4.0 mph).

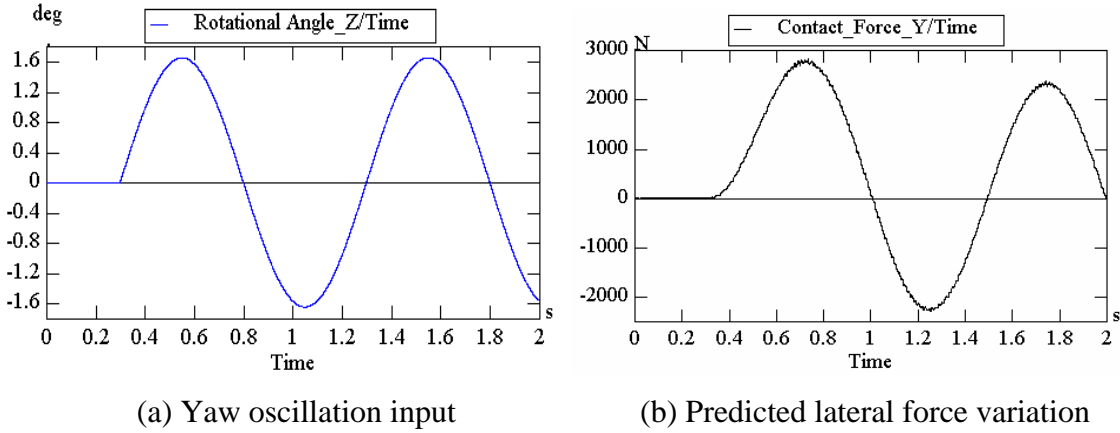


Figure 4-13 Yaw Oscillation Input and Lateral Force Output at the Frequency of 1 Hz

After the virtual yaw oscillation tests are completed with all the different speeds up to 40.2 km/h (25.0 mph), the amplitude ratios of the dynamic lateral forces to the steady state cornering force are plotted as a function of the path frequency [Equation (4-2)] as seen in Figure 4-14. Since the values from physical yaw oscillation tests using the truck tire are not provided to compare with the predicted values, the experimental and calculated amplitude ratio [Equation (4-5)] values obtained from Loeb *et al.*'s study are plotted together in Figure 4-14 to verify the FEA tire model dynamic response to sinusoidal steering input. Results of all cases generally show the same trend, i.e., as the path frequency increases, the amplitude ratio values decrease. It is also noted that the amplitude ratio values are all less than one, which means that the dynamic lateral forces are less than their steady state cornering forces as the path frequency increases.

The phase angles obtained from the virtual FEA yaw oscillation test are calculated based on the time delay and Equation (4-1), and plotted as a function of the path frequency as seen in Figure 4-15. Similar to Figure 4-14, Loeb *et al.*'s experimental and predicted phase angle [Equation (4-6)] values are also plotted together in the figure to compare the trends of the results obtained from the FEA yaw oscillation test with the measured and calculated results by Loeb *et al.* (1990). It is observed that as the path frequency

increases, the phase angles of all cases decrease. For more accurate validation of the FEA truck tire model, physical yaw oscillation tests are required using the same truck tire as the FEA truck tire model.

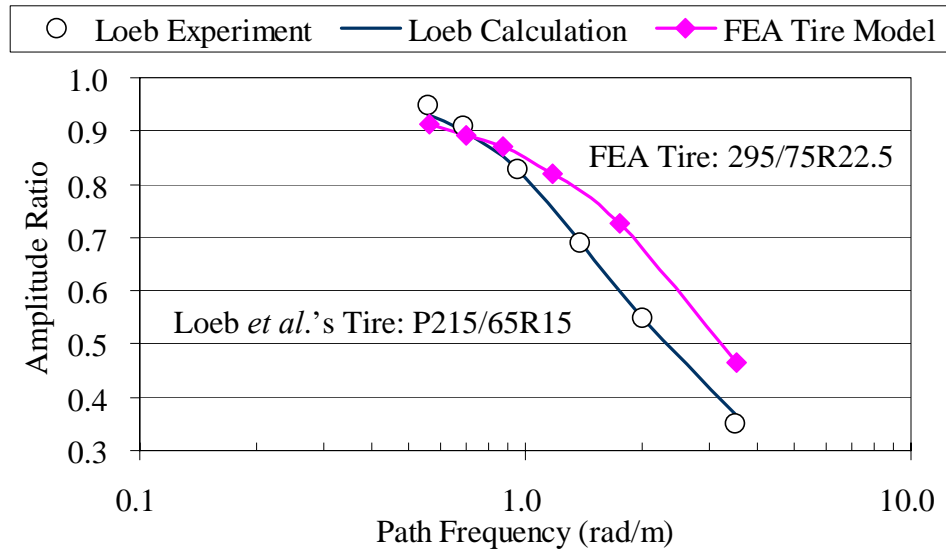


Figure 4-14 Tire Lateral Force Magnitude as a Function of Path Frequency

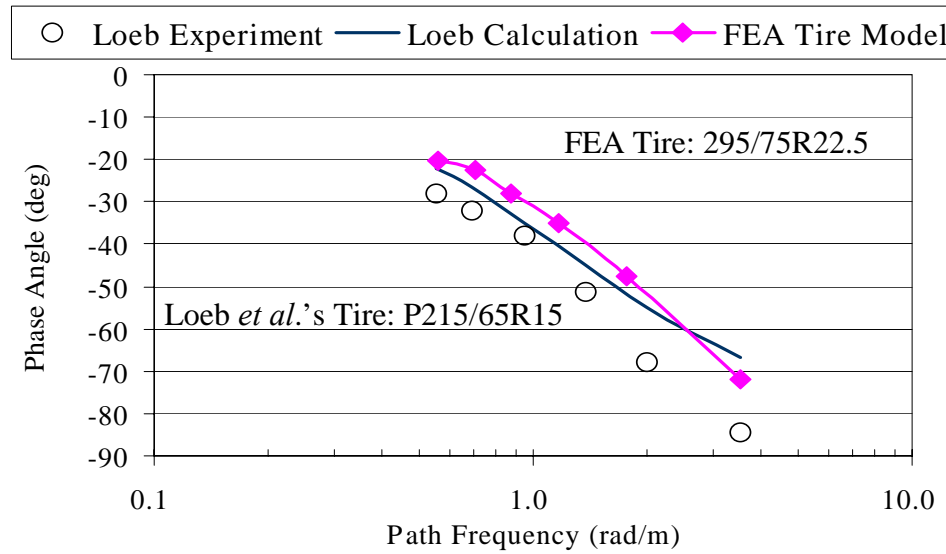


Figure 4-15 Tire Phase Angle as a Function of Path Frequency

4.3 Summary

In this chapter, validation tasks of the FEA truck tire model are conducted through virtual static and dynamic tire tests. The static tests include vertical tire load-deflection and footprint area prediction tests. The dynamic tests consist of the first free vertical vibration mode, cornering, and yaw oscillation tests. The first free vertical vibration mode test is conducted on a rotating cleat-drum, and the first vertical mode of the FEA tire is obtained by applying an FFT algorithm to the predicted vertical force time history at the tire spindle. For the validation of the model in terms of steady state out-of-plane motions, cornering simulations are conducted to predict cornering forces and aligning moments at various slip angles and tire loads. Yaw oscillation tests are also conducted to examine the dynamic tire responses to sinusoidal steering angle input. As a result, the amplitude ratio and phase angle are plotted as a function of the path frequency.

The in-plane tire responses of the FEA tire model, such as tire load-deflection, footprint area, and the free vertical vibration mode predictions, are in good agreement with physical measurements. To the contrary, the out-of-plane tire responses, such as steady state cornering and dynamic yaw oscillation tests, generally show limited agreement with measured or published test data. The predicted cornering forces in cases of tire loads less than the rated tire load show good agreement with measurements. The predicted aligning moments agree with measured data in a slip angle range less than 4° . Therefore, the FEA tire model is expected to predict in-plane tire responses better than out-of-plane responses.

The virtual yaw oscillation tire test is performed successfully for the first time in the FEA environment. Thus, the dynamic lateral force and time delay of the force development from the steering input are obtained from the virtual test result. The amplitude ratio can be calculated by dividing the dynamic lateral force by the steady state cornering force. The phase angle can be calculated from the time delay. Both the amplitude ratio and phase angle values are plotted as a function of the path frequency to examine the effect of the input frequency on the dynamic tire response. The predicted dynamic tire response as

a function of the path frequency show good agreement in trend of the published measurements and calculations.

CHAPTER 5

DETERMINATION OF THE IN-PLANE AND OUT-OF-PLANE PARAMETERS OF A RIGID RING TIRE MODEL USING THE FEA TRUCK TIRE MODEL

In this chapter, the developed three-dimensional FEA truck tire model is used to virtually predict the in-plane and out-of-plane parameters of a rigid ring tire model (Figures 5-1 and 5-18, respectively). The predicted parameters are used in the rigid ring tire model established in Volvo 3P's multi-body truck simulation environment for efficient analyses, which is the objective of this research. This effort is conducted as a part of a research project sponsored by Volvo 3P.

In the 1980s and 1990s, many researchers used rigid ring tire models to efficiently predict dynamic tire responses during tire running on irregular road surfaces. In the rigid ring tire model, the ring represents the tire tread and belts, and it is connected to a rigid rim through the elastic sidewall springs and dampers of the tire. Due to the nature of the rigid ring tire model, a point contact between the rigid ring and a road surface is used. Thus, a few more parameters for the tire-road contact interface need to be incorporated in the rigid ring tire model to represent the contact interaction closer to actual tire responses. All of the in-plane and out-of-plane parameters have been determined by performing appropriate experimental tire tests. However, in this chapter, those parameters are predicted by performing virtual tire tests using the FEA truck tire model.

For the in-plane tire motions, the elastic sidewall is modeled by using translational stiffness and damping. Since the tread band and belts also contribute to the vertical tire deformation at the contact area, the residual vertical stiffness is introduced. Eventually,

both the translational sidewall and the residual vertical stiffness contribute to the total vertical motion of the wheel rim. Similarly, the relative rotational motion of the rigid tread band to the rim can be modeled by using rotational sidewall stiffness and its damping constant. The longitudinal slip during braking and accelerating can be modeled by using longitudinal slip stiffness and damping.

For the out-of-plane motions, the relative translational motion of the elastic sidewall to the wheel plane is modeled by implementing lateral stiffness and damping. Similarly, the relative rotational motion of the elastic sidewall to the wheel plane is modeled by using rotational stiffness and damping. The lateral slip stiffness and damping constant are also included in the rigid ring model to simulate the lateral slip motions.

In addition, at the end of this chapter, durability tests are performed using the FEA tire model and the rigid ring tire model in which the predicted in-plane and out-of plane parameters are implemented. The FEA tire model runs at a speed of 19.3 km/h (12.0 mph) over two water drainage ditches to examine in-plane and out-of-plane dynamic tire responses at various tire loads. For the in-plane tire responses, the tire model runs over a ditch perpendicular to the tire traveling direction while the tire model runs over a ditch 45° to the tire traveling direction for the out-of-plane tire responses. Then, the vertical displacements of the tire spindle, the contact forces between the tire and the ditches, and the moments applied at tire spindle are inspected. The responses of the FEA tire model are compared with the responses of the rigid ring model. The comparison results show a successful attempt to capture the transient response of a tire rolling over the complex road profiles.

5.1 In-Plane Parameters Determination

As mentioned above, many in-plane characteristic parameters are required for the rigid ring tire model as seen in Figure 5-1. Normally, those parameters are measured from extensive laboratory tire tests. However, in this chapter, the laboratory tire tests are

virtually duplicated to predict the in-plane tire parameters by using the FEA truck tire model. The in-plane translational stiffness (k_{bx} , k_{bz}), translational damping constant (c_{bx} , c_{bz}), residual stiffness (k_{vr}), and residual damping constant (c_{vr}) are determined by the results of the tire load-deflection and free vertical vibration mode tests. The rotational stiffness ($k_{b\theta}$) and damping constant ($c_{b\theta}$) are determined by applying and releasing a tangential force on the rigid tread band of the FEA tire model. The longitudinal slip stiffness (k_k), and tread stiffness (k_{cx}) are calculated based on the results of a braking test on the smooth drum model. The effective rolling radius is calculated for the rolling radius of the rigid ring tire model.

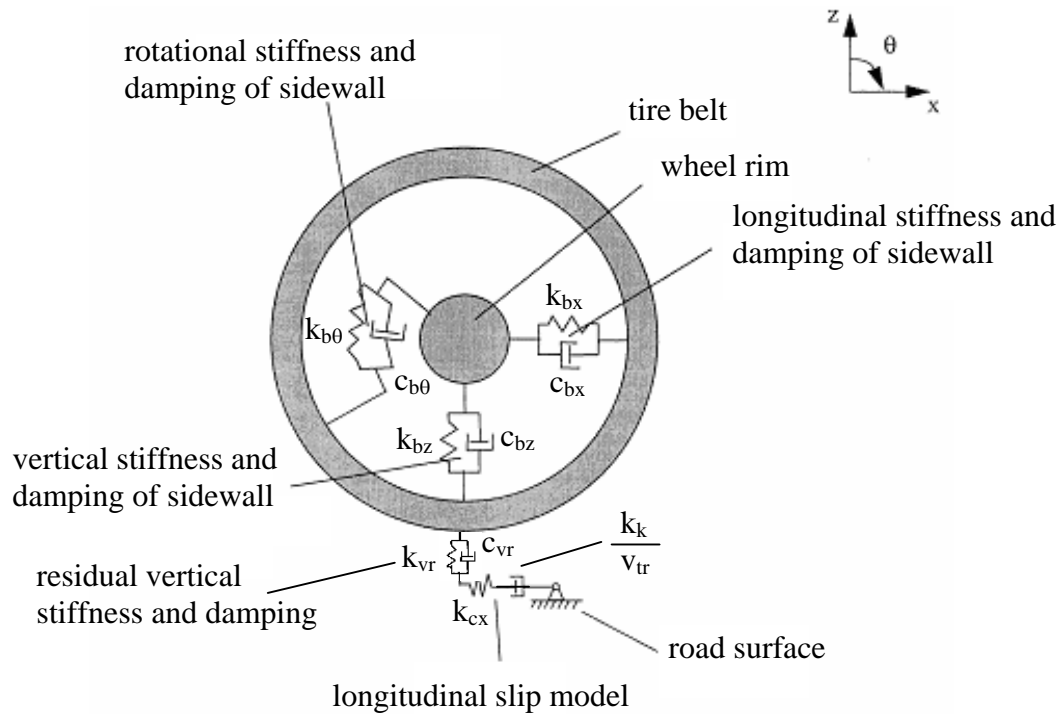


Figure 5-1 In-Plane Rigid Ring Tire Model (Zegelaar and Pacejka, 1997)

The FEA tire model is inflated at a rated pressure of 0.759 MPa (110 psi). In order to determine the in-plane parameters at various tire loads, the tire loads ranging from 13.3 kN (3,000 lb) to 40.0 kN (9,000 lb) are covered. In this chapter, the sample calculations presented are for the rated tire load of 26.7 kN (6,000 lb). The predicted parameters for all loads are summarized in Table 5-4.

5.1.1 Effective Rolling Radius

When an inflated tire is subjected to a vertical load of F_z at its center against road surface, the tire has a certain level of deflection, d , as shown in Figure 5-2. Then, when the tire rolls at an angular velocity, ω , and runs at a longitudinal velocity, v , an effective rolling radius, v/ω , is not just the original inflated tire radius before loading, R , nor $R \cdot \cos(\theta)$. The effective rolling radius is considered to be between R and $R \cdot \cos(\theta)$.

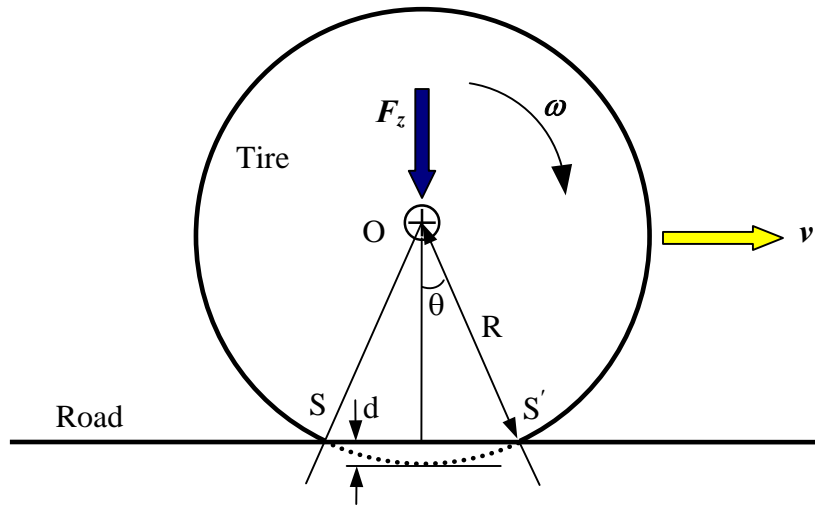


Figure 5-2 Tire Deflection during Rolling

Figure 5-2 shows that the tire has a straight contact length from S to S' on the road surface. However, even though the tire has a straight line of contact, the actual travel length of the tire during the 2θ of rotation is not the straight line distance but the arc length from S to S' . The arc length can be drawn as the same length of a straight dashed line from T to T' during the 2θ of rotation as shown in Figure 5-3.

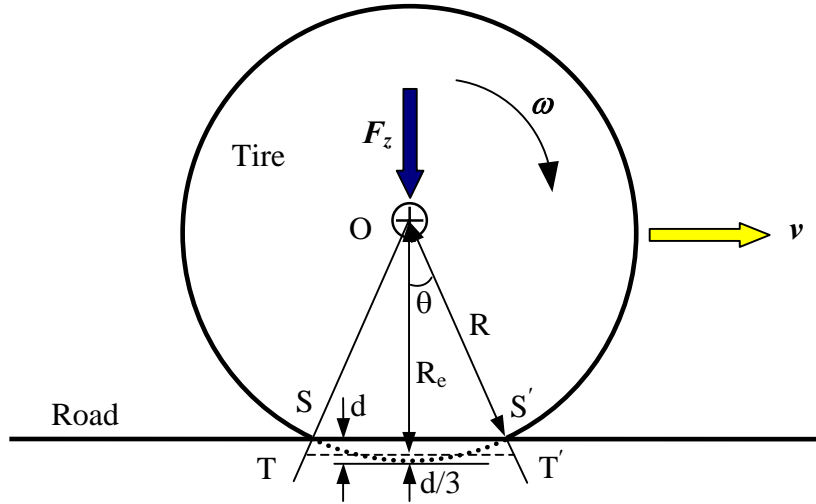


Figure 5-3 Effective Rolling Radius, R_e

In other words, the tire travels the straight distance from T to T' with the angular velocity of ω during the 2θ of rotation. Therefore, the effective rolling radius is the shortest distance from O to the line $T-T'$, which is shown as R_e in Figure 5-3 and calculated using Equation (5-1).

$$R_e = \frac{v}{\omega} = \frac{R \cdot \theta}{\tan(\theta)} \quad (5-1)$$

Geometrically, the rolling radius is also obtained approximately by using Equation (5-2).

$$R_e \approx R - \frac{d}{3} \quad (5-2)$$

Where, R : the radius of the inflated tire before loading,

d : the deflection due to loading.

Under ordinary circumstances, the effective rolling radius is no more than a few percent less than the unloaded radius. The calculated effective rolling radii at various tire loads are summarized in Table 5-4.

5.1.2 In-Plane Translational Stiffness of the Sidewall and Residual Vertical Stiffness at Contact Area

From the in-plane free vertical vibration mode test using the FEA tire and cleat-drum models, the first natural frequency, 73 Hz, is observed as shown in Figure 4-7. Based on this frequency, the in-plane translational stiffness of the sidewall and the residual stiffness at the contact area can be calculated by using Equation (5-3).

$$\omega_n = \sqrt{\frac{k_{bz} + k_{vr}}{m_b}} \quad (5-3)$$

Where, ω_n : natural frequency (rad/s),

k_{bz} : in-plane vertical stiffness of the sidewall,

k_{vr} : residual vertical stiffness at contact area,

m_b : mass of the tire belt.

The index ‘b’ in the symbols represents the association with the behavior of the sidewall. For the calculation, the whole tire mass without wheel rim is used for the tire belt mass in the rigid ring tire model. The vertical stiffness (k_{bz}) is regarded the same as the longitudinal stiffness (k_{bx}) due to the symmetry about the tire spindle.

When the tire model is driven over the cleat-drum with the wheel rim fixed vertically after loading, the vertical sidewall stiffness and the residual vertical stiffness contribute to the tire belt in parallel. Thus, the sum of those stiffnesses is included in Equation (5-3). However, in the tire load-deflection test, the tire spindle is vertically free during loading. In this case, the vertical displacement of the tire spindle is affected by both the sidewall and the residual stiffness in series. Therefore, Equation (5-4) is formed for the serial connection of those two stiffness, k_{bz} and k_{vr} .

$$\frac{1}{k_{bz}} + \frac{1}{k_{vr}} = \frac{1}{k_{tot}} \quad (5-4)$$

The k_{tot} in Equation (5-4) is the total stiffness that can be obtained from the vertical load-deflection curve (Figure 4-2). By using Equations (5-3) and (5-4), the in-plane translational stiffness (k_{bx}), and the residual vertical stiffness (k_{vr}), can be calculated for the vertical load 26.7 kN (6,000 lb). These are summarized in Table 5-1.

Table 5-1 In-plane Translational and Residual Vertical Stiffness of Sidewall
at Tire Load of 26.7 kN

In-Plane Tire Parameter	Symbol	Value	Unit
Total vertical stiffness	k_{tot}	992	kN/m
Longitudinal and vertical stiffness of the sidewall	k_{bx}, k_{bz}	9,620	kN/m
Residual vertical stiffness at contact area	k_{vr}	1,110	kN/m

5.1.3 In-Plane Longitudinal and Vertical Damping Constants of Sidewall and Residual Damping Constant at Contact Area

In the free vertical vibration mode test on the cleat-drum, the in-plane sidewall and the residual damping are also connected to the tire belts in parallel, similar to the stiffness connection. Thus, the sum of the two damping constants is used in Equation (5-5). In the equation, 5% of critical damping effect is used that is observed in most tire response.

$$c_{bz} + c_{vr} = 2 \cdot \zeta \cdot \sqrt{(k_{bz} + k_{vr}) \cdot m_b} \quad (5-5)$$

Where, c_{bz} : in-plane vertical damping constant of sidewall,

c_{vr} : residual damping constant in contact area,

ζ : damping ratio (= 0.05).

Meanwhile, the residual damping constant can be calculated by using Equation (5-6).

$$c_{vr} = 2 \cdot \zeta \cdot \sqrt{k_{vr} \cdot (m_a + m_b)} \quad (5-6)$$

Where, m_a : rim mass.

The in-plane vertical damping constant of the sidewall and residual damping constant at contact area are calculated at a tire load of 26.7 kN, which are summarized in Table 5-2. The in-plane vertical and longitudinal damping constants of the sidewall are considered to be the same due to the symmetrical nature of the tire about tire center.

Table 5-2 In-plane Longitudinal and Vertical Damping Constants of the Sidewall and Residual Damping Constant at Contact Area at Tire Load of 26.7 kN

In-Plane Tire Parameter	Symbol	Value	Unit
Longitudinal and vertical damping constant of sidewall	c_{bx}, c_{bz}	1.38	kN s/m
Residual damping constant at contact area	c_{vr}	0.96	kN s/m

5.1.4 In-Plane Rotational Stiffness and Damping Constant of the Sidewall

In order to virtually predict the in-plane sidewall rotational stiffness and damping constant, the rim is defined as a rigid body and constrained not to be translated and rotated. The tread base, tread, and belts are also defined as a rigid body but free in the tire rolling direction. Then, a tangential force of 25.0 kN (5,620 lb) is applied to the node on the rigid tread to rotate the rigid tread band about the tire spindle as shown in Figure 5-4.



Figure 5-4 Rotational Excitation on FEA Truck Tire

Due to the sidewall rotational stiffness ($k_{b\theta}$), the rigid tread band is rotated and stops at a certain angular displacement as seen in Figure 5-5. Then, the tangential load is quickly removed to excite the rotational vibration to predict a rotational damping constant ($c_{b\theta}$).

5.1.4.1 In-Plane Rotational Stiffness of the Sidewall

Figure 5-5 shows the tire angular displacement of 0.0214 radian about the tire spindle due to the applied tangential force, 25.0 kN, on the rigid tread band. By using this angular displacement and the applied moment, the in-plane rotational stiffness of the sidewall ($k_{b\theta}$) can be calculated as follows:

$$k_{b\theta} = \frac{\text{Moment}}{\text{Angular_Displacement}} = 577 \frac{kN \cdot m}{rad} \quad (5-7)$$

5.1.4.2 In-Plane Rotational Damping Constant of the Sidewall

When the applied tangential force is quickly removed, the rigid tread band undergoes rotational vibrations, and the magnitudes of the vibrations decrease with time due to the damping nature of the sidewall as seen in Figure 5-5.

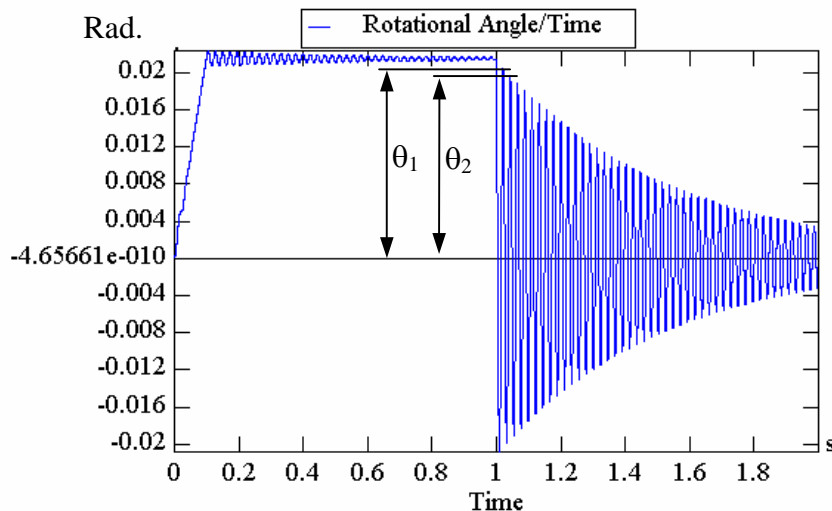


Figure 5-5 Angular Displacement of the Tread and Damping Response of the Sidewall

This logarithmic decrement of the angular displacements is adopted to calculate the in-plane rotational damping constant of the sidewall. From Figure 5-5, two neighboring peak points are selected to calculate the damping constant. These are:

Angular displacement $\theta_1 = 0.0205$ radian at time $t_1 = 1.023$ second,

Angular displacement $\theta_2 = 0.0196$ radian at time $t_2 = 1.045$ second.

Then, the logarithmic decrement (δ) becomes

$$\delta = \ln\left(\frac{\theta_1}{\theta_2}\right) = 0.045 \quad (5-8)$$

From Equation (5-9),

$$\delta = \frac{2\pi \cdot \zeta}{\sqrt{1 - \zeta^2}} \quad (5-9)$$

the dimensionless damping ratio (ζ) is found to be 0.00716. The damped period of vibration ($\tau_d = t_2 - t_1$) is 0.022 second. From Equation (5-10), the undamped natural frequency, ω_n , can be calculated as 286 rad/sec.

$$\tau_d = \frac{2\pi}{\omega_d} = \frac{2\pi}{\omega_n \sqrt{1 - \zeta^2}} \quad (5-10)$$

Where, ω_d : damped natural frequency (rad/sec),

ω_n : undamped natural frequency (rad/sec).

Therefore, the critical damping constant (c_c) can be obtained by using Equation (5-11) with the moment of inertia of the tire belt (I_{by} : 8.35 kg m²).

$$c_c = 2 I_{by} \omega_n \quad (5-11)$$

$$= 4.78 \text{ kN m s/rad}$$

Eventually, the in-plane rotational damping constant ($c_{b\theta}$) is calculated by using Equation (5-12).

$$c_{b\theta} = \zeta c_c = 0.034 \text{ kN m s/rad} \quad (5-12)$$

This in-plane rotational damping constant obtained from the FEA tire model will be used in the rigid ring tire model for the ditch running simulations. Meanwhile, the in-plane rotational stiffness can also be calculated from the undamped natural frequency and the moment of inertia of the tire belt.

Table 5-3 In-plane Rotational Stiffness and Damping Constants of Sidewall at Tire Load:
26.7 kN

In-Plane Tire Parameter	Symbol	Value	Unit
Rotational stiffness of sidewall	$k_{b\theta}$	577	kN m/rad
Rotational damping constant of the sidewall	$c_{b\theta}$	0.034	kN m s/rad

5.1.5 Longitudinal Tread Stiffness and Longitudinal Slip Stiffness

The FEA truck tire model is loaded at 26.7 kN on a 3.4 m-diameter smooth drum, and linear speed from 0 to 10 km/h is given at the tire spindle during a very short period of time as a simulation input. As a result, even though the tire model reaches a speed from 0 to 10 km/h in a very short time, the drum model cannot follow the exact tire speed due to its inertia. During this slip period, the longitudinal friction force is generated at the contact area, as seen in Figure 5-6.

In the case of a tire longitudinal slip test on a drum, the slip ratio during tire acceleration is calculated by using Equation (5-13).

$$\text{Slip Ratio} = \frac{\mathbf{v}_{tire} - \mathbf{v}_{drum}}{\mathbf{v}_{tire}} = 1 - \frac{R_{drum} \cdot \omega_{drum}}{\mathbf{v}_{tire}} \quad (5-13)$$

Where, v_{tire} : tire velocity (m/s),

v_{drum} : drum velocity (m/s),

R_{drum} : drum radius (m),

ω_{drum} : drum angular velocity (rad/sec).

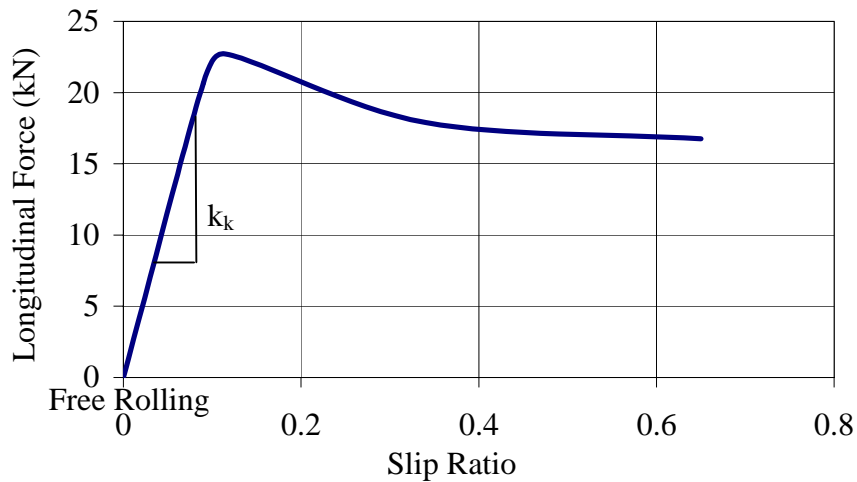


Figure 5-6 Longitudinal Force versus Slip Ratio

When the tire rolls without acceleration or braking effort, the tire and drum velocities are equal, and no slip occurs between the tire and drum, i.e., a free rolling state is observed. The slip ratio is zero according to Equation (5-13), thus, no longitudinal friction force is obtained. On the contrary, while the tire is rolling on a stationary drum, full slip between the tire and drum is observed. The slip ratio is one, and a longitudinal force is developed at the contact area according to the friction coefficient between the tire and drum.

It should be noted that a maximum longitudinal friction force is observed when the tire undergoes some amount of slip. Gillespie (1992) demonstrated that the longitudinal friction force reaches the maximum at a slip ratio ranging between 0.15 and 0.20 on a dry road surface. The developed maximum force is normally in the range of 70% to 90% of the vertical tire load. As the slip ratio increases further, the friction force decreases as the slip region in the rear of the contact area extends further forward.

5.1.5.1 Longitudinal Slip Stiffness

The slope at zero slip ratio is defined as longitudinal slip stiffness (k_k). The longitudinal slip stiffness for the tire load 26.7 kN (6,000 lb) is calculated as follows:

$$k_k = \left. \frac{\partial \text{Longitudinal Force}}{\partial \text{Slip Ratio}} \right|_{\text{Slip Ratio}=0} = 230 \frac{\text{kN}}{\text{slip unit}} \quad (5-14)$$

This longitudinal slip stiffness is used to calculate the damping constant in the slip model in Figure 5-1. The damping constant is obtained by dividing the longitudinal slip stiffness by the linear velocity of the tire center, v_{tr} .

5.1.5.2 Longitudinal Tread Stiffness

The longitudinal tread stiffness (k_{cx}) can be calculated by using Equation (5-15) at tire load 26.7 kN (6,000 lb) (Zegelaar and Pacejka, 1997).

$$k_{cx} = \frac{k_k}{a} = 2,210 \frac{\text{kN}}{\text{m}} \quad (5-15)$$

Where, a is a half the contact length (m).

In the case of full adhesion contact between a tire and road surface, the longitudinal relaxation length at the contact area equals half the contact length. Thus, using Equation (5-15) to calculate the longitudinal tread stiffness is only valid for slip ratios less than 0.1, where full adhesion contact exists. Equation (5-15) is no longer valid for slip ratios greater than 0.1.

Table 5-4 summarizes the in-plane parameters of the rigid ring tire model determined by the virtual FEA truck tire tests at various tire loading conditions.

Table 5-4 Predicted Rigid Ring Tire Model Parameters at Given Tire Load

C: Damping constant, K: Stiffness

In-Plane Parameter	Symbol	Unit	13.3 kN (3000 lb)	26.7 kN (6000 lb)	40.0 kN (9000 lb)
Half contact length	a	m	0.087	0.104	0.153
Translational C of Sidewall	c_{bx}, c_{bz}	kN s/m	1.49	1.38	1.02
Rotational C of Sidewall	$c_{b\theta}$	kN m s/rad	0.034	0.034	0.034
Translational K of Sidewall	k_{bx}, k_{bz}	kN/m	9,860	9,620	9,490
Longitudinal tread stiffness	k_{cx}	kN/m	1,780	2,210	1,990
Longitudinal slip stiffness	k_k	kN/slip unit	155	230	290
Residual damping	c_{vr}	kN s/m	0.852	0.958	1.020
Rim moment of inertia (X, Z)	I_{ax}, I_{az}	kg m ²	1.61	1.61	1.61
Rim moment of inertia (Y)	I_{ay}	kg m ²	2.80	2.80	2.80
Tire belt moment of inertia(X,Z)	I_{bx}, I_{bz}	kg m ²	4.59	4.59	4.59
Tire belt moment of inertia (Y)	I_{by}	kg m ²	8.35	8.35	8.35
Rotational K of Sidewall	$k_{b\theta}$	kN m/rad	577	577	577
Residual stiffness	k_{vr}	kN/m	875	1,110	1,240
Rim mass	m_a	kg	32	32	32
Tire belt mass	m_b	kg	51	51	51
Rolling radius	R_e	m	0.504	0.499	0.495

5.1.6 Comparison of In-plane Tire Responses between the FEA and Rigid Ring Tire Models

Both the FEA tire and the rigid ring tire models are run over a water drainage ditch at a constant speed of 19.3 km/h (12.0 mph) to predict dynamic tire responses. The applied tire loads are 13.3 kN (3,000 lb), 26.7 kN (6,000 lb), and 40.0 kN (9,000 lb). The predicted dynamic responses from the FEA tire model, such as the vertical displacement of the tire spindle, longitudinal contact force, and vertical contact force, are compared with those from the rigid ring tire model as seen in Figures 5-9 to 5-17. The abscissa in the figures represents the tire spindle position from the ditch entry to the exit. When the tire spindle is exactly above the ditch entry edge, the tire spindle is at zero ditch length as seen in Figure 5-7.

5.1.6.1 90° Water Drainage Ditch Profile

The ditch profile used for in-plane dynamic tire responses is a 690 mm-long and 120 mm-deep water drainage ditch as seen in Figure 5-7. The radius of curvature is 0.78 m. The digitized ditch profile is shown in Appendix B. The ditch lies perpendicular to the tire traveling direction as seen in Figure 5-8. Thus, no out-of-plane tire responses are expected. The road including the ditch is modeled as an undeformable rigid material.

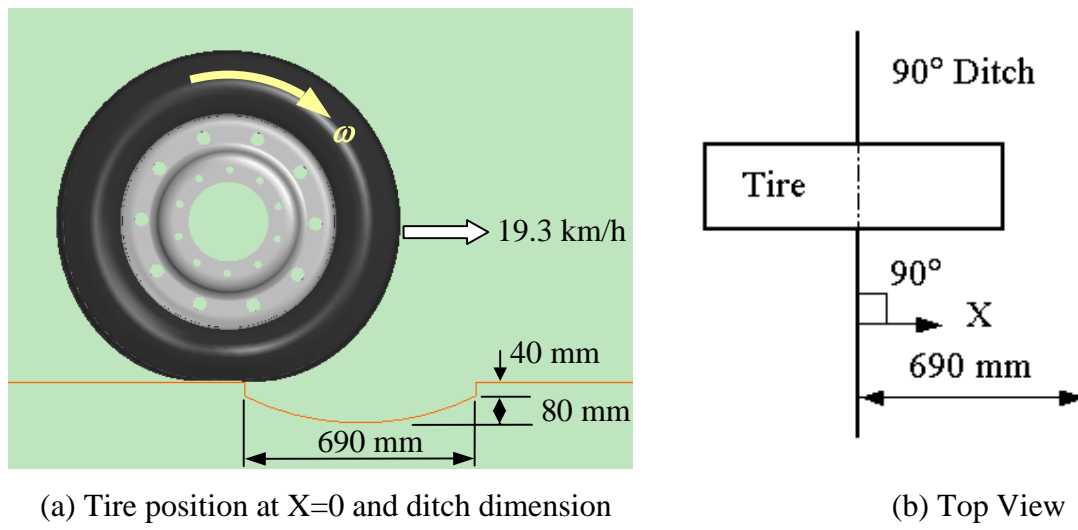


Figure 5-7 90° Water Drainage Ditch Profile

5.1.6.2 Comparison of the Predicted Vertical Displacements

The predicted vertical displacements of the tire spindle during the ditch runs of the FEA and the rigid ring tire models are plotted at various tire loads as shown in Figures 5-8 to 5-10. The vertical displacements at the ditch entrance show the different displacements at the applied tire loads. As the tire models run over the ditch at a constant speed of 19.3 km/h (12 mph), the tire spindles drop down and reach the maximum displacement around a ditch length of 35 cm. In the case of the tire load of 13.3 kN, it is observed that the tire models lose contact with the road surface when the tire exits the ditch. Both models show reasonable vertical displacement responses and correlate well each other.

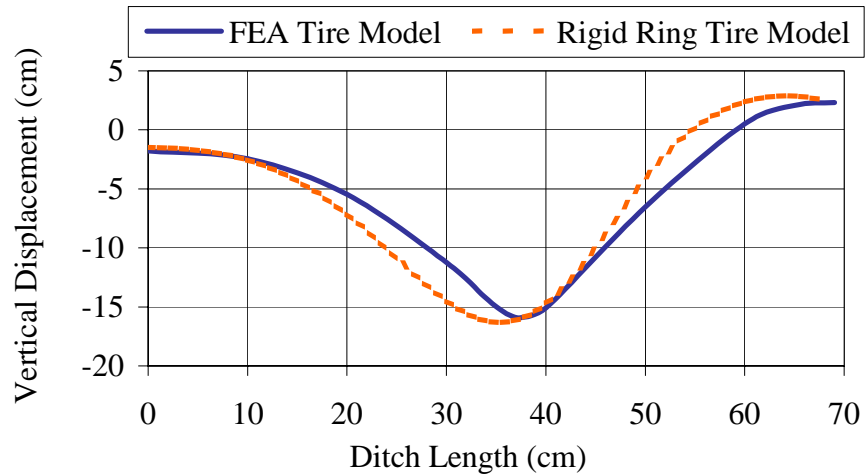


Figure 5-8 Tire Spindle Vertical Displacements at Tire Load of 13.3 kN

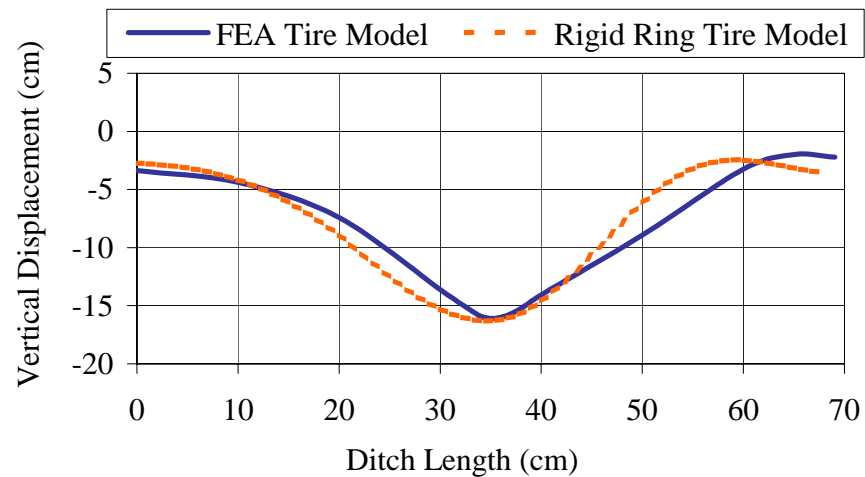


Figure 5-9 Tire Spindle Vertical Displacements at Tire Load of 26.7 kN

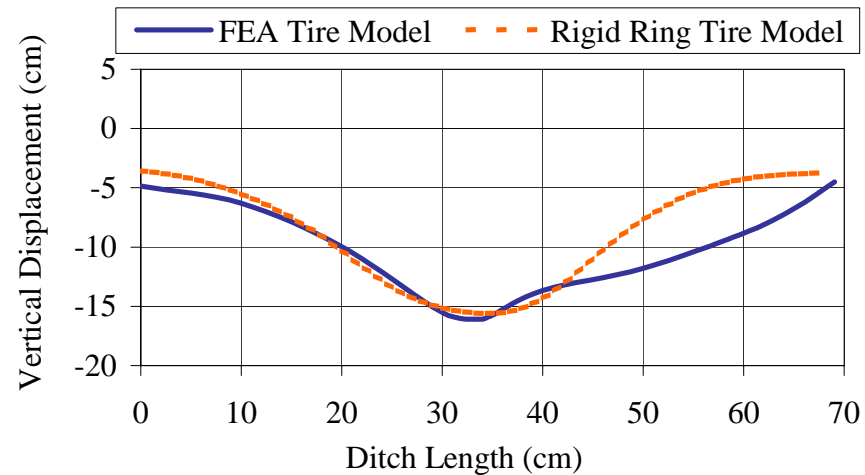


Figure 5-10 Tire Spindle Vertical Displacements at Tire Load of 40.0 kN

5.1.6.3 Comparison of the Predicted Longitudinal Contact Forces

The predicted longitudinal contact forces acting on the FEA and rigid ring tire models during the ditch runs are plotted at various tire loads as seen in Figures 5-11 to 5-13. When the tire models run on a flat road before entering the ditch, only the rolling resistance forces are exerted on the tire models against the tire movement direction. However, when the tire models roll over the ditch profile, longitudinal impact forces are added to the longitudinal contact forces.

As the tire models continue to roll and enter the ditch at a constant speed of 19.3 km/h (12.0 mph), the longitudinal contact forces are highly dependent on the tire reaction forces. While the tire models enter the ditch, the resultant reaction force changes the direction from vertical toward the tire center. Thus, positively increasing longitudinal contact forces are observed during ditch entry. On the other hand, when the tire models exit the ditch, the reaction forces are applied to the tire models against the tire rolling direction due to the impact with the right ditch edge. Thus, negatively increasing longitudinal contact forces are observed while the tire models exit the ditch.

As seen in Figures 5-11 to 5-13, as the vertical tire loads on the tire models increase, it is observed that the positive longitudinal peak forces during ditch entry tend to increase and occur earlier. The higher longitudinal forces are due to the increased tire loads, and the peak forces are observed earlier due to the larger tire contact area at the higher vertical tire loads. This observation is more noticeable in the FEA tire model than in the rigid ring tire model because the FEA tire model is deformable.

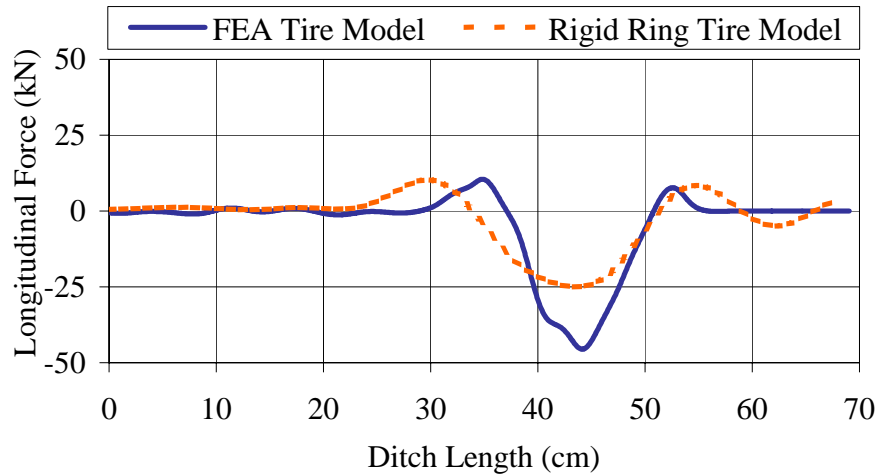


Figure 5-11 Longitudinal Contact Force at Tire Load of 13.3 kN

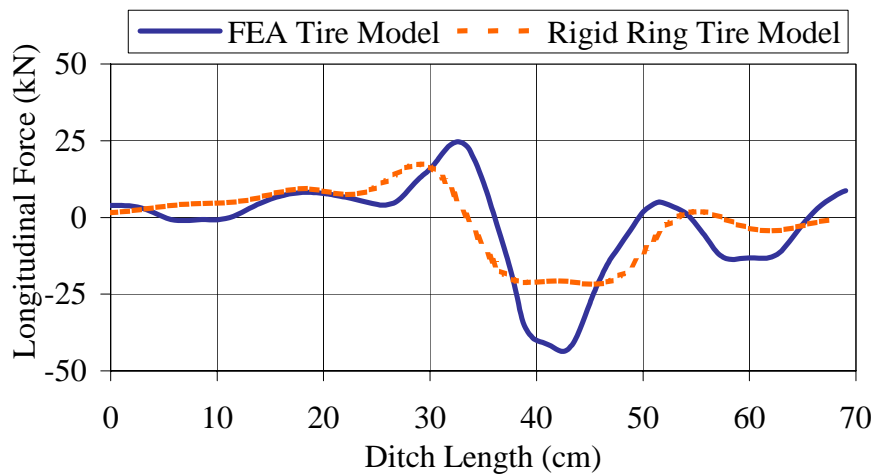


Figure 5-12 Longitudinal Contact Force at Tire Load of 26.7 kN

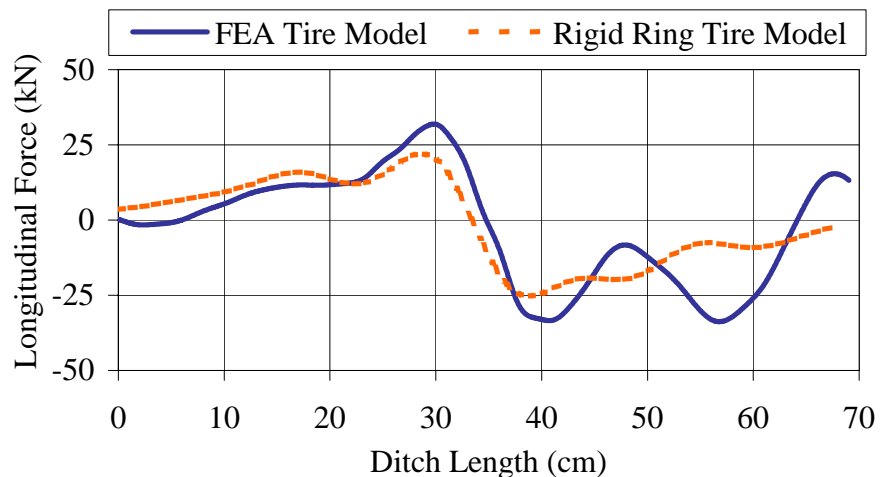


Figure 5-13 Longitudinal Contact Force at Tire Load of 40.0 kN

5.1.6.4 Comparison of the Predicted Vertical Contact Forces

The vertical contact forces acting on the FEA and rigid ring tire models during the ditch run are plotted at various tire loads in Figures 5-14 to 5-16. In the figures, the vertical forces at the ditch entrance show the applied vertical tire loads. As the tire models enter the ditch, the vertical forces decrease somewhat until the tire models touch the round bottom of the ditch. As soon as the tire models touch the ditch bottom, the maximum vertical contact forces are observed. As the vertical tire loads increase, the vertical force peaks tend to occur earlier since the larger tire contact area enable the tire model to touch the ditch bottom earlier.

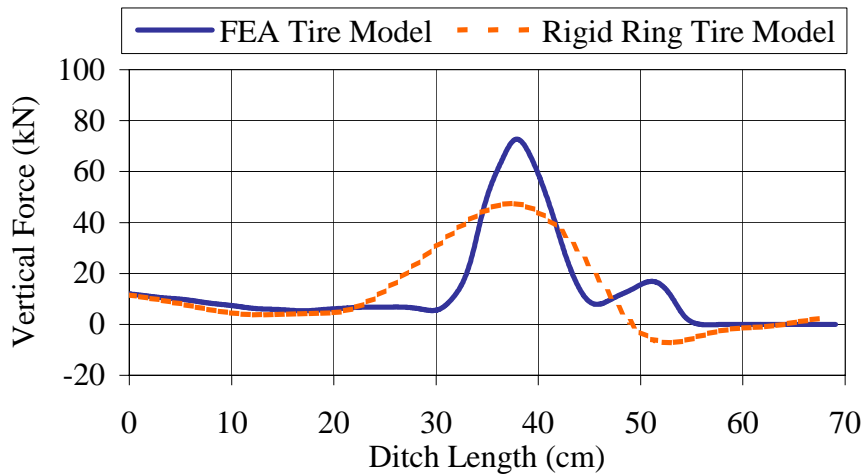


Figure 5-14 Vertical Contact Force at Tire Load of 13.3 kN

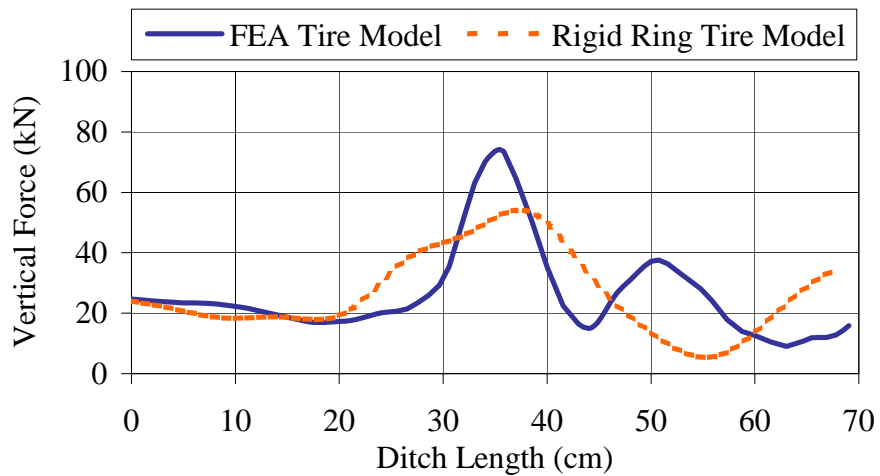


Figure 5-15 Vertical Contact Force at Tire Load of 26.7 kN

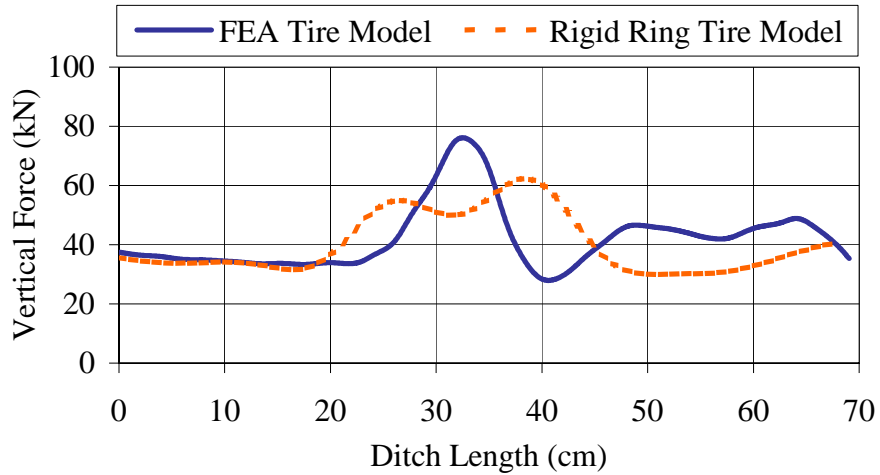


Figure 5-16 Vertical Contact Force at Tire Load of 40.0 kN

The discrepancies in the longitudinal and vertical contact forces between the two tire models are mainly due to the different tire-road contact conditions. The FEA tire model has a contact area similar to an actual tire contact area, and the contact length is variable during the ditch run due to varying vertical contact forces and contacting road geometry. On the other hand, the rigid ring tire model has a single point contact with the road surface, and a single contact length is used as an input parameter in the contact force calculations. Thus, the rigid ring tire model cannot handle multiple contact points observed in the FEA tire model runs, nor does the model handle variable contact lengths during the ditch run.

Compared with the FEA tire model, the rigid ring tire model seems to have more limitations at higher tire loads due to the failure in complex multiple contacts with the ditch surfaces. Because the multiple contact points are more likely to occur at higher tire loads, the advantage of the FEA tire is greater at higher tire loads. The out-of-plane tire responses such as lateral contact force, overturning moment, rolling resistance moment, and vertical moment during 90° ditch runs are negligible because no lateral excitation is provided on the tire models.

5.2 Out-of-Plane Parameters Determination

In this section, the out-of-plane parameters of the rigid ring tire model are virtually predicted by applying and releasing appropriate tire loadings on the FEA truck tire model similar to Section 5.1. The out-of-plane parameters are as follows: the lateral stiffness (k_{by}) and its damping constant (c_{by}) of the sidewall, rotational stiffness ($k_{b\gamma}$) and its damping constant ($c_{b\gamma}$) of the sidewall, lateral slip stiffness (k_l) and its damping constant (c_l) of the tread at contact area, lateral relaxation length (σ), cornering stiffness (k_F), and self-aligning stiffness (k_M). A schematic drawing of the out-of-plane tire parameters are shown in Figure 5-17. The out-of-plane parameters are calculated based on the FEA truck tire simulation results at various vertical tire loads of 13.3 kN (3,000 lb), 26.7 kN (6,000 lb), and 40.0 kN (9,000 lb).

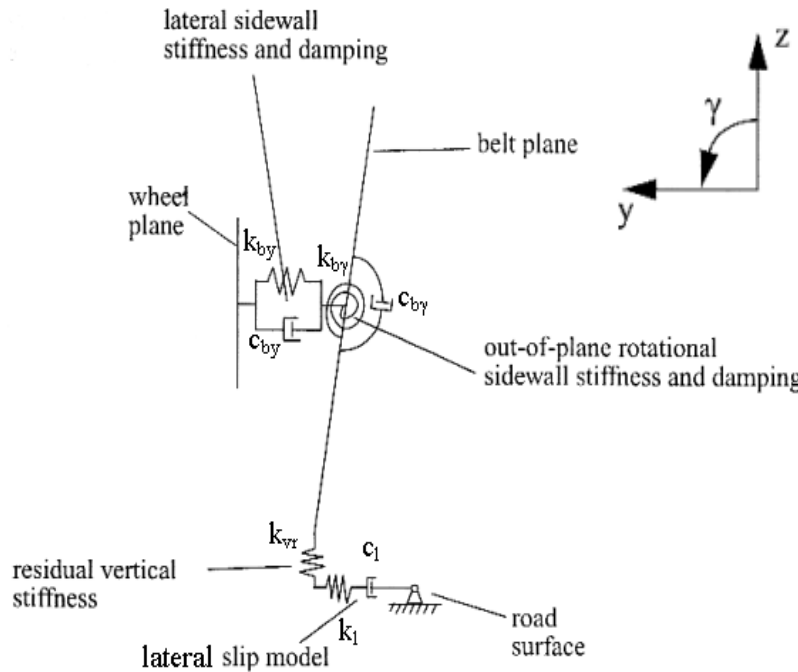


Figure 5-17 Out-of-Plane Parameters for the Rigid Ring Tire Model (Volvo 3P, 2004)

5.2.1 Out-of-Plane Translational Stiffness and Damping Constant of the Sidewall

In order to virtually predict the out-of-plane sidewall translational stiffness (k_{by}) and its damping constant (c_{by}), the rim is set to an undeformable rigid body and constrained not to be translated and rotated. The treadbase, tread, and belts of the tire model are also set to an undeformable rigid body, but free only in lateral direction (Y-axis). Only the sidewall is elastically deformable, which enables the prediction of the sidewall stiffness and damping constant. Then, the FEA tire model is inflated at a rated pressure of 0.759 MPa (110 psi). A lateral force of 15.0 kN (3,370 lb) is applied on the selected two nodes of the rigid tread to excite the elastic sidewall laterally as shown in Figure 5-18. A total lateral force of 30.0 kN (6,740 lb) is applied to the sidewall. Due to the translational stiffness of the sidewall, the rigid tread band is shifted left and stops at a certain lateral displacement. Then, the two lateral loads are quickly removed to observe the lateral damping effect of the sidewall.

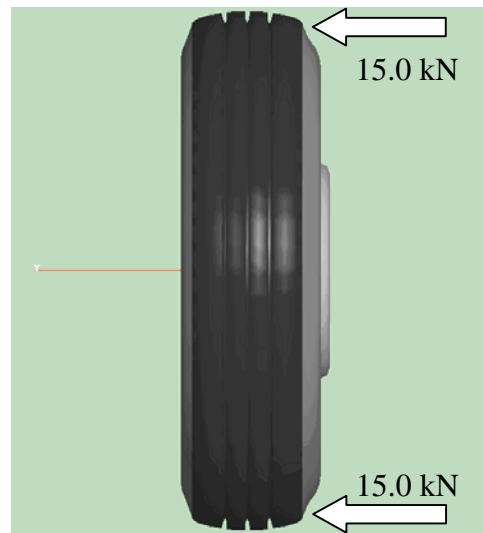


Figure 5-18 Out-of-Plane Translational Excitation on Sidewall

As a result, the steady state lateral displacement of the rigid tread band and transient state of damping response of the sidewall are obtained as shown in Figure 5-19. The lateral displacement of 15.3 mm is observed due to the applied lateral force of 30.0 kN. By using

this applied force and the displacement, the out-of-plane translational stiffness (k_{by}) can be calculated as follow:

$$k_{by} = \frac{\text{Lateral Force}}{\text{Lateral Displacement}} = 1,960 \frac{kN}{m} \quad (5-16)$$

When the applied lateral forces are quickly removed, the rigid tread band undergoes out-of-plane translational vibrations and response amplitude decays exponentially as seen in Figure 5-19. The logarithmic decrement of the lateral displacements is adopted to calculate the out-of-plane translational damping constant of the sidewall.

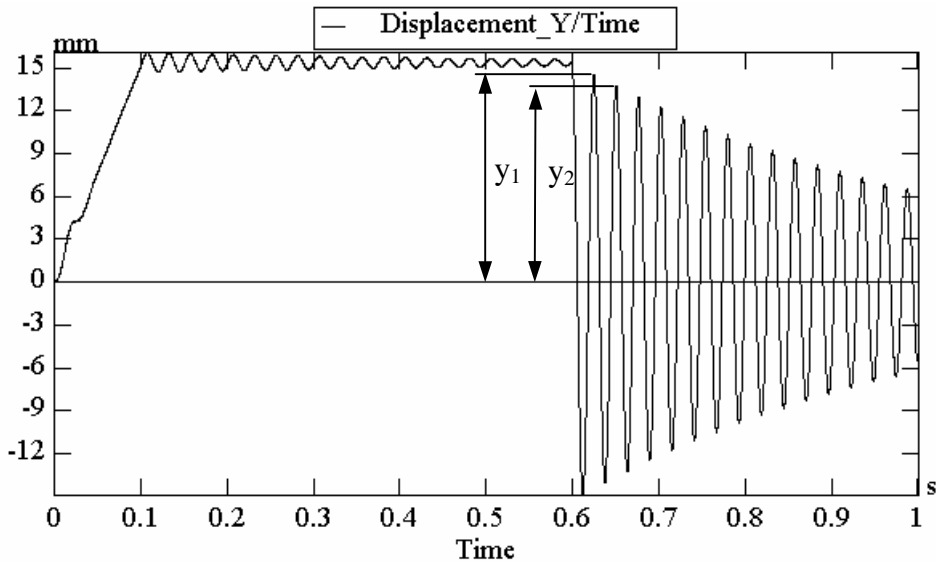


Figure 5-19 Lateral Displacement and Damping Response of the Sidewall

From Figure 5-19, two neighboring peak points are selected to calculate damping constant such as:

Lateral displacement $y_1=13.68$ mm at time $t_1=0.652$ second,

Lateral displacement $y_2=12.92$ mm at time $t_2=0.678$ second.

Then, the out-of-plane translational damping constant (c_{by}) of the sidewall is calculated by using similar equations as used in Section 5.1.4.2. In the calculations, the critical

damping constant (c_c) is obtained by multiplying the belt mass with the undamped natural frequency as follow:

$$c_c = 2 m_b \omega_n = 14.0 \text{ kN s/m} \quad (5-17)$$

$$c_{by} = \zeta c_c = 0.129 \text{ kN s/m} \quad (5-18)$$

Table 5-5 shows the parameters used for the calculation of the out-of-plane translational damping constant (c_{by}).

Table 5-5 Parameters Used for the Out-of-Plane Translational Damping Constant

Parameter	Symbol	Value	Unit
Logarithmic decrement	δ	0.057	-
Dimensionless damping ratio	ζ	0.0092	-
Damped period of vibration	τ_d	0.026	second
Undamped natural frequency	ω_n	244	rad/sec

5.2.2 Out-of-Plane Rotational Stiffness and Damping Constant of the Sidewall

In order to virtually predict the out-of-plane rotational stiffness (k_{by}) and damping constant (c_{by}) of the sidewall, the rim of the tire model is set to a rigid body and constrained not to be translated and rotated. The tread base and tread parts are also set to a rigid body but free only in out-of-plane rotational direction (X-axis). The tire model is inflated at the rated pressure of 0.759 MPa (110 psi). Then, a lateral force of 15.0 kN is applied to two nodes on the rigid tread in opposite direction to rotate the rigid tread band about the longitudinal axis as shown in Figure 5-20.

Then, the applied lateral loads are quickly removed to observe the damping response of the sidewall. As a result, the rigid tread band is rotated and stops at a certain angular displacement due to the out-of-plane rotational stiffness of the sidewall as shown in Figure 5-20. When the applied lateral forces are quickly removed, the rigid tread band undergoes out-of-plane rotational vibration. Figure 5-21 shows the steady state angular

displacement of the rigid tread band and the transient state of the damping response of the sidewall.



Figure 5-20 Out-of-Plane Rotational Excitation on Sidewall

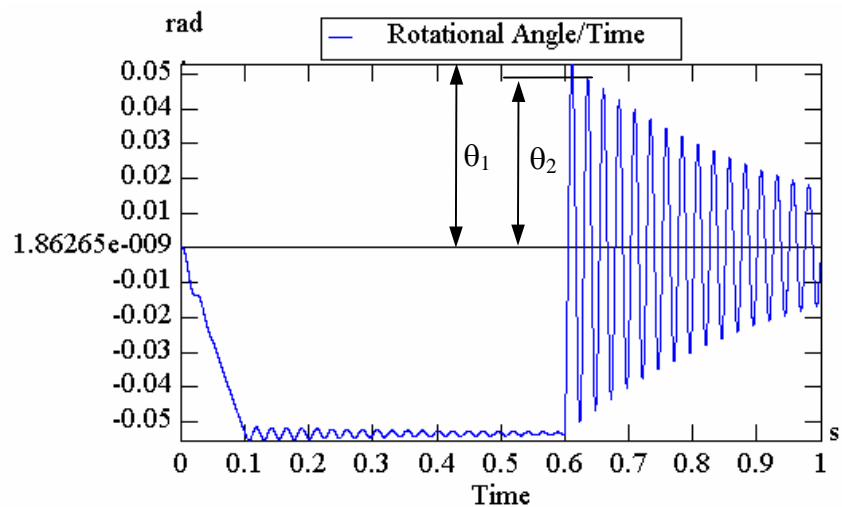


Figure 5-21 Out-of-Plane Rotational Displacement and Damping Response of the Sidewall

Figure 5-21 shows the angular displacement of 0.0536 radian due to the applied moment on the tire model. By using this applied moment and the displacement, the out-of-plane rotational stiffness (k_{by}) can be calculated as follows:

$$k_{by} = \frac{\text{Moment}}{\text{Angular_Displacement}} = 277 \frac{kN \cdot m}{rad} \quad (5-19)$$

In order to calculate the out-of-plane rotational damping constant of the sidewall, the logarithmic decrement of the angular displacements is adopted. From Figure 5-21, two neighboring peak points are selected to calculate the damping constant such as:

Angular displacement $\theta_1=0.0525$ radian at time $t_1=0.612$ second,

Angular displacement $\theta_2=0.0489$ radian at time $t_2=0.637$ second.

The out-of-plane rotational damping constant (c_{by}) is calculated by using similar equations used in Section 5.1.4.2.

$$c_{by} = \zeta c_c = 0.027 \text{ kN m s/rad} \quad (5-20)$$

Table 5-6 shows the parameters values used for the calculation of the out-of-plane rotational damping constant (c_{by}).

Table 5-6 Parameters Used for the Out-of-plane Rotational Damping Constant

Parameter	Symbol	Value	Unit
Logarithmic decrement	δ	0.071	-
Dimensionless damping ratio	ζ	0.0113	-
Damped period of vibration	τ_d	0.025	second
Undamped natural frequency	ω_n	257	rad/sec
Moment of inertia of tire belt	I_{bx}	4.59	kg m^2
Critical damping constant	c_c	2.36	kN m s/rad

5.2.3 Lateral Free Vibration Tests

The lateral slip stiffness (k_l) and damping constant (c_l) of the tire at the contact area can be predicted by the lateral free vibration test at various tire loads. In this test, a lateral load of 5.0 kN is applied as shown in Figure 5-22 and suddenly released. The applied vertical tire loads are 13.3 kN (3,000 lb), 26.7 kN (6,000 lb), and 40.0 kN (9,000 lb). The steady state lateral displacement and transient state of damping response of the tire are observed in Figure 5-23.



Figure 5-22 Lateral Excitation at Tire Spindle

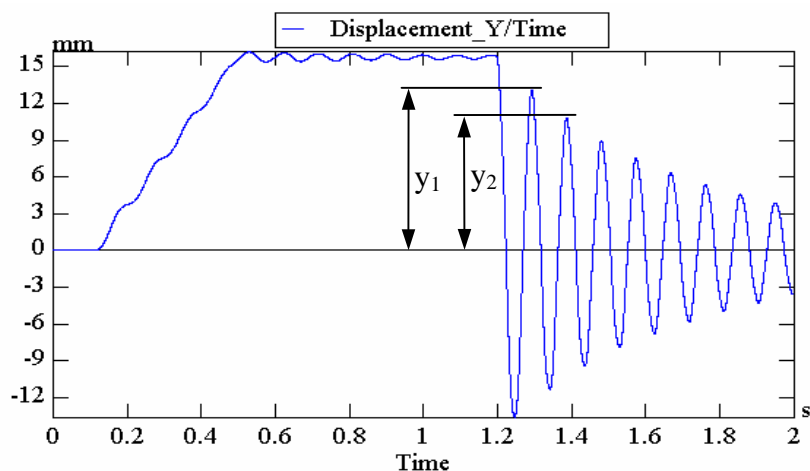


Figure 5-23 Lateral Free Vibration Test Result at Vertical Tire Load 26.7 kN

Figure 5-23 shows the lateral displacement of 15.7 mm due to the applied lateral force of 5.0 kN on the tire center. By using this applied force and the displacement, the out-of-plane slip stiffness (k_l) of the tire at contact area can be calculated as follows:

$$k_l = \frac{\text{Lateral Force}}{\text{Lateral Displacement}} = 318 \frac{\text{kN}}{\text{m}} \quad (5-21)$$

When the applied lateral forces are quickly removed, the tire undergoes out-of-plane translational vibration as seen in Figure 5-23. The logarithmic decrement of the angular displacements is adopted to calculate the out-of-plane slip stiffness and damping at the contact area. From Figure 5-23, two neighboring peak points are selected to calculate damping constant such as:

Lateral displacement $y_1=13.06$ mm at time $t_1=1.294$ second,

Lateral displacement $y_2=10.74$ mm at time $t_2=1.388$ second.

Then, the out-of-plane slip damping constant at the contact area (c_l) is calculated by using similar equations used in Section 5.1.4.2.

$$c_l = \zeta c_c = 0.344 \text{ kN s/m} \quad (5-22)$$

Table 5-7 shows the parameters used for the calculation of the out-of-plane slip damping constant at the contact area.

Table 5-7 Parameters Used for the Out-of-plane Slip Damping Constant

Parameter	Symbol	Value	Unit
Logarithmic decrement	δ	0.196	-
Dimensionless damping ratio	ζ	0.031	-
Damped period of vibration	τ_d	0.094	second
Undamped natural frequency	ω_n	66.9	rad/sec
Mass of wheel	m_{wheel}	83	kg
Critical damping constant	c_c	11.1	kN s/m

5.2.4 Cornering Stiffness

Cornering stiffness (k_f) is defined as the derivative of the cornering force (F_y) with respect to slip angle (α) evaluated at zero slip angle:

$$k_f = \left. \frac{\partial F_y}{\partial \alpha} \right|_{\alpha=0} \quad (5-23)$$

Thus, the cornering stiffness is predicted as the slope at zero slip angle as shown in Figure 5-24.

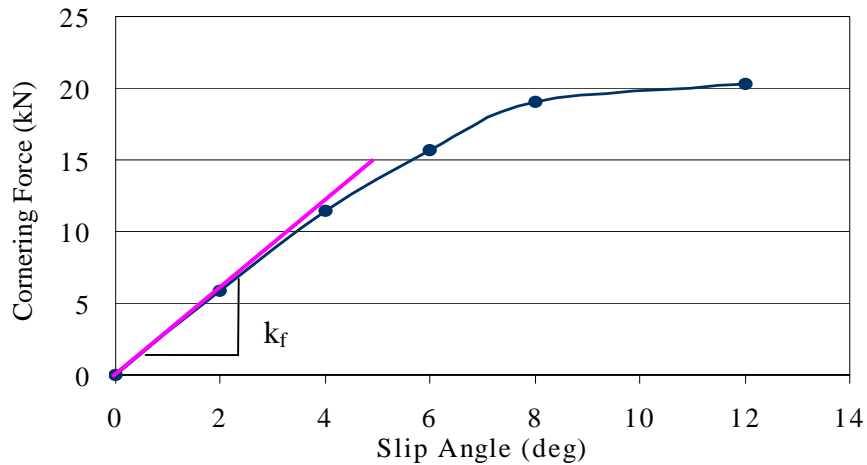


Figure 5-24 Cornering Stiffness Prediction at Vertical Load of 26.7 kN

A cornering stiffness of 172 kN/rad is calculated at tire load of 26.7 kN from Figure 5-24, and the cornering stiffness at other tire loads are listed in Table 5-8.

5.2.5. Self-Aligning Stiffness

Self-aligning stiffness (k_M) is defined as the derivative of the self-aligning moment (M_y) with respect to slip angle (α) evaluated at zero slip angle:

$$k_M = \left. \frac{\partial M_y}{\partial \alpha} \right|_{\alpha=0} \quad (5-24)$$

Therefore, the self-aligning stiffness is predicted as the slope at zero slip angle as shown in Figure 5-25. A self-aligning stiffness of 10.0 kN m/rad is calculated at tire load of 26.7 kN from Figure 5-25, and the self-aligning moments at other tire loads are listed in Table 5-8.

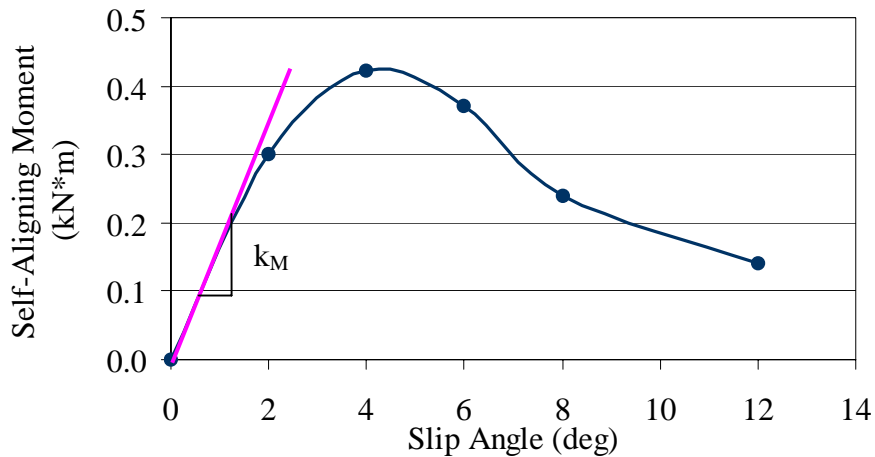


Figure 5-25 Self-Aligning Stiffness Prediction at Vertical Load of 26.7 kN

5.2.6 Relaxation Length

The relaxation length (σ) is described in Section 4.2.3.1 in detail and can be calculated by Equation (5-25).

$$\sigma = \frac{k_f}{k_l} \quad (5-25)$$

Where, k_f : the cornering stiffness and

k_l : the lateral slip stiffness of the tire.

The cornering stiffness has been already determined in Section 5.2.4. The lateral slip stiffness determined in Section 5.2.3 is used for the lateral stiffness to calculate the

relaxation length. The relaxation length is dependent on the applied tire load and tire size. However, it is not significantly influenced by other operation conditions, such as speed. Thus, the relaxation length is predicted at low tire speed of 5 km/h.

Eventually, all the out-of-plane characteristic parameters of the rigid ring tire model have been predicted by performing appropriate virtual FEA tire tests. The parameters are summarized in Table 5-8 at various vertical tire loads.

Table 5-8 Out-of-Plane Characteristic Parameters of the Rigid Ring Tire Model

C: Damping constant, K: Stiffness

Out-of-Plane parameter	Symbol	Unit	13.3 kN (3,000 lb)	26.7 kN (6,000 lb)	40.0 kN (9,000 lb)
Translational K of sidewall	k_{by}	kN/m	1,960	1,960	1,960
Translational C of sidewall	c_{by}	kNs/m	0.128	0.128	0.128
Rotational K of sidewall	$k_{b\gamma}$	kNm/rad	277	277	277
Rotational C of sidewall	$c_{b\gamma}$	kNms/rad	0.020	0.020	0.020
Lateral slip stiffness	k_l	kN/m	361	371	346
Lateral slip damping	c_l	kN s/m	0.346	0.344	0.374
Cornering stiffness	k_f	kN/rad	131	172	168
Self-aligning stiffness	k_M	kN m/rad	3.2	10.0	18.9
Relaxation length	σ	m	0.36	0.46	0.49

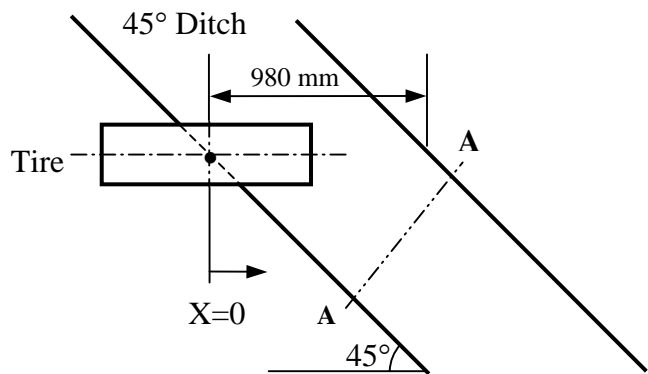
5.2.7 Comparison of Out-of-Plane Tire Responses between the FEA and Rigid Ring Tire Models

Both the FEA and the rigid ring tire models run over a 45° ditch to the tire running direction to predict in-plane and out-of-plane dynamic tire responses. The tire models run at a constant speed of 19.3 km/h (12.0 mph). The applied tire loads are 13.3 kN (3,000 lb), 26.7 kN (6,000 lb), and 40.0 kN (9,000 lb). The predicted dynamic responses from the tire models are as follows: the vertical displacement of the tire spindle, dynamic

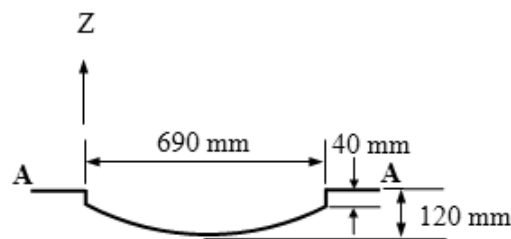
longitudinal, lateral, and vertical contact forces, vertical moment, and overturning moment applied at tire spindle during the ditch runs. The predicted FEA tire responses are compared with those obtained from the rigid ring tire model simulations. Figures 5-27 to 5-44 show the comparisons of the predicted dynamic tire responses from both the FEA and rigid ring tire models runs as a function of the ditch length. The ditch length is measured from the ditch entrance to the exit, which is illustrated in Figure 5-26 (a).

5.2.7.1 45° Water Drainage Ditch Profile

The road profile for an out-of-plane durability test is 45° and 12-cm deep water drainage ditch as seen in Figure 5-26. The radius of curvature is 0.78 m. This road profile generates lateral force, vertical moment, and overturning moment at the tire spindle due to the asymmetric road geometry about the longitudinal axis during tire entry and exit of the ditch. The ditch model is defined as a rigid body material and the digitized profile is included in Appendix B.



(a) Tire position at $X=0$ and ditch dimension



(b) Cross-sectional shape and dimension along a line A-A

Figure 5-26 45° Water Drainage Ditch Profile

5.2.7.2 Comparison of the Predicted Vertical Displacements

In Figures 5-27 to 5-29, the predicted vertical displacements of the tire spindles during the 45° ditch runs of the FEA and the rigid ring tire models are plotted for various vertical tire loads. The vertical displacements at the ditch length of zero show the vertical deflections of the tire models due to the applied vertical tire loads.

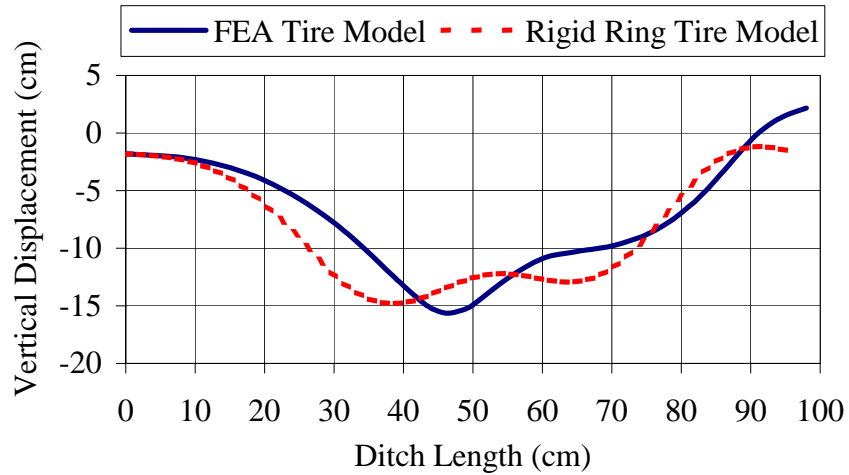


Figure 5-27 Tire Spindle Vertical Displacements at Tire Load of 13.3 kN

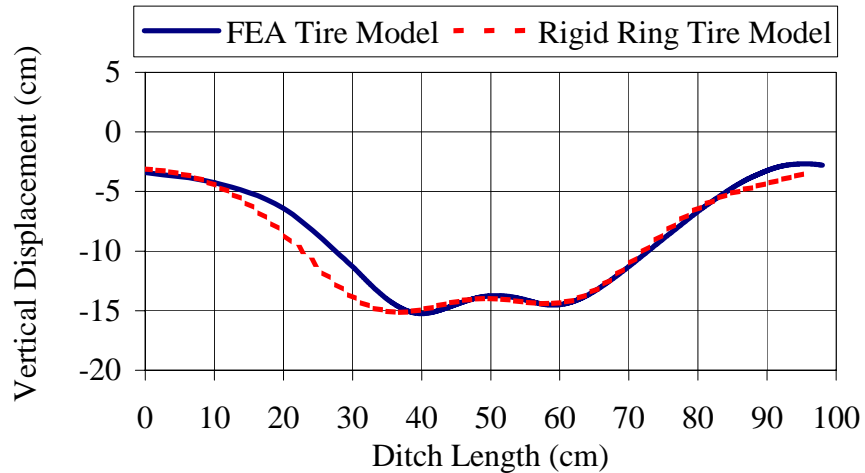


Figure 5-28 Tire Spindle Vertical Displacements at Tire Load of 26.7 kN

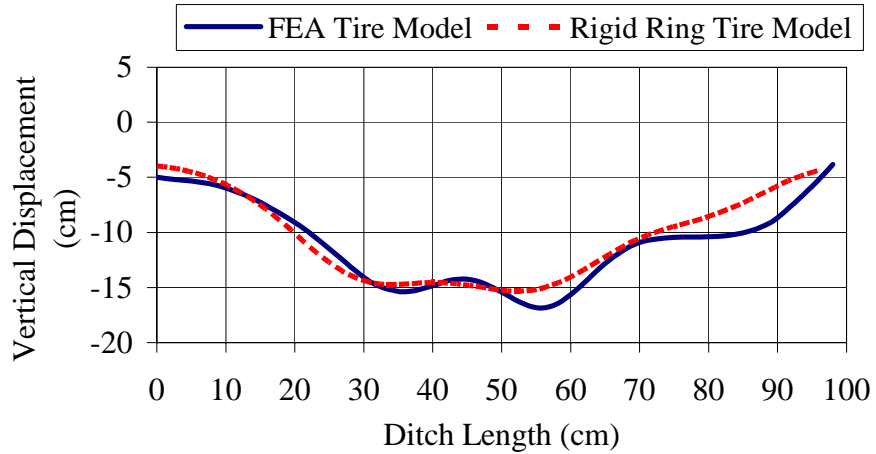


Figure 5-29 Tire Spindle Vertical Displacements at Tire Load of 40.0 kN

As the vertical tire load increases, the locations of the maximum deflection occur earlier for both the FEA and rigid ring tire models due to larger contact area. It is also observed that the vertical displacement discrepancies between the two models become smaller as the vertical loads increase. The vertical displacement predictions from the FEA and rigid ring tire model runs are in good agreement.

5.2.7.3 Comparison of the Predicted Longitudinal Contact Forces

The predicted longitudinal contact forces acting on the FEA and rigid ring tire models at the contact area during the ditch runs are plotted in Figures 5-30 to 5-32 for various tire loads. The longitudinal contact forces running over the 45° ditch show positive forces due to the left ditch edge during ditch entry and, later, negative forces due to the right edge during ditch exit similar to the trend of the longitudinal contact forces during tire running over the 90° ditch of Section 5.1.6.4. The observed forces are relatively lower than those of Section 5.1.6.4 because the tire models enter a 45° ditch. In other words, since the 45° ditch lies in the tire running direction, the treads at the contact area enter and exit the ditch gradually. Thus, reduced vertical acceleration of the tire spindle is observed. As a result, lower contact forces are observed in the tire models.

It can be seen from these figures that the positive and negative peak values from the rigid ring tire model runs are lower than those from the FEA tire model runs. The longitudinal

contact forces are not only due to impact with the ditch surface and edges but also due to adhesion friction force at the contact area. In addition, the magnitude of the longitudinal impact force is highly dependent on the deformable elements of the FEA model. Such flexibility is absent in the rigid ring tire model, which leads to lower longitudinal peak forces at the points of impact.

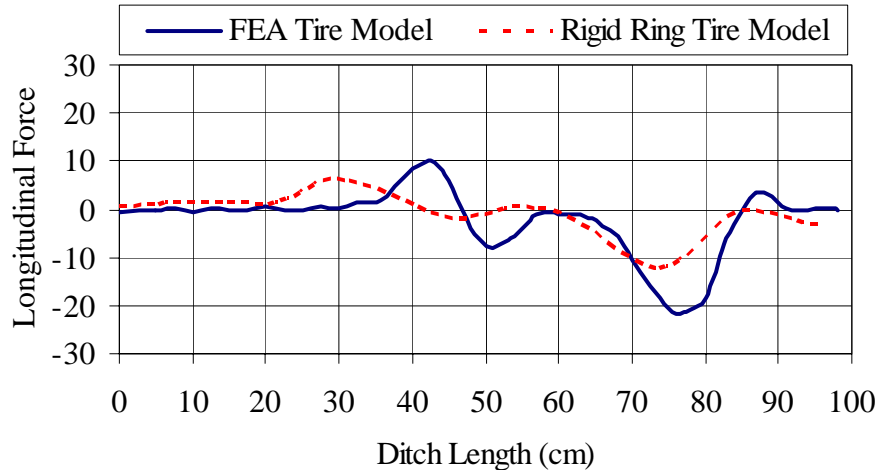


Figure 5-30 Longitudinal Contact Forces at Tire Load of 13.3 kN

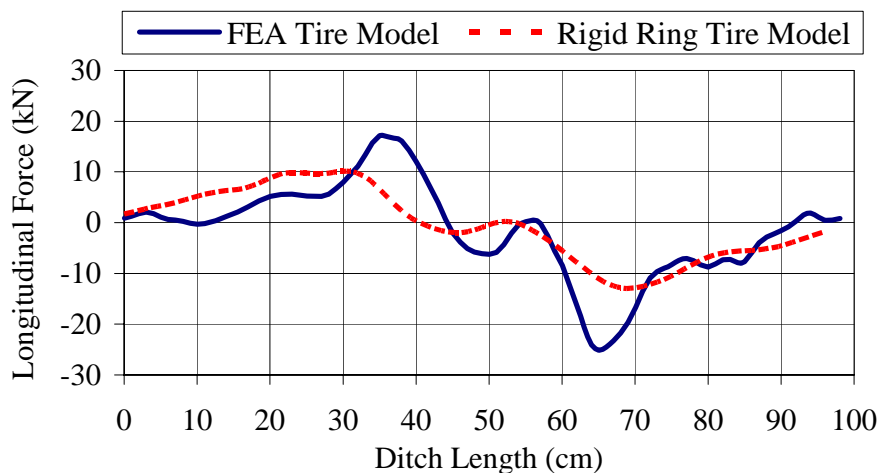


Figure 5-31 Longitudinal Contact Forces at Tire Load of 26.7 kN

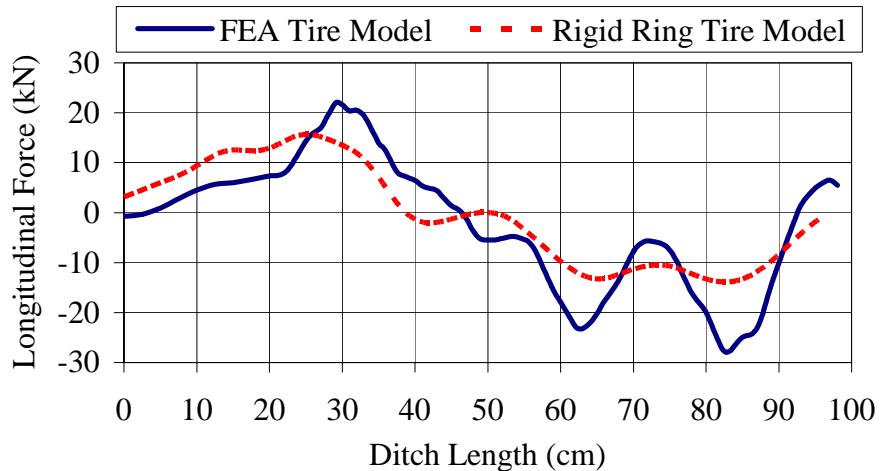
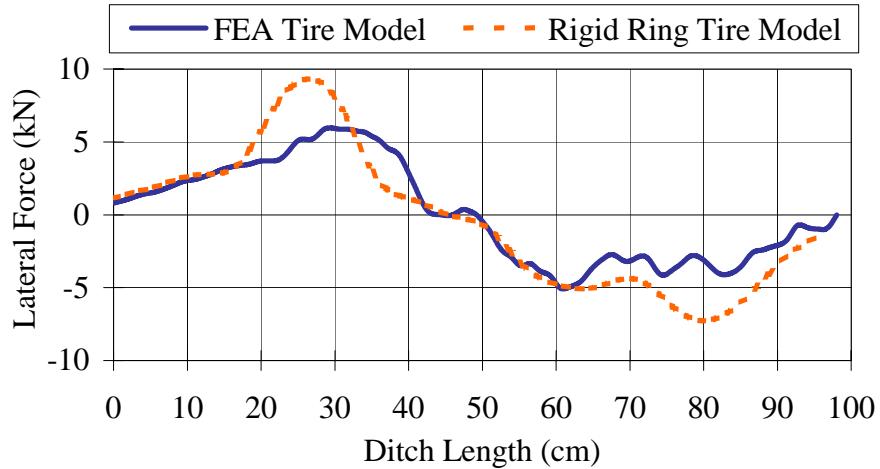
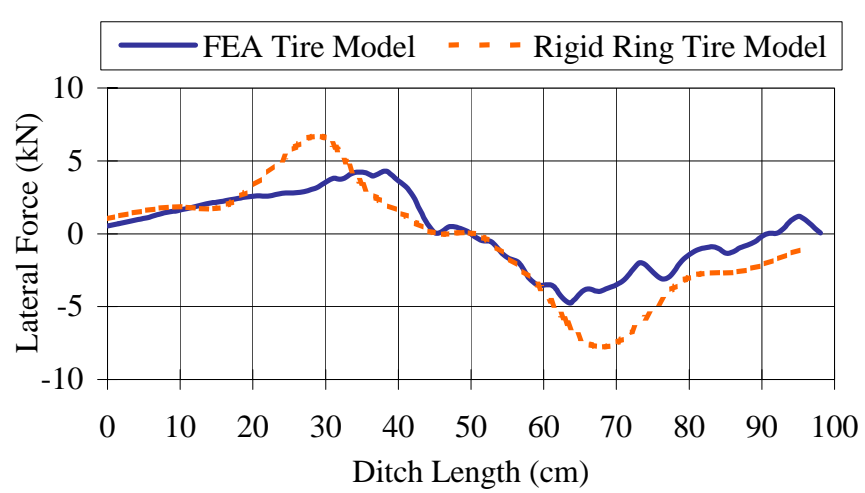
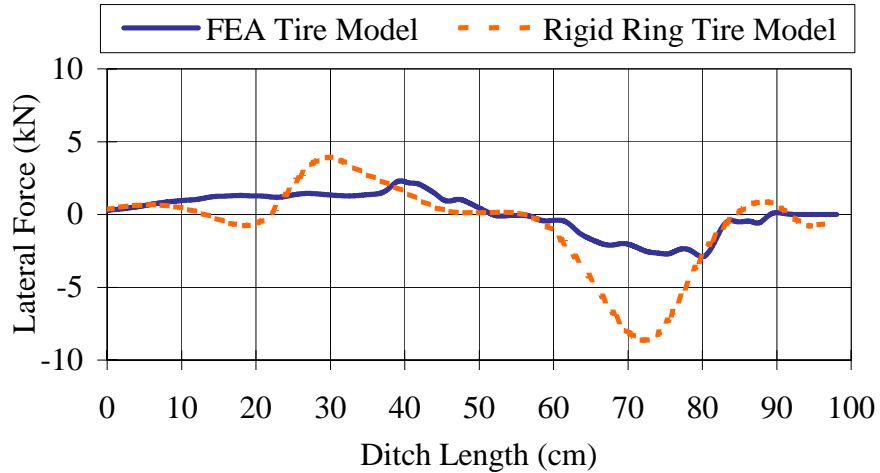


Figure 5-32 Longitudinal Contact Forces at Tire Load of 40.0 kN

5.2.7.4 Comparison of the Predicted Lateral Contact Forces

A lateral contact force is observed in the tire-ditch contact area during the 45° ditch entry and exit due to the different contact geometry between the left and right contact areas. The predicted lateral contact forces acting on the FEA and rigid ring tire models during the ditch run are plotted in Figures 5-33 to 5-35 at various tire loads. It is observed that a lateral contact force is applied to the left on the tire models during the ditch entry, which shows positive forces in the figures. To the contrary, the force is applied to the right during the ditch exit, which shows negative forces.

As the vertical tire load increases, the increased lateral peak forces are observed because the lateral contact force is dependent on the tire reaction force from the ditch, and the reaction force is directly dependent on the vertical tire loads. However, compared to the longitudinal peak contact forces of Section 5.2.7.3, lower peak contact forces are applied laterally to the tire models. The lateral contact forces are generated by only the tread deformation and the different contact geometry between the left and right contact areas which is relatively less dependent on the reaction force from the ditch. In general, reasonable agreements in trends are observed between the predicted lateral forces of the two models at all vertical tire loads.



5.2.7.5 Comparison of the Predicted Vertical Contact Forces

The predicted vertical contact forces acting on the FEA and rigid ring tire models in the contact area during the ditch runs are plotted in Figures 5-36 to 5-38 for various vertical tire loads. The response patterns of the vertical contact forces from the both model runs are observed to be similar to those of the 90° ditch runs in Section 5.1.6.4. The vertical contact forces at zero ditch length show the corresponding vertical tire loads. When the tire models enter the ditch, the vertical contact forces decrease somewhat until the tire models impact the ditch bottom surface. As soon as the tire models impact with the ditch bottom, the vertical contact forces increase to reach maximum values.

However, lower magnitudes of the vertical contact forces during 45° ditch runs are observed than during 90° ditch runs, because the tire models enter the 45° ditch more gradually. The vertical accelerations of the tire spindles are lower than those of the 90° ditch runs.

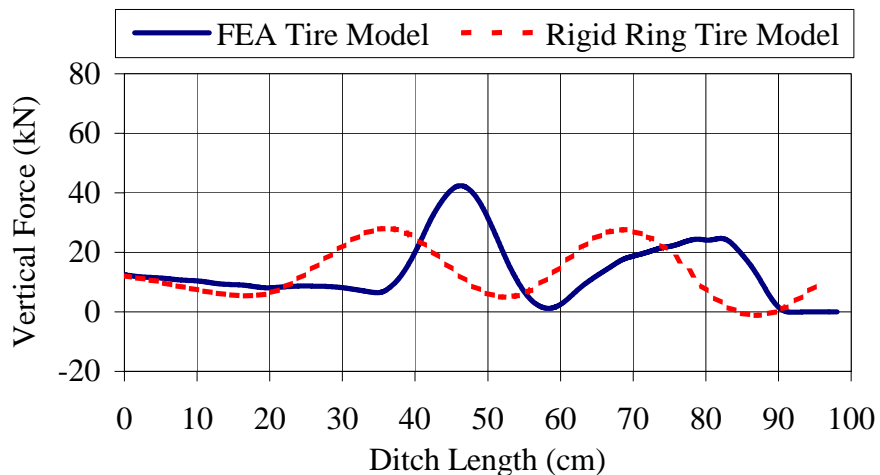


Figure 5-36 Vertical Contact Forces at Tire Load of 13.3 kN

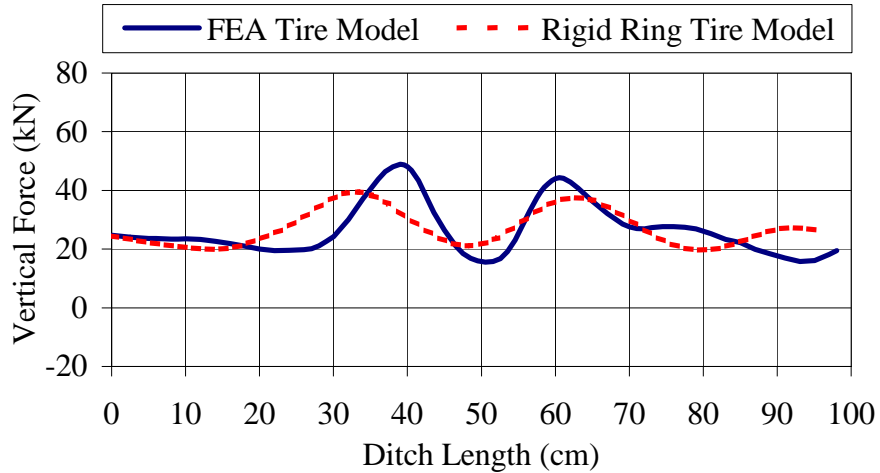


Figure 5-37 Vertical Contact Forces at Tire Load of 26.7 kN

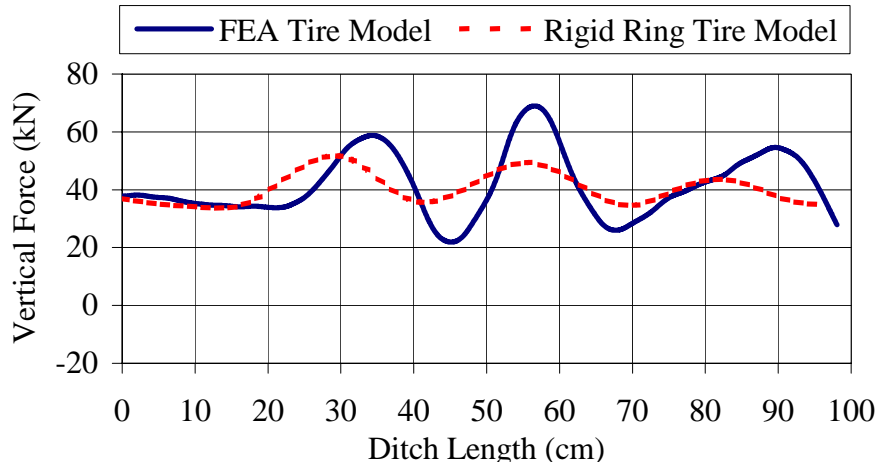


Figure 5-38 Vertical Contact Forces at Tire Load of 40.0 kN

5.2.7.6 Comparison of the Predicted Overturning Moments

The predicted overturning moments acting at the tire spindles of the FEA and rigid ring tire models during the ditch runs are plotted in Figures 5-39 to 5-41 for various vertical tire loads. In the figures, the overturning moments predicted by both models are in reasonable agreement from the point of view of the trend and phase. In terms of the magnitude of the predicted moments, the moments from the rigid ring tire model runs are lower than the moments from the FEA tire model runs due to the limitations of the rigid ring tire model mentioned in previous sections.

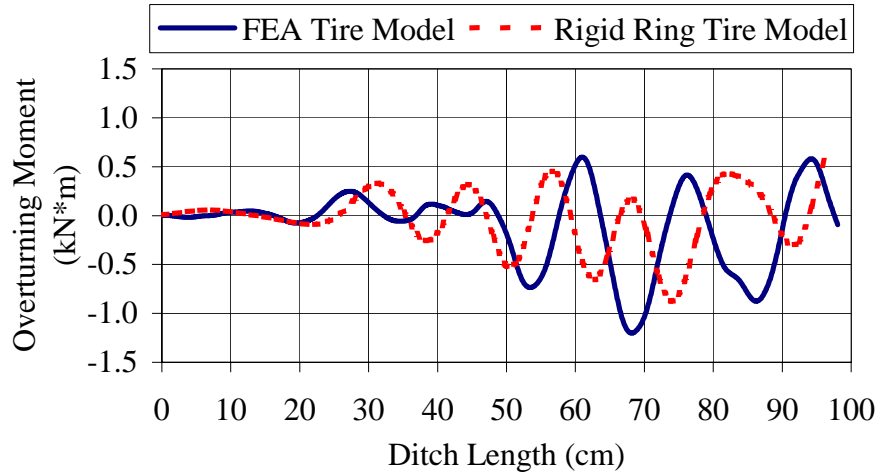


Figure 5-39 Tire Spindle Overturning Moment at Tire Load of 13.3 kN

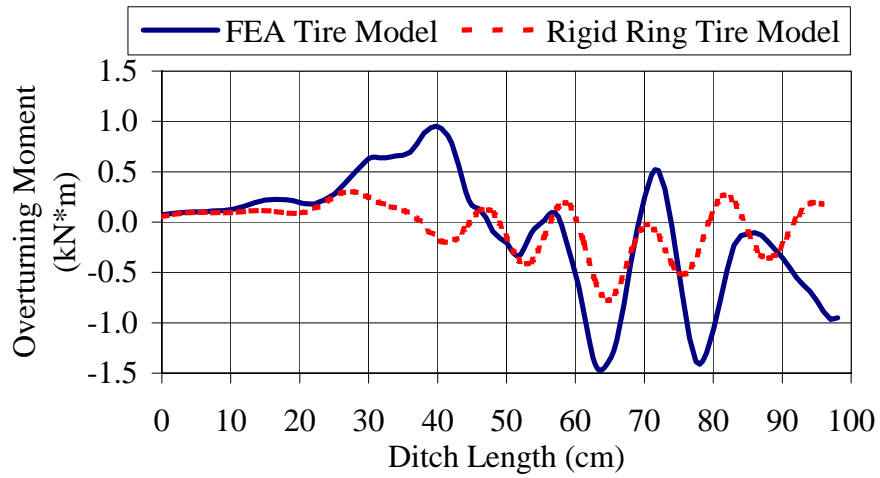


Figure 5-40 Tire Spindle Overturning Moment at Tire Load of 26.7 kN

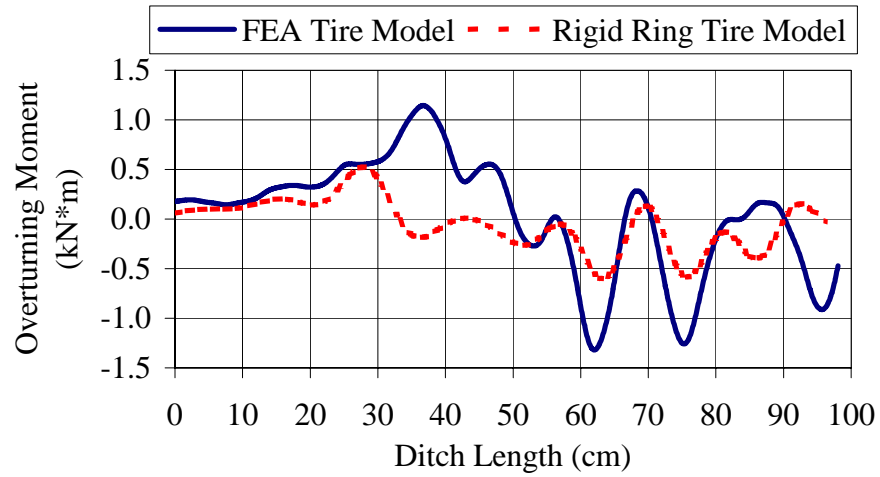


Figure 5-41 Tire Spindle Overturning Moment at Tire Load of 40.0 kN

5.2.7.7 Comparison of the Predicted Vertical Moments

The predicted vertical moments acting at the tire spindles of the FEA and rigid ring tire models during the ditch runs are plotted in Figures 5-42 to 5-44 for various vertical tire loads. In the figures, some discrepancies are observed in magnitude and phase between the results of the two models due to the different contact conditions. The moments from the rigid ring tire model runs seem to represent mean values of the moments from the FEA model runs.

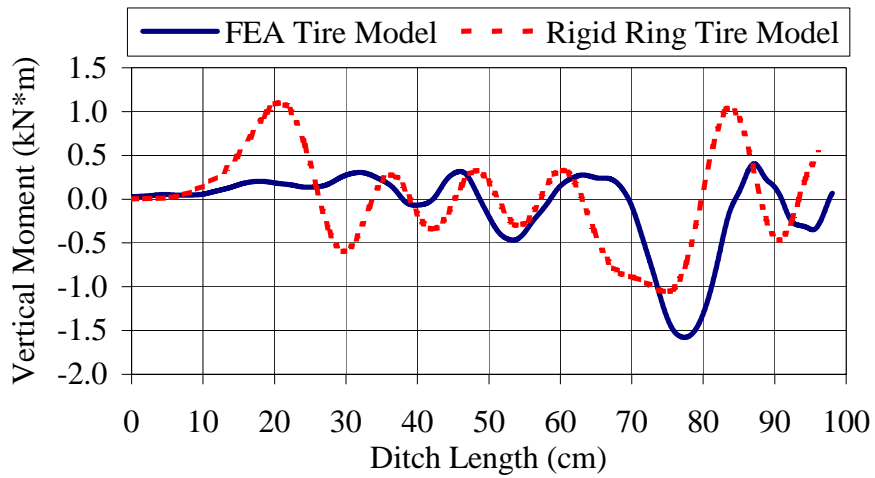


Figure 5-42 Tire Spindle Vertical Moments at Tire Load of 13.3 kN

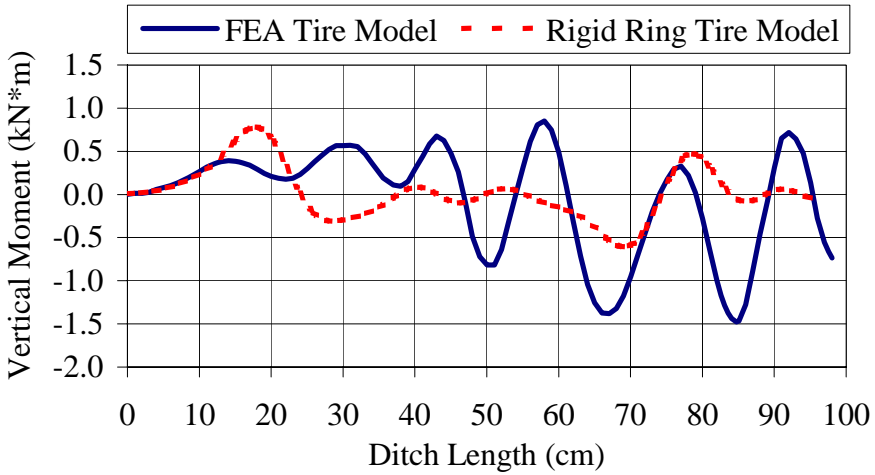


Figure 5-43 Tire Spindle Vertical Moments at Tire Load of 26.7 kN

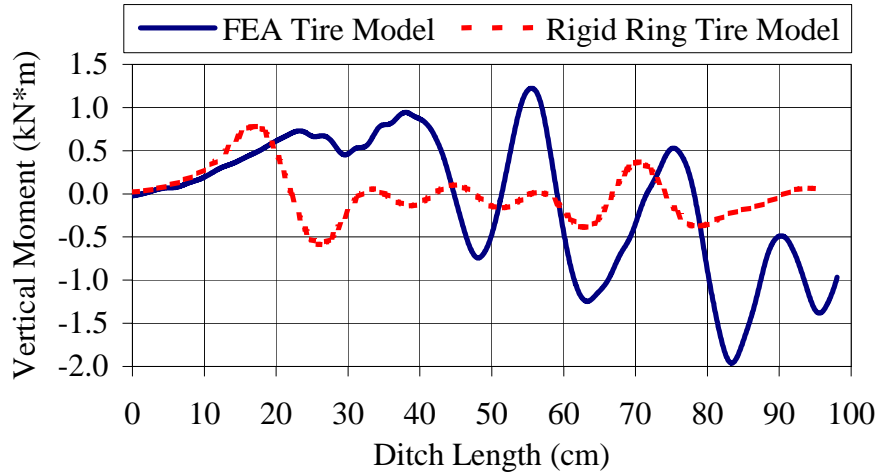


Figure 5-44 Tire Spindle Vertical Moments at Tire Load of 40.0 kN

5.3 Summary

In this chapter, in-plane and out-of-plane tire parameters for the rigid ring truck tire model have been predicted by virtually testing the FEA truck tire model. Before the FEA truck tire model is used to predict the parameters, the FEA tire model was successfully validated by comparing the selected in-plane and out-of-plane test responses of the FEA tire with physical measurement data in Chapter 4. Thus, the predicted in-plane and out-of-plane tire parameters are considered to be reasonable for a rigid ring tire model.

In addition, the FEA tire model has undergone durability tests on 90° and 45° water drainage ditches to predict in-plane and out-of-plane dynamic tire responses. In the 90° ditch runs, only in-plane tire responses are observed because no lateral excitations are provided on the tire models. The in-plane tire responses of the FEA tire model are compared with the results of the Volvo3P's rigid ring tire model runs using the 90° ditch. The results obtained from the two tire models generally show good agreement.

Meanwhile, in case of the 45° ditch runs, not only in-plane but also out-of-plane tire responses are predicted due to the different contact area geometries between the left and right contact areas during the ditch entry and exit. The tire responses of the FEA tire

model are compared with the results of the Volvo 3P's rigid ring tire model runs on the 45° ditch. The in-plane tire responses and the lateral contact forces show good agreement with the two tire models. However, the vertical and overturning moments between the two results are not in good agreement due to the limitations of the rigid ring tire model in predicting out-of-plane tire responses.

The FEA tire model has a definite contact area on the road surface due to a tire load and an elastic tire deformation. During the ditch runs, the FEA tire model is observed to have varying contact areas and tread deformations according to varying vertical contact forces and ditch geometry, which plays an important role in determining the out-of-plane tire moments. However, the rigid ring tire model does not have a contact area and tread deformation during the ditch runs, which makes the tire model limited especially, in the prediction of the out-of-plane tire moments. Moreover, the rigid ring tire model uses linear spring stiffness and constant rolling radius. Thus, in order to obtain better results from the rigid ring tire model, the limitations mentioned above need to be overcome.

In general, the results from the FEA and rigid ring tire model runs show a successful attempt to capture the transient responses of a tire rolling over a complex road profile. The completed research on the parameter determinations and ditch runs were presented at the ASME Conference. (Chae *et al.*, 2004; Chae *et al.*, 2005).

CHAPTER 6

QUARTER-VEHICLE MODELS USING RIGID RING AND FEA TIRE MODELS

In Chapter 5, in-plane and out-of-plane parameters for the rigid ring tire model have been predicted through the FEA virtual tire tests. In addition, the FEA tire model undergoes the durability tests on the water drainage ditches 90° and 45° to the tire running direction to predict dynamic in-plane and out-of-plane tire responses at various tire loads. Meanwhile, the predicted parameters are implemented in the rigid ring tire model, and the model undergoes the same durability tests. The predicted tire responses of the two tire models are compared to each other and show good agreements.

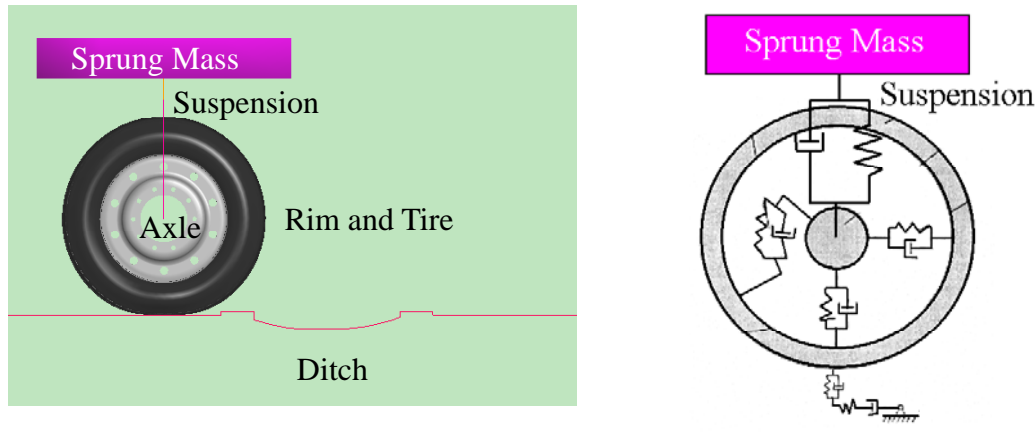
In the simulations of the tire models in Chapter 5, only constant vertical tire loads are applied to the FEA and rigid ring tire models. Additional tire loads due to the vertical acceleration of the sprung mass during tire operations are not considered in the simulations of the models. Thus, a quarter sprung mass and suspension system is assembled with the tire models to include the effect of the vertical sprung mass motion, which represents a quarter-vehicle model and a closer model to real vehicle applications. Then, the quarter-vehicle models undergo a 90° ditch at various running speeds. The tire spindle vertical accelerations of the FEA and rigid ring quarter vehicle models are predicted during the ditch runs and compared each other. In addition, the predicted accelerations are compared with the measurement results obtained from tractor-semitrailer full vehicle tests on the ditch.

The objective of this chapter is to assess the performances of the rigid ring tire model in

the quarter-vehicle model environment that includes the effect of the sprung mass vertical acceleration during the durability tests. By comparing the performances of the rigid ring with the FEA tire model responses in the quarter-vehicle models and tractor-semitrailer measurements, it will be determined whether the rigid ring quarter vehicle model properly predicts dynamic tire responses during the durability test simulations.

6.1 FEA and Rigid Ring Quarter-Vehicle Models

A quarter-vehicle model is developed using the FEA tire model to represent a front axle tire of the tractor-semitrailer. A quarter-vehicle model consists of a sprung mass, tire, rim, axle, and suspension as shown in Figure 6-1 (a). The sprung mass is modeled with a solid rigid body and moves only along vertical direction. The axle is modeled in one-dimensional rigid beam elements and assembled with the rim using a revolute joint. Thus, the axle does not rotate with rim. The suspension connects the sprung mass and axle using a spring-damper translational joint. The suspension isolates the sprung mass from tire vibrations by spring deflection and damping. A quarter-vehicle model using the rigid ring tire model is developed by Volvo3P and is shown in Figure 6-1 (b).



(a) FEA Quarter-Vehicle Model (b) Rigid Ring Quarter-Vehicle Model

Figure 6-1 Quarter-Vehicle Models

6.1.1 Sprung Mass

The sprung mass is modeled using rigid solid elements and represents a quarter vehicle body imposed on suspension and tire system. In the FEA quarter-vehicle model, vertical tire load is significantly dependent on the sprung mass weight. Thus, the density of the solid sprung mass is adjusted to obtain desired tire loads. Then, the suspension and tire model is loaded and deflected due to the sprung mass weight in the gravitational field. Because only the single degree of freedom sprung mass displacement is allowed in the quarter-vehicle model, the effects of pitch and roll motions of the sprung mass observed from full vehicle tests are not considered.

6.1.2 Front Axle Suspension Characteristics

The suspension in a vehicle consists of spring, shock absorber, and neighboring link arms between sprung mass and unsprung mass. The suspension isolates the sprung mass from the tire vibrations due to road irregularities, thus, it provides a comfortable environment for passengers and freights. In the quarter vehicle models, the suspension is modeled by using a simple spring-shock absorber system neglecting the kinematic effect of the link arms as shown in Figure 6-1. A linear spring stiffness during compression and extension provided by Volvo3P is used in the quarter-vehicle models as shown in Figure 6-2.

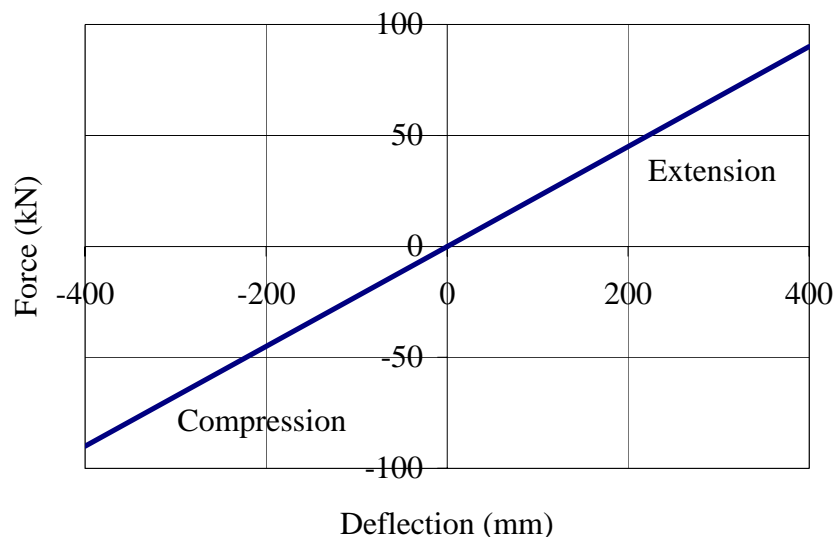


Figure 6-2 Spring Characteristics of the Suspension

Different linear damping constants during compression and extension are used in the quarter-vehicle models as shown in Figure 6-3. The damping constant during extension is typically higher than that observed during compression.

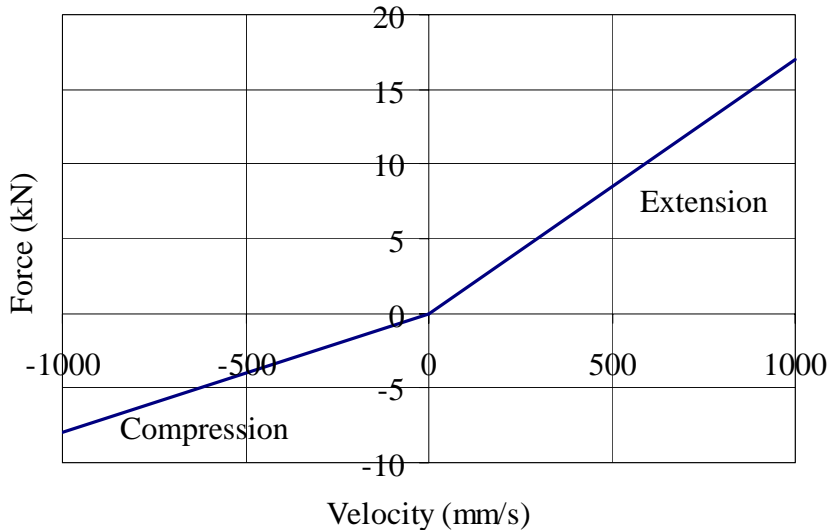


Figure 6-3 Shock Absorber Characteristics of the Suspension

6.2 Durability Tests Using a Tractor-Semitrailer and Quarter-Vehicle Models

The developed FEA quarter-vehicle model undergoes durability tests on a water drainage ditch similar to the 90-degree ditch used in Section 5.1.6. The road surface is driven toward the quarter-vehicle model to provide a constant speed during the tests. The quarter-vehicle model is constrained not to move in the longitudinal direction. The sprung and unsprung masses are free to move only in the vertical direction. After completion of each FEA quarter-vehicle model simulation, the vertical acceleration of the tire spindle is plotted in terms of the ditch length and compared with the results from the rigid ring quarter-vehicle model simulation and measurement using tractor-semitrailer conducted by Volvo 3P.

6.2.1 90° Water Drainage Ditch

A 90° water drainage ditch used for the durability tests is 736 mm-long and 86 mm-deep. The actual ditch profile was measured at the Volvo 3P durability test site and its dimensions are shown in Figure 6-4 and 6-5. The new ditch is longer and shallower than that ditch used for simulation in Section 5.1.6.



Figure 6-4 Measurement of the 90° Ditch Profile

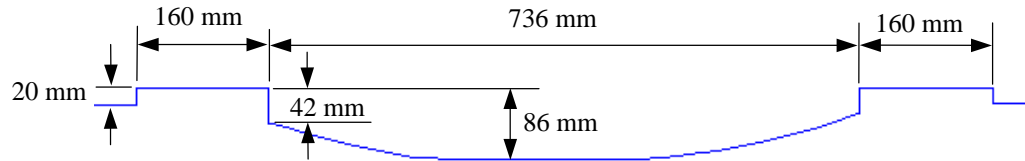


Figure 6-5 90° Ditch Profile

As it can be seen from Figure 6-5, the ditch has lips before and after the ditch. These lips were observed during ditch profile measurement and added to the model. In this simulation, the road including the ditch is modeled as a rigid body in the FEA quarter-vehicle model.

6.2.2 Vertical Acceleration Measurements on the Ditch Using Tractor-Semitrailer

The vertical accelerations of the front axle are measured at various speeds by using tractor-semitrailer as shown in Figure 6-6. Different front axle loads are obtained by adjusting the fifth-wheel load. The fifth-wheel load was varied by adjusting the location of concrete blocks on the flat-bed test trailer. The tests were performed at front axle load 54.3 kN (12,200 lb).



Figure 6-6 Test Tractor-Semitrailer Running over the Ditch

Since it is difficult to install an accelerometer at the center of a tire, the accelerometer is installed on the rigid front axle as close as possible to the tire center as indicated by arrow in Figure 6-7. Two tri-axial accelerometers were mounted to the left and right sides of the front axle. The vertical accelerations measured from the right side accelerometer will be compared to those from the FEA quarter-vehicle model and rigid ring quarter vehicle model.

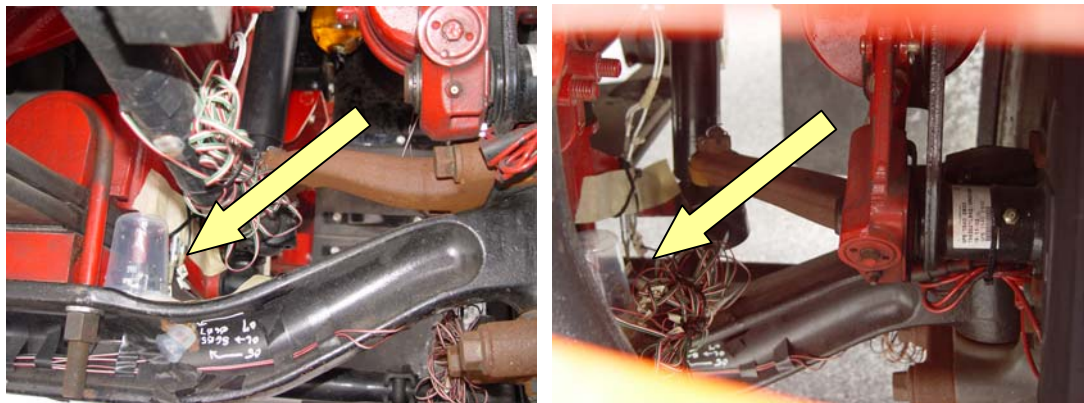


Figure 6-7 Accelerometer Location at Front Left Wheel

6.2.3 Vertical Acceleration Predictions on the Ditch Using Quarter-Vehicle Models

The FEA and rigid ring quarter-vehicle models undergo the ditch test at various speeds of 8.2 km/h, 11.1 km/h, and 21.3 km/h. The rated tire load of 26.7 kN (6,020) is applied on the inflation pressure of 0.759 MPa (110 psi) truck tire models. The vertical accelerations at the tire spindles of the FEA and rigid ring quarter-vehicle models are predicted and plotted in terms of the ditch length as shown in Figures 6-8 to 6-10. The ditch shape and dimension is attached below each acceleration plot to clearly show the accelerations before, inside, and after the ditch. The predicted values are compared with the measured values at the front axle of the tractor-semitrailer.

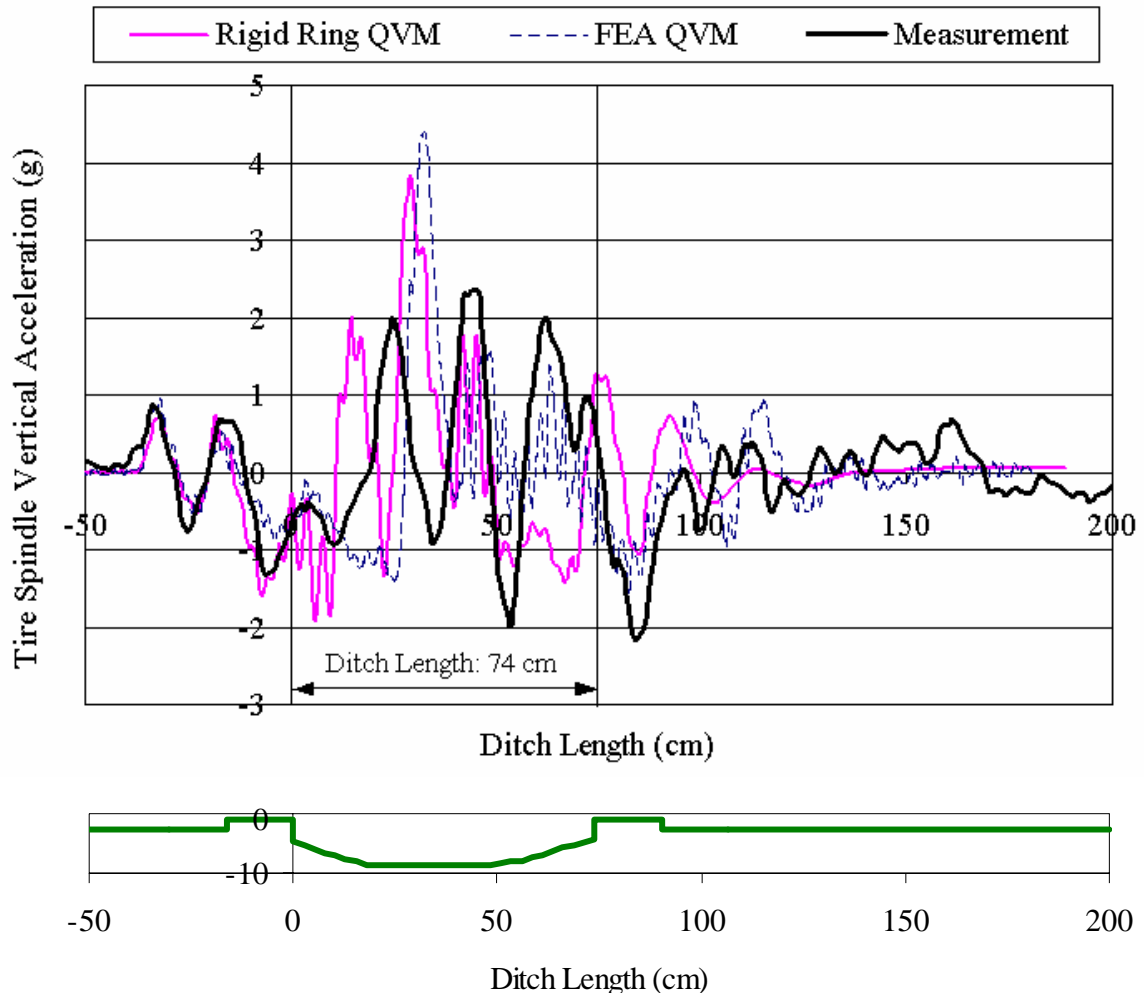


Figure 6-8 Tire Spindle Vertical Accelerations at 8.2 km/h (Rated Tire Load: 26.7 kN)

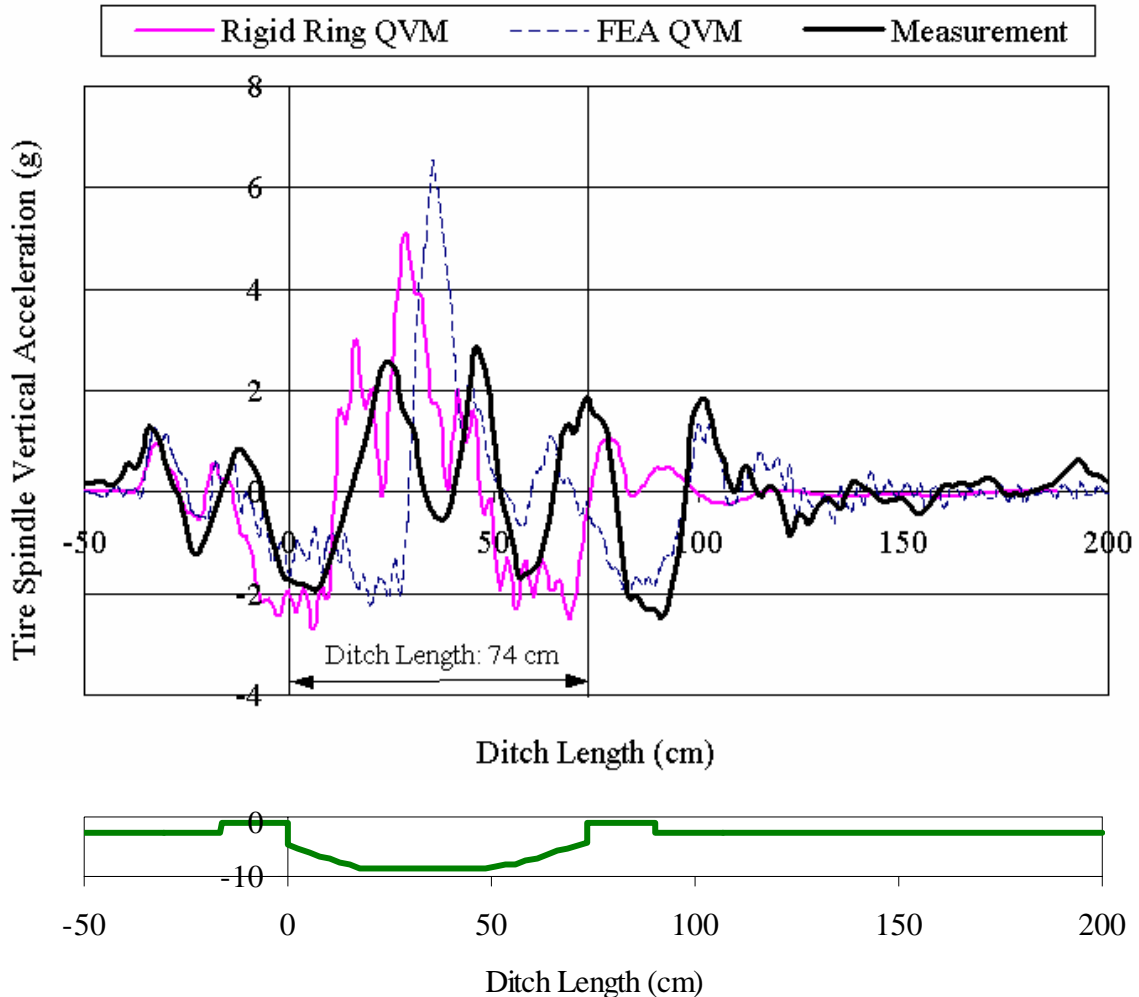


Figure 6-9 Tire Spindle Vertical Accelerations at 11.1 km/h (Rated Tire Load: 26.7 kN)

When the tire enters the ditch from the left ditch lip, the predicted and measured vertical accelerations show good agreement in magnitude and phase each other. However, within the ditch, the predicted and measured values are somewhat different in magnitude and phase. In terms of the magnitude of the maximum peak, the predicted values show higher than measured values because of the lack of dynamic couplings from the other locations of suspension in the quarter-vehicle models. In the quarter-vehicle model, only the single degree of freedom of vertical motion of the sprung mass affects the suspension and tire responses. However, in the tractor-semitrailer, dynamic roll and pitch motions as well as the vertical motion of the tractor sprung mass are coupled in responses of the suspension and tire. In addition, the interference of the semitrailer through the kingpin-fifth wheel connection influences the dynamic behavior of the tractor. Therefore, the vertical

acceleration of the front axle of the tractor-semitrailer during the ditch test does not respond in the same manner as that of the quarter-vehicle model. Instead, a highly damped response is observed in vertical motion of the front axle. Thus, lower vertical accelerations are observed in the ditch tests using full-vehicle, tractor-semitrailer, than those from the quarter-vehicle models.

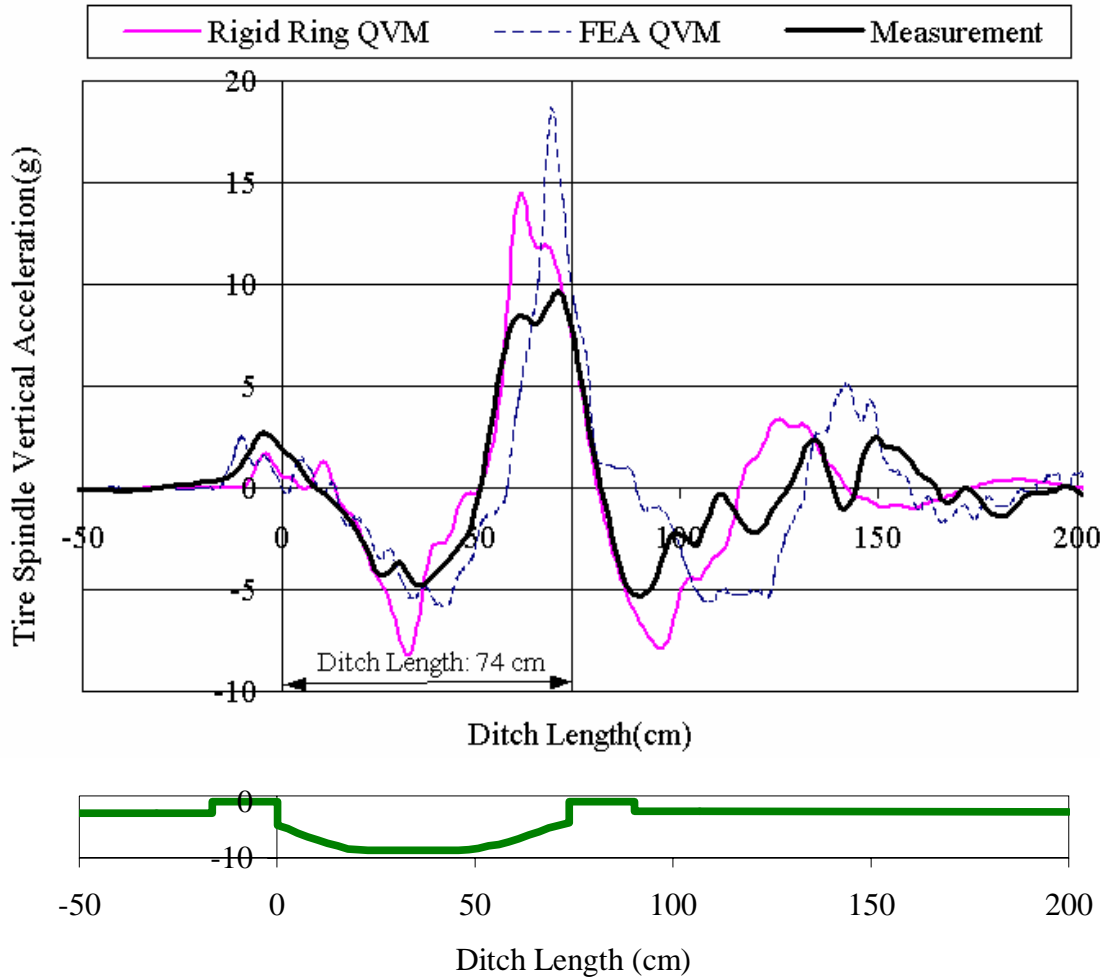


Figure 6-10 Tire Spindle Vertical Accelerations at 21.3 km/h (Rated Tire Load: 26.7 kN)

The above simulation results are supported by Levesley *et al.*'s study in 2003. In their study, they compared the vertical displacements of the sprung and unsprung masses in quarter-vehicle and full-vehicle models when the vehicle models underwent step and pothole inputs. It was found that the displacements were lower for the full-vehicle model because the full-vehicle model response appeared more heavily damped than the quarter-

vehicle model. It was concluded that the dynamic response at other wheel stations contributed to the behavior of the wheel station directly subjected to the step or pothole input even for independent suspensions.

Regarding the locations of the local peaks, it is observed that the local peak locations of the rigid ring quarter-vehicle model are relatively in-phase with those of the FEA quarter-vehicle model over the whole plot range. On the other hand, the maximum peak location of the rigid ring quarter-vehicle model is somewhat out-of-phase with that of the measurement at the two low speeds due to the front axle vibrations of the tractor-semitrailer during the ditch runs. At the speed of 21.3 km/h, the local peak locations of the rigid ring are relatively in-phase with other two results because the effect of the front axle vibrations are relatively less at the high speed compared to those at the two lower speeds.

It is also observed from Figures 6-8 to 6-10 that as the tire speed increases, higher peak values of vertical acceleration are observed due to higher contact forces exerted to the tire during ditch runs. It is concluded that the rigid ring tire model in the quarter-vehicle environment predict the vertical acceleration at the tire spindle closer to that of the FEA quarter-vehicle model rather than to the measured values using the tractor-semitrailer. In order to compare the response of the rigid ring tire model in quarter-vehicle environment, the tire test measurement using the same kind of quarter-vehicle equipment needs to be conducted to eliminate the effect of the dynamic couplings of the sprung mass or other dynamic inputs on the front axle of the tractor-semitrailer.

6.2.4 Model Validations

The validation methodology was set by US-Army Aberdeen Test Center (ATC) engineers along with the expertise of the colleagues at the Vehicle Dynamics and Simulation Research Division at Applied Research Laboratory of the Pennsylvania State University. In 2005, Hillegass *et al.* created a combat vehicle model and predicted the vertical acceleration at the vehicle center of gravity during running on a 6-inch washboard. Then,

by using the ATC validation criteria, the combat vehicle model was validated.

The validation criterion for acceleration is that the predicted root-mean-square (RMS) and standard deviation (SD) values from model simulations should fall within $\pm 10\%$ of the measurements. SD is a statistical measure that identifies how the data is scattered around the mean of a set of data, which is calculated by Equation (6-1).

$$SD = \sqrt{\frac{\sum (x - \bar{x})^2}{n - 1}} \quad (6-1)$$

Where, x : individual data value,

\bar{x} : mean of the set of data,

n : number of data in the set.

RMS is the magnitude of varying quantity of data. RMS is used by ATC as statistical measurement to validate simulated data versus measured test data that is calculated by using Equation (6-2). It is relatively insensitive to wild points, and it does not provide an indication of variation about the mean.

$$RMS = \sqrt{\frac{1}{n} \sum_{i=1}^n x^2} = \sqrt{\frac{x_1^2 + x_2^2 + \dots + x_n^2}{n}} \quad (6-2)$$

This validation criterion is used to validate the predicted vertical acceleration of the rigid ring quarter-vehicle model at the three speeds as shown in Tables 6-1 to 6-3. The SD and RMS values of the rigid ring quarter-vehicle model fall within $\pm 10\%$ of the measured values only at tire speed of 8.2 km/h. However, the SD and RMS values of the rigid ring quarter-vehicle model at the cases of the two higher speeds do not fall within the validation ranges due to higher values around the maximum peak accelerations than measured values.

Table 6-1 Statistical Validation of Tire Spindle Vertical Acceleration at 8.2 km/h

	Vertical Acceleration at Tire Spindle (g's)			
			ATC Validation Criteria	
	Measurement	Rigid Ring QVM	Min.	Max.
SD	0.892	0.831	0.803	0.981
RMS	0.886	0.830	0.797	0.975

Table 6-2 Statistical Validation of Tire Spindle Vertical Acceleration at 11.1 km/h

	Vertical Acceleration at Tire Spindle (g's)			
			ATC Validation Criteria	
	Measurement	Rigid Ring QVM	Min.	Max.
SD	1.07	1.26	0.963	1.18
RMS	1.07	1.26	0.963	1.18

Table 6-3 Statistical Validation of Tire Spindle Vertical Acceleration at 21.3 km/h

	Vertical Acceleration at Tire Spindle (g's)			
			ATC Validation Criteria	
	Measurement	Rigid Ring QVM	Min.	Max.
SD	3.13	4.11	2.82	3.44
RMS	3.11	4.10	2.80	3.41

6.3 Summary

In this chapter, a rigid ring quarter-vehicle model has been constructed to test the rigid ring tire model in the quarter-vehicle environment. The quarter-vehicle model consists of the rigid ring tire model, sprung mass, and suspension. Thus, the rigid ring tire model is under the influence of the vertical motion of the sprung mass during the ditch test. The vertical accelerations at the tire spindle are predicted at various tire speeds. The predicted values are compared with those of the FEA quarter-vehicle model and measured values on the front axle of the tractor-semitrailer. The rigid ring quarter-vehicle model generates the vertical accelerations at the tire spindle similar to those from the FEA quarter-vehicle model in magnitude and locations of the peak values. In the measurements, lower maximum peak values are observed, and the locations of the local peak values are somewhat out-of-phase between the ditch lips at the two low speeds. This is because the tire responses in the quarter-vehicle model are only influenced by the vertical motion of

the sprung mass. On the other hand, the front axle response of the tractor-semitrailer is governed by not only the vertical motion of the sprung mass but also by dynamic pitch and roll motions of the sprung mass.

In addition, the sprung mass is interfered by the semitrailer through kingpin-fifth wheel connection and an unexpected vibration can exist during the ditch runs. Thus, less-damped responses or higher vertical accelerations are observed in the tire responses of the quarter-vehicle models. At higher speed, the maximum peak locations of all three results are in-phase since the effect of the tire speed is more dominant and less dynamic coupling is exerted on the front axle. However, higher peak values are observed from the quarter-vehicle models than measurement due to the less-damping nature of the quarter-vehicle model.

It is concluded that the rigid ring tire model in the quarter-vehicle environment predicts the vertical accelerations of tire spindle closer to those of the FEA quarter-vehicle model than to the measured values using tractor-semitrailer. In order to compare the responses of the rigid ring tire model in the quarter-vehicle environment, the actual tire also needs to be tested in the same quarter-vehicle environment where only the vertical motion of the sprung mass influence the tire responses.

CHAPTER 7

CONCLUSIONS AND FUTURE WORK

Conclusions and major contributions throughout this doctoral research are summarized in Sections 7.1 and 7.2, respectively. Also, future research topics using the developed FEA truck tire model are recommended in Section 7.3. Much work needs to be completed regarding the FEA tire model and its applications.

7.1 Conclusions

A rigid ring tire model is frequently used in a multi-body vehicle simulation model due to its simplicity and efficiency. The rigid ring tire model requires several parameters to represent an actual pneumatic tire, and they are determined by comprehensive and costly tire tests. Alternatively, in this study, an FEA truck tire model and its testing environments are successfully established to virtually predict the required parameters for the rigid ring tire model. The completed rigid ring tire model is tested by running the model on 45° and 90° water drainage ditches. The in-plane and out-of-plane tire responses are plotted and compared with the results of the FEA tire model simulations. The tire responses from both models are generally in good agreement. Therefore, for complete vehicle simulations, a simplified rigid ring tire model is required for efficient analysis.

Further, in order to test the rigid ring tire model including an effect of a sprung mass motion, a quarter-vehicle model of two-degree of freedom is developed by associating the rigid ring tire model, solid sprung mass, and spring-shock absorber suspension. In the

quarter-vehicle model, dynamic tire load originated from the vertical acceleration of the sprung mass is applied to the tire through the suspension during the ditch tests. Under this circumstance, the vertical acceleration of the tire spindle is predicted and compared with the results from the FEA quarter-vehicle model and tractor-semitrailer measurements.

The vertical accelerations from the rigid ring quarter-vehicle model agree well with the results from the FEA quarter-vehicle model both in shape and peak values. The results from the quarter-vehicle models show similar shapes of vertical accelerations to the measurement plots. However, the maximum peak values observed from both quarter-vehicle model simulations are higher than measured values. It is attributed to the lack of the dynamic couplings from other locations of suspensions, such as pitch and roll motions of the sprung mass, in the quarter-vehicle models. Thus, the tire responses of the quarter-vehicle models are less damped and show higher vertical accelerations than those observed from the measured values using tractor-semitrailer. Even though the quarter-vehicle models have some discrepancies in magnitude compared with measurements, it is concluded that the rigid ring tire model in a quarter-vehicle environment predicts closer vertical accelerations at the tire spindle to the real tire applications.

It is also concluded that the ring tire model has limitations in prediction of dynamic tire forces and moments due to its point-contact nature with road surface. The limitations are more noticeable in out-of-plane tire moment predictions. In order to overcome the deficiency of the single-point contact with road surface and make the rigid ring tire model more realistic, an effective road profile needs to be used instead of an exact road profile. In addition, multiple-point contacts on uneven road profile cannot be achievable due to lack of a contact area in a quarter-vehicle model. Thus, the predicted magnitude and phase might be different from the results of the FEA or measured tire forces and moments.

7.2 Major Contributions

Throughout this study, the following major contributions are achieved in this virtual tire modeling and testing area:

1. The three-dimensional nonlinear FEA truck tire model, 295/75R22.5, and the detailed rim for the tire model have been built. The developed FEA truck tire model was validated by comparing its in-plane and out-of-plane responses with measurements. Therefore, many truck tire applications can be simulated by using the truck tire model to predict reliable tire responses.
2. The virtual tire test environments have been established that can replace difficult and costly physical tire tests. By using the virtual test environments, boundary conditions, tire speeds, and loadings are easily controlled. In addition, tire tests under high loads and/or high speeds that are hardly achieved in physical tests can also be easily simulated. The virtual tire test environments used to test the FEA truck tire model are listed as follows:
 - Tire vertical load-deflection test for tire stiffness and footprint area predictions,
 - Cornering test for cornering force and aligning moment predictions,
 - Longitudinal slip test for longitudinal force predictions,
 - Yaw oscillation test for transient lateral force predictions,
 - Tire-cleat drum test for vibration modes prediction,
 - In-plane and out-of-plane tire stiffness and damping constant tests,
 - 45° and 90° ditch tests for dynamic tire response predictions.
3. Yaw oscillation test was virtually conducted to determine dynamic cornering forces and phase angle versus path frequency by using the developed FEA truck tire model for the first time.

4. The in-plane and out-of-plane parameters for a rigid ring tire model have been predicted for the first time by conducting the comprehensive virtual FEA truck tire model tests. The parameter predictions were completed for one of the prestigious truck manufacturer. The rigid ring tire model implemented with the predicted parameters has proved to generate efficient and reliable tire responses. Therefore, the rigid ring tire model will contribute to obtain efficient and reliable simulation results of a multi-body vehicle model.

5. The FEA quarter-vehicle model has been built by assembling a solid sprung mass, the FEA truck tire model, and spring-shock absorber suspension system to include the effect of the vertical acceleration of the sprung mass on the tire model responses during ditch runs. The quarter-vehicle model can be used to predict the vertical accelerations of not only the tire spindle but also sprung mass, which is a closer model to real applications of a vehicle. Therefore, the quarter-vehicle model plays an important roll in conducting tire durability tests, evaluating passengers' ride quality, and optimizing suspension characteristics.

7.3 Recommended Future Work

Some recommended future topics related to the FEA truck tire model are presented. They are the dynamic performances of the FEA truck tire model in a full vehicle model, FEA tire model responses on a soft terrain, and FEA vehicle/tire model for hydro-planning prediction.

7.3.1 FEA Truck Tire Model in a Full-Vehicle Model

The vertical accelerations of the FEA truck tire model in a quarter-vehicle model have already been predicted during the ditch runs at various tire loads and speeds. However, in a quarter-vehicle model environment, higher peak acceleration values than measured values using tractor-semitrailer are observed due to lack of dynamic couplings from other

locations of suspensions. Thus, the vertical accelerations of the FEA truck tire model in a full-vehicle model running over the ditch need to be predicted and compared with those in the quarter-vehicle model.

7.3.2 FEA Tire Model on a Soft Soil Terrain

In this study, the FEA truck tire model has always run on a rigid road surface. No deformation of the road model was observed. Thus, energy dissipation of the tire model due to the road deformation was not expected. Instead, when the road surface is covered with a wet mud or snow, some amount of tire energy is dissipated by the deformation of the mud or snow as shown in Figure 7-1, the tire model responses will be different from those on a rigid road surface. The responses will be a function of density, viscosity, and thickness of the covered material. The sensitivity analysis of those factors on the tire responses needs to be accomplished.

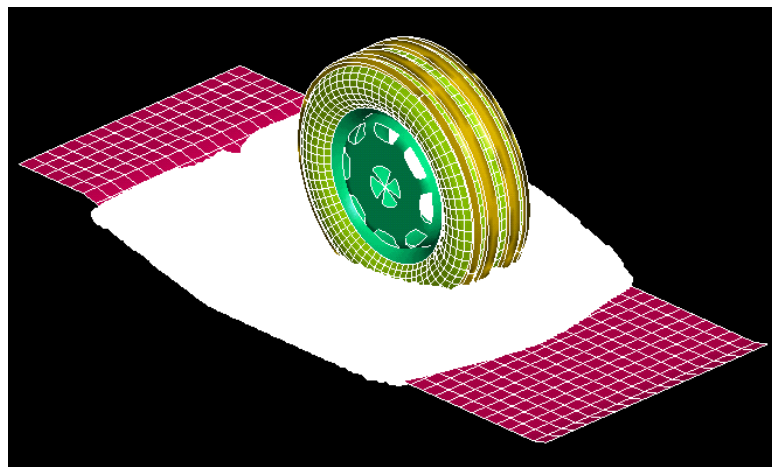


Figure 7-1 FEA Tire Model on a Soft Soil Terrain

7.3.3 FEA Vehicle/Tire Model for Hydroplaning Prediction

When the tire tread enters flooded pavements as shown in Figure 7-2, the effective contact area between the tire and the road surface is reduced compared with dry

pavement conditions. This is because the mass and viscosity of the fluid resists displacement from the area between the tire and the pavement. This resistance generates lift forces on the tire contact surface as it moves through the fluid film. When these lift forces under thick film conditions become great enough to completely support the tire load, tire contact with road surface does not exist and dynamic hydroplaning occurs. Under this condition, the tire contact with the pavement is through the fluid film. Thus, braking, acceleration, and steering operations will be quite different compared to a dry pavement.

Many factors affect the wet traction performances of a tire. They are tread pattern, tread materials, fluid depth, tire running speed, and tire load. The tire performances at various combinations of those factors need to be determined through an FEA tire/vehicle model.

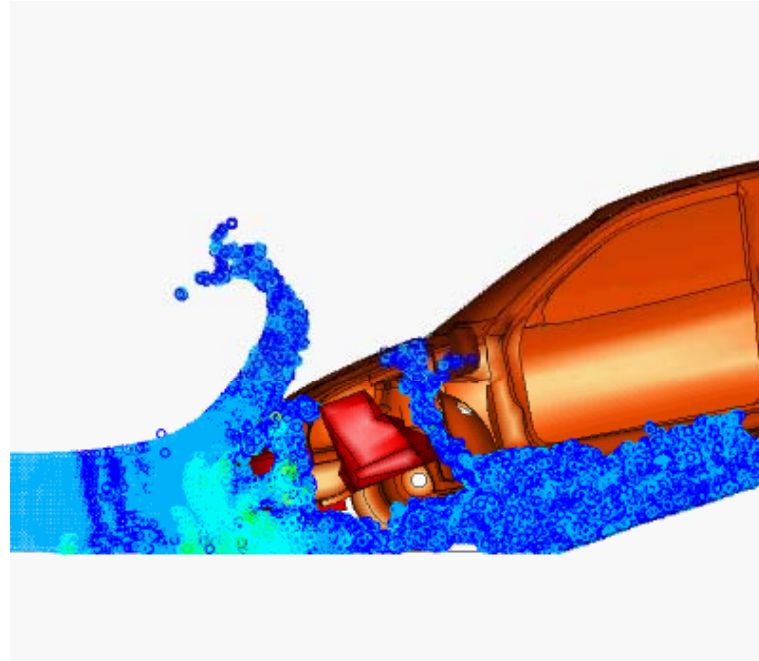


Figure 7-2 FEA Vehicle/Tire Model for Hydroplaning Prediction

REFERENCES

- Allen, R. W. and Klyde, D.H., (2001), "Tire Maneuvering Properties and Their Effect on Vehicle Handling and Stability," Tire Industry Conference Paper No. 577.
- Allen, R. W., Magdaleno, R. E., Rosenthal, T. J., Klyde, D. H., Hogue, J. R., (1995), "Tire Modeling Requirements for Vehicle Dynamic Simulation," *SAE Paper 950312*.
- Allison, D. J., and Sharp, R. S., (1997), "On the low Frequency in-plane forced Vibrations of Pneumatic Tire/Wheel/Suspension Assemblies," International Colloquium on Tire Models for Vehicle Dynamic Analysis, Proceedings of the Second International Colloquium on Tire Models for Vehicle Dynamic Analysis, pp. 151-162.
- Altena, P. H. van., (1975), "Design of an Air Bearing, V.R.L.D. Report No. 763, June.
- Apetaur, M., (1991), "Modeling of Transient Nonlinear Tire Responses," International Colloquium on Tire Models for Vehicle Dynamics Analysis, Proceedings of the First International Colloquium on Tire Models for Vehicle Dynamics Analysis, pp. 116-126.
- Askeland, D. R., (1994), The Science and Engineering of Materials, PWS publishing Company, p. 488.
- Automotive News Europe, (2001), The brothers who seized an opportunity; Andre Michelin, Edouard Michelin, December.
- Bakker, E., Lidner, L., and Pacejka, H. B., (1989), "A new Tire Model with an Application in Vehicle Dynamics Studies," *SAE paper 890087*.
- Bakker, E., Nyborg, L., and Pacejka, H. B., (1987), "Tire Modeling for Use in Vehicle Dynamic Studies," *SAE paper 870421*.
- Bathe, K. J. and Chaudhary, A., (1985), "A Solution Method for Planar and Axisymmetric Contact Problems," *International Journal of Numerical Methods in Engineering*, Vol. 21, pp. 65-88.
- Bellis, M., (2006), "The History of Pneumatic Devices; Pneumatic Devices - Pneumatic Tube," <http://inventors.about.com/library/inventors/blpneumatic.htm>.
- Benson, D. J. and Hallquist, J. O., (1990), "A Single Surface Contact Algorithm for the Post-Buckling Analysis of Shell Structures," *Computer Methods in Applied Mechanics and Engineering*, Vol. 78, pp. 141-163.

- Bird, K. D. and Martin, J. F., (1973), "The Calspan Tire Research Facility; Design, Development and Initial Test Results, *SAE Paper 730582*.
- Browne, A., Ludema, K. C., and Clark, S. K., (1981), "Contact between the Tire and Roadway," Mechanics of Pneumatic Tires, Chapter 5, National Bureau of Standards, Monograph 122, Washington, D.C.
- Bruinsma, F., (1968), Design and Measurements of an Air Bearing for a Running Belt with an Electro-Hydraulic Vibrator System, V.R.L.D. Report No. 472, September.
- Bruni, S., Cheli, F., and Resta, F., (1997), "On the Identification in Time Domain of the Parameters of a Tire Model for the Study of In-plane Dynamics," International Colloquium on Tire Models for Vehicle Dynamic Analysis, Proceedings of the Second International Colloquium on Tire Models for Vehicle Dynamic Analysis, pp. 136-150.
- Captain, K. M., Boghani, A. B. and Wormley D. N, (1979), "Analytical Tire Models for Vehicle Dynamic Simulation", *Vehicle System Dynamics*, Vol. 8.
- Chae, S., Chang, Y. P., El-Gindy, M., Streit, D. A., (2001), "Standing Wave Prediction of a Racing Car Tire," CSME-MDE-2001, November 21-22, Montreal, Canada.
- Chae, S., El-Gindy, M., Trivedi, M., Johansson, I., and Öijer, F., (2004), "Dynamic Response Predictions of a Truck Tire Using Detailed Finite Element and Rigid Ring Models," 2004 ASME International Mechanical Engineering Congress and Exposition, Proceedings of IMECE'04, Paper No. IMECE2004-61111, November 13-19, California.
- Chae, S., Öijer, F., El-Gindy, M., Trivedi, M., and Johansson, I., (2005), "In-Plane and Out-of-Plane Dynamic Response Predictions of a Truck Tire Using Detailed Finite Element and Rigid Ring Models," 2005 ASME International Mechanical Engineering Congress and Exposition, Proceedings of IMECE'05, Paper No. IMECE2005-79083, November 5-11, Florida.
- Chan, C. H. and Tuba, I. S., (1971), "A Finite Element Method for Contact Problems of Solid Bodies," *International Journal of Mechanics and Science*, Vol. 13.
- Chang, Y. P., (2002), Nonlinear Rotating Tire Modeling for Transient Response Simulations, Ph.D. Thesis, The Pennsylvania State University, University Park, PA, USA.
- Chang, Y. P. and El-Gindy, M., (2002), "FEA Rotating Tire Modeling for Transient Response Simulation," Paper No. IMECE2002/DE-33200, Proceedings of IMECE'02, 2002 ASME International Mechanical Engineering Congress & Exposition, November 12-17, New Orleans, Louisiana.

- Chang, Y. P., El-Gindy, M., and Streit, D. A., (2002), "Influence of Tire Loading and Inflation Pressure on Standing Waves Phenomena using PAM-SHOCK," a special issue on "New Development in Heavy Vehicle Simulation," *International Journal of Heavy Vehicle Systems*.
- Davis, D. C, (1974), "A Radial-Spring Terrain-Enveloping Tire Model," *Vehicle System Dynamics*, Vol. 3.
- Davis, P. A., (1997), "Quasi-Static and Dynamic Response Characteristics of F-4 Bias-Ply and Radial-Belted Main Gear Tires," NASA Technical Paper 3586, Langley Research Center.
- Davisson, J. A., (1969), "Design and Application of Commercial Type Tyres," *SAE Paper 690001*, SP-344.
- Dillion, D. and J. Rockefeller, (1999), "A Sketch of the Evolution of Transportation," *Strut & Axle*, Vol. XX, No. 2, Summer/Fall, pp. 6-29.
- Eldik Thieme, H. C. A. van, (1982), Straight Line Rolling Experiments, Section 8.2, Mechanics of Pneumatic Tires, p. 547.
- El-Gindy, M. and Chae, S., (2001), "Examination of Steering Wheel Lateral Saturation of DaimlerChrysler Transport Trucks", Final Report, No. PTI-2001-21, Pennsylvania Transportation institute, The Pennsylvania State University, January.
- ESI, (2000), PAM-SHOCK User Manual, PAM System International.
- de Eskinazi, J., Ishihara, K., Volk, H., and Warholic, T. C., (1990), "Towards Predicting Relative Belt Edge Endurance with the Finite Element Method," *Tire Science and Technology*, TSTCA, Vol. 18, No. 4, pp. 216-235.
- Ford, T. L. and Charles, F. S., (1988), "Heavy Duty Truck Tire Engineering," *SAE Paper 880001*.
- Freitag, D. R. and Green, A. J., (1962), "Distribution of Stresses on an Unyielding Surface beneath a Pneumatic Tire," Highway Research Board Bulletin 342, pp. 14-23.
- Gardner, E. R., and Worswick, T., (1951), "Behavior of Tires at High Speed," *Transaction of the proceeding of Institution of Rubber Industry*, Vol. 27, pp. 127-146.
- Gillespie, T. D., (1992), Fundamentals of Vehicle Dynamics, published by Society of Automotive Engineers, Inc.

- Goodman, R. E., Taylor, R. L., and Brekke, T. L., (1968), "A Model for the Mechanics of Jointed Rock," *Journal of the Soil Mechanics and Foundations Division of ASCE*, Vol. 94 (SM 3), pp. 637-649.
- Goodyear, C., (1853), "Gum elastic and its varieties: with a detailed account of its applications and uses and of the discovery of vulcanization," New Haven, 1853.
- Gough, V. E., (1981), "Structure of the Pneumatic Tire," Chapter 4, Mechanics of Pneumatic Tires, Editor: S. K. Clark, U.S. Department of Transportation National Highway Traffic Administration, U.S. Government Printing Office, Washington, D.C., pp. 209.
- Gough, V. E. and Robert, G. B., (1957), "Dunlop Cornering Force Machine," *Transaction of the proceeding of Institution of Rubber Industry*, Volume 33, No. 5.
- Guerra, F. M. and Browning, R. V., (1983), "Comparison of Two Slideline Methods Using ADINA," *Computers and Structures*, Vol. 17, pp. 819-834.
- Guo, K., (1993), "Tire Roller Contact Model for Simulation of Vehicle Vibration Input," *SAE Paper 932998*.
- Guo, K., (1998), "A Model of Tire Enveloping Properties and Its Application on Modeling of Automobile Vibration System," *SAE Paper 980253*.
- Hallquist, J. O., Goudreau, G. L., and Benson, D. J., (1985), "Sliding Interfaces with Contact-Impact in Large Scale Lagrangian Computations," *Computer Methods in Applied Mechanics and Engineering*, Vol. 51, No. 1/3, pp. 107-137.
- Haney, P., (2004), Rubber Friction, The Racing & High-Performance Tire, Sports Car Magazine, January.
- Hillegass, M., Faller, J. G., Bounds, M. S., El-Gindy, M., and Chae, S., (2005) "Validating the Vertical Dynamic Performance of a Multi-Wheeled Combat Vehicle Computer Simulation Model," Proceedings of IMECE'05, Paper No. 2005- ASME International Mechanical Engineering Congress and Exposition, November 5-11, Florida.
- Hirota, G., Fisher, S., State, A., Lee., C., and Fuchs, H., (2001), "An Implicit Finite Element Method for Elastic Solids in Contact," *Proceeding of Computer Animation 2001* (Seoul, South Korea, Nov 7-8, 2001).
- Hirschberg, W., (1991), "Tire Force Computation Module DTIRT," International Colloquium on Tire Models for Vehicle Dynamics Analysis, Proceedings of the First International Colloquium on Tire Models for Vehicle Dynamics Analysis, pp. 167-174.

- Ishihara, K., (1991), "Development of a Three-Dimensional Membrane Element for the Finite Element Analysis of Tires," *Tire Science and Technology*, TSTCA, Vol. 19, No. 1, pp. 23-36.
- Kamoulakos, A., and Kao, B.G., (1998), "Transient Dynamics of a Tire Rolling over Small Obstacles - A Finite Element Approach with PAM-SHOCK," *Tire Science and Technology*, TSTCA, Vol. 26, No. 2, pp. 84-108.
- Kao, B.G., and Muthukrishnan, M., (1997), "Tire Transient Analysis with an Explicit Finite Element Program," *Tire Science and Technology*, TSTCA, Vol. 25, No. 4, pp. 230-244.
- Kenny, T. M. and Stechschulte, R. A., (1988), "Application of Finite Element Analysis in Tire Design," *Tire Science and Technology*, TSTCA, Vol. 16, No. 2, pp. 96-117.
- Kim, S., and Savkoor, A. R., (1997), "The Contact Problem of In-Plane Rolling of Tires on a Flat Road," International Colloquium on Tire Models for Vehicle Dynamic Analysis, Proceedings of the Second International Colloquium on Tire Models for Vehicle Dynamic Analysis, pp. 189-206.
- Koishi, M., Kabe, K., and Shiratori, M., (1998), "Tire Cornering Simulation Using an Explicit Finite Element Analysis Code," *Tire Science and Technology*, TSTCA, Vol. 26, No. 2, April-June, pp. 109-119.
- Kollmann, K., (1959), "New Testing Machine for the Study of Tires," *Revue Gén. du Caoutchouc*, Vol 10.
- Krigbaum, W. and Roe, R., (1965), "Survey of the Theory of Rubberlike Elasticity," *Rubber Chemistry and Technology*, Vol. 38, No. 5.
- Levesley, M. C., Kember, S. A., Barton, D. C., Brooks, P. C., and Querin, O. M., (2003), "Dynamic Simulation of Vehicle Suspension Systems for Durability Analysis," *Material Science Forum*, Vols. 440-441, pp. 103-110.
- Lidner, L., (1991), "Experience with the Magic Formula Tire Model," International Colloquium on Tire Models for Vehicle Dynamics Analysis, Proceedings of the First International Colloquium on Tire Models for Vehicle Dynamics Analysis, pp. 30-46.
- Lippmann, S. A., Oblizajek, K. L., (1976), "Lateral Forces of Passenger Tires and Effects on Vehicle Response During Dynamic Steering," *SAE Paper 760033*.
- Loeb, J. S., Guenther, D. A., Chen, H. F., and Ellis, J. R., (1990), "Lateral Stiffness, Cornering Stiffness, and Relaxation Length of the Pneumatic Tire," *SAE Paper 900129*.

- Loo, M., (1985), "A Model Analysis of Tire Behavior Under Vertical Loading and Straight-Line Free Rolling," *Tire Science and Technology*, TSTCA, Vol. 13, No. 2, pp. 67-90.
- Marques, J. M. and Martin, A. F., (1990), "Three-Dimensional Finite Element Contact Algorithm for Metal Forming," *International Journal for Numerical Methods in Engineering*, Vol. 30, pp. 1341-1354.
- Mooney, M., (1940), "A Theory of Large Elastic Deformation," *Journal of Applied Physics*, Vol. 11, September.
- Munjiza, A., Owen, D. R. J., and Bicanic, N., (1995), "A Combined Finite-Discrete Element Method in Transient Dynamics of Fracturing Solids," *Engineering Computations*, Vol. 12, pp. 145-174.
- Nakajima, Y. and Padovan, J., (1986), "Numerical Simulation of Tire Sliding Events Involving Impacts with Holes and Bumps," *Tire Science and Technology*, TSTCA, Vol. 14, No. 2, April-June, pp. 125-136.
- Noor, A. K., and Anderson, C. M., (1982), "Finite Element Modeling and Analysis of Tires," *Tire Modeling*, Proceedings of a workshop held at Langley Research Center, Hampton, Virginia, September 7-9, series NASA conference publication 2264, pp. 1-37.
- Noor, A. K., Anderson, C. M., and Tanner, J. A., (1985), "Exploiting Symmetries in the Modeling and Analysis of Tires," Computational methods for structural mechanics and dynamics, Proceedings of a workshop held at NASA Langley Research Center, Hampton, Virginia, June 19-21, pp. 317-329.
- Padovan, J., (1977), "On Standing Waves in Tires," *Tire Science and Technology*, TSTCA, Vol. 5, No. 2, pp. 83-101.
- Oden, J. T., Becker, E. B., Miller, T. H., Endo, T., and Pires, E. B., (1982), "Finite Element Methods for Nonlinear Elastostatics," *Tire Modeling*, Proceedings of a workshop held at Langley Research Center, Hampton, Virginia, September 7-9, series NASA conference publication 2264, pp. 39-70.
- Oosten, J. J. M., and Bakker, E. (1991), "Determination of Magic Tire Model Parameters," International Colloquium on Tire Models for Vehicle Dynamics Analysis, Proceedings of the First International Colloquium on Tire Models for Vehicle Dynamics Analysis, pp. 19-29.
- Pacejka, H. B., and Bakker, E., (1991), "The Magic Formula Tire Model," International Colloquium on Tire Models for Vehicle Dynamics Analysis, Proceedings of the First International Colloquium on Tire Models for Vehicle Dynamics Analysis, pp. 1-18.

- Pacejka, H. B., and Besselink, I. J. M., (1997), "Magic Formula Tire Model with Transient Properties," International Colloquium on Tire Models for Vehicle Dynamic Analysis, Proceedings of the Second International Colloquium on Tire Models for Vehicle Dynamic Analysis, pp. 234-249.
- Padovan, J., (1977), "Numerical Simulation of Rolling Tires," Tire rolling losses and fuel economy, an R & D Planning Workshop, October 19-20, series SAE conference proceedings P-74. pp. 87-94.
- Potts, G. R., and Csora, T. T., (1975), "Tire Vibration Studies: The State of the Art," *Tire Science and Technology*, TSTCA, Vol. 3, No. 3, pp. 196-210.
- Powell, E. F., (1957), "Testing High Speed Tires," *SAE Journal*, pp. 25-27.
- Rhyne, T. B., Gall, R., and Chang, L. Y., (1994), "Influence of Rim Run-Out on the Nonuniformity of Tire-Wheel Assemblies," *Tire Science and Technology*, TSTCA, Vol. 22, No. 2, pp. 99-120.
- Ridha, R. A. and Clark, S. K., (1981), Chapter 7: Tire Stress and Deformation, Mechanics of Pneumatic Tires, Editor: Clark, S. K., U.S. Department of Transportation National Highway Traffic Administration, U.S. Government Printing Office, Washington, D.C., pp. 490.
- Rivlin, R. S., (1956), "Large Elastic deformations," in "Rheology: Theory and Applications Vol. 1," Academic Press, New York.
- Rother, H., Idelberger, H., and Jacobi, W., (1984), "On the Finite Element Solution of the Three Dimensional Tire Contact Problem," *Nuclear Engineering and Design*, Vol. 78, pp. 363-375.
- Sakai, E. H., (1995), "Measurement and Visualization of the Contact Pressure Distribution of Rubber Disks and Tires," *Tire Science and Technology*, TSTCA, Vol. 23, No. 4, October-December, pp. 238-255.
- Scavuzzo, R. W., Richards, T. R., and Charek, L. T., (1993), "Tire Vibration Modes and Effects on Vehicle Ride Quality," *Tire Science and Technology*, TSTCA, Vol. 21, No. 1, pp. 23-39.
- Schmeitz, A. J. C., Jansen, S. T. H., Pacejka, H. B., Davis, J. C., Kota, N. N., Liang, C. G., and Lodewijks, G., (2004), "Application of a Semi-emphirical Dynamic Tyre Model for Rolling over Arbitrary Road Profiles," *Internal Journal of Vehicle Design*, Vol. 36, Nos. 2/3, pp. 194-215.
- Schuring, D. J., (1976), "Dynamic response of Tires," *Tire Science and Technology*, TSTCA, Vol. 4, No. 2, May, pp. 115-145.

- Shaw, M. C. and Young, E., (1988), "Rubber Elasticity and Fracture," *Journal of Engineering Materials and Technology*, Vol. 110, No. 3, pp. 258-265.
- Sui, J. and Hirshey, J., (1999), "Evaluation on Analytical Tire Models for Vehicle Vertical Vibration Simulation Using Virtual Tire Testing Method," *SAE Paper 1999-01-0786*.
- Takayama, M., and Yamagishi, K., (1984), "Simulation Model of Tire Vibration," *Tire Science and Technology*, TSTCA, Vol. 1, No. 1, pp. 38-49.
- Tekscan, (2006), Pictures retrieved from the website:
http://www.tekscan.com/industrial/tirescan_system.html
- The Evolution of the Wheel, (2006), A historical retrospective, Retrieved from the website: <http://www.ohtm.org/wheel.html>
- Tielking, J. T., (1984), "A Finite Element Tire Model," *Tire Science and Technology*, TSTCA, Vol. 11, No. 1-4, January- December, pp. 50-63.
- Tire and Rim Association Year Book, (1996), Tire and Rim Association, Inc.
- Treolar, L. R. G., "The Physics of Rubber Elasticity," 2nd Ed., Oxford University Press, England.
- Trivisonno, N. M., (1977), "Applications of Tire Thermograph to Rolling Resistance," Tire rolling losses and fuel economy, an R & D Planning Workshop, October 19-20, series SAE conference proceedings P-74. pp. 103-109.
- Tseng, N. T., Pelle, R. G., and Chang J. P., (1989), "Finite Element Simulation of Tire-rim Interface," *Tire Science and Technology*, TSTCA, Vol. 17, No. 4, pp. 305-325.
- Tunis, E., (2002), Wheels: A Pictorial History, Johns Hopkins University Press.
- Turner, D. M., (1954), "Wave Phenomena in Tires at High Speeds," *Proceedings of the Rubber Technology Conference*, pp. 735-748.
- Varga, O. H., (1966), Stress-Strain Behavior of Elastic Materials, Wiley, New York.
- Vehicle Dynamics Terminology, (1978), SAE J670e, *Society of Automotive Engineers*.
- Volvo 3P, (2004), Volvo Tire Model, Sweden.
- Weber, R. and Persch, H. G., (1976), "Frequency Response of Tires-Slip Angle and Lateral Force," *SAE Paper 760030*.

- Wilson, E. A. and Parsons, B., (1970), "Finite Element Analysis of Elastic Contact Problems using Differential Displacements," *International Journal of Numerical Methods in Engineering*, Vol. 2, pp. 387-395.
- Wong, J. Y., (2001), Theory of Ground Vehicle, 3rd Edition, John Wiley & Sons, Inc.
- Wu, G. Z., and He X. M., (1992), "Effects of Aspect Ratio on the Stresses and Deformations of Radial Passenger Tires," *Tire Science and Technology*, TSTCA, Vol. 20, No. 2, pp. 74-82.
- Yan, X., (2003), "Nonlinear Three-Dimensional Finite Element Analysis of Steady Rolling Radial Tires," *Journal of Reinforced Plastics and Composites*, Vol. 22, No. 8. pp. 733-750.
- Yan, X., (2005), "Finite Element Formulation of Tire with Static Foundation Contact and Its Application," *Journal of Reinforced Plastics and Composites*, Vol. 24, No. 16, pp. 1671-1696.
- Yap, P., (1991), "Measurement of Radial Truck Tire Dry Cornering Characteristics," *SAE Paper 912677*.
- Yeoh, O. H., (1990), "Some Forms of the Strain Energy Function for Rubber," *Rubber Chemistry and Technology*, Vol. 63, No. 5, pp 792-805.
- Yeoh, O. H., (1993), "Characterization of Elastic Properties of Carbon-Black-Filled Rubber Vulcanizates," *Rubber Chemistry and Technology*, Vol. 66, No. 5, pp 754-771.
- Zegelaar, P. W. A. and Pacejka, H. B., (1997), "The In-Plane Dynamics of Tyres on Uneven Roads," *Vehicle System Dynamics Supplement*, Vol. 25, pp. 65-79.
- Zegelaar, P. W. A. and Pacejka, H. B., (1997), "Dynamic Tyre Responses to Brake Torque Variations," *Vehicle System Dynamics Supplement*, Vol. 27, pp. 65-79.
- Zhang, X., Rakheja, S., and Ganesan, R., (2001), "Estimation of tire-road contact pressure distribution based on nonlinear finite element analysis", *Heavy Vehicle Systems, Series B, International Journal of Vehicle Dynamics*, Vol. 8 No.3/4, pp. 197-217.
- Zhang, X., Rakheja, S., and Ganesan, R., (2001), "Estimation of Tire-Road Contact Pressure Distribution Based on Nonlinear Finite Element Analysis," *International Journal of Heavy Vehicle Systems*, Vol. 8, No. 3/4, pp. 197-217.

Zhang, Y. and Hazard, C., (1999), "The Effects of Tire Properties and Their Interaction with the Ground and Suspension with the Ground and Suspension on Vehicle Dynamic Behavior-A Finite Element Approach," *Tire Science and Technology*, TSTCA, Vol. 27, No. 4, October-December, pp. 227-249.

Zhong, Z., (1988), "On Contact-Impact Problems," Thesis 178, Department of Mechanical Engineering, Linköping University, Linköping, Sweden.

APPENDIX A

SIDEWALL DAMPING COEFFICIENT CALCULATION

This Appendix A is obtained from Chang's Ph.D. Thesis, Section 8.2.5, which is for the calculation of the mass-proportional damping coefficient at the sidewall region of Chang's FEA passenger car tire model. New damping coefficient for the FEA truck tire model is calculated by using the same equations as shown in Chang's Thesis.

From literature survey (Kamoulakos and Kao, 1998; Kao and Muthukrishnan 1997), the tire damping effect ranges from 5 to 70 percent of critical damping through trial and error process. Therefore, the tire damping effect needs more advanced studies in the future.

In this research, a 5 percent critical damping was adopted in the tire model. The equation of motion of an n-DOF system with viscous damping and arbitrary excitation $F(t)$ can be presented in the form as:

$$M\ddot{X} + C\dot{X} + KX = F \quad (B-1)$$

With the homogeneous equation as:

$$M\ddot{X} + C\dot{X} + KX = 0 \quad (B-2)$$

The traditional approach is to assume a solution of the form

$$X = X_0 e^{st} \quad (B-3)$$

Upon the substitution into the differential equation (B-2) will result in:

$$(Ms^2 + Cs + K)X_0 e^{st} = 0 \quad (B-4)$$

which will be satisfied for all values of t when

$$s^2 + \frac{C}{M}s + \frac{K}{M} = 0 \quad (B-5)$$

Equation (B-5) is known as the characteristic equation with two roots:

$$s_{1,2} = -\frac{C}{2M} \pm \sqrt{\left(\frac{C}{2M}\right)^2 - \frac{K}{M}} \quad (B-6)$$

In the limiting case, when $\left(\frac{C}{2M}\right)^2 = \frac{K}{M}$, the radical is zero. The damping corresponding to this case is called critical damping, C_c :

$$C_c = 2M\sqrt{\frac{K}{M}} = 2M\omega_n = 2\sqrt{KM} \quad (B-7)$$

Theoretically, any damping can then be expressed in terms of the critical damping by nondimensional numbers ζ , called the damping ratio:

$$\zeta = \frac{C}{C_c} \quad (B-8)$$

Rayleigh introduced proportional damping in the form with constants α and β :

$$C = \alpha M + \beta K \quad (B-9)$$

In PAM-SHOCK, only the mass-proportional damping was formulated, which will degenerate equation (B-9) to a simpler form as:

$$C = \alpha M \quad (B-10)$$

Substitute equations (B-7) and (B-8) into (B-10) will get

$$C = \alpha M = \zeta C_c = \zeta 2\sqrt{KM} \quad (B-11)$$

Where $\zeta = 5\% = 0.05$, is a 5 percent critical damping effect; and $\omega = 73$ Hz, derived from chapter 5. These will result in the damping coefficient α as:

$$\alpha = \frac{\zeta 2\sqrt{KM}}{M} = \zeta 2\sqrt{\frac{K}{M}} = \zeta 2\omega = 0.05 \times 2 \times (2\pi \times 73) = 45.9 \approx 46 \quad (B-12)$$

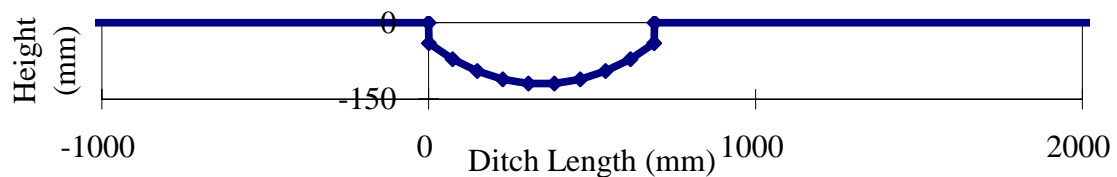
Therefore a damping coefficient of 46 was introduced to the sidewall region in the FEA tire model in this research to simulate the damping effect.

APPENDIX B

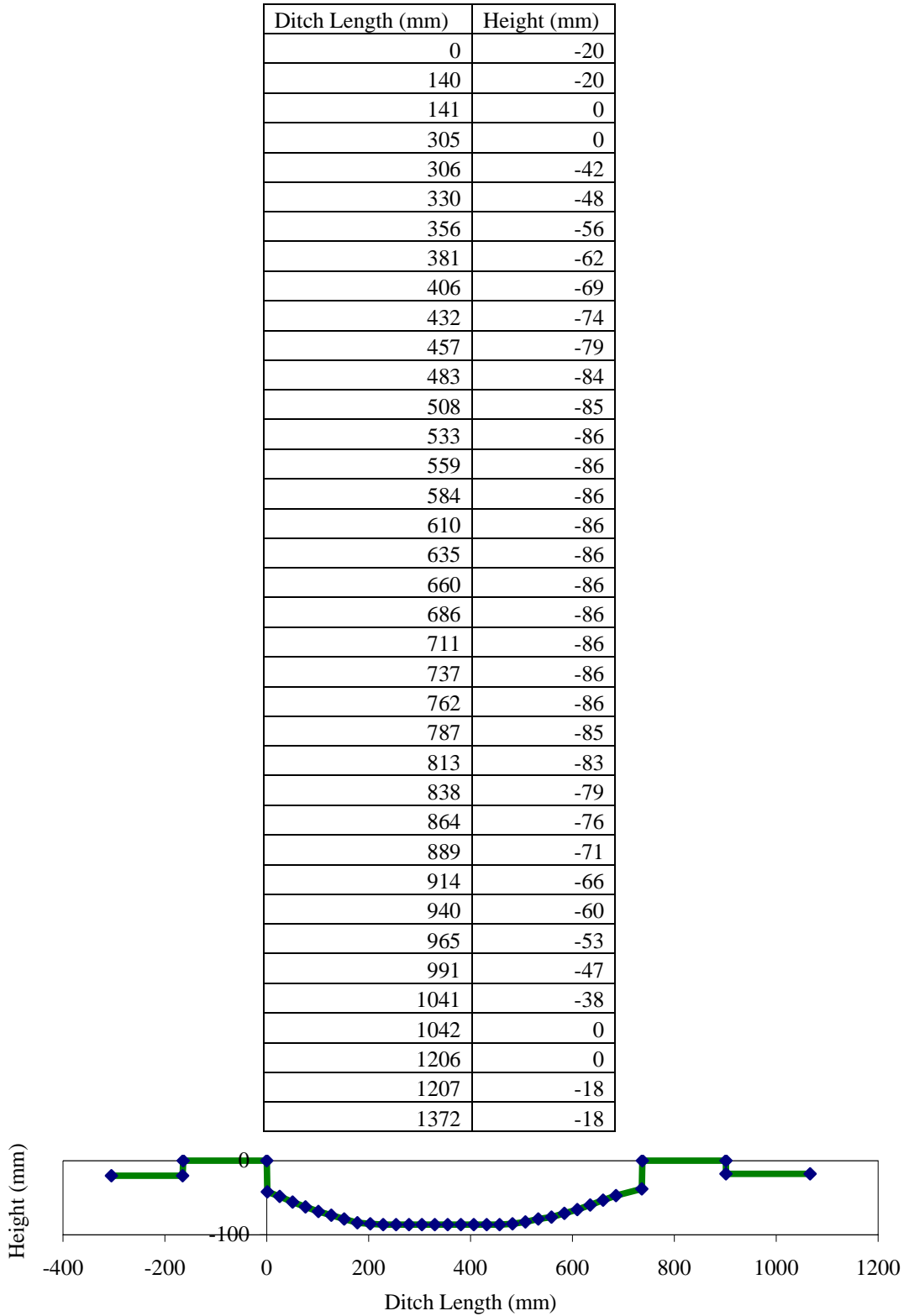
DIGITIZED DITCH PROFILES

1. 690 mm-long and 120 mm-deep ditch

Ditch Length (mm)	Height (mm)
-10000	0
0	0
1	-40
73	-71
149	-95
226	-111
305	-119
385	-119
464	-111
541	-95
617	-71
690	-40
691	0
20000	0



2. 736 mm-long and 86 mm-deep ditch



VITA

Seokyong Chae

Seokyong Chae was born in Daegu, Republic of Korea on March 23rd, 1969, as the youngest son amongst two sons and two daughters of Jungmin Chae and Taesun Son.

He received his B.S. degree from Department of Mechanical Engineering, Yeungnam University, Korea, in March 1993 and his M.S. degree from Department of Mechanical Engineering, the Pennsylvania State University, United States, in December 1997.

He joined the Vehicle Crash and Safety Research Center at the Pennsylvania Transportation Institute (PTI) in 1998 and had been involved many crash tests against roadside barriers for two years. Thereafter, he was also involved in various funded research projects: 1) Cornering characteristics of DaimlerChrysler tractor-semitrailers, 2) Transit bus, motor coach, and tractor-semitrailer axle weights study, 3) Kingpin load of a US Navy tractor-semitrailer, 4) Model validations of two US Army combat vehicles stability tests, and 5) FEA truck tire model durability tests.

He had been assigned as a teaching assistant on many undergraduate level courses from the Department of Mechanical Engineering since 1997 for two years. He moved to the Intercollege Graduate Program in Materials in 2000. Since then, he has conducted various FEA tire models and vehicle crash test simulations for his doctoral study.

He will begin his first professional career at R&D division of Hyundai Motors in Korea in July 2006.